The Pennsylvania State University
The Graduate School
College of Engineering

INVESTIGATION OF SURF-ZONE PLUMES WITH A TWO-DIMENSIONAL BISTATIC LIDAR AND THE POLARIZATION RATIO METHOD

A Thesis in
Electrical Engineering
by
Christophe F. Bas

Submitted in Partial Fulfillment
of the Requirements
for the Degree of

Doctor of Philosophy

May 2002

We approve the thesis of Christophe F. Bas

Date of Signature

_____	_____
C. Russell Philbrick Professor of Electrical Engineering Thesis Advisor Chair of the Committee	
_____	_____
Nirmal K. Bose HRB-Systems Professor of Electrical Engineering	
_____	_____
Craig F. Bohren Distinguished Professor Emeritus of Meteorology	
_____	_____
Kenneth L. Davidson Professor of Meteorology Naval Postgraduate School Special Member	
_____	_____
Stewart K. Kurtz Murata Professor of Material Research Professor of Electrical Engineering	
_____	_____
W. Kenneth Jenkins Professor of Electrical Engineering Head of the Department of Electrical Engineering	

ABSTRACT

A vertically fanned argon-ion laser beam revealed tall plumes suspended over surf zones during Electro-Optical Propagation Assessment in Coastal Environments (EOPACE) experiments. A simple (albeit versatile) non-iterative estimator using the polarization-ratio method was derived and then applied to images taken by two distant CCD cameras to estimate the aerosol concentrations over the surf zone near the Pier of the Scripps Institution of Oceanography (La Jolla, CA). The use of this estimator bypassed the need for both calibration and a first guess, but required the postulation of an aerosol model such as the Hybrid Coastal Aerosol Model (HCAM). HCAM modified the Navy Oceanic Vertical Aerosol Model (NOVAM – a multimodal aerosol model designed for open-ocean use) for optical use and for an additional suspected mode radius at 15 micrometers. HCAM fulfilled three goals: (1) delivery of a baseline of concentrations expected over the open ocean, (2) estimation of concentrations over the surf zone by applying a best fit of HCAM onto rotorod data, and (3) determination of the reliability of the concentrations estimated by the polarization-ratio method. Once the two-dimensional concentrations estimated *via* the polarization-ratio method were reduced to a most-likely value, the estimated concentrations (on average) revealed an increase in concentrations by 57% (mode 2) and by a factor of 6 (mode 3), as compared to the baseline concentrations, while falling below those from the HCAM fits by 38% (mode 2) and by a factor of 46 (mode 3). Similarly, extinction estimations from the polarization-ratio method slightly exceeded those from the baseline by 27% (on average). Those results confirm both the success of the polarization-ratio method at statistically estimating concentrations within the self-consistent framework of HCAM and the role of the surf zone as a source of aerosols. The two-dimensional estimated concentrations described inconclusive shapes. This result is attributed to the inhomogeneity of the concentrations over the surf zone, to atmospheric motion, and to errors associated with applying HCAM over the surf zone.

TABLE OF CONTENTS

LIST OF FIGURES

LIST OF TABLES

PREFACE

When questioned by family members and friends about the topic which has occupied the last few years of my life, I found myself in the humbling situation of vulgarizing my work. To the *naïve*, this thesis reinvents the wheel the same way as car makers reinvent cars. It addresses overlooked details pertaining to the ability of an instrument to tell an accurate story.

The problem refers to the use of light to remotely obtain information about the concentration of water droplets (spherical objects) in tall structures above surf-zones. These water droplets needed to be measured remotely because *in-situ* measurements would have both perturbed the environment in which these droplets evolved and limited the extent of their observation. Their motion is of interest to micrometeorologists. Their interaction with light is of interest to us.

The instrumental method is based on the variation of optical energy scattered toward two CCD cameras upon a change by 90° in the linear polarization of the incident energy. Stevens (1996) used the ratio of these two scattered fields (called the polarization ratio method) along a horizontally illuminated line while assuming homogeneity in the characteristics of the scatterers. The experimental images to analyze were no longer of one dimension but two as the captured energy from the scattering off of a fanned beam revealed considerable inhomogeneity. Hence, it became necessary to reduce the volume simultaneously studied which, in turn, enhanced the role of noise in the determination of the concentrations. "Noise" has been defined as anything which prevented the polarization ratio from giving the correct answer.

After several versions of Chapters 1 and 2, the refinement of the instrument in its retrieval of the concentrations to uncertainties became the focus of this thesis. This goal required postulating a model for the scatterers to study their relationship to the instrument and the observed images.

Several assessments of the tradeoffs among computational accuracy, speed, stability, and adjustability of the aerosol models led to the selection of one similar to NOVAM (a Navy aerosol model - cf. Chapter 2) appended by both molecular species and a 15 μm mode-radius distribution made of ejected water droplets, resulting in the Hybrid Coastal Aerosol Model (HCAM). HCAM follows NOVAM, except in the determination of the concentrations (HCAM uses both the captured images and a restricted set of micrometeorological measurements whereas NOVAM uses micrometeorological measurements exclusively). A parametric fit of HCAM onto rotorod (a particle air sampling device) data determined typical concentrations under which the stability of the instrument was analyzed. The fitted HCAM distributions revealed the limitations of the model to follow the smooth curves of the measurements. Even

though it might have been preferable to allow all the distribution parameters to be adjustable (concentrations, mode radii, and mode logarithmic-variances) three major difficulties rejected this implementation: (1) the degree of freedom of this model introduced discontinuities between consecutive measurements (2) the estimators for those parameters rely on a subjective good first guess, and (3) the accuracy of the $F(\theta,\varphi)$ function (cf. Chapter 2) for each distribution had to be sacrificed to the benefit of computational speed.

Once HCAM defined and typical concentrations extracted from the fits, scattering functions were computed to reproduce the amount of expected radiant energy recorded by CCD cameras which, subsequently, was processed by two estimators to attempt retrieval of the original concentrations. These newly designed estimators were compared. The estimation process has been made linear by parts, but is not linear when considered as a whole (hint: polarization **ratio**). Hence, error bars could not be derived along the estimated concentrations which is my biggest frustration. Estimation of the typical concentrations under idealized conditions already proved to be difficult. Noise has been categorized either as deterministic or stochastic. The former included uncertainties due to the instrument (transmittance through the retarder plate, angle made by the vertical laser sheet with respect to the shore line oriented from South to North, offset in counts in the captured images, and alignment of the electric field with the true local vertical). The latter included uncertainties combining both instrumental and environmental sources resulting in CCD fluctuations originating either in processes internal to the CCD or in external atmospheric motion while the camera shutter remains open. Relatively small quantities in either deterministic or stochastic noise significantly influenced the retrieved concentrations. Dr. Earle Williams of MIT-Lincoln Laboratory (Bedford, Massachusetts) suggests increasing the signal-to-noise ratio (SNR) by using a pencil beam reflected off of a faceted rotating mirror instead of fanning the beam, in future experiments.

Application of the algorithm to the images resulted in distribution of concentrations which logarithmically agreed with those from fitting aerosol distribution curves onto the rotorod data, although areas of negative concentrations appeared. Time between the capture of images of complementary polarizations has become a challenge motivating the design of the next generation of instruments.

This thesis has been written with the intent to be accessible to readers who want to understand, use, or refine the polarization ratio method, but who may not necessarily be experts. To this aim, only bare-bone references have been included (also to avoid cluttering the document).

It has been my experience that general statements vaguely supported by approximate equations without explicit assumptions result not only in a frustrated reader but also in errors of interpretations by

authors themselves. Despite a risk in decreasing accessibility of the material, I preferred to let equations speak for themselves within a context of assumptions. Science is a domain in which physically-based mathematical-arguments are more convincing than hand-waving explanations. This statement does not reject contrasting observations to mathematical expressions, but it requires that interpretations be contained within a physical context, supported by mathematical tools. In some instances, physical phenomena have been deliberately excluded (often due to their computational complexity). The reader is encouraged to read the corresponding results as a best case. The examples which I have in mind are the rejection of both diffraction at the CCD cameras and beam divergence, in the simulations of Chapter 3.

The road to completing a thesis is winding. I strolled along with many people. I thank Dr. C. Russell Philbrick (The Pennsylvania State University, Department of Electrical Engineering), my thesis advisor, for encouraging me to become a “curious observer.” I deeply thank Dr. Craig F. Bohren (The Pennsylvania State University, Department of Meteorology) whose guidance made each verbal stroll a motivating lesson in ethics and integrity. Dr. Nirmal K. Bose (The Pennsylvania State University, Department of Electrical Engineering) has been a role model in mathematical rigor and determination. Dr. Kenneth L. Davidson (The Naval Postgraduate School, Monterey, CA, Department of Meteorology) has been a strong motivator, subtly influencing many parts of the material. Also, I wish to thank Dr. Stewart K. Kurtz (The Pennsylvania State University, Department of Electrical Engineering) for contributing to the discussion of the logarithmic widths of aerosol models and the calculation of the F-functions. In the Lidar Laboratory of the Electrical Engineering Department, I wish to thank Steve Esposito and Gregg O’Marr who have collected 610 Mbytes of images which I processed to assess both noise effects and non-linearity of the MEADE cameras containing cooled Kodak chips. The data from the EOPACE experiments were collected at different instances by Dr. Daniel Lysak, Jr., Dr. Franz Balsiger, Dr. Timothy Stevens, Michael O’Brien, William Durbin, Savyasachee Mathur, Thomas Petach, and Glenn Pancoast.

Within the Department of Electrical Engineering, at Penn State, I have learned from Dean Dr. Burton, former head of the Department, Dr. Mitchell with whom I have taught a few classes, Dr. Croskey, Dr. Kane, and Dr. Ruf for their past research cooperation. In the Department of Meteorology, Dr. Thomson (former Head of Department), Dr. Wyngaard, Dr. Bannon, Dr. Fraser, and Dr. Clark have been strong stimulators of my interest in micrometeorology and meteorology associated with the difficulties of remote sensing.

Within the Scripps Institution of Oceanography (SIO), two key players have helped the current work to come to maturity. Ron van Boxten, Facilities Manager at the SIO, has been a sharp sounding board from the very beginning. Mode 4 of HCAM would have had a blind index of refraction without the

diligent search by Connie L. Fey throughout the SIO databases for salinity and sea-surface temperatures measured near the pier.

At the Naval Postgraduate School in Monterey, CA, I wish to thank Dr. Jerry Lenz who reminded me of a few rules of thumbs, one of which was incorporated in Chapter 2.

Upon joining the Raytheon Systems Company in August 1998 I have had the chance to learn about estimation theory to investigate and correct error parameters in the performance of the Theater High Altitude Area Defense (THAAD) radar. It was a challenging and exciting job within the context of which I have benefited from the teachings of my boss, Dennis Nieskoski, to whom I am grateful. Thanks shall also be extended to Daniel Odom for helping me develop a "nice warm feeling" about the present work.

At the MITRE Corporation, which I joined in January 2001, I wish to thank both my current boss, Moise Solomon, for constantly asking about the status of the present work and Dr. Lisa Costa whose position on "living the problem to solve the problem" I have come to swear by.

On a more personal note, this thesis would have never seen the day without the attentive guidance from Drs. John and Jeannette Esposito who have been more than "cultural parents" to me. Subtly, Drs. John and Sarah Voll have deeply influenced the present work (…). Finally, suggestions, patience, and encouragement from my wife, Natana, made the long road toward completion of the present work a constructive time strengthening our relationship. Our daughter, Aurora, and our son, Gabriel, have been a constant source of diversion and entertainment which, at times, was necessary.

Christophe F. Bas
Bedford, Massachusetts
September, 2001

CHAPTER 1
RAISON D'ÊTRE

1.1 Introduction

Micrometeorological and meteorological processes of coastal areas need to be better understood. This realization initiated a study on coastal meteorology written by the National Research Council (U.S.) Panel on Coastal Meteorology (1992).

Atmospheric transport and diffusion models which have been designed around idealized coastlines need to be improved to be applicable to actual ones. Advected salt-water droplets, a major coastal aerosol, originate from breaking waves, bursting bubbles, and shearing of wave crests. Kraus and Businger (1994, p.68) quote Erikson who estimates that 1000 million tons of salt are yearly passed into the atmosphere from the oceans through these processes. Damage sustained by Swedish coniferous forests is attributed to the deposition of salt-water droplets (Gustafsson and Franzén, 1996). As coastlines change[1], their orographic influence on the structure of the Coastal Atmospheric Boundary Layer and its ability to disperse both aerosols and pollutants remains largely unknown.

Electro-Optical Propagation Assessment in Coastal Environment (EOPACE) is a North Atlantic Treaty Organization (NATO) project designed to answer some of these concerns and more. One aspect of EOPACE deals with the degradation in performance of optical devices in coastal areas due to the presence of coastal aerosols (Kiser, 1997). Navy models designed to predict optical extinction over the open ocean have performed inadequately in coastal areas (Gathman, 1992).

1.2 History, motivation, and objectives

EOPACE participants have recorded various experimental data: both meteorological and micro-meteorological (temperature, relative humidity, barometric pressure, wind, etc.), oceanographic (wave height, tide, etc.), aerosols (size distribution, concentration, etc.), and transmittances (optical and IR transmissiometers, etc.).

[1] A recent report ("Coastal cautions: Sea panel at work," 2001) has updated the estimation of the U.S. population living near coastlines by the end of the millennium to two-thirds from its original projection of one half.

The Applied Research Laboratory at The Pennsylvania State University (ARL/PSU) joined as a participant in the EOPACE project with the goal of determining the distributions of coastal aerosols in order to compute extinction along any path. Fanning a laser beam to illuminate aerosols above the surf zone revealed the tall structures which are shown in Figure 1. It has been speculated that these plumes were the reasons for the shortfall of the Navy aerosol models. Kiser (1997) analyzed correlation among the plume features, the environmental conditions, and the transmittance across the surf zone without addressing the Navy aerosol models.

When the author joined the lidar (a laser radar) group of ARL/PSU in the Summer of 1996, plumes had just been observed for the first time over a surf zone (Hooper and Martin, 1999, captured similar images using a monostatic lidar) and their images recorded both at the Scripps Institution of Oceanography (La Jolla, California) and at Moss Landing (near Monterey, California). Stevens' (1996) approach on the use of the polarization-ratio method to determine aerosol size-distributions along a horizontal line (both in stationary and homogenous conditions) was found inapplicable to EOPACE images. The purpose of the present study is to understand the limitations of the polarization-ratio method, to enhance its performance, and to apply the improved technique to EOPACE images to estimate aerosol concentrations over the surf zone.

Figure 1. Representative sample of surf-zone plumes taken at the Scripps Institution of Oceanography (La Jolla, CA) when illuminated by a vertically fanned argon-ion laser. (Photo by C. R. Philbrick.)

Three main steps ensure reaching this goal. The first one introduces the EOPACE context (Chapter 2). The second one investigates the possibilities of the duo polarization-ratio method and concentration estimator, including its performance in non-ideal situations (Chapter 3). The third one estimates the content of EOPACE averaged plumes (Chapter 4).

1.3 Organization

The purpose of an organization is to build a structure around the present analysis both to guide the reader and to document improvements drawn from the author's work. Whenever appropriate, comparison with other authors' techniques are carried out.

The first objective consists of tracing the fate of photons from their transmission to their storage as images. Their path encounters (1) a scattering environment and (2) the influence of the instruments. The former is modeled by the Hybrid Coastal Aerosol Model (HCAM), a combination of the Navy Aerosol Model (Gathman, 1983) and the Navy Oceanic Vertical Aerosol Model (Gathman and Davidson, 1993) appended by a new distribution of scatterers suspected of contributing to the plumes (where both single scattering and elastic scattering by spherical particles is postulated). Other variables (such as the location of devices) are ultimately related to the recorded radiant energy through scattering.

The second objective consists of three sub-objectives: (1) definition and limitations of the polarization ratio, (2) derivation of estimators of the aerosol concentrations from measurements, and (3) assessment of the complementary types of noises and their independent effects on the quality of the estimated concentrations. Subsequent analyses show that selected restrictions on the general expression of the polarization ratio can lead to expressions which yield little to no information about the aerosol concentrations. In other analyses, sources of noise also represent uncertainties whose influences are assessed via simulations (inside a controlled environment). Such an extensive study is being carried out for the first time within the context of the polarization ratio.

The third objective consists of applying the most successful method tested in the second objective to the EOPACE images of the mean plumes to estimate their aerosol concentrations as precisely as possible, toward both the calculation of extinction along any path across them and the correlation between those concentrations and micrometeorological conditions. The method includes assessment of the nature and quantity of noise, extraction of statistical parameters at each pixel for each camera at each polarization, and verification of relevant assumptions. Similarity between both estimated aerosol distributions (one from the optical data and one from simultaneous measurements taken by rotorods – devices designed to collect air particles, de Leeuw, 1986 – over 30 minute intervals) attests to the degree of success of each recovery.

Another originality in the present work is its application to a laser fan rather than a laser beam. This unusual geometry generalizes the algorithm reconstructing the scattering angles (defined in Section 2.3) from measuring strategic locations (such as those of the cameras, the laser, etc.) at the cost of making the mathematics tedious. For comparison, Stevens (1996) positioned his camera at a precisely-measured position whose height matched that of the laser beam.

The present organization directs the content of subsequent chapters. Details are revealed as analyses are carried out. Accomplishments, difficulties, and foreseeable solutions are listed in the conclusion (Chapter 5).

1.4 Introduction to the polarization-ratio method

The polarization ratio method has two major advantages over conventional remote-sensing techniques to acquire concentrations. First, effects introduced by the instrumentation ideally vanish, rendering calibration unnecessary. Second, information about a scattering volume of interest is ideally independent from any other scattering volume along the path, including the definition of volume.

Light scattered by an illuminated volume depends on the properties of the incident illumination, those of the scatterers, and the direction of observation. The incident illumination is characterized by its irradiance, frequency (or wavelength), and polarization. The scatterers are characterized by their complex indices of refraction (intimately related to their chemical composition), concentrations, shapes, and sizes.

The first advantage assumes that the devices making the instrument are polarization independent so that the recorded energy (i.e., irradiance incident onto a detector surface over a finite period of time) is equally affected by emitter and receiver imperfections at two complementary polarizations[2]. If the imperfections slowly change with respect to two finite periods of time needed to capture consecutive images (one at each polarization), the ratio of intensities contains approximately the same multiplicative factor at both the numerator and denominator, resulting in its cancellation. But caveats complicate this oversimplification. Internally, CCD detectors have shown non-linear behavior and self generation of inhomogeneous counts, in addition to manufacturing imperfections (Janesick et al., 1987). Externally, at the emitter, a retarder plate exclusively introduced to generate the horizontal outgoing polarization from the vertical outgoing polarization violates the operational symmetry of the instrument.

[2]One polarization is called parallel (linearly) and the other one is called perpendicular (linearly). Chapter 2 clarifies the frame of reference associated with those two adjectives.

The second advantage assumes that the total amount of radiant energy removed between the emitter and the receiver, scattering by the volume of interest excluded, remains constant over the recording of consecutive images at complementary polarization. But, again, caveats complicate this oversimplification. Atmospheric motion which entrains the scatterers during the capture of the images of complementary polarizations may violate this assumption.

If taken for granted, these two *a-priori* advantages bias the estimation process due to the additional noise injected by each one. The first example displays a DC-type noise (i.e., an offset) whereas the second one is AC-type (i.e., fluctuations around a mean). Other sources of noise exist. Evaluation of the tolerable amount of noise to ensure that a satisfactory level of accuracy be met in the estimation of the parameters describing the scatterers is essential to assess the credibility of this EOPACE instrument. This is the *raison d'être* of the present document.

1.5 The ARL/PSU EOPACE-instrument (hardware)

The bi-static two-dimensional lidar consisted of an argon ion American Laser Model 909 (continuous wave of 1.3 W at 514.5 nm), two MEADE low-noise (electrically cooled) sensitive (16 bits) CCD cameras (with a Kodak KAF-0400 CCD-array of 768x512 pixels) and one SONY digital video camera (DCR-VX700). One cylindrical lens reference 01 LCN 123 by Melles Griot. Two spectral filters centered around 514.5 nm, lenses of variable focal lengths, a mirror, and one retarder plate whose general features are known (although its specific references are not).

Other indirect devices included one video camera for partial documentation and a theodolite to measure, indirectly, the locations of the lidar, the cameras, and a reference point. The reference point helped determine the orientation of the cameras.

The images were recorded by two independent MEADE CCD-cameras in a 16-bit TIFF-format using MEADE's software in Windows 3.11 via SCSI cards on two 120 MHz Pentium computers. At a later date, they were transferred onto CDROMs.

1.6 Organization of the present document

Chapter 1 presents both objectives and methods thereafter addressed then refined, while underlining novelties of the present work whose completion is split into three chapters to which a concluding chapter is appended.

Chapter 2 answers the first objective by reviewing, enhancing, and mathematically expressing concepts helpful in reaching subsequent objectives. It covers the Navy aerosol models, HCAM, the molecular background atmosphere, light scattering, the expressions for the scattering angles from the reconstructed experimental set-up, and the calculation of the scattering functions over the experimental range of angles.

Chapter 3 includes the design of a method to estimate aerosol concentrations using the polarization ratio method, properties of the polarization ratio method, and robustness of the recovery to both deterministic and stochastic noise. It also includes both the design of two estimators and their comparison.

Chapter 4 applies the most successful estimation-technique from Chapter 3 to the EOPACE data and compares the estimated concentrations (and extinction values) to those both from the rotorod data and NOVAM to assess the credibility of the instrument.

Chapter 5 concludes on both the accomplishments and use of the present work, and then describes the desirable evolution of the present instrument for subsequent experiments.

1.7 Conclusion and motivation for subsequent chapters

The advantage of the bi-static lidar set-up is to have captured two-dimensional pictures of the surf-zone plumes (without having disturbed their motion) whose content is suspected to affect significantly transmission of optical energy. These images constitute unique documents of the plumes.

Chapter 2 dispels the notion that the plumes would be exclusively associated with changes in concentrations over the narrow range of angles captured by the cameras by showing that scattering by homogeneous aerosol concentrations generate features which look like plumes. These features are introduced by changes in both the scattering angle and outgoing polarization, at a fixed laser wavelength. Actual observations results from the combination of those features (as homogeneity in concentrations is likely never met over the surf zone) and changes in concentrations.

The present research further suggests a method of organization which encompasses pre-experimental, experimental, and post-experimental phases. The pre-experimental phase (highly recommended for proposals) consists of gathering information on scatterers likely to be encountered, of running simulations on the scattered intensities so as to assess the potential success of the instruments to achieve reliable estimates using the polarization ratio, and optimizing their locations. The experimental phase consists of confirming the pre-experimental information on the scatterers while allowing re-location to increase the

reliability of the estimates. The post-experimental phase consists of quantifying the amount of experimental noise to carry out the estimation from series of images, speeding-up the data-analysis task.

CHAPTER 2
PRELIMINARIES

2.1 Introduction

The present chapter qualifies and quantifies the optical processes relevant both to a conceptual and an instrumental understanding of the EOPACE images.

As light propagates above the surf zone, its scattering is observed. The composition of the scattering environment is described in Sections 2.2 and 2.4. Interaction between light and this environment is covered both in Sections 2.3 and 2.4, and subsequently discussed in Section 2.7 within the context of EOPACE. Section 2.5 reconstructs the experimental set-up toward the derivation of both the scattering and tilt angles (defined in Section 2.3). Section 2.6 touches on the topic of incident illumination when both extinction and the shape of a fanned beam are combined. Section 2.8 concludes the present chapter and motivates subsequent readings.

2.2 Aerosol models

The air above the surf zone consists of a mixture of aerosols inside a background of atmospheric molecules.

An aerosol is defined as an aggregate of molecules which forms a particle (solid or liquid) surrounded by gas, irrespectively of its lifetime or the way in which the molecules combine. General aerosols are heterogeneous and irregularly shaped. Hygroscopic aerosols change in size as they travel through atmospheric regions of different relative humidity. Soluble hygroscopic aerosols deliquesce when water condenses onto them. Non-soluble hygroscopic ones form an inner core on the surface of which water condenses. From this definition, a salt-water droplet is a soluble hygroscopic aerosol.

Analyses by Volz (1972 and 1973) of world-wide collected samples motivated classification of aerosols into sharply defined categories subsequently appended to typical distributions afterward integrated into the Air Force MODTRAN computer-program to estimate the interaction of electromagnetic radiation with atmospheric constituents (Shettle and Fenn, 1979). Starting in the 1980s, the Navy developed three generations of aerosol models: the Navy Aerosol Model (NAM) (Gathman, 1983), the Navy Oceanic Vertical Aerosol Model (NOVAM) (Gathman and Davidson, 1993), and the Advanced Navy Aerosol

Model (ANAM) (Gathman and van Eijk, 1998). All were designed to estimate the value of extinction over wavelenghts from 0.2 to 40 μm from meteorological measurements by assessing the aerosol size-distributions and their indices of refraction (an essential frequency-dependent parameter which characterizes interaction of light and matter). NAM operates at shipboard height (approximately 10 m), NOVAM extends NAM upward (up to 3 or 6 km, depending on the model version), and ANAM extends NOVAM downward to the sea surface, including rough seas and coastal areas (under development). All Navy models assume both spherical aerosols and horizontal homogeneity and use Volz's (1972, 1973) indices of refraction.

Subsection 2.2.1 reviews the Navy aerosol models. Subsection 2.2.2 argues for modifications to the Navy aerosol models to take full advantage of the optical data, resulting in the Hybrid Coastal Aerosol Model (HCAM), and Subsection 2.2.3 discusses the consequences of aerosol modeling.

2.2.1 The Navy aerosol models

An aerosol model may comprise several modes (one per aerosol size distribution). Each mode consists of a size distribution and a chemical composition, both of which are characterized by parameters whose values are derived from environmental conditions. Unless specified otherwise, those values are given at 80% relative humidity.

The Navy aerosol models contain as many as five lognormal modes distributed in radii:

$$\frac{dN(a)}{da} = \sum_{j=0}^{4} A_j \exp\left\{ - C_j \ln^2\left(\frac{a}{a_{0,j}} \right) \right\} \qquad (2.1)$$

where, for the j[th] mode, A_j represents its magnitude (in cm^{-3} μm^{-1}), C_j characterizes its width ($C_{j=0..3} = 1$ and $C_4 = 5$), and $a_{0,j}$ stands for its mode radius (in μm).

The mode radius of mode 1 is 0.03 μm. It consists of background aerosols divided into water soluble (of oceanic origin) and dry dust (of rural origin), the latter of which has become mode 0 in models after NAM. Their magnitudes depend on an empirical parameter (the Air Mass Parameter, or AMP) to quantify the oceanic and rural concentrations in a probed volume (from Radon counts)[3]. The mode radii of modes 2 and 3 respectively are 0.24 μm and 1.3 μm. They both consist of salt-water droplets whose magnitudes are

[3] The Air Mass Parameter (AMP) is calculated from Radon counts, *Rn* (in pCi m^{-3}), $AMP = \text{int}\left(Rn/4\right) + 1$.

based on a 24-hour-average and a 1-hour-average wind-speed. A range of mode radii of mode 4 has been documented between 1.3 μm (Gathman and Smith, 1997) and 15 μm (Gathman and van Eijk, 1998), although the upper bound has been chosen in ANAM. Table 2.1 summarizes the models, their versions, and their equations.

Relative humidity (RH) requires special considerations because it affects the indices of refraction, the mode radii, and the magnitudes of hygroscopic aerosols.

Its influence on the j[th] mode of the Navy aerosol model uses an *f*-factor defined in NOVAM (Gathman, 1989):

$$f_j \triangleq \frac{a_{0,j}(RH)}{a_{0,j}(80\%)} = \left(\frac{C7_j - RH/100}{C8_j\left(1 - RH/100\right)} \right)^{1/3} \tag{2.2}$$

where both $C7_j$ and $C8_j$ are empirical coefficients (cf. Table 2.2) describing the expansion or contraction of the j[th] mode radius with respect to its nominal value at 80% relative humidity.

Table 2.1. Summary of the different versions of the Navy aerosol models characterized by Eq. (2.1) where $C_j = 1$ (when $j \neq 4$) and $C_4 = 5$. Each column describes the name, version, number of modes, mode radii at 80% relative humidity (a_0), mode magnitude (A_j), and observations for each mode. AMP stands for the Air Mass Parameter (see footnote #3), $\langle u \rangle_h$ denotes the time-averaging operator over the length of time h on the instantaneous wind speed u (in m·s^{-1}) at deck height, and max{x} denotes the operator which selects the greatest number in the list x whose elements are separated by commas.

Model	Ver.	Mode	a_0 [μm]	A [cm^{-3}μm^{-1}]	Observations
NAM	1.0	1	0.03	$2000 \cdot AMP^2$	Background aerosol
(Basic		2	0.24	$\max\{0.5, 5.866(U_0-2.2)\}$	$U_0 = \langle u \rangle_{24\ hrs}$
and		3	2.00	$\max\{14 \cdot 10^{-6}, 0.01527(U-2.2)\}$	$U = \langle u \rangle_{1\ hr}$
Fortran)	2.0	All	$f \cdot a_0$	A/f	Gathman (1989)
NOVAM	1.0	0	0.03	$0\ (AMP \leq 5), 600 \cdot AMP^2\ (AMP > 5)$	Shettle & Fenn (1979)
(Basic,		1	0.03	$2000 \cdot AMP^2\ (AMP \leq 5), 1400 \cdot AMP^2\ (>5)$	Volz's B1 (1972)
Turbo		2	0.24	$\max\{0.5, 5.85(U_{24}-2.2)\}$	$U_{24} = \langle u \rangle_{24\ hrs}$
Pascal,		3	2.00	$10^{(0.06\ U_1 - 2.8)}$	$U_1 = \langle u \rangle_{1\ hr}$
and		All	$f \cdot a_0$	A/f	Except mode 0
Fortran)	2.0	All	Same	Same	MODTRAN
ANAM	Beta	0	0.03	$0\ (AMP \leq 5), 600 \cdot AMP^2\ (AMP > 5)$	Shettle & Fenn (1979)
(Fortran)		1	0.03	$2000 \cdot AMP^2\ (AMP \leq 5), 1400 \cdot AMP^2\ (>5)$	Volz's B1 (1972)
		2	0.24	$\max\{0.5, 5.85(U_{24}-2.2)\}$	$U_{24} = \langle u \rangle_{24\ hrs}$
		3	2.00	$10^{(0.06\ U_1 - 2.8)}$	$U_1 = \langle u \rangle_{1\ hr}$
		4	15.0	$g(U_{1/6})\ p(z,L)$	$U_{1/6} = \langle u \rangle_{10\ mn}$
		All	$f \cdot a_0$	A/f	Except mode 0

Table 2.2. NOVAM aerosol characteristics compiled from Gathman (1989) and Shettle and Fenn (1979). Indices of refraction (m) are at a wavelength of 514.5 nm. Mode 0 is neither hygroscopic nor soluble.

Mode	Composition	m	$C7_j$	$C8_j$
0	Dust	$1.530\text{-}i*8\text{x}10^{-3}$	N/A	N/A
1	Water soluble	$1.530\text{-}i*5\text{x}10^{-3}$	1.17	1.87
2	Sea salt	$1.500\text{-}i*1\text{x}10^{-8}$	1.83	5.13
3	Sea salt	$1.500\text{-}i*1\text{x}10^{-8}$	1.97	5.83
N/A	Water	$1.334\text{-}i*1.18\text{x}10^{-9}$	N/A	N/A

Table 2.2 displays extracted values for the indices of refraction of aerosols from Shettle and Fenn (1979). Evaporation and condensation processes are accounted for by volume averaging indices of refraction (a method used by Shettle and Fenn, 1979, and Volz, 1972). Combining the equation for the index of refraction from Shettle and Fenn (1979, p. 16) and Eq. (2.2) yields:

$$m_{RH,j} = m_{water} + \left(m_{dry,j} - m_{water}\right) \times C7_j \left(\frac{1 - RH/100}{C7_j - RH/100} \right) \tag{2.3}$$

for the value of the index of refraction of the j^{th} mode.

Once the Navy model selected and the magnitude (A_j), logarithmic width (C_j), mode radius ($a_{0,j}$), and index of refraction ($m_{RH,j}$) determined for all modes, extinction (defined in Section 2.3) through a volume containing these aerosols is calculated.

2.2.2 Necessity to adapt the aerosol models

The strengths of the Navy aerosol models are both in their classifications into chemical modes whose magnitudes depend on actual measurements and in their multimodal structure which is still applicable to coastal areas (cf. Fig. 2.1). Their limitations are found in their three major assumptions: horizontal homogeneity, parameters[4] which are either constant or whose values depend on micrometeorological conditions, and predetermined values of the indices of refraction. HCAM inherited the characteristics of the NOVAM model, but removed its dependency on micrometeorological variables, appended a molecular mode (for $j = -1$), and added mode 4 of ANAM whose dependence on relative humidity was neglected (this mode consists of droplets having just been ejected from the water surface).

[4] Those parameters also depend on the slope of the coastal sea-bottom (Zieliński et al., 1997, and Chomka and Patelski, 1997).

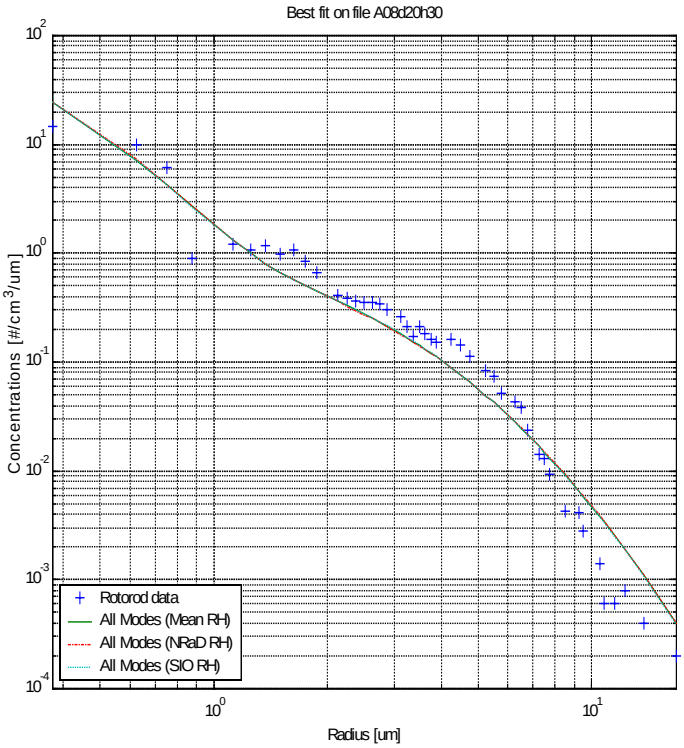

Figure 2.1. Sample data set of aerosol radial distribution (taken by rotorod on 8 April, 1997, between 20:30 and 21:00) and HCAM total distributions (Eq. 2.4). The concentrations, $n_{0,j}$, contributed by each mode were estimated by applying a best-fit procedure (in the logarithmic domain) to the rotorod data for 3 values of relative humidity (RH) (the logarithmic width, $\sigma_{0,j}$, was both set by and translated from NOVAM and the mode radius, $a_{0,j}$, was adjusted by relative humidity). The 3 curves, which mainly overlap, reveal difficulties by the HCAM model to follow the data (NOVAM encounters the same difficulty), although the data points support a multimodal aerosol model.

Indeed, doubts are cast on the legitimate use of the Monin-Obukhov similarity arguments invoked in the computation of the parameters (Panin et al., 1997) because coastal areas are inhomogeneous transitional regions. Coastal waters are susceptible to, among other factors, tides, inlet configurations, proximity to estuaries, civil engineering design, and nearby industries. Mobley (1994) refers to coastal waters as a "witch's brew," citing the yellowish brown color of dissolved organic matter (from decaying terrestrial vegetation, plankton, etc.), in addition to soil erosion (quartz sand, clay minerals, etc.) and pollution. Pollution and other chemicals react with salty particles in the marine air (Roth and Okada, 1997, and Vignati et al., 1997). Volz (1972) warns of errors up to 5% in volume averaging indices of refraction. Indices of refraction have not been measured during EOPACE experiments[5], leaving uncertainties in the data sets. Hence, assuming that the indices of refraction only depend on a combination of predetermined chemical species whose proportions are dictated by relative humidity exclusively is potentially erroneous.

[5] During Stevens' (1996) experiment, neither aerosol chemical composition nor aerosol radial distribution was measured.

Consequently, micrometeorological variables are excluded from the present analysis. Heterogeneity in the length-scales supports a local analysis of the plume content, partially explaining why Stevens' (1996) procedure has been unsuccessfully applied to EOPACE data.

The Navy aerosol models and MODTRAN slightly differ in their definitions of lognormal size-distributions, their number of modes, their sizes of the mode radii, and their logarithmic widths. The latter model allows a maximum of two modes whose expressions are closer to the statistical lognormal equation, whose mode radii (within a range from 70% to 80% in relative humidity) are 0.03 μm for continental origin and 0.3 μm (instead of 0.24 μm) for oceanic origin, whose logarithmic widths of 0.35 and 0.4 translate into 0.77 and 0.589 for NOVAM (instead of $C_j = 1, j \neq 4$). Extinction is significantly sensitive to the logarithmic width (cf. Table 2.5).

Drawing upon similarity with the statistical Gaussian function, the present analysis defines the lognormal function for the j[th] mode of the Hybrid Coastal Aerosol Model (HCAM) as:

$$\left.\frac{dN(a)}{da}\right|_j = \frac{n_{0,j}}{a\sqrt{2\pi}\,\sigma_{0,j}} \exp\left\{-\frac{1}{2\sigma_{0,j}^2}\ln^2\left(\frac{a}{a_{0,j}}\right)\right\} \tag{2.4}$$

where $n_{0,j}$ is the mode concentration (in cm^{-3}), $\sigma_{0,j}$ is its logarithmic width, and $a_{0,j}$ is its mode[6] radius (in μm). The model superposes modes -1 through 4 where modes 0 to 3 are the same as those of NOVAM, mode -1 represents the atmospheric molecular composition, and mode 4 targets water-droplets freshly ejected by breaking waves thereafter entrained above the surf zone. An equation (available in the MATLAB program called SeaRefractiveIndex in Appendix A) by Quan and Fry (1995) and Huibers (1997) confirms the magnitude of the real part of the index of refraction of water of Table 2.2 when salinity is set to 0‰. The same equation fed with both the sea-surface temperature and salinity led to the determination of the complex index of refraction of mode 4, first by estimating the real value of the index of refraction of sea-water and second by recursively determining the proportion of water to salt needed to match the real parts.

Translation of the Navy aerosol model parameters into those of HCAM is performed by equating the total number of aerosols for a single mode in Eqs. (2.1) and (2.4) and by identification:

[6] Strictly, $a_{0,j}$ denotes the median radius of mode j, but $a_{0,j}$ has the same value in both HCAM and NOVAM. The terminology introduced for the Navy aerosol models is kept.

$$n_{0,j} = A_j \, a_{0,j} \sqrt{\frac{\pi}{C_j}} \exp\left(\frac{1}{4C_j}\right) \qquad (2.5)$$

$$\sigma_{0,j} = 1/\sqrt{2C_j}$$

Translating MODTRAN into HCAM only requires multiplying the logarithmic width of the former by $\log_e(10)$; all other terms remain the same.

Physical processes generating skewed distributions tend to display a unique value for the coefficient of variation (COV, defined as the ratio of the standard deviation to the mean) as exemplified by Kumar et al (1997), Grandqvist and Buhrman (1976), Kurtz and Carpay (1980), Kurtz (1993), and Jacobson (1999). In the context of HCAM, $COV_j = \sqrt{\exp\left(\sigma_{0,j}^2\right) - 1}$ for each lognormal distribution and the uniform values for the logarithmic widths of modes 0 through 3 might overconstrain the physical processes behind the aerosol model, as it could be hypothesized from differences observed in Fig. 2.1. However, one aim of the present document is to assist ANAM in estimating the spatial distribution of the concentrations while all other parameters (including logarithmic widths) are constant.

The final structure of HCAM benefits from the maturity of the Navy aerosol models while adapting it for both optical use and coastal areas. In HCAM, the logarithmic widths are fixed, relative humidity drives the values of both the mode radii and indices of refraction (for modes 1, 2, and 3 only – the other modes already have fixed values), and concentrations are determined from optical data (except mode -1) through the use of the polarization-ratio method. HCAM is not an isolated model; its behavior and results translate into the formats of the Navy aerosol models and MODTRAN with minor calculations.

2.2.3 Conclusion

Departure from representative collections, contamination during storage, and instrumental errors all contribute to total uncertainties. The bi-static lidar skips the second error source and allows quantification of the third one via simulations (cf. Chapter 3). Discrepancies between the models and the data (cf. Fig. 2.1) raise the question as to whether data sets constitute representativeness or require modification of the model (the usual struggle between developing either a robust or a tactical model). Shettle and Fenn (1979) have acknowledged this limitation to aerosol-distribution modeling[7].

[7] "However, it must be emphasize that these models represent only a simple, generalized version of typical conditions (…) Given the natural variability of the atmospheric aerosols almost any aerosol model is supported by some measurements and no model (or set of models) will be consistent with all measurements." (p. 12)

Table 2.3. Time frames over which measurements of relative humidity (RH) by two distant sensors (independently operated by the Scripps Institution of Oceanography and NRaD) display close values, during the second experimental phase on the pier of the Scripps Institution of Oceanography, La Jolla, CA, from 31 March to 11 April, 1997. The measurements on 9 April were less stationary.

Day	Time (PST)	RH (SIO) [%]	RH (NRaD) [%]	Mean RH [%]
April 4th, 1997	20:15 - 21:45	68.7	70.1	69.4
April 5th, 1997	21:15 - 22:30	62.5	62.7	62.6
April 8th, 1997	20:15 - 21:30	77.0	78.2	77.6
April 9th, 1997	19:15 - 20:45	63.5	64.5	64.0
April 9th, 1997	19:45 - 21:00	65.3	62.9	64.1
April 9th, 1997	20:15 - 21:30	67.1	63.4	65.25
April 9th, 1997	20:45 - 21:45	68.3	66.7	67.5

The Hybrid Coastal Aerosol Model (HCAM) has been defined. HCAM concentrations are estimated using the lidar measurements via the polarization-ratio method on selected images. The estimated concentrations obtained via HCAM either depict an accurate image of the monitored environment (from representative collections) or its model equivalent (an interpretation of the measurements through the eyes of the model), otherwise. Data sets used throughout the present document (cf. Table 2.3) were selected based on minimum differences in measured relative humidity by two distant sensors along the pier.

Appendix A contains both the programs used to estimate the HCAM concentrations (without mode -1) from a best-fit onto the rotorod data of the aerosol model and the final values of all the parameters for HCAM. All rotorod channels combined cover a range in aerosol radius from slightly below 0.4 to almost 20 μm (cf. Fig. 2.1)[8]. This range delivers relatively large approximations for the concentrations of both modes 0 and 1 which are only separated by relative humidity. For instance, a maximum fractional change of 1% in relative humidity results in a maximum fractional change in concentrations (from the best-fit procedure) of 2050%, 600%, 0.4%, 1.56%, and 0% for modes 0, 1, 2, 3, and 4 (whereas the maximum fractional changes in mode radii are 0.4%, 0.72%, and 0.74% for modes 1, 2, and 3). The values of the logarithmic widths have overshadowed the concentration of mode 4 (the rotorod measurements near the radius of 15 μm are located below the HCAM line in Fig. 2.1) to its lower-bound value. Although the values of the concentrations estimated through this procedure are consistent with those estimated from the NOVAM equations (cf. Table 2.1 for equations and Appendix A for values) and those reported by de Leeuw et al. (2000) (for modes 2 and 3 exclusively), concerns subsist (Philbrick, 2002, and Bohren, 2002) that those values are much lower than those reported by other authors such as Twomey (1977) (especially for modes 0, 1, and 4).

[8] This range of radii is strictly based on the reported rotorod measurements instead of relying on the collection efficiency by those rotorods to water droplets because such a function has yet to be formulated.

2.3 Light scattering

Light scattering addresses the topic of interaction of light and matter. In EOPACE, the fanned laser-beam is scattered both by aerosols and molecules above the surf zone toward observers, including digital cameras. HCAM postulates that those aerosols are both spherical[9] and of known nature.

The purpose of the present section is fourfold: to introduce scattering notations (Subsection 2.3.1), to express scattering by spheres (Subsections 2.3.2 and 2.3.3), to define and to explore properties of extinction (Subsection 2.3.4), and to combine those concepts toward a first expression of the polarization ratio (Subsection 2.3.5). Subsection 2.3.6 concludes Section 2.3 and motivates Section 2.7 which applies those notions and expressions to EOPACE images.

2.3.1 Notations and definitions

Three points define a scattering plane: a transmitter, a scattering location, and a receiver (cf. Fig. 2.2 where the subscripts *i* and *s* refer to the incident and scattered fields, respectively). The perpendicular component of the electric field ($E_{i,r}\,\hat{e}_{i,r}$) is perpendicular to the scattering plane and the parallel component of the electric field ($E_{i,l}\,\hat{e}_{i,l}$) is inside the scattering plane. The former component is almost vertical (perpendicular to the Earth's local surface). θ_s is known as the scattering angle and φ_s will be referred to as the tilt angle.

2.3.2 Single scattering by a homogeneous sphere

Incident and scattered fields are conventionally related through the following equation (van de Hulst, 1957, and Bohren and Huffman, 1983, with different sign conventions):

$$\begin{pmatrix} E_{s,l} \\ E_{s,r} \end{pmatrix} = \frac{e^{-ik(R_s - z)}}{ikR_s} \begin{pmatrix} S_2 & S_3 \\ S_4 & S_1 \end{pmatrix} \begin{pmatrix} E_{i,l} \\ E_{i,r} \end{pmatrix} \tag{2.6}$$

where S_1, S_2, S_3, and S_4 are the angle-dependent complex-amplitude functions, z is both the direction of pro-pagation of the incident infinite plane-wave onto the scattering volume and its distance from the transmitter R_s is the distance of observation from the scattering volume, and $k = 2n\pi/\lambda$ is the wave-number (simplified to $k \approx 2\pi/\lambda$ at the denominator, $\lambda = 514.5$ nm) where $n = n' - in''$ denotes the

[9] The humid coastal environment likely produces spherical aerosols for modes 1 through 4.

index of refraction of the surrounding medium. The complex-amplitude functions contain information about the nature of the scatterers.

If incoherent and single scattering by spherical scatterers are correct assumptions, both S_3 and S_4 are set to zero and the scattered irradiance produced by each scatterer is added to form the total scattered irradiance. In this context, closed mathematical expressions are known for which programs to compute S_1 and S_2 (derived from the Mie coefficients a_n and b_n) abound. The one by Bohren and Huffman (1983) has been adapted to interface directly with MATLAB (both in Windows and SUN-Solaris programming environments) via a MEX-compilation procedure (Appendix B contains both versions of the scattering program and the configuration file necessary to MEX-compile on SUN-Solaris when the FORTAN compi-

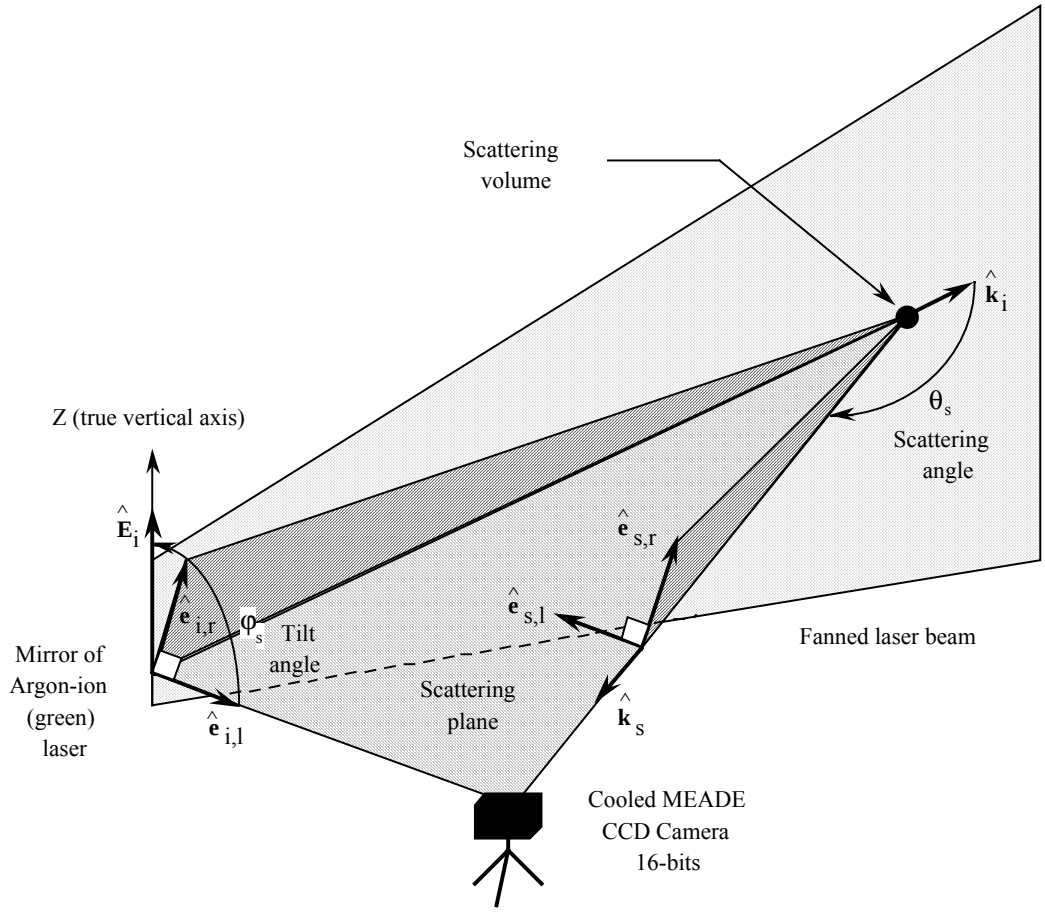

Figure 2.2. Labels assisting in reconstructing the observed scattered energy during the EOPACE experiments. The *i* and *s* subscripts refer to incident and scattered fields. The *r*, and *l* subscripts refer to perpendicular and parallel polarizations. θ_s and φ_s denote the scattering and tilt angles. Each scattering location inside the fanned beam (or, equivalently, each pixel in a CCD image) necessitated the decomposition of the incident irradiance onto $(\hat{e}_{i,l}, \hat{e}_{i,r})$ prior to applying Eq. (2.9). To simplify the diagram and subsequent mathematics, the present analysis excludes beam divergence (the fanned beam remains an infinitesimally thin plane).

ler is g77 instead of f77), to allow greater flexibility in the selection of the scattering angle, and to minimize the size of the returned arguments by computing i_1 and i_2 (the magnitudes squared of S_1 and S_2). The original program is known to tackle successfully computations involving spheres whose radii are several 1000 times greater than the incident wavelength (Bohren, 1999).

The scattering program generated matrices of 800x1000 (one matrix per i_1 and i_2) for scatterer radii logarithmically ranging from 0.002 μm to 250 μm over scattering angles from 159.5° to 179.5° by steps of 0.025° (typical angular differences between consecutive pixels range from 0.033° to 0.035°) per pre-selected relative humidity (cf. Subsection 2.2.3). The angular step-size is sufficient to resolve scattering features over 180° as the number of peaks (or troughs) for the highest expected radius, a, is approximated by the value of the size parameter (defined as $2\pi a/\lambda$).

The results from these computations served to find the domain of integration of the F-functions by combining the magnitude of the scattered intensity and the lognormal distribution function.

2.3.3 Single scattering by a distribution of homogeneous spheres

van de Hust (1957, pp. 12 and 127) relates the incident (I_i) and scattered (I_s) irradiance (in units of W/m^2) by an isolated cloud of volume V containing $N \cdot V$ identically homogeneous spheres (cf. Eq. 2.6) as follows:

$$I_s = I_i \frac{NV}{k^2 R_s^2} F(\theta, \varphi) \tag{2.7}$$

where:

$$F(\theta, \varphi) = i_2 \cos^2(\varphi_s) + i_1 \sin^2(\varphi_s) \tag{2.8}$$

by denoting $i_2 = |S_2|^2$ and $i_1 = |S_1|^2$.

In the presence of a particle size distribution (i.e., lognormal), Eqs. (2.7) and (2.8) are slightly redefined as follows for computational convenience:

$$I_s = I_i \frac{Vn_0}{k^2 R_s^2} \left[F_2(\theta_s) \cos^2(\varphi_s) + F_1(\theta_s) \sin^2(\varphi_s) \right] \tag{2.9}$$

where the unitless F-functions defined as:

Table 2.4. Effects of the choice of a step-size in radius on the computation of Eqs. (2.10) and (2.11) as measured by the mean (over both relative humidity and expected range of scattering angles) relative fractional differences (in percent) using a reference step-size and an evaluated step-size, for modes 1 to 3.

	$100 \cdot \frac{\left\|F_{2,eval} - F_{2,ref}\right\|}{F_{2,ref}} \Big/ 100 \cdot \frac{\left\|F_{1,eval} - F_{1,ref}\right\|}{F_{1,ref}}$			
Evaluated step-size	1000 nm	100 nm	10 nm	1 nm
Reference step-size	100 nm	10 nm	1 nm	0.1 nm
Mode 1	99.5 / 99.4	29.2 / 21	0.001 / 0.0004	2×10^{-6} / 2×10^{-6}
Mode 2	63.7 / 52.8	4.1 / 2.8	0.077 / 0.071	0.01 / 0.01
Mode3	19.4 / 15.7	2.2 / 2.2	0.29 / 0.29	0.04 / 0.04

$$F_2(\theta_s) \triangleq \frac{1}{n_0} \int_0^{+\infty} \frac{dN}{da} i_2 \, da \tag{2.10}$$

$$F_1(\theta_s) \triangleq \frac{1}{n_0} \int_0^{+\infty} \frac{dN}{da} i_1 \, da \tag{2.11}$$

can be computed once for each mode and relative humidity, if necessary, over the expected range of the scattering angles. Physically, the F-functions describe observed variations in scattered intensity by each mode of the aerosol model from various scattering angles when a constant intensity source at a chosen incident polarization illuminates a constant test-volume containing fixed concentrations.

Equations (2.10) and (2.11) are difficult to compute accurately because they require accuracy in both their integrands and the numerical scheme to carry out the quadrature. A finite upper limit was decided upon before applying any procedure. The matrices generated in Subsection 2.3.2 helped determine the radius for which the magnitude of each integrand fell to 1000th of its maximum value. The upper limit became twice this radius. Appendix C shows weaknesses in all 8 MATLAB prepackaged quadrature techniques when compared to one in which the numerical integrals are transformed into summations proceeding by linear step sizes of 0.1 nm for which a MEX-compiled version of BMIE.F is called (cf. Appendix B). Table 2.4 summarizes errors in results for several step sizes. Those values are to be contrasted with the maximum cross-platform calculation errors (when the same F-function is computed on both Windows and SUN platforms then compared) of 10^{-4}% for mode 1, 10^{-3}% for mode 2, and 10^{-2}% for mode 3.

The major drawback of the elected technique is a waiting time (for each quadrature to deliver its results) counted in days at each relative humidity. Hence, adaptive logarithmic widths in HCAM would have required powerful computational resources. Section 2.7 plots the resulting functions at different relative humidity.

2.3.4 Extinction: definition and properties

The current perspective is one in which an empty medium is injected with a controlled amount of scatterers (from an aerosol-distribution model). Extinction quantifies the rate of radiant energy removed by the scatterers along the line of propagation of the incident field.

If a single particle were illuminated, it would display an electromagnetic-equivalent surface C_{ext} (called the extinction cross-section) which, when multiplied by the incident irradiance, would equal the rate of energy removed in the forward direction by the same particle through both absorption and scattering (cf. Bohren and Huffman, 1983, pp. 70-71). Its expression stated by van de Hulst (1957, p. 36) for an homogeneous sphere is:

$$C_{ext} = \frac{\lambda^2}{\pi} \Re_e \left\{ S\big|_{\theta_s = 0} \right\}$$

where, in the forward direction (the scattering angle is null), S denotes the value of the complex-amplitude functions: $S = S_1 = S_2$. A related quantity called the extinction efficiency (factor) is defined as follows for a sphere of radius a:

$$Q_{ext} = \frac{C_{ext}}{a^2 \pi} = \left(\frac{\lambda}{a\pi} \right)^2 \Re_e \left\{ S\big|_{\theta_s = 0} \right\} \tag{2.12}$$

The extinction coefficient of a size distribution of homogeneous spheres is (van de Hulst, 1957):

$$\gamma = \int_0^{+\infty} Q_{ext} \frac{dN}{da} a^2 \pi \, da \tag{2.13}$$

thereafter integrated in the Bouguer (or Lambert-Beer) law to predict the value of irradiance a distance R away from a source of irradiance I_0:

$$I(R) = I_0 \exp(-\gamma R) = I_0 \prod_{j=-1\ldots4} \exp(-\gamma_j R) = I_0 \prod_{j=-1\ldots4} T_j \tag{2.14}$$

where T_j denotes the transmittance due to mode j.

Table 2.5. Sensitivity of Eq. (2.15) resulting from a fractional change in $n_{0,j}$, m, $a_{0,j}$, or $\sigma_{0,j}$.

	$\delta n_{0,j}/n_{0,j}$	$\delta m/m$	$\delta a_{0,j}/a_{0,j}$	$\delta \sigma_{0,j}/\sigma_{0,j}$
$\delta\gamma_{Rayleigh}/\gamma_{Rayleigh}$	1	$2m/(m-1)$	6	$36\sigma_{o,j}^2$
$\delta\gamma_{optical}/\gamma_{optical}$	1	0	2	$4\sigma_{o,j}^2$

A sensitivity study of the extinction coefficient splits Q_{ext} into the Rayleigh $\left(2a\pi/\lambda << 1\right)$ and optical $\left(2a\pi/\lambda >> 1\right)$ regions (although HCAM modes overlap those two regions, the present idealized analysis aims at developing an appreciation for the influence of the aerosol model on extinction). The index of refraction of the aerosols is denoted *m* (assumed to be real only) and using Eq. (2.13) for mode *j*, both extinctions become:

$$\gamma_{Rayleigh,j} \propto n_{0,j}(m-1)^2 \frac{a_{0,j}^6}{\lambda^4}\exp\left(18\sigma_{0,j}^2\right)$$
$$\gamma_{optical,j} \propto n_{0,j}\, a_{0,j}^2 \exp\left(2\sigma_{0,j}^2\right) \qquad (2.15)$$

Table 2.5 summarizes sensitivity of both extinctions. Despite their influence, the mode radii, logarithmic widths, and indices of refraction are fixed in both the Navy aerosol models and HCAM. The future of any aerosol model whose interaction with light is of interest lies in its variability of the logarithmic widths.

The general extinction equation in inhomogeneous media is more complex, especially in an environment modeled as a succession of homogeneous slabs, giving rise to a problem of multiple reflections. However, this concern is incompatible with the assumption of single scattering adhered to in Subsection 2.3.2 and, consequently, will not be considered any further. Equation (2.14) then becomes:

$$I(R) = I_0 \exp\left[-\int_0^R \gamma(r)dr\right] = I_0 \prod_{j=-1..4} \exp\left[-\int_0^R \gamma_j(r)dr\right] \qquad (2.16)$$

Hence, to assess transmittance throughout the plumes, extinction shall be determined at different locations along a given line and added-up, assuming that the integral in Eq. (2.16) may still be represented by a summation of discrete intervals of constant extinctions.

2.3.5 Polarization ratio

From Eq. (2.9), the scattered irradiance a distance R_s away from a local distribution of spheres in the geometry of Fig. 2.2 (but in which the fanned beam remains a beam) is:

$$I_s = \frac{I_0 V}{k^2 R_s^2} \exp\left[-\int_{-z}^{0} \gamma(z)dz - \int_{0}^{R_s} \gamma(r)dr \right] \sum_{j=-1}^{4} n_{0,j} \left[F_{2,j}(\theta_s) \cos^2(\varphi_s) + F_{1,j}(\theta_s) \sin^2(\varphi_s) \right] \qquad (2.17)$$

where the subscript *j* refers to the j[th] mode of HCAM.

The polarization-ratio method consists of dividing the scattered irradiances at parallel incident-polarization by the one at perpendicular incident-polarization:

$$\frac{I_s(\varphi_s \approx 0)}{I_s(\varphi_s \approx \pi/2)} \approx \frac{\sum_{j=-1}^{4} n_{0,j} F_{2,j}(\theta_s)}{\sum_{j=-1}^{4} n_{0,j} F_{1,j}(\theta_s)} \qquad (2.18)$$

The first explicit use of angular variation (from near 0° to about 60°) associated with the computation of the polarization-ratio method to determine the radius of aerosols appears in a conference paper by Sinclair and La Mer (1948). Stevens (1996) applied the method to a range of scattering angles from 155° to 175°. The present work refines the polarization-ratio method by requiring only a few pixels from EOPACE images to estimate aerosol concentrations. Section 2.7 places Eq. (2.17) in the context of a fanned beam.

2.3.6 Conclusion

Essential variables and expressions have been defined. Computational issues have been discussed and solved. Properties and robustness of the polarization-ratio method are addressed in Chapter 3.

2.4 Molecular background

The atmospheric molecular background is represented by spheres of a single radius whose scattering cross-sections match those of the molecular atmosphere, for an arbitrarily chosen index of refraction.

The radius (denoted a_{atmr}) is found by matching the empirical Rayleigh backscattering function of Collis and Russel (1976) to the Rayleigh differential scattering cross-section. An arbitrary[10] nominal index of refraction m=1.36 gives a radius $a_{atm} \approx 0.2$ nm, and the F-functions are (the real parts of the complex-amplitude functions have been neglected):

[10] This value is justified by mathematical convenience only: using the same equations with a physically meaningful value of $m = 1$ for the index of refraction results in an infinite a_{atmr}.

$$F_2(\theta_s)=\left(\frac{2\pi\, a_{atm}}{\lambda}\right)^6\left|\frac{m^2-1}{m^2+2}\right|^2\cos^2(\theta_s) \text{ and } F_1(\theta_s)=\left(\frac{2\pi\, a_{atm}}{\lambda}\right)^6\left|\frac{m^2-1}{m^2+2}\right|^2 \qquad (2.19)$$

The molecular scatterers are included as mode -1 in HCAM with $n_{0,-1}\approx 2.69\times 10^{19}$ cm^{-3} and $a_{0,-1}=a_{atm}$, resulting in $n_{0,-1}F_2(\theta_s)\approx 285.5\cdot\cos^2(\theta_s)$ cm^{-3} and $n_{0,-1}F_1(\theta_s)\approx 285.5$ cm^{-3} (for all θ_s). Concentrations are usually expressed in units of cm^{-3} (as opposed to m^{-3}). Indeed, the units of those last two products drive the units of the concentrations for the other modes, in the polarization ratio[11].

The extinction coefficient for the above radius is 0.016 km^{-1} (due to the 0.6 x 10^{-33} m^2 scattering cross-section and the 2.69 x 10^{25} atmospheric molecules per m^3). The bulk value of this temperature and pressure dependent extinction (Penndorf, 1957) is confirmed by MODTRAN, although HCAM does not take this additional effect into account.

2.5 Reconstruction of the experimental set-up

The purpose of this section is to estimate the values of both the scattering and tilt angles (cf. Fig. 2.2) and to locate the image position of the scattering location of interest on the recorded image. To this aim, the geometry of the Physical Space (the actual three-dimensional experimental environment), the position and orientation of the cameras, and the position of the laser fan must be known. This context leads to defining several reference spaces. Images belong to both the Image and Pixel Spaces (the latter refers to pixel location as integers – this is the space where images are recorded – and the former as reals – where images are displayed) and the scattering locations belongs to the Plume Space (a subset of the Physical Space).

Subsection 2.5.1 lays out the procedure and equations to resolve the orientation of the camera. Subsection 2.5.2 addresses projecting an Image/Pixel Space coordinate onto the Plume Space. Subsection 2.5.3 gives expressions to calculate the scattering angles, and Subsection 2.5.4 concludes. In all subsections, the frame of reference of the Physical Space is denoted $\Omega=(O,\hat{x},\hat{y},\hat{z})$ where $\hat{x}$ roughly follows the northward coastline, $\hat{y}$ points toward the open sea, along the pier, and $\hat{z}$ is directed upward (cf. Fig. 2.3).

[11] This explains the drastic improvement in stability of the results observed by Stevens (1996) once this mode was added (Philbrick, 1997).

(a)

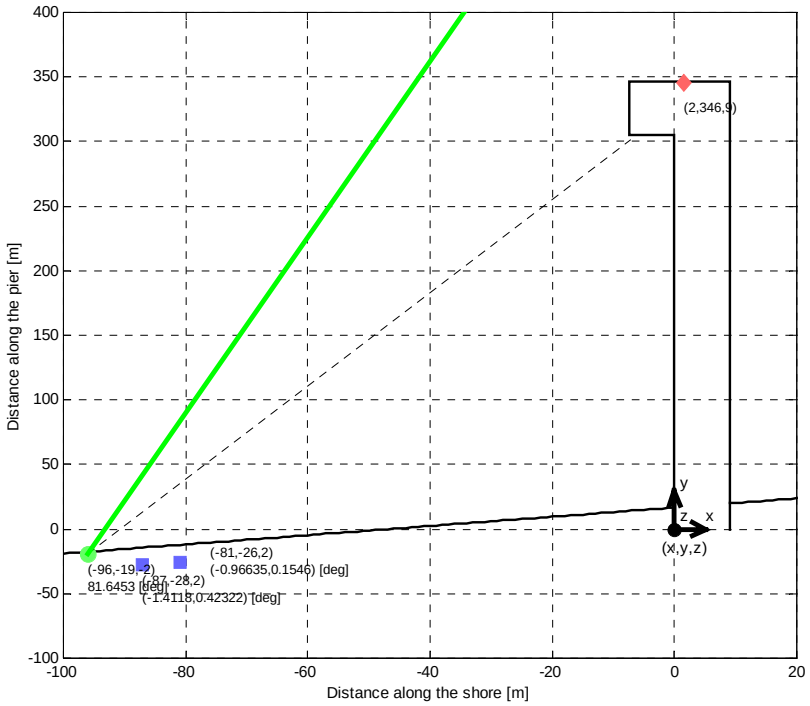

(b)

Figure 2.3. Experimental site of the Scripps Institution of Oceanography (SIO), La Jolla, California. (a) Pier of the SIO. (b) Simplified top-view of the devices and their locations (all in meters) during March-April, 1997. Green refers to the emitter and the laser fan, red is the color of the reference light, and cyan denotes the locations of the CCD cameras. Location of each camera and its orientation, the location of the mirror of the laser fan, and the Laser Sheet Angle (LSA, of 81.6º on 4 April, 1997) are displayed in (b). Pier orientation: 277/97degrees magnetic, 14 degrees East variation.

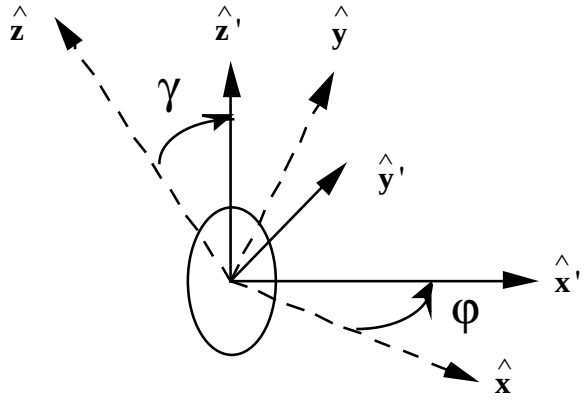

Figure 2.4. Sketch defining the camera angles with respect to the frame of reference of the Physical Space, Ω. The Ω' frame of reference is centered on the lens center. The camera is not allowed to roll around the normal to the lens defined by $\hat{y}'$ ($\hat{x}'$ remains within the $(\hat{x},\hat{y})$ plane). The $(\hat{x}',\hat{y}')$ plane follows the back-plane of the camera, leading to a positive γ when the camera points below the $(\hat{x},\hat{y})$ plane.

2.5.1 Camera orientation

Orientation of the camera is determined by matching the coordinates of the reference point in an image (Pixel Space) to the projection of the actual location of the reference point (Physical Space) onto the CCD (Image Space). Assumptions are that the camera cannot rotate around the axis normal to the lens (roll angle), thin lens approximation is valid, the lens is centered with respect to the CCD array, and all features are in focus.

Let the frame of reference centered on the middle of the camera lens be $\Omega'=\left(O',\hat{x}',\hat{y}',\hat{z}'\right)$. Figure 2.4 illustrates the orientation of the unit vectors of Ω' which are aligned with those of Ω when both φ and γ are zero.

For all $P \in \Omega$, projection onto Ω' is obtained by:

$$\begin{pmatrix} x_p' \\ y_p' \\ z_p' \end{pmatrix} = M \begin{pmatrix} x_p - x_c \\ y_p - y_c \\ z_p - z_c \end{pmatrix} \text{ defining } M = \begin{pmatrix} \cos\varphi & \sin\varphi & o \\ -\sin\varphi\cos\gamma & \cos\varphi\cos\gamma & -\sin\gamma \\ -\sin\varphi\sin\gamma & \cos\varphi\sin\gamma & \cos\gamma \end{pmatrix} \tag{2.20}$$

where the subscripts p and c refer to the location of P and the camera. Projection onto the Image Space (via the lens of focal length f – cf. Table 4.1 – onto 9 μm-wide squared-pixels) is:

$$\begin{pmatrix} X_p \\ Y_p \end{pmatrix} = \begin{pmatrix} 384.5 \\ 256.5 \end{pmatrix} + \frac{1}{9\times10^{-6}} \begin{pmatrix} -X'_p \\ Y'_p \end{pmatrix} \text{ using } \begin{pmatrix} X'_p \\ Y'_p \end{pmatrix} = -\frac{f}{y'_p - f} \begin{pmatrix} x'_p \\ z'_p \end{pmatrix} \tag{2.21}$$

where, when facing the displayed image, the (1,1) pixel is located on the upper left corner and (768,512) is on the lower right one. Both X'_p and Y'_p are distances from the center of the CCD array.

Hence, the orientation of the camera, (φ,γ), is determined by comparing the projection of the reference point to its recorded position onto the images.

2.5.2 From Image/Pixel Space to Plume Space

The fanned beam is the Plume Space. It is defined by $\Omega'' = \left(O'', \hat{y}'', \hat{z}\right)$ whose origin is at the center of the mirror and $\hat{y}''$ denotes the unit vector of the local horizontal line contained inside the laser fan. Knowledge of the geometry of the fanned beam permits projection of the images onto the Physical Space. Although both the original and final spaces are two dimensional, the intermediary step is three dimensional.

Let (x_r,y_r,z_r) be the location of the reference point, (x_m,y_m,z_m) the one of the mirror, and (x_p,y_p,z_p) the one of a point inside the laser fan projected onto the CCD array as (X_p,Y_p). These three dimensional vectors belong to the Physical Space. Seen from the top in the Physical Space the fanned beam describes a line:

$$y_p = \frac{y_m - y_i}{x_m - x_r} x_p + \frac{y_i x_m - y_m x_r}{x_m - x_r} = a\, x_p + b \tag{2.22}$$

with:

$$y_i = y_m + \left(x_r - x_m\right)\tan\left(LSA\right), \quad LSA \equiv LA + \arctan\left(\frac{y_r - y_m}{x_r - x_m}\right) \tag{2.23}$$

where LA stands for the laser angle (made by the laser sheet with reference to the line defined by the mirror and the reference point – cf. dashed line on Fig. 2.3) and LSA for laser-sheet angle (made by the laser sheet and $\hat{x}$). Projecting Eq. (2.22) onto Ω', including dimensions along the CCD array, and solving for y'_p gives:

$$\begin{pmatrix} x'_p \\ y'_p \\ z'_p \end{pmatrix} = \begin{pmatrix} X'_p (1 - y'_f) \\ f\, y'_f \\ Y'_p (1 - y'_f) \end{pmatrix} \tag{2.24}$$

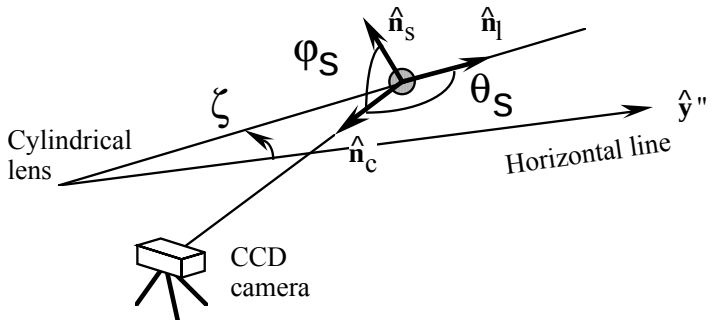

Figure 2.5. Geometry to obtain both the tilt (φ_s) and scattering (θ_s) angles.

where $y_f' \triangleq \dfrac{b + \left(\Delta X_c + X_p'\right)\left(a\cos\varphi - \sin\varphi\right) - \left[\Delta Y_c \cos\gamma + \left(\Delta Z_c + Y_p'\right)\sin\gamma\right]\left(\cos\varphi + a\sin\varphi\right)}{X_p'\left(a\cos\varphi - \sin\varphi\right) + \left(f\cos\gamma - Y_p'\sin\gamma\right)\left(\cos\varphi - a\sin\varphi\right)}$, for

which $\begin{pmatrix}\Delta X_c \\ \Delta Y_c \\ \Delta Z_c\end{pmatrix} = M\begin{pmatrix}x_c \\ y_c \\ z_c\end{pmatrix}$, and $\begin{pmatrix}X_p' \\ Y_p'\end{pmatrix} = 9\times10^{-6}\begin{pmatrix}384.5 - X_p \\ Y_p - 256.5\end{pmatrix}$. Finally, the (X_p,Y_p) point in the Image Space has the following coordinates in the Plume Space :

$$\begin{pmatrix}x_p \\ y_p \\ z_p\end{pmatrix} = M^{-1}\begin{pmatrix}x_p' \\ y_p' \\ z_p'\end{pmatrix} + \begin{pmatrix}x_c \\ y_c \\ z_c\end{pmatrix} \tag{2.25}$$

Hence, the Image or Pixel Space coordinate (X_p,Y_p) is found in the plumes at location (x_p,y_p,z_p) in the Physical Space. The procedure to obtain (X_p,Y_p) from (x_p,y_p,z_p) has been presented in Subsection 2.5.1.

2.5.3 Scattering angles

The tilt and scattering angles require additional preparation because these angles involve both the orientation of the electric field at the scattering volume in the laser sheet and the position of the camera. The cylindrical lens produces several lines converging to its focal point. The distance from the mirror to this point is about 24.1 cm. Let ζ denote the angle made by the $z = z_m$ line and the converging line leading to the scattering volume of interest (Fig. 2.5):

$$\tan(\zeta) = \frac{z_p - z_m}{0.241 + \sqrt{\left(x_p - x_m\right)^2 + \left(y_p - y_m\right)^2}} \tag{2.26}$$

In conjunction with Eq. (2.22), only x_p is required to ensure that the line be inside the fanned beam:

$$z_p = z_m + \left(0.241 + \left|x_p - x_m\right|\sqrt{1+a^2}\right)\tan(\zeta) \tag{2.27}$$

From Fig. 2.5, both the tilt and the scattering angles are computed from the $\left(\hat{n}_l, \hat{n}_s, \hat{n}_c\right)$ unit vectors through trigonometric means:

$$\theta_s = \arccos\left(\hat{n}_l \bullet \hat{n}_c\right) \qquad \varphi_s = \arccos\left(\hat{n}_s \bullet \hat{n}_c\right) \tag{2.28}$$

where $\hat{n}_c = \begin{pmatrix} x_c - x_p \\ y_c - y_p \\ z_c - z_p \end{pmatrix} \Bigg/ \sqrt{\left(x_c - x_p\right)^2 + \left(y_c - y_p\right)^2 + \left(z_c - z_p\right)^2}$, $\hat{n}_l = \begin{pmatrix} \cos(LSA)\cos(\zeta) \\ \sin(LSA)\cos(\zeta) \\ \sin(\zeta) \end{pmatrix}$, and $\hat{n}_s = \begin{pmatrix} -\cos(LSA)\sin(\zeta) \\ \sin(LSA)\sin(\zeta) \\ \cos(\zeta) \end{pmatrix}$.

The goal of determining the scattering and tilt angles is complete. These calculations are carried out for each pixel whose intensity reflects the amount of scattering from a given location in the laser fan. By example, a typical camera orientation is found to be $\gamma \approx$ -1.2° and $\varphi \approx$ -1.7°. A scattering volume located at $x_p = x_c$, $y_p = a*x_c + b$ and $z_p = z_c$ corresponds to $\zeta \approx 5.15°$, $\theta_s \approx 166.8°$, and $\varphi_s \approx 85°$.

2.5.4 Conclusion

The Scripps Institution of Oceanography hosted two experimental periods (22 January-5 February, 1996, and 31 March-11 April, 1997). Moss Landing hosted one such period (4-15 March, 1996). The data taken during the second experiment at the Scripps Institution of Oceanography reflect the lessons learned from previous experiments. Measurements of the locations of a few devices have been found to be erroneous and schemes to correct them have been developed. For instance, the laser-sheet angle was iteratively determined using user-positioned points at the intersection of water and the laser fan. The points were projected onto the images taken by the opposite camera, the angle between vectors collinear to the mean lines made by the points in the original image and by those projected was minimized by changing the value of the laser-sheet angle. Original values reported at 75.3° were subsequently found to be closer to 79.2°. Figure 2.6 exemplifies the projection of plume contours from the Pixel Space into the Physical Space.

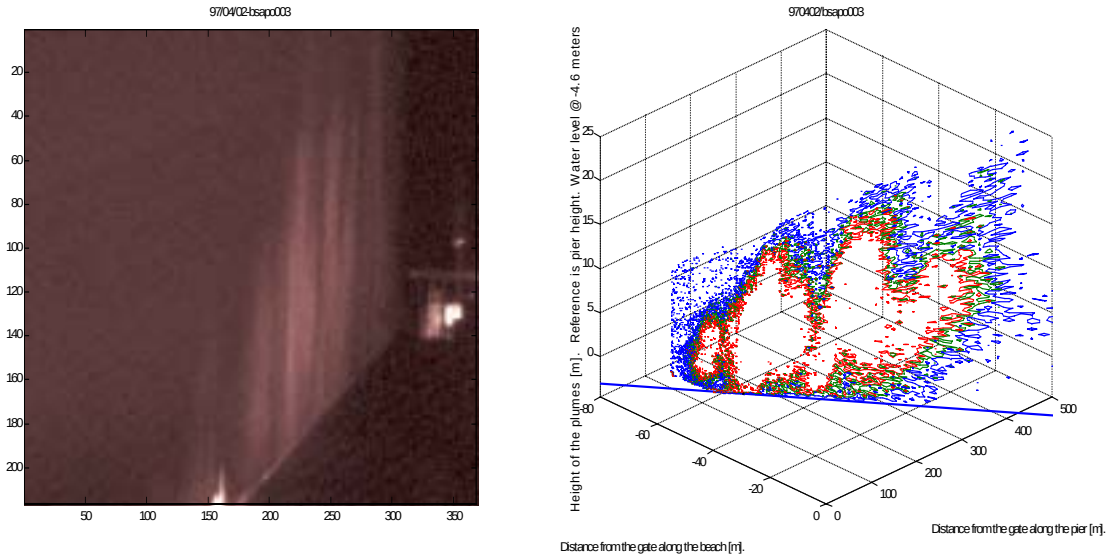

(a) (b)

Figure 2.6. (a) Cut CCD image taken 2 April 1997 at 23:36 and (b) its three-dimensional reconstruction based on scattered intensity contours set near 3315 digital counts.

2.6 Extinction and fanned beam combined

The 514.5 nm laser source emits a vertically polarized continuous wave (CW) beam of 1.3 Watts assumed to be homogeneously distributed over its 1.2 mm diameter (this simplification is mathematically motivated – the actual intensity is Gaussian distributed). This beam is incident onto a cylindrical lens of -6.35 mm in focal length *f*. The cylindrical lens vertically stretches the incident beam, leaving its horizontal radius unmodified (beam divergence is deliberately omitted). The shape of the fanned beam describes an ellipse projected onto a sphere centered at *f*. Using ray optics and conservation of radiant energy, the spatial distribution of irradiance is:

$$I\left(y_L, r_L\right) = \begin{cases} 0 & \text{if } \left|r_L\right| \geq \left|r_i\left(1 - y_L / f\right)\right| \\ I_0 r_i^2 \Big/ \left(r_\alpha r_\beta\right) & \text{otherwise} \end{cases} \tag{2.29}$$

where the respective lengths of the semimajor and semiminor axes are $r_\alpha = \left(r_i / \left|f\right|\right)\sqrt{r_L^2 + \left(y_L - f\right)^2}$ and $r_\beta = r_i = 0.6 \times 10^{-3}$, in meters, and $\left(y_L, r_L\right)$ refers to the location of interest inside the fan of origin the center of the lens, instead of the Ω'' coordinate system, although y_L is supported by $\hat{y}''$ and r_L is supported by the perpendicular to $\hat{y}''$, both contained within the fanned beam.

But this derivation has neglected extinction. By symmetry with the propagation of a spherical wave, of which the present case is a restriction, this results in:

$$I(R_L) = \frac{r_i^2}{r_\alpha r_\beta} I_0 \exp\left[-\int_0^{R_L} \gamma(\vec{R}) dR \right] \qquad \text{if } |r_L| \le |r_i (1 - y_L / f)| \qquad (2.30)$$

where $R_L = \sqrt{(y_L - f)^2 + r_L^2}$ is the distance from the focal point to the location of interest denoted (y_L, r_L) of origin the center of the lens, $\vec{R} = (y - f, r)$ follows this line where $r = \frac{y - f}{y_L - f} r_L$.

The incident intensity at a given location inside the laser fan has been formulated. The observed scattered intensity by a known concentration of aerosols has also been quantified. Those concepts help read the EOPACE images.

2.7 Reading EOPACE images

Reading the EOPACE images requires an understanding of several processes; the energy captured by each pixel does not depend exclusively on the aerosols (Subsection 2.7.1). The F-functions (computed Subsection 2.3.3) are presented for each mode to caution against hasty conclusions regarding plume characteristics (Subsection 2.7.2), followed by a conclusion (Subsection 2.7.3). More extensive analyses are conducted in Chapter 3.

2.7.1 Energy at a CCD pixel

In the context of EOPACE: light leaves the transmitter to reach a scattering volume where its irradiance has been diminished by both fanning and extinction (beam divergence also contributes, although excluded from the present analysis), it interacts with each aerosol (assumed to be correctly modeled by HCAM) inside the volume to scatter light in all directions by different amounts, again endures extinction while propagating away from the scattering volume, and meets the lens of a CCD camera where it is oriented toward a particular pixel on the CCD.

Including a few notational shortcuts, Eq. (2.17) becomes:

$$I_s = \frac{I_0 r_i^2}{r_\alpha r_\beta} \cdot \exp\left[-\int_0^{R_L} \gamma(\vec{R}) dR \right] \cdot \sum_{i=-1}^{4} V n_{0,j} \left[F_{2,j}(\theta_s) \cos^2(\varphi_s) + F_{1,j}(\theta_s) \sin^2(\varphi_s) \right] \cdot \frac{1}{(kR_s)^2} \exp\left[-\int_0^{R_C} \gamma(\vec{r}) dr \right] \tag{2.31}$$

where R_L and R_C respectively denote the distances to the center of the scattering volume from the transmitter and to the camera from the center of the scattering volume.

Images of the plumes reflect the amount of energy captured by each pixel of the CCD array (related to the exposure time). Equation (2.31) becomes:

$$K = \int_{t_{initial}}^{t_{final}} \int_{\substack{Pixel \\ area}} \frac{\eta I_0 V r_i^2}{r_\alpha r_\beta k^2 R_s^2} \exp\left[-\int_0^{R_L} \gamma(\vec{R}) dR - \int_0^{R_C} \gamma(\vec{r}) dr \right] \sum_{j=-1}^{4} n_{0,j} \left[F_{2,j}(\theta_s) \cos^2(\varphi_s) + F_{1,j}(\theta_s) \sin^2(\varphi_s) \right] dA dt \tag{2.32}$$

where diffraction by the aperture of the camera has been deliberately omitted.

Hence, fanning, extinction (γ), polarization, optical properties of the aerosols, integration time, size of pixels, and device losses (η) affect the captured radiant energy. Equation (2.32) expresses the noiseless amount of energy at each pixel of the CCD arrays. Noise is considered in Chapter 3.

2.7.2 HCAM scattering

Figures (2.7) to (2.10) display the F-functions for all modes of HCAM over a scattering angle domain ranging from 159.5º to 179.5º.

As the scattering angle reaches 180º, the F-functions converge toward each other (even for modes 3 and 4 although invisible on the plots). Both perpendicular and parallel components vary relatively smoothly over all scattering angles, modes, and relative humidity values. Modes -1, 0, and 1 are monotone whereas mode 2 oscillates by approximately one period over the angular domain, and mode 4 remains relatively flat but a sharp peak appears near 178º. In some conditions, F_1 and F_2 intersect, for the same last two modes.

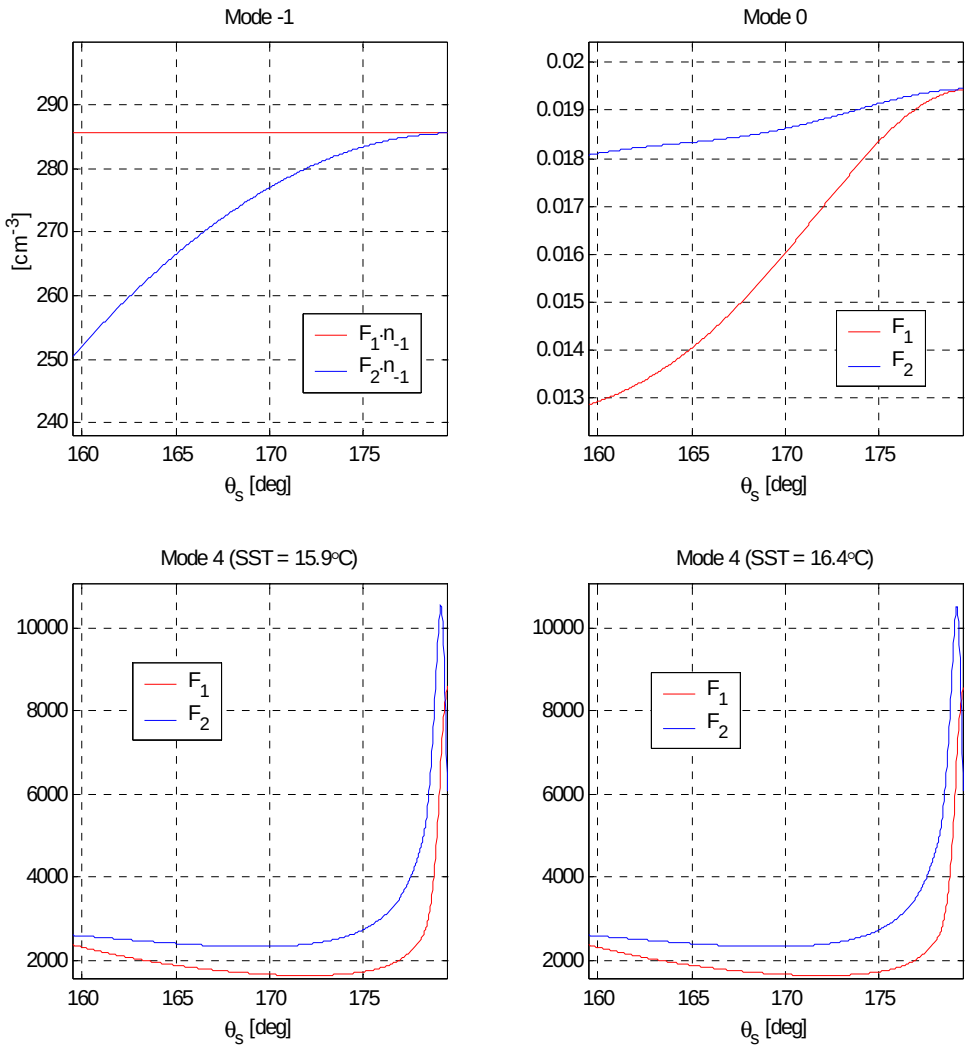

Figure 2.7. Results from Eq. (2.19) for mode -1 (upper left), and from Eqs. (2.10) and (2.11) for modes 0 (upper right) and 4 at sea-surface temperatures (SST) of 15.9ºC (bottom left) and 16.4ºC (bottom right). Half a degree in sea surface temperature invisibly affects mode 4. In all 4 cases, $F_1 = F_2$ at 180º (the maximum displayed abscissa is 179.5º).

If the scattering region had homogeneous concentrations at each mode (assuming ideal experimental conditions and devices), then mode -1 would scatter more energy at perpendicular than at parallel incident polarizations, although this difference would decrease farther away from the shore. Modes 0 and 1 would scatter more energy at parallel rather than at perpendicular incident polarizations. Mode 2 would scatter more at parallel than perpendicular incident polarization (at the same scattering angle) as long as relative humidity remains below 66%. As relative humidity increases, the order is reversed from lower scattering

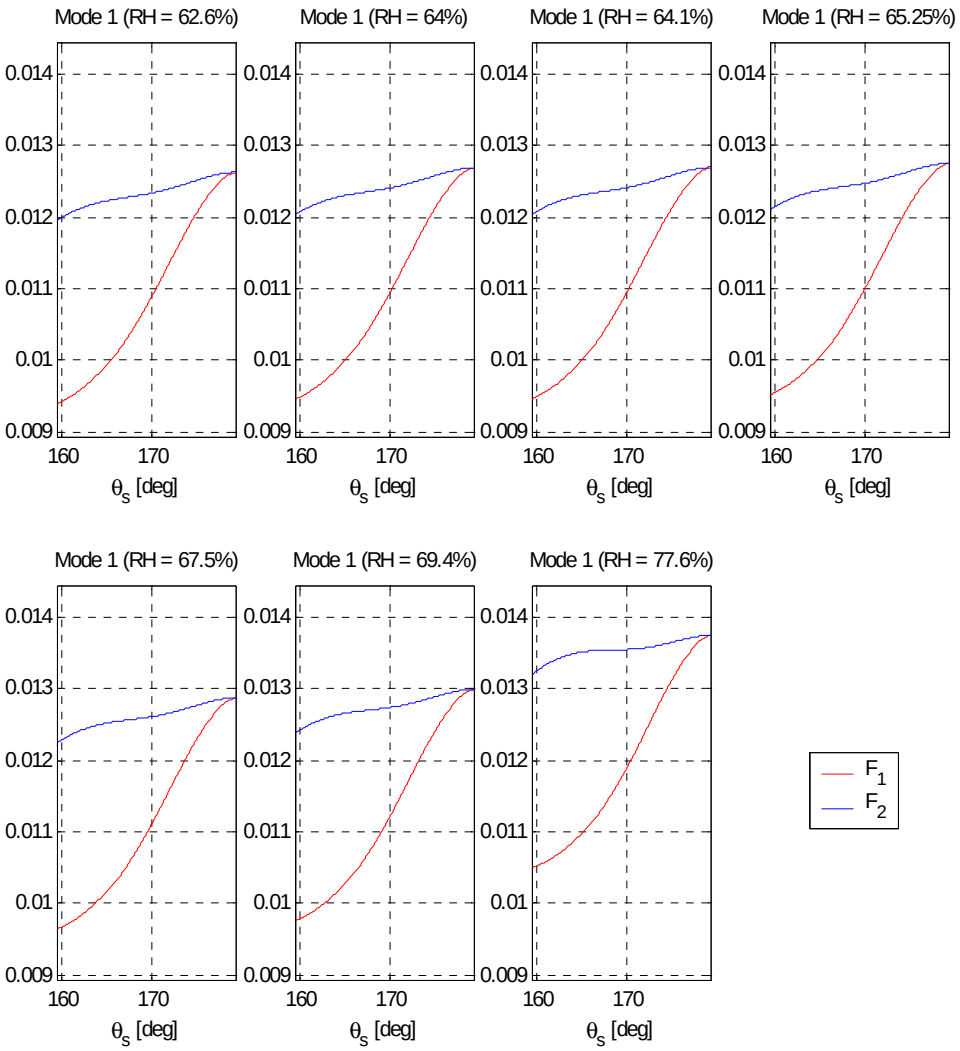

Figure 2.8. Results from Eqs. (2.10) and (2.11) for mode 1 for the mean relative humidity (RH) values indicated in Table 2.3. The title of each subplot specifies its RH value. Relative humidity visibly affects mode 1. In all cases, $F_1 = F_2$ at 180º (the maximum displayed abscissa is 179.5º).

angles to higher ones. If mode 2 were the primary scattering mode, then the shape of the plumes would follow the circular characteristics of the F-functions. This means that the widths and locations of the plumes would depend on the incident polarization, the scattering angle, and relative humidity rather than just their concentration. If either mode 3 or 4 was the primary scattering modes, an artificial plume would be seen near 178° upon parallel incident polarization.

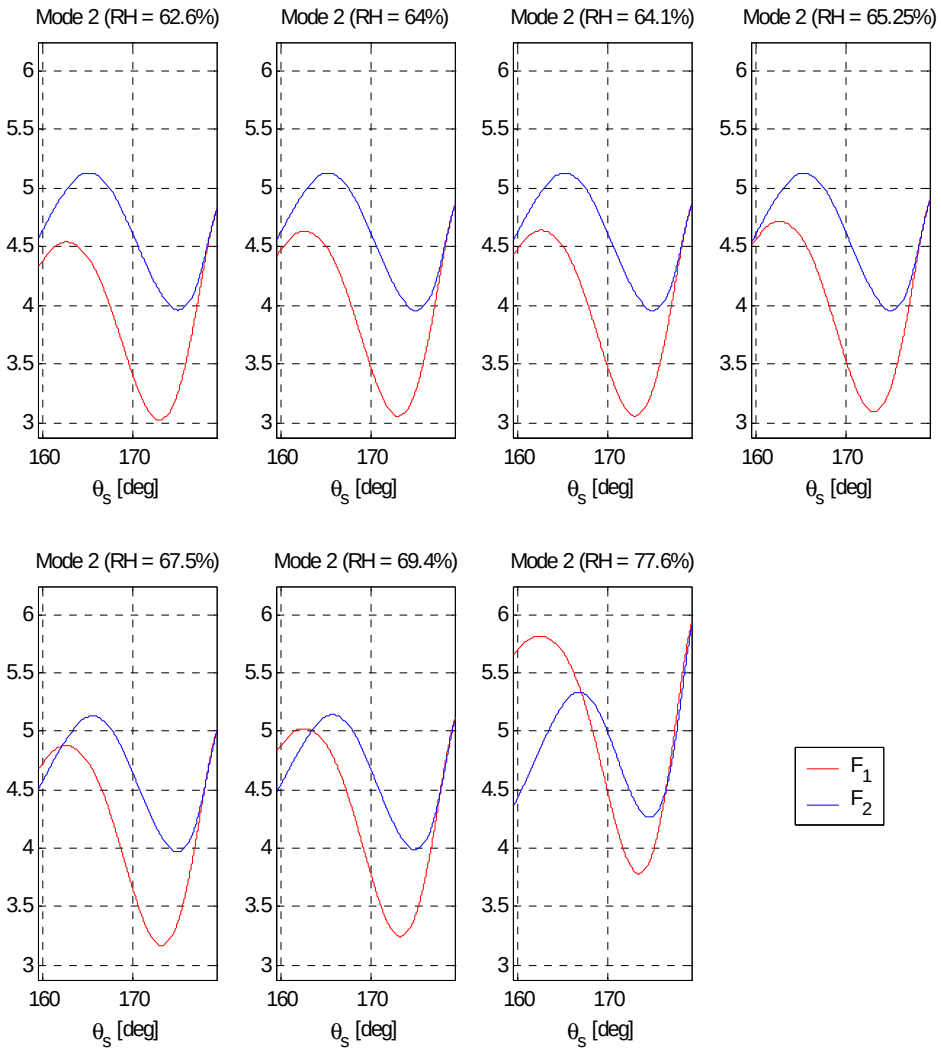

Figure 2.9. Results from Eqs. (2.10) and (2.11) for mode 2 for the mean relative humidity (RH) values indicated in Table 2.3. The title of each subplot specifies its RH value. Relative humidity visibly affects the relative magnitudes of both F_1 and F_2. In all cases, $F_1 = F_2$ at 180º (the maximum displayed abscissa is 179.5º).

2.7.3 Conclusion

Interpretation of the plumes in the EOPACE images requires care due to the bias introduced by the F-functions of the HCAM modes.

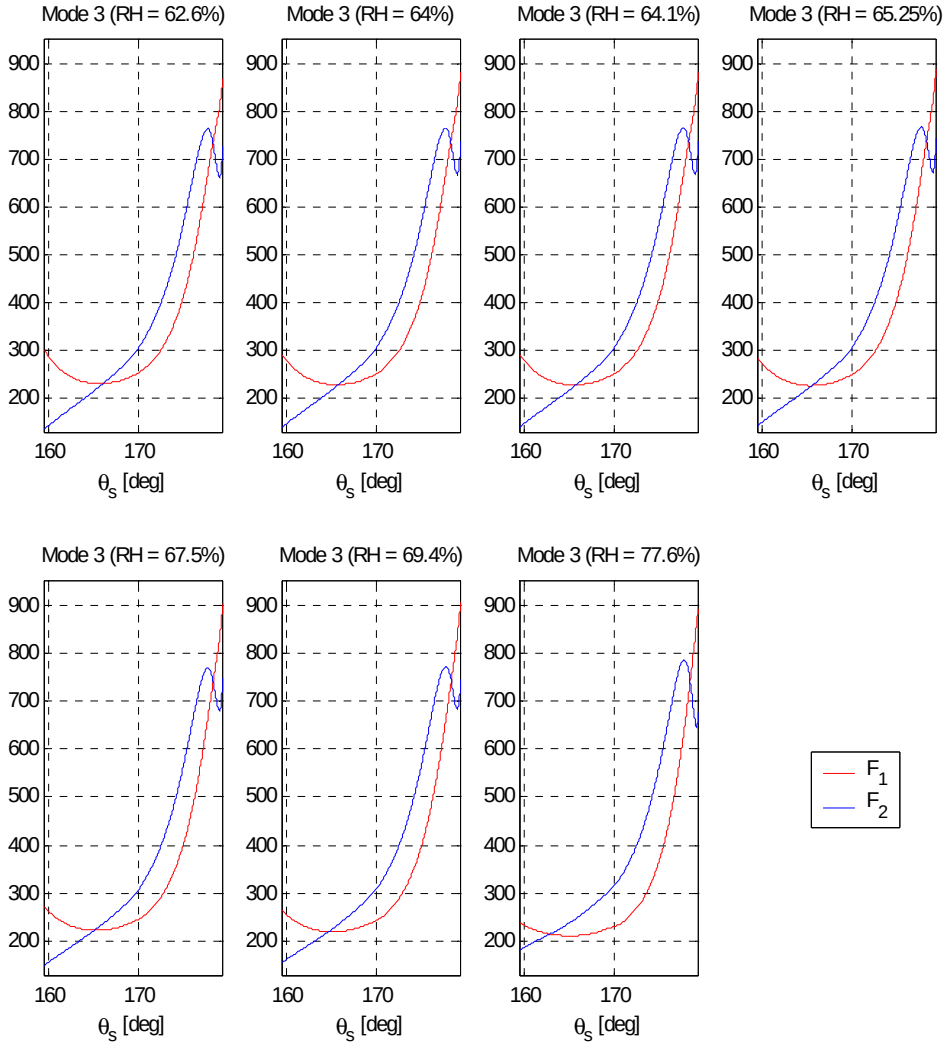

Figure 2.10. Results from Eqs. (2.10) and (2.11) for mode 3 for the mean relative humidity (RH) values indicated in Table 2.3. The title of each subplot specifies its RH value. Relative humidity invisibly affects both F_1 and F_2, despite a relatively large range of values. In all cases, $F_1 = F_2$ at 180º (the maximum displayed abscissa is 179.5º).

2.8 Conclusion

The EOPACE images of plumes consist of scattered energy by solution droplets whose exact index of refraction has not been measured. Section 2.7.2 has argued that changes in intensity in the EOPACE images may not exclusively be attributed to changes in concentrations.

It may now be appropriate to ask what is meant by a plume whose width is 50 meters? This question was probably based on the observed scattered intensity off of the plume content, which has just been

shown to be misleading (Fig. 2.6(b) testifies to the arbitrary width of the plumes as intensity contours in counts are varied – at one specific wavelength). How differently should the characteristics of the plumes be measured? Is it the concentration of each aerosol mode, the widths of the distribution functions, the change in median radius, or the change in index of refraction? This situation is what it may be referred to as the plume's identity crisis.

Subjectivity in the first (and subsequent) lidar observations of boundary-layer plumes (cf. Kunkel et al., 1977, followed by Hooper and Martin, 1999) consisted both in an attenuation compensation model and an intensity chosen to define a plume contour. As previously emphasized, the wavelength of the source, the aerosol modal decomposition, the exposure time (to capture a complete data set), and the outgoing polarization (especially in a bi-static topology) underlyingly influence those observations. Before theorizing on the generation and dispersion of the plumes, it is necessary to define them, uncorrupted by observational factors, both human and instrumental.

Chapter 3 investigates the limitations both of the instrument and the method to recover the HCAM concentrations. Chapter 4 applies the best method from Chapter 3 to analyze EOPACE images.

CHAPTER 3
THE POLARIZATION-RATIO METHOD TO ESTIMATE AEROSOL CONCENTRATIONS IN NOISY ENVIRONMENTS

3.1 Introduction

Expressions developed in Chapter 2 lead to the polarization ratio from the concentration of each mode (the direct problem). The present chapter aims at estimating the concentration of each mode from a series of noisy measurements (the inverse problem). Noise is defined as any effect which leads astray the procedure to determine the actual aerosol content at a given location from its scattered irradiance.

Estimation of linearly combined concentrations is a difficult enough problem, their noisy ratio renders the situation even tougher (Kay, 1993). The quality of the outcome from an estimation procedure depends on its sensitivity to uncertainties. Deterministic (systematic) and stochastic uncertainties are analyzed, at typical concentrations, to infer their influence on the design of the experiment and the choice of the instrumental devices.

Section 3.2 reviews the expression of the polarization ratio to address both its assumptions and properties. Section 3.3 covers deterministic uncertainties (correctable or adjustable instrumental variables) and Section 3.4 covers stochastic uncertainties (uncorrectable, but constrainable, errors) when the mirror of the transmitter, the scattering volumes, the receivers, and the outgoing parallel electric-field share the same horizontal plane. Chapter 4 applies the best technique to EOPACE images.

3.2 Polarization ratio: expressions, assumptions, properties, and estimation of concentrations

Chapters 1 and 2 have both introduced the polarization-ratio method and covered the necessary tools to reconstruct stored CCD-images when the beam of the bi-static instrument is fanned. Subsection 3.2.1 adjusts the latter to account for numerous sources of noise (including the insertion of a retarder plate) and refines the definition of the polarization ratio for noisy conditions. Subsection 3.2.2 estimates the concentrations from a noise-free polarization-ratio. Subsection 3.2.3 lists properties limiting the success of the method, and Subsection 3.2.4 concludes.

3.2.1 Expressions for the polarization ratio

Subsection 2.3.5 defined the polarization ratio as the ratio of the scattered intensities at parallel incidence to perpendicular incidence which, from Eq. (2.32) where $F_{1,j}$ and $F_{2,j}$ at the center of a pixel represent approximations of their averages over both the pixel area and scattering volume, becomes[12]:

$$PR \triangleq \frac{\sum_{j=-1}^{4} n_{0,j}\left[F_{2,j}\cos^2(\varphi_s) + F_{1,j}\sin^2(\varphi_s)\right]}{\sum_{j=-1}^{4} n_{0,j}\left[F_{2,j}\sin^2(\varphi_s) + F_{1,j}\cos^2(\varphi_s)\right]} \tag{3.1}$$

Equation (3.1) defines the polarization ratio as a physical quantity whereas a measured quantity would account for sources of noise. Ideally, both scattered fields should be captured simultaneously, but this impossibility necessitates that the concentrations be stationary over the integration time covering illumination at both incident polarizations.

Measured intensities (those recorded by the CCD cameras) must be cleaned from their noises to formulate an experimental polarization ratio. Expressed in units of counts, and based upon physical principles, the recorded images are modeled as follows:

$$I_{//} = Q\left(N'_{//} + \int_{t_0}^{t_0+\Delta t}\int_{\substack{Pixel\\area}} \frac{\eta I_0 V r_i^2}{r_\alpha r_\beta k^2 R_s^2}\exp\left\{-\left[\int_0^{R_L}\gamma(\vec{R})dR + \int_{R_L}^{R_R}\gamma(\vec{R})dR\right]\right\} T_R \sum_{j=-1}^{4} n_{0,j}\left[F_{2,j}\cos^2(\varphi_s) + F_{1,j}\sin^2(\varphi_s)\right]dAdt\right)$$

$$I_{\perp} = Q\left(N'_{\perp} + \int_{t_1}^{t_1+\Delta t}\int_{\substack{Pixel\\area}} \frac{\eta I_0 V r_i^2}{r_\alpha r_\beta k^2 R_s^2}\exp\left\{-\left[\int_0^{R_L}\gamma(\vec{R})dR + \int_{R_L}^{R_R}\gamma(\vec{R})dR\right]\right\} \sum_{j=-1}^{4} n_{0,j}\left[F_{2,j}\sin^2(\varphi_s) + F_{1,j}\cos^2(\varphi_s)\right]dAdt\right) \tag{3.2}$$

where N' denotes the combination of both atmospheric and CCD noises[13], T_R represents the amount of radiant energy passing through the retarder plate (transmittance), Q is a quantization function, and Δt is the duration of the integration (exposure). This model is applicable to both original and estimated concentrations. If Q is linear (to minimize quantization effects), in addition to assuming that all fluctuations

[12] The denominator of Eq. (3.1) accounts for the 90° rotation of the outgoing polarization induced by the insertion of a retarder plate at the transmitter. Hence, the tilt angle (φ_s) denotes the position of the outgoing electric field with respect to the scattering plane in the absence of the retarder plate, both presently and subsequently.

[13] For detailed description of CCD noise-sources, cf. Janesick et al. (1987) and Prytherch (1996), the latter of whom explored a chip of the same family as the one used inside the MEADE cameras (i.e., the Kodak KAF series).

are negligible, Eq. set (3.2) combines to yield Eq. (3.1) where most of the unpredictable instrumental and environmental unknowns cancel out:

$$PR = \frac{I_{//} - N_{//}}{\left(I_{\perp} - N_{\perp}\right)T_R} \tag{3.3}$$

where $N = Q(N')$. Equation (3.3) separates measured quantities (on the right side of the equal sign) from the physical ones (on the left side of the equal sign). These notations are preserved to analyze the EOPACE data for which both $I_{//}$ and $I_{\perp}$ refer to experimental images.

3.2.2 Estimation

Assuming that *PR* contains no uncertainties for each camera and pixel, estimation of the concentration vector[14], $\underline{n} = \left[n_{0,0} \quad n_{0,1} \quad n_{0,2} \quad n_{0,3} \quad n_{0,4}\right]^T$, uses a direct scheme. In this scheme, Eq. (3.1) is vectorized:

$$\left[d_0 \quad d_1 \quad d_2 \quad d_3 \quad d_4\right] \cdot \underline{n} = -d_{-1} \cdot n_{0,-1} \tag{3.4}$$

where $d_j \hat{=} \left(F_{1,j} - F_{2,j} PR\right)\sin^2\left(\varphi_s\right) + \left(F_{2,j} - F_{1,j} PR\right)\cos^2\left(\varphi_s\right), \quad j \in [-1,4]$, measures the contrast between the polarization ratio of mode *j* and *PR*.

Equation (3.4) is underdetermined (i.e., it contains more unknowns than equations). To overcome this limitation, the number of independent rows must equal the number of unknown concentrations, resulting in:

$$D \cdot \underline{n} = -\underline{d}_{-1} \cdot n_{0,-1} \tag{3.5}$$

by considering additional cameras and adjacent pixels. However, adjacent pixels from the same camera likely display similarities while requiring that the concentrations be the same over a larger area.

Equation (3.5) becomes overdetermined when even more pixels are included. Concentrations are estimated either via the Singular Value Decomposition (SVD), already used by Bas et al. (1997), or the pseudoinverse (Press et al., 1988, Kay, 1993):

[14] Notational conventions are a superscript *T* for the operator of transposition, an underline for a vector, and a circumflex for an estimated variable.

$$\underline{\hat{n}} = \left(D^T \cdot D\right)^{-1} \cdot D^T \cdot \left(-\underline{d}_{-1} \cdot n_{0,-1}\right) \tag{3.6}$$

Both methods limit the effect of statistical uncertainties, in a least-square sense.

3.2.3 Properties of the polarization ratio

The following properties illustrate conditions (beyond those encountered during EOPACE) in which the polarization-ratio method inaccurately estimates concentrations.

Property #1: A volume containing aerosols whose modes are exclusively distributed within the Rayleigh scattering region is illuminated by a source whose polarization is perfectly aligned with the scattering plane at parallel polarization and with its perpendicular at perpendicular polarization. The polarization ratio defined by Eq. (3.1) is reduced to $\cos^2\left(\theta_s\right)$. (This property checks the validity of assumptions that bi-static lidar measurements occur within this regime.) In those conditions, the estimated concentrations are unreliable.

Property #2: A volume of aerosols whose modes are exclusively distributed within the Rayleigh scattering region is illuminated by a source whose polarization is not necessarily perfectly aligned with either the scattering plane or its perpendicular. The polarization ratio defined by Eq. (3.1) becomes:

$$PR = \frac{\cos^2\left(\theta_s\right)\cos^2\left(\varphi_s\right) + \sin^2\left(\varphi_s\right)}{\cos^2\left(\theta_s\right)\sin^2\left(\varphi_s\right) + \cos^2\left(\varphi_s\right)}$$

which reduces further either to $PR = \cos^2\left(\theta_s\right)$ when $\varphi_s = 0$ (cf. Property #1) or $PR = 1$ when $\varphi_s = 45°$. All concentrations estimated in those conditions are erroneous.

Property #3: If $\varphi_s = 45°$, then Eq. (3.1) is reduced to 1, independently of the number of modes and their scattering regimes. All concentrations estimated in those conditions are erroneous.

Property #4: If one mode dominates all the others over a range of observed scattering angles, it masks the contributions by the other modes, resulting in the cancellation of its own concentration. All concentrations estimated in those conditions are erroneous.

Property #5: To estimate the concentration vector $\underline{n}$, the minimum number of independent sets of measurements (defined as one measurement at parallel incident-polarization and one measurement at

perpendicular incident-polarization by one camera at one pixel) equals the number of aerosol modes whose concentrations are sought.

Other properties cannot be expressed other than by choosing an equilibrium point around which to conduct stability analyses (cf. Sections 3.3 and 3.4).

3.2.4 Conclusion

The polarization-ratio equation has been refined and an estimation scheme has been presented. Under limited conditions the polarization ratio fails to recover the original concentrations. Awareness of the fragility of the polarization ratio in specific situations helps build the credibility of the instrument (consisting of the bi-static lidar, the polarization-ratio method, and the estimation of concentrations together) by either avoiding those conditions or by developing schemes to counteract those situations.

In general, Eq. (3.3) contains both systematic and stochastic uncertainties. The first category includes *LSA* (the Laser Sheet Angle), $\overline{N}$ (the mean background counts from the CCD images when both the laser and the camera cap are off), φ_s (the tilt angle), and T_R (the transmittance through the polarizer plate). The second category includes $\tilde{N}$ (variations in the CCD noise). Past studies of the polarization ratio have ignored sensitivity issues with respect to instrumental parameters. Sections 3.3 and 3.4 fill this gap.

3.3 Estimation of concentrations under deterministic uncertainties

Sensitivity analysis of the recovery of all possible concentrations via the polarization-ratio method for Eq. (3.3) is unrealistic. Instead, representative concentrations ($5\text{x}10^{-4}$ cm^{-3} for mode 0, $5\text{x}10^{-4}$ cm^{-3} for mode 1, 30 cm^{-3} for mode 2, 0.75 cm^{-3} for mode 3, and $1\text{x}10^{-15}$ cm^{-3} for mode 4) obtained by fitting the HCAM model onto rotorod data [15] (cf. Appendix A) serve as an equilibrium point for the analysis.

Subsection 3.3.1 presents the method used. Errors produced by uncertainties in LSA (defined in Subsection 2.5.2) are studied in Subsection 3.3.2, φ_s (defined in Subsection 3.2.1 – cf. footnote #12) in Subsection 3.3.3, $\overline{N}$ (defined in Subsections 3.2.1 and 3.2.4) in Subsection 3.3.4, and T_R (defined in Subsection 3.2.1) in Subsection 3.3.5.

[15] This method delivers results of limited reliability, as explained and emphasized in Subsections 2.2.2 and 2.2.3. The estimation of aerosol concentrations by fitting the HCAM aerosol model onto mechanical measurements leads to the indirect comparisons in consistency of NOVAM (a model applicable to open-ocean estimations). However, the procedure which consists in estimating errors from simulations should be considered a promising avenue for improving the current understanding of the polarization-ratio method.

3.3.1 Deterministic estimation

Equation set (3.2) applies to both actual (superscript A in subsequent terms) experimental circumstances and those of the reconstruction (or estimated conditions – superscript E in subsequent terms). Equating both intensities (at the same polarization) and rearranging terms toward expressing the estimated polarization ratio yields:

$$PR^E = \frac{\left(N_{//}^A - N_{//}^E\right) + \delta^A T_R^A \sum_{j=-1}^{4} n_{0,j}\left[F_{2,j}^A \cos^2\left(\varphi_s^A\right) + F_{1,j}^A \sin^2\left(\varphi_s^A\right)\right]}{T_R^E\left\{\left(N_{\perp}^A - N_{\perp}^E\right) + \delta^A \sum_{j=-1}^{4} n_{0,j}\left[F_{2,j}^A \sin^2\left(\varphi_s^A\right) + F_{1,j}^A \cos^2\left(\varphi_s^A\right)\right]\right\}} \tag{3.7}$$

where δ^A comprises both instrumental and environmental terms and $\varphi_S^E = 90°$ as $\hat{E}_i$ in Fig. 2.2 is assumed to remain perpendicular to the scattering plane which contains the non-fanned laser beam and both cameras, in a simplified actual experimental set-up. The estimation procedure uses Eq. (3.7) to estimate the concentrations for which values of the variables in the reconstructed experimental set-up differ from those in the actual experiment. The present section analyzes these implications.

The estimation procedure in Subsection 3.2.2 is still applicable once d_j is updated as follows:

$$\begin{aligned} d_j \triangleq & \left(N_{\perp}^A - N_{\perp}^E\right)F_{2,j}^E T_R^E - \left(N_{//}^A - N_{//}^E\right)F_{1,j}^E \\ & + \delta^A \sum_{i=-1}^{4} n_{0,i}\left[\left(F_{2,i}^A \sin^2\varphi_s^A + F_{1,i}^A \cos^2\varphi_s^A\right)F_{2,j}^E T_R^E - F_{1,j}^E\left(F_{2,i}^A \cos^2\varphi_s^A + F_{1,i}^A \sin^2\varphi_s^A\right)T_R^A\right] \end{aligned} \tag{3.8}$$

in which PR^E has been explicitly expressed. Equations (3.7) and (3.8) encompass all the necessary parameters to simulate both systematic and statistical uncertainties. Already, if either both *N*-noise differences are null (when the estimated noise-means equal the actual ones) or δ^A is large enough to neglect *N*-noise terms, then δ^A disappears from Eq. (3.7); which is one of the original consequences of the polarization-ratio method.

Subsections 3.3.2 to 3.3.5 calculate errors in estimated concentrations when one instrumental variable (at a time) is improperly measured (simulating its DC uncertainty) at the equilibrium concentrations stated previously. Several neighborhood (adjacent pixels in an image) sizes are tried to determine if it is possible to diminish simultaneously both deterministic and statistical uncertainties. The same neighborhood is applied to images from cameras A and B considered either separately or together.

3.3.2 Errors in estimated concentrations resulting from uncertainties in *LSA*

The present Subsection seeks to determine the precision with which the Laser Sheet Angle (*LSA*) should be refined by the triangulation technique mentioned in Section 2.5.4.

The conditions of the simulation are: (1) an arbitrary reference *LSA* of 79.2°, (2) an evaluated *LSA* departure from the reference one by a controlled amount, (3) representative concentrations seen from all scattering angles, (4) an arbitrary neighborhood size consisting of adjacent pixels (including the choice in camera), (5) estimation via Eq. (3.6) at every scattering angle, (6) calculation of the absolute value of the difference between estimated and original concentrations subsequently divided by the original concentrations averaged over all relative humidities (cf. Table 2.3) and scattering angles; called the Mean Fractional Error (MFE).

Figure 3.1(a) displays results for modes 2 and 3 only, using both cameras A and B together. Other modes were estimated with an approximate MFE per degree of $5\text{x}10^{11}$% for modes 0 and 1, and 10^{16}% for mode 4.

In most cases, estimation using both cameras outperforms those using only one, although errors in the estimation of *LSA* rapidly drive the estimation astray: a 2.5 mdeg error results in a 10% MFE for both modes 2 and 3 with a 5 pixel neighborhood. These numbers justify the procedure mentioned in Section 2.5 to refine the estimation of the *LSA*.

3.3.3 Errors in estimated concentrations resulting from uncertainties in φ_s

Section 2.3 defines φ_s**,** the tilt angle, and Section 2.5 expresses means to calculate it. The conditions of the simulation are the same as those of Subsection 3.3.2, except that the evaluated tilt angle departure (instead of variations in the *LSA*) ranges from -10° to 10°, and that *LSA* is assumed perfectly measured.

Figure 3.1(b) displays results for modes 2 and 3, using both cameras A and B together. Other modes have an approximate MFE per degree of 10^{9}% for both modes 0 and 1, and 10^{14}% for mode 4.

In most cases, estimation using both cameras outperforms those using only one (for the same neighborhood size). A 5° error in the estimation of φ_s results in a 10% MFE, approximately, for both modes 2 and 3.

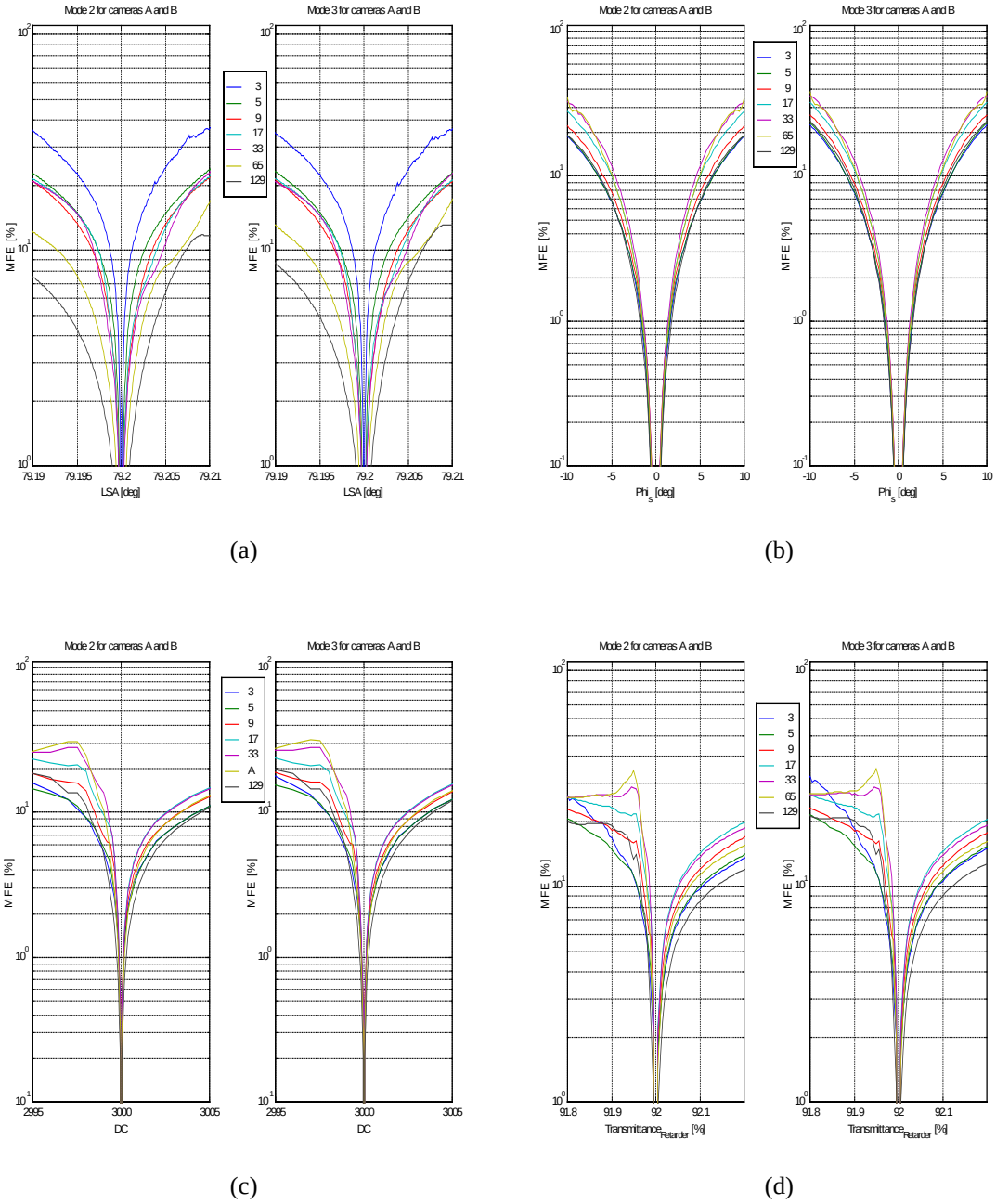

Figure 3.1. The Mean Fractional Error (MFE) of estimated concentrations for modes 2 and 3 using both cameras (A and B, positioned at the same height as the one of the non-fanned laser beam) resulting from deterministic uncertainties in the (a) position of the Laser Sheet Angle, (b) departure from true vertical for φ_s when the retarder plate is not inserted, (c) mean noise $\overline{N}$, and (d) transmittance through the retarder plate (inserted to rotate the outgoing polarization by 90°). The legend between each pair of plots refers to the number of adjacent pixels in each neighborhood used by each camera in the recovery process via Eq. (3.6). The number of adjacent pixels may be approximated into degrees simultaneously processed by multiplying the number of pixels (minus one) by 0.034°. For instance, 129 pixels simultaneously cover about 4.35°.

3.3.4 Errors in estimated concentrations resulting from uncertainties in $\overline{N}$

$\overline{N}$ is defined as the mean part of the noise in Eq. (3.3). The conditions of the simulation are the same as those of Subsection 3.3.2, except that *LSA* is assumed perfectly measured, T_R is set to its nominal value of 0.92, and δ^A is calibrated against approximate experimental values around a relative $\overline{N}$ of 3000 where Eq. set (3.2) results in a maximum of 3300 counts. For the purpose of the simulations, $\Delta N = \Delta N_{\perp} = \Delta N_{//}$ (where $\Delta N \hat{=} N^A - N^E$ – cf. Subsection 3.3.1 for notational conventions), $N^A = 3000$, and $DC \hat{=} N^E$ varies from 2995 to 3005 for both cameras together.

Figure 3.1(c) displays results for modes 2 and 3, using both cameras A and B together. Over the offset range, modes 0 and 1 reach 10^{10}% MFE, mode 4 reaches 10^{14}% MFE, but modes 2 and 3 approximately remain within a 10% MFE.

3.3.5 Errors in estimated concentrations resulting from uncertainties in $T_{Retarder}$

T_R is the transmittance through the retarder plate which is inserted to rotate the outgoing polarization from vertical to horizontal. The conditions of the simulation are the same as those of Subsection 3.3.2, except that the evaluated T_R departure ranges from -0.1 to 0.1% of the arbitrary chosen T_R of 92%[16] and that *LSA* is assumed perfectly measured.

Figure 3.1(d) displays results for modes 2 and 3, using both cameras A and B together. Other modes have an approximate MFE around the assumed T_R of 10^{11}% for modes 0 and 1, and $5\text{x}10^{14}$% for mode 4.

Estimation using both cameras is not consistently better than the one using either camera alone. Errors in the estimation of T_R rapidly led the estimation astray: a 0.1% error in T_R results, approximately, in a 10% MFE for both modes 2 and 3.

3.3.6 Conclusion

The simulations show that (1) increasing the number of neighbors does not necessarily lead to a better estimation, (2) errors in *LSA* and T_R significantly deteriorate the quality of the estimation (the former of which is refined from values originally 5% off, the latter of which still contains uncertainties with respect to its true transmittance during EOPACE), and (3) the estimated concentrations of modes 2 and 3 are the

most plausible (these modes contribute mainly to the visible plumes) reducing the total required number of equations to two (i.e., two cameras and one pixel per camera). The simple estimation via Eq. (3.6) originates in the knowledge of the deterministic expression for the true polarization ratio. Deterministic uncertainties are solved by accurately measuring instrumental variables.

3.4 Estimation of concentrations under stochastic uncertainties

Assuming that all errors in Section 3.3 have been corrected, this section aims to estimate the concentrations in the presence of stochastic noise which originates both internally and externally to the cameras. The former results from a multitude of processes inherent to CCD arrays (cf. Janesick et al., 1987) and the latter from the dynamics of the surveyed environment (attributed to fluctuations in concentrations).

Conceptually, the problem is to estimate $\underline{n}$ such that Eq. (3.1) and Eq. (3.3) be equal, in probabilistic terms. To properly reach this aim, these and other equations need to be revisited to include explicitly both sources of fluctuations:

$$\begin{aligned} I_{//,i} &= \overline{N}_{//} + \delta T_R \left(\underline{F}_{//}^T \underline{n} + F_{//,-1} n_{-1} \right) + \delta T_R \underline{F}_{//}^T \underline{\tilde{n}}_i + \tilde{w}'_{//,i} \\ I_{\perp,i} &= \overline{N}_{\perp} + \delta \left(\underline{F}_{\perp}^T \underline{n} + F_{\perp,-1} n_{-1} \right) + \delta \underline{F}_{\perp}^T \underline{\tilde{n}}_i + \tilde{w}'_{\perp,i} \end{aligned} \tag{3.9}$$

where $\overline{N}$ denotes a background offset, a tilde denotes fluctuations, δ is as defined in Subsection 3.3.1, $\underline{F}_{//}^T \underline{n} \hat{=} \sum_{j=0}^{4} n_{0,j} \left[F_{2,j} \cos^2(\varphi_s) + F_{1,j} \sin^2(\varphi_s) \right]$, $\underline{F}_{\perp}^T \underline{n} \hat{=} \sum_{j=0}^{4} n_{0,j} \left[F_{2,j} \sin^2(\varphi_s) + F_{1,j} \cos^2(\varphi_s) \right]$, and the subscript *i* refers to the image number *i* out of a series of *M*. Fluctuations in concentrations ($\underline{\tilde{n}}$) disappear from Eq. (3.9) either by assuming that the atmosphere is frozen over the total collection period or by amalgamating them with the CCD fluctuations ($\tilde{w}'_{//,i}$ and $\tilde{w}'_{\perp,i}$) for the purpose of analyses. Those CCD fluctuations are modeled as a zero-mean, independent, Gaussian random variable of standard deviation σ_{CCD} over all samples (this model was selected after successfully applying a series of χ^2 tests over each pixel with different probability density functions at different integration times and incident intensities – cf. Appendix D). From Eq. (3.3), the polarization ratio of the i^{th} image becomes:

---

[16] This value originates from commercial retarder plates of similar characteristics as the one used during EOPACE. Once Chapter 3 completed, two retarder plates were found in the ARL/PSU laboratory. Chapter 4 assigns a value of 99.2585% to T_R ; a value obtained from actual measurements.

$$PR_i = \frac{\Delta I_{//,i}}{\Delta I_{\perp,i} T_R} = \frac{\left(\underline{F}_{//}^T \underline{n} + F_{//,-1} n_{-1}\right) + \tilde{w}_{//,i}}{\left(\underline{F}_{\perp}^T \underline{n} + F_{\perp,-1} n_{-1}\right) + \tilde{w}_{\perp,i}} \tag{3.10}$$

where $\Delta I_{//,i} \hat{=} I_{//,i} - \overline{N}_{//}$, $\Delta I_{\perp,i} \hat{=} I_{\perp,i} - \overline{N}_{\perp}$, $\tilde{w}_{//,i} \sim N\left(0, \sigma_{CCD} / \left(T_R \delta\right)\right)$, and $\tilde{w}_{\perp,i} \sim N\left(0, \sigma_{CCD} / \delta\right)$. In the absence of fluctuations, Eqs. (3.10) and (3.1) are equal.

Subsection 3.4.1 describes the process by which an objective non-iterative procedure estimates the concentration vector $\underline{n}$ from a series of noisy images. Subsection 3.4.2 presents the probability density function of the ratio of two (possibly correlated) Gaussian random variables. The first part of the estimation process is both defined and analyzed in Subsection 3.4.3 for two estimators of the polarization ratio. The second part which is addressed in Subsection 3.4.4 consists of inverting a matrix. Subsection 3.4.5 assesses the performance in the estimation procedure under representative concentrations for a variety of signal-to-noise ratios and neighborhood sizes. Subsection 3.4.6 concludes on the method to apply in Chapter 4.

3.4.1 Stochastic estimation

Non-Bayesian stochastic estimation techniques operate by postulating both a deterministic function of parameters and a stochastic model for the noise and by either minimizing or maximizing a criterion (a cost or fitness function) to define appropriate estimators for the estimated parameters. The methods briefly reviewed by Goldberg (1989, pp. 2-7) are methodically described by Kay (1993)[17] to seek the best possible estimator and are computationally detailed by Press et al. (1988). The ease of access of the parameters to estimate determines whether an iterative search-scheme is necessary.

Despite an arsenal of techniques, a Minimum Variance Unbiased (MVU) estimator (Kay, 1993) cannot be found for estimating the concentrations from Eq. (3.10). Among the remaining schemes, those iterative are the Maximum Likelihood and Least Square criteria, the latter of which resembles the approach taken by Stevens (1996, p. 94, to minimize “the error between the model and the data”).

In Stevens’ (1996) estimation scheme, the nine parameters of the ambitious model are resolved iteratively through a two-step process involving an operator (to find a good initial nine-parameter vector) followed by the Newton-Raphson numerical driver (to refine the initial nine-parameter vector). However, no iterative technique guarantees finding the correct answer (cf. Goldberg, 1989, Press et al., 1988, Kay,

[17] Bard (1974) and Kendall and Stuart (1967, vol. II) are also recommended, although less recent.

1993, and Stevens, 1996[18]). In addition, the assistance of an operator makes the estimation both time consuming and subjective (to the operator's definition of goodness of fit).

However, an objective non-iterative technique appears when breaking the estimation into two independent steps: the first one estimates the polarization ratio from a series of noisy images at both parallel
and perpendicular incident-polarizations and the second one estimates the concentrations via the technique introduced in Subsection 3.2.2. These estimators are defined and their performance assessed in Subsections 3.4.3 to 3.4.5.

3.4.2 Probability Density Function (pdf) of the ratio of two Gaussian random variables

Equation (3.10) divides one Gaussian random variable by another, each of which being either a measurement or the model of one. Different reasons have, in the past, led to the derivation of the pdf of this ratio by Fieller (1932, p. 432). Using modern notations, and denoting $Z = X/Y$ where $X \sim N(m_x, \sigma_x)$, $Y \sim N(m_y, \sigma_y)$, and r is the correlation coefficient between *X* and *Y*, the pdf of the ratio, *Z*, is (the derivation is detailed in Appendix E):

$$f_Z(z) = \frac{\exp(-c)}{2\pi\sigma_x\sigma_y a\sqrt{1-r^2}}\left[\sqrt{\pi}\frac{b}{2\sqrt{a}}\exp\left(\frac{b^2}{4a}\right)\mathrm{erf}\left(\frac{b}{2\sqrt{a}}\right)+1\right] \tag{3.11}$$

where:

$$\begin{aligned} a &\triangleq \frac{1}{2(1-r^2)}\left(\frac{z^2}{\sigma_x^2}+\frac{1}{\sigma_y^2}-\frac{2zr}{\sigma_x\sigma_y}\right) \\ b &\triangleq \frac{1}{(1-r^2)}\left(\frac{m_x}{\sigma_x^2}z+\frac{m_y}{\sigma_y^2}-\frac{r}{\sigma_x\sigma_y}\left(z\,m_y+m_x\right)\right) \\ c &\triangleq \frac{1}{2(1-r^2)}\left(\frac{m_x^2}{\sigma_x^2}+\frac{m_y^2}{\sigma_y^2}-\frac{2r}{\sigma_x\sigma_y}m_x m_y\right) \end{aligned} \tag{3.12}$$

and:

$$erf(x) \triangleq \frac{2}{\sqrt{\pi}}\int_0^x \exp\left(-t^2\right)dt$$

[18] "there are far too many local extremum on the way to the true root." (p. 155)

Equation (3.11) contains the Cauchy density which induces divergence for the second and higher moments. Another difficulty resides in the calculation of the first moment which uses the principal value argument, conventionally rejected by authors such as Kendall and Stuart (1967, p. 59).

Yet, $f_Z(z)$ is the door to estimate the polarization ratio. In addition to decorrelated variables $(r = 0)$, decompositions of Eq. (3.14) in Subsection 3.4.3 isolate m_x from the noise term so that $m_x = 0$ at the numerator. This fortunate development allows the definition of a threshold *T* to quantify the presence of the Cauchy term in $f_Z(z)$ [19]: if $SNR_y \triangleq m_y^2 / \sigma_y^2 < -2\ln(T)$ then the Cauchy term dominates $f_Z(z)$ and both terms contribute equally ($T = 0.5$) when $SNR_y = 1.42$ dB. This practical criterion was derived for one image, although the influence and availability of multiple images (cf. Subsection 3.4.3) result in a slightly different expression.

3.4.3 Estimators of the polarization ratio: $\hat{PR}$ and $\check{PR}$

This subsection characterizes two estimators of the polarization ratio.

The first one computes the ratio of the sample means of *M* images at each polarization whereas the second one computes the sample mean of their ratios. In mathematical terminology (T_R being a deterministic correction-factor) and translating notations into those of the previous subsection:

$$\hat{PR} \triangleq \frac{\frac{1}{M}\sum_{i=1}^{M} \Delta I_{//,i}}{\frac{T_R}{M}\sum_{i=1}^{M} \Delta I_{\perp,i}} = \frac{\frac{1}{M}\sum_{i=1}^{M} X_i}{\frac{1}{M}\sum_{i=1}^{M} Y_i} = \frac{\overline{X}}{\overline{Y}} \qquad \check{PR} \triangleq \frac{1}{M\,T_R}\sum_{i=1}^{M} \frac{\Delta I_{//,i}}{\Delta I_{\perp,i}} = \frac{1}{M}\sum_{i=1}^{M} \frac{X_i}{Y_i} \tag{3.13}$$

To show that both $\hat{PR}$ and $\check{PR}$ are unbiased estimators, they are decomposed into their expected means and additive noise terms (cf. Appendix F for details):

$$\hat{PR} = \frac{\frac{1}{M}\sum_{i=1}^{M} \left(m_x + w_{x,i}\right)}{\frac{1}{M}\sum_{i=1}^{M} \left(m_y + w_{y,i}\right)} = \frac{m_x}{m_y} + w_{\wedge} \qquad \check{PR} = \frac{1}{M}\sum_{i=1}^{M} \frac{\left(m_x + w_{x,i}\right)}{\left(m_y + w_{y,i}\right)} = \frac{m_x}{m_y} + w_{\vee} \tag{3.14}$$

---

[19] Specifically the contribution by the Cauchy term is $T \triangleq \int_{-\infty}^{+\infty} \frac{\exp(-c)}{2\pi\sigma_x\sigma_y a\sqrt{1-r^2}}\,dz$ where $T \in [0,1]$.

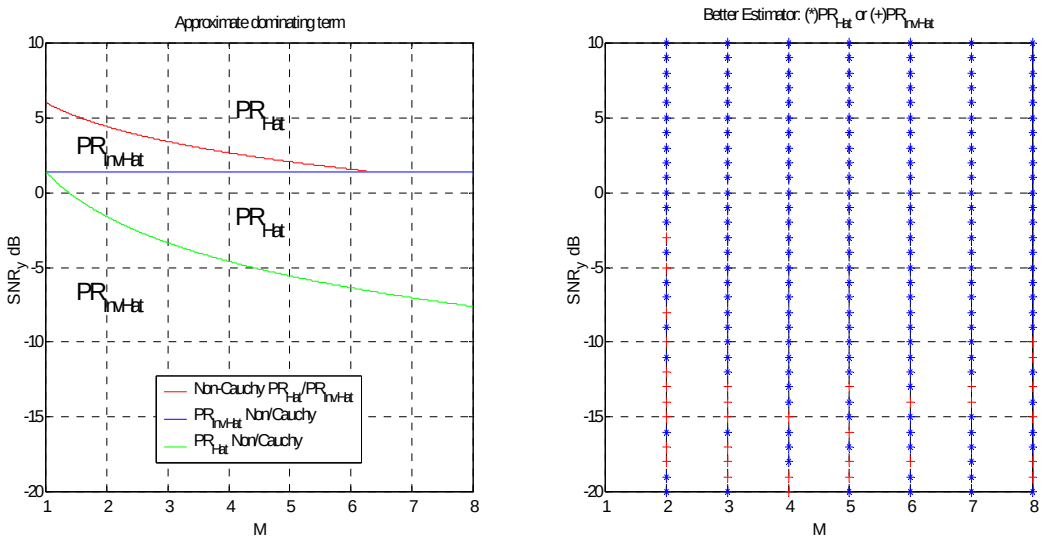

(a) (b)

Figure 3.2. Regions of the (M,SNR_y) plane in which (a) either estimator is analytically expected to outperform the other (green and blue lines delimit T = 0.5 with their respective Cauchy terms below the former line for PR_{Hat} and below the latter line for PR_{InvHat}. The red line marks the separation between the better estimator when their non-Cauchy terms compete) and (b) simulations from 1 million variances (at each SNR_y, M, and various σ_x).

where $w_{x,i} \sim N(0,\sigma_x)$, $w_{y,i} \sim N(0,\sigma_y)$, zero correlation, $w_{\wedge}$ ~ ratio of $N\left(0,\sqrt{m_y^2\sigma_x^2/M + m_x^2\sigma_y^2/M}\right)$ to $N\left(m_y^2, m_y\sigma_y/\sqrt{M}\right)$, and $w_{\vee}$ ~ sample mean of the ratio of $N\left(0,\sqrt{m_y^2\sigma_x^2 + m_x^2\sigma_y^2}\right)$ to $N\left(m_y^2, m_y\sigma_y\right)$. When only one image is available at each polarization, both estimators are equal. The means of $w_{\wedge}$ and $w_{\vee}$ are zero (in both cases $f_Z(z)$ is even and the integration bounds are symmetric, despite the position taken by Kendall and Stuart, 1967), making both estimators unbiased (cf. Appendix F for details).

From Eq. (3.14), the variances of both $\hat{PR}$ and $\check{PR}$ are the same as those of their respective additive noises $w_{\wedge}$ and $w_{\vee}$; infinity. The Cauchy term dominates when $SNR_y \hat{=} m_y^2/\sigma_y^2 < -2\ln(T)/M$ in $\hat{PR}$ and $SNR_y \hat{=} m_y^2/\sigma_y^2 < -2\ln(T)$ in $\check{PR}$.

Those relations between SNR_y and M suggest dividing this space into regions within which one term dominates $f_Z(z)$ for each estimator, easing the process which determines the conditions under which $\hat{PR}$ outperforms $\check{PR}$ and *vice-versa*. The results both from this analysis (detailed in Appendix F) and from simulations are displayed Fig. 3.2 in which the threshold T has been set to 50%.

In conclusion, $\hat{PR}$ clearly dominates $\check{PR}$ at an SNR_y greater than 0 dB, although the situation is more confused below this value. The outcomes of the simulations were consistently independent of σ_x.

3.4.4 Estimators of the concentrations from the polarization-ratio vector

Once estimated for selected pixels and cameras, the polarization ratios are placed into Eq. (3.5) to estimate the concentration vector $\underline{n}$ (so defining a neighborhood in the Plume Space). This subsection addresses issues pertaining to this inversion (cf. Eq. (3.6)).

Each estimator of the polarization ratio may preserve its expression when placed into Eq. (3.1) where rearranged terms lead to two slightly different equations, both based on Eq. (3.4), where a horizontal bar atop *X* and *Y* denotes the sample-mean operator (cf. Eq. (3.13)):

$$\begin{aligned}
\hat{PR}:\ d_j &\hat{=} \left(\overline{Y}\,F_{1,j} - \overline{X}\,F_{2,j}\right)\sin^2(\varphi_s) + \left(\overline{Y}\,F_{2,j} - \overline{X}\,F_{1,j}\right)\cos^2(\varphi_s) \\
\check{PR}:\ d_j &\hat{=} \left(F_{1,j} - F_{2,j}\,\check{PR}\right)\sin^2(\varphi_s) + \left(F_{2,j} - F_{1,j}\,\check{PR}\right)\cos^2(\varphi_s)
\end{aligned} \tag{3.15}$$

Two perspectives may be taken on the inversion leading to the concentrations: in the first one all the polarization-ratio values are fixed parameters and in the second one the polarization-ratio values may depart from their expected values. The latter case opens the door (which shall remain ajar) onto the field of random matrix algebra.

To diagnose potential inversion difficulties, the condition number[20] is computed. Figure 3.3 illustrates the noiseless condition numbers of neighborhoods composed of pixels from camera A alone, B alone, and A and B together, at representative concentrations. Three comments are in order. First, the closer the scattering angles captured by adjacent pixels included in a neighborhood, the more alike the scattered irrandiance, resulting in higher condition numbers. Second, an increase in the number of neighbors decreases the condition number. Third, the combination of data from sensors of complementary views reduces the condition number.

[20] Defined as the ratio of the highest to the smallest singular values of a given matrix (also called 2-norm). The higher the condition number the closer to singular the matrix. Demmel (1988) reports inverse proportionality between the condition number and the nearest singular matrix (cf. Edelman, 1992, and Shen, 2000, for further properties, especially as the condition number relates to random matrices).

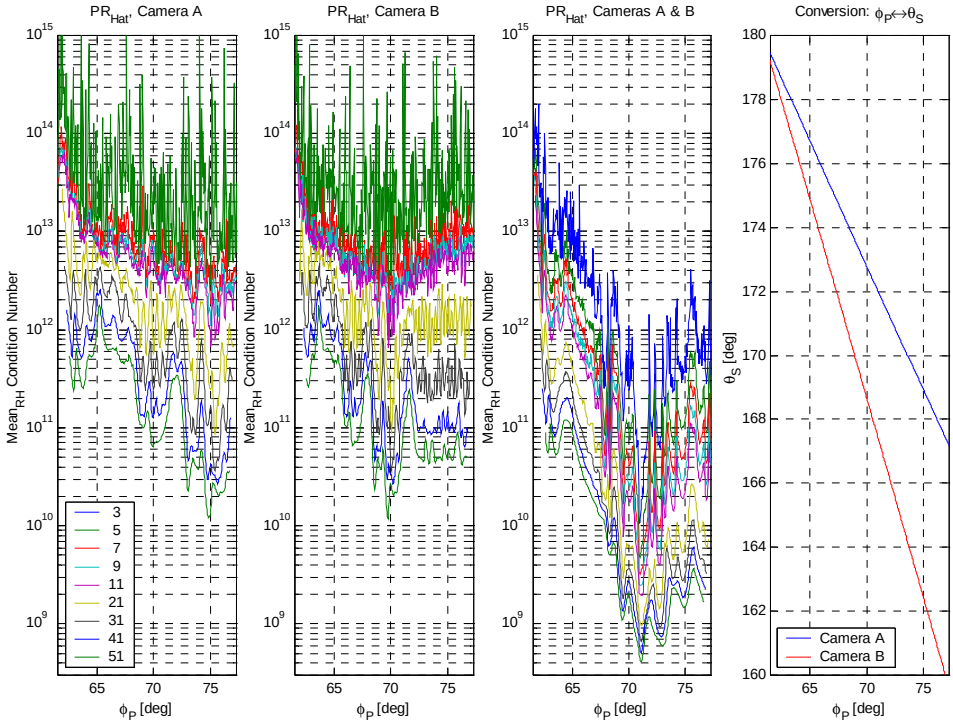

(a) (b) (c) (d)

Figure 3.3. Condition numbers averaged over all considered relative humidities (of the matrix *D* defined in Subsection 3.2.2) for (a) camera A (closer to the laser transmitter), (b) camera B (closer to the pier), or (c) cameras A and B together. The legend inside (a) displays the number of adjacent pixels contributed by each camera to form a neighborhood. ϕ_P is the angle defined by the vector from camera A to B and the vector from the point equidistant to both cameras on the line stretched between them to the point P sliding along the laser beam. For each camera, (d) converts ϕ_P into θ_S, the scattering angle, and *vice-versa*.

The absence of simulated receiver-noise does not imply an error free estimation of the concentrations. Numerical limitations introduce a subtle noise. Above 10^{12}, the condition number signals that numerical limitations deteriorate the quality of the inverse matrix (Press et al., 1988). For instance, the estimated concentrations of modes 0 to 3 (not shown) improve as the condition number reaches the trough near 71° from MFE values of 1%, 1%, 10^{-8}%, and 10^{-8}% to 10^{-2}%, 10^{-2}%, 10^{-10}%, and 10^{-9}% while mode 4 plateaus at 10^{5}%, when both cameras are used simultaneously. The estimated concentrations of modes 0 through 4 (not shown) using either camera (A or B) averaged over all the observable angles (ϕ_P) result in approximate MFE values of 10%, 10%, 10^{-8}%, 10^{-8}%, and 10^{4}% whereas both cameras (A and B) decrease those numbers to 10^{-1}%, 10^{-1}%, 10^{-9}%, 10^{-9}%, and 10^{3}%.

The condition number measures the numerical contrast (rather, its lack thereof) resulting from combining the use of the polarization ratio, the experimental data (i.e., their fusion), and the models. Even in a noiseless case the estimated concentrations are biased due to numerical limitations. One way to solve

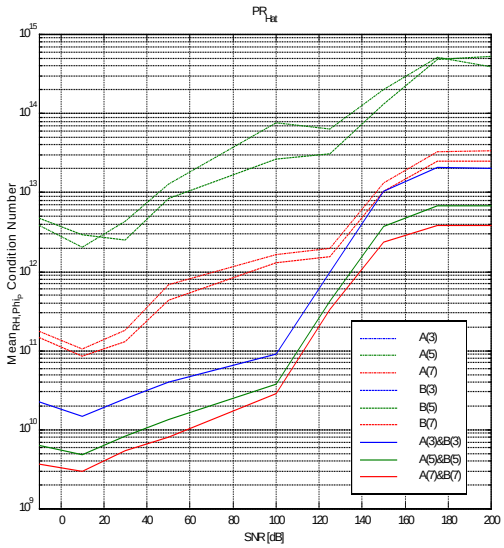

Figure 3.4. Average (over all scattering angles and relative humidities) influence of Gaussian fluctuations toward a given signal-to-noise ratio (SNR) onto the condition number of Eq. (3.15). Little difference was noticed between approaches of Eq. (3.15).

this limitation is to increase the number of bits over which numbers are encoded. But this approach is worthwhile only if the total magnitude of the noise injected into the data is less that the least significant bit.

3.4.5 Errors in estimated concentrations resulting from stochastic uncertainties

Subsections 3.4.3 and 3.4.4 have identified the regions of performance of both estimators and pointed to the noiseless condition number as a measure of the overall quality of the experiment. In the present subsection, effects introduced by noisy data are simulated at representative concentrations where only one image is analyzed to approximate results from either estimator (i.e., $\hat{PR}$ or $\check{PR}$).

To control the amount of injected noise, its standard deviation is adjusted to maintain a desired signal-to-noise ratio (SNR) for the received signal by the central pixel of a neighborhood at parallel incident polarization over all scattering angles. The simulations average both the condition numbers and the estimated concentrations over both all relative humidities and 3000 iterations at each sampled SNR values of -10, 0, 10, 30, 50, 100, 125, 150, 175, and 200 dB while combining both neighborhood sizes of 3, 5, and 7 adjacent pixels and cameras.

The condition number decreases as the amount of noise increases (cf. Fig. 3.4). In the noiseless case, the condition number approaches 10^{13} (both cameras with a neighborhood size of 3 pixels each), but progressively drops to 10^{10} at 10 dB while the Mean Fractional Error (MFE) at all modes increases (cf. Fig.

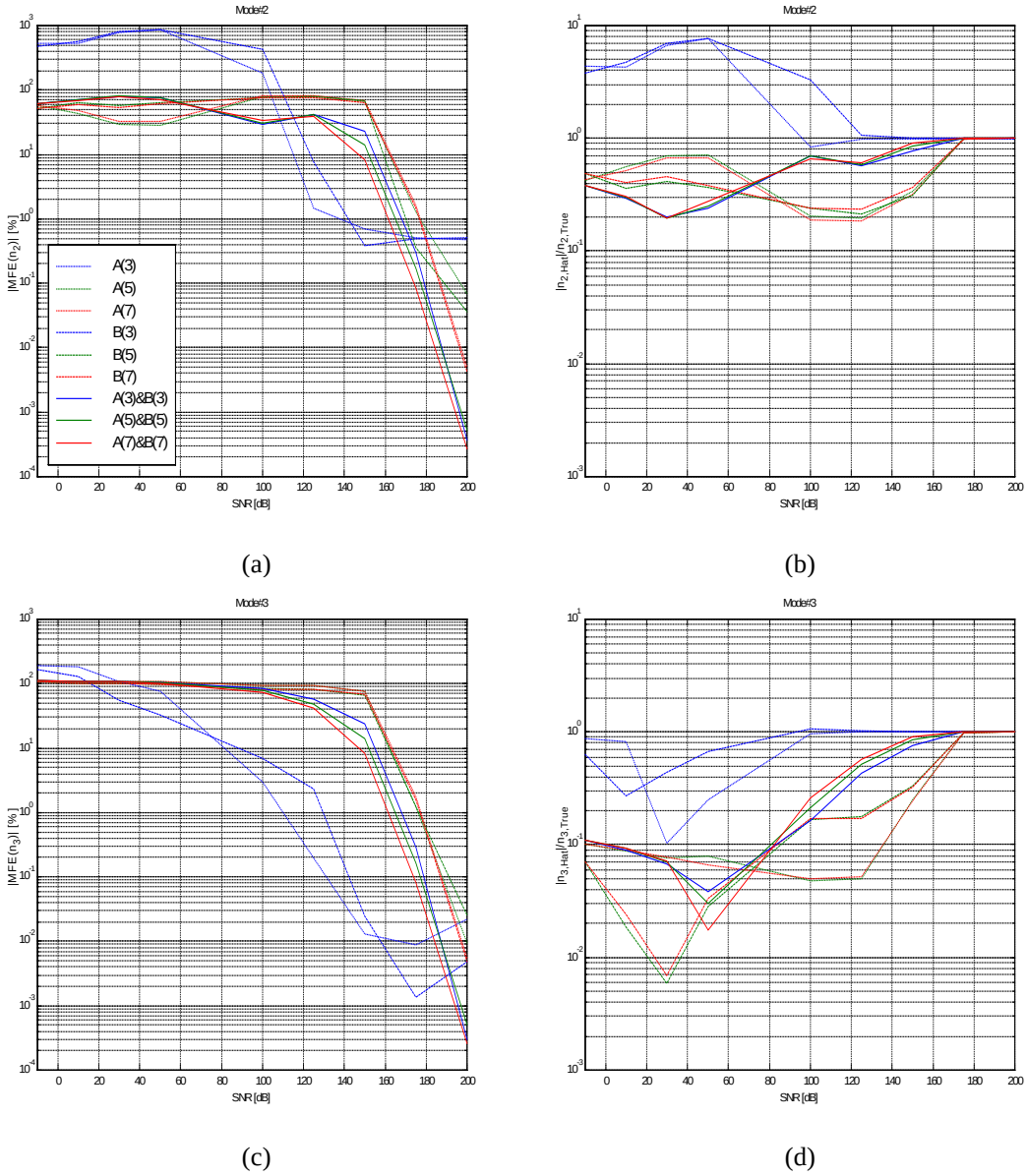

Figure 3.5. Average (over all scattering angles and relative humidities) influence of Gaussian fluctuations toward a given signal-to-noise ratios (SNR) onto the estimation of the concentrations of both mode 2 plotted as (a) the Mean Fractional Error and (b) the ratio of the estimated to the true concentration and mode 3 plotted as (c) the Mean Fractional Error and (d) the ratio of the estimated to the true concentration.

3.5(a,c)). This seemingly paradoxical behavior occurs from the dissimilarities introduced by the injected noise into the original sets of very similar equations. The inversion heavily relies on those differences to formulate a solution. In most cases, modes 2 and 3 offer the most stable estimated concentrations as their MFEs remain below 10^2%, compared to values within 10^4% to 10^{10}% for mode 0, 10^5% to 10^{10}% for mode 1, and 10^7% to 10^{16}% for mode 4. The condition number computed for each set composed of both pixels and cameras conserves its order over all SNR values, advising again to combine large numbers of pixels and cameras (especially noted is the poorer performance by either 5 or 7 pixels associated with either

camera compared to the one by 3 pixels per camera, but combined, resulting in a total of 6 pixels for cameras A and B together). This observation is supported by the MFE plots.

All overconstrained estimation procedures see their MFE decrease to 10%, 1%, and 0.1% near SNR values of 150, 170, and 180 dB for modes 2 and 3. Those SNR values are difficult to attained in real-world lidar experiments.

Another means to visualize errors in the estimated concentrations is the ratio of the estimated to the true concentration at each mode (cf. Fig. 3.5(b,d)). Modes 2 and 3 are consistently underestimated by a factor of 10 for the former and 100 for the latter. Modes 0, 1, and 4 are overestimated by factors of 10^8, 10^8, and 10^{12}. Kay (1993) warns of biases introduced by the inversion of overconstrained systems.

The challenge of the estimation process is to estimate the values of all concentrations despite large differences in their contribution to the total radiant energy, at representative concentrations (cf. Fig. 3.6). Hence, the weak optical presence of modes 0, 1, and 4 renders a system of 5 equations overconstrained.

3.4.6 Conclusion

Two objective estimators of the HCAM concentrations have been presented and their performances assessed. The relatively high values of the noiseless condition number at typical concentrations warn of the limitations encountered by a combination of numerical difficulties and overconstrained systems resulting in biased estimated concentrations.

Fluctuations affect both modes 2 and 3 the least. Values for the SNR to limit errors in the estimated concentration below 10% are far above those measured during EOPACE. Yet, estimation needs to proceed. The existing trade-off between choosing large neighborhoods and the scale of inhomogeneities in concentrations during EOPACE, the latter of which being still unknown, advocates using the smallest possible neighborhood which combines both cameras (A and B).

The current investigation recommends attempting a reduction in the effect of the bias by inverting modes 2 and 3 exclusively. Such a study is estimated to require 3 months in simulation time. As the present analysis considers the optical behavior of the NOVAM/ANAM aerosol models, the recommended investigation is not undertaken.

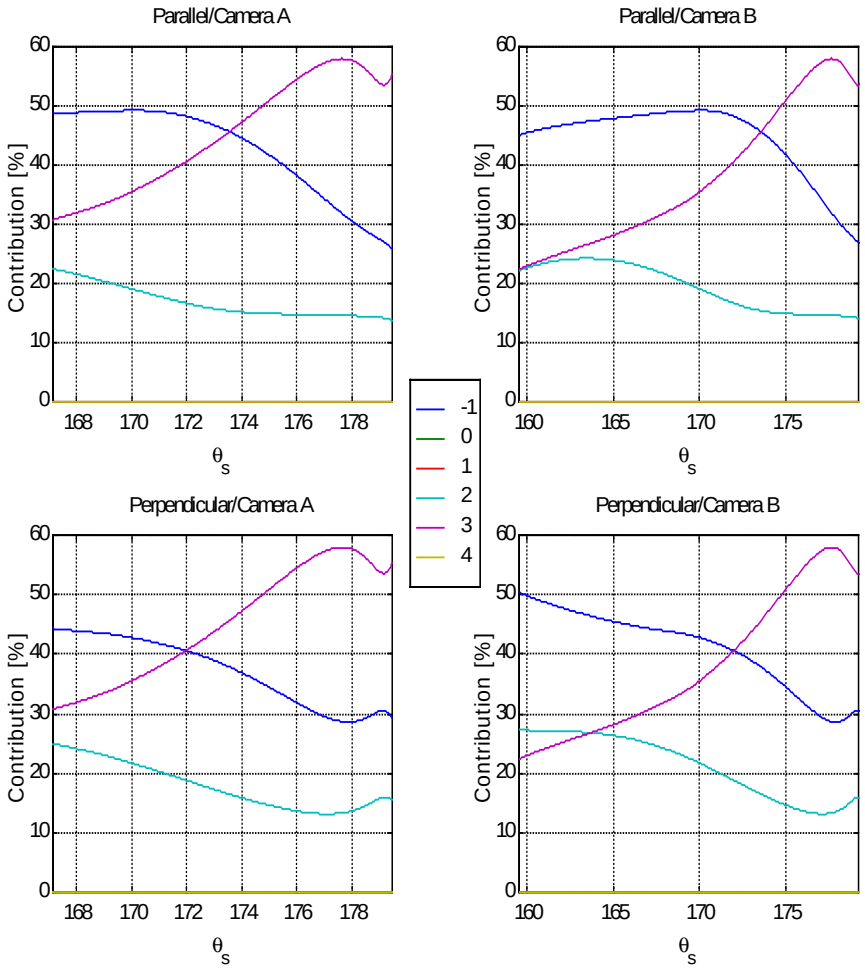

Figure 3.6. Noiseless contribution by each mode to the recorded radiant energy at typical concentrations. Modes 0 and 1 approximately contribute to 10^{-6}%. Mode 4 contributes to 10^{-13}%. Each quadrant shows contributions by each camera at each outgoing polarization. The weak contribution of modes 0, 1, and 4 explains the difficulty encountered by the inversion process to estimate concentrations with equal accuracy at all modes. (The legend displays the color associated to the mode number which it precedes.)

3.5 Conclusion

The present chapter produced objective estimators of the HCAM concentrations (neither an operator nor a first guess are necessary). Equation (3.5) confirms that estimation of the concentrations of several modes necessitates knowing the contribution by a reference mode (in this case, the mode of the atmospheric molecules – In a different context, the reference mode may be artificially injected). Sensitivity of the recovery process to four instrumental parameters (considered independently) and fluctuations has been quantified at representative concentrations (themselves estimated from the rotorod data). Modes 2 and 3 remain the most stable of all. Chapter 4 focuses on these two modes.

The noiseless condition number quantifies the maturity of an experimental set-up. It reflects the opportunity to obtain the highest possible optical contrast at images of complementary incident polarizations in the context of the polarization-ratio method. Additional simulations quantify the influence of fluctuations (i.e., SNR) onto each estimated concentration.

Without the analyses of Chapter 3, claim to perfect recovery at all modes over all SNR values might have erroneously been made. Through an iterative process relocating the cameras, the polarization-ratio method might deliver better results in subsequent experiments, transferring some of the estimation burden from a post-experimental task to one pre-experimental.

Despite significant contributions to the understanding of the polarization-ratio method, the author admits his frustration at the inability to derive (1) an MVU estimator for all the concentrations, (2) error-bars around estimated concentrations at all modes, and (3) results generalized for concentrations other than those representative of EOPACE.

CHAPTER 4
ESTIMATION OF THE AEROSOL CONCENTRATIONS USING THE POLARIZATION-RATIO METHOD ON THE EOPACE IMAGES

4.1 Introduction

Chapters 1, 2, and 3 have presented the purpose of the experiment, argued in favor of the HCAM aerosol-model, both defined and computed the F-functions, derived equations both to estimate and refine the parameters associated with values of the F-functions, and both designed and assessed the robustness of an objective algorithm to estimate aerosol concentrations from just a handful of pixels.

Chapter 4 applies the functions and algorithms of Chapters 2 and 3 to estimate aerosol concentrations (as seen by HCAM) from recorded EOPACE images. Section 4.2 specifies the EOPACE context by describing both the experimental organization and circumstances proper to the collection conducted at the Scripps Institution of Oceanography (March-April 1997). Estimated concentrations are both presented and discussed in Sections 4.3 and 4.4. The latter section preserves the spatial distribution of the concentrations whereas the former reduces the spatial distribution of each mode to a single concentration. Section 4.5 concludes Chapter 4. Chapter 5 addresses the success of the present analysis and suggests further research directions.

4.2 The EOPACE experimental and analytical contexts

EOPACE was first invoked in Chapter 1 to define the aim of the research conducted herein. Chapter 2 detailed the experimental set-up (sketched in Fig. 2.3) and Chapter 3 evaluated means to estimate the aerosol concentrations from simulated images. The complete procedure pertaining to the EOPACE experiment is divided into two steps: (1) data collection and (2) data analysis. The former is further described in Subsection 4.2.1 and the latter in Subsection 4.2.2, as they both specifically relate to the conditions isolated in Chapter 2 (cf. Table 2.3).

4.2.1 Data collection at the Scripps Institution of Oceanography (SIO)

Chapter 3 emphasized the importance of choices made at the experimental site, such as the precision with which the location and orientation of each critical device is measured (i.e., mirror, laser, cameras, etc.).

Table 4.1. Critical instrumental values for the experiment at the Scripps Institution of Oceanography (La Jolla, CA), from 31 March to 11 April 1997. Transmittance has been refined from recent measurements (simulations in Chapter 3 used the nominal value of 0.92).

Device	Device-Field	Field-Value [Units]
Camera A	Location (x,y,z) in Physical Space	(-87.0,-27.6,1.97) [m]
Camera A	Focal length	16 [mm]
Camera A	CCD array	KODAK KAF-0400
Camera A	Pixel dimension on CCD	9E-6 x 9E-6 [m^2]
Camera B	Location (x,y,z) in Physical Space	(-81.0,-25.77,1.95) [m]
Camera B	Focal length	16 [mm]
Camera B	CCD array	KODAK KAF-0400
Camera B	Pixel dimension on CCD	9E-6 x 9E-6 [m^2]
Emitter (laser)	Wavelength	514.5 [nm]
Emitter (laser)	Power	1.3 [W]
Emitter (laser)	Diameter of beam	1.2 [mm]
Emitter (mirror)	Location (x,y,z) in Physical Space	(-96,-18.8,-1.9) [m]
Emitter (cylindrical lens)	Focal length	-6.35 [mm]
Emitter (retarder plate)	Transmittance	0.992585
Red/Reference light	Location (x,y,z) in Physical Space	(1.54, 345.9, 9.44) [m]

This subsection documents both choices made and organizational steps undertaken during the data-collection phase of EOPACE at the SIO.

Two manually-synchronized CCD-cameras named A and B (the former of which was closer to the emitter mirror – cf. Table 4.1) recorded EOPACE images over various exposure times (from 5 to 300 seconds to cover a wide range of experimental conditions – from short-term variations to approximate steady states). Both cameras were switched on at least 20 minutes prior to collecting images (to allow the CCD cooling-system to reach thermal equilibrium). The last preparatory steps consisted in aligning the lidar beam with the ending edge of the pier (cf. Fig 2.3) then in fanning the beam by inserting a cylindrical lens and steering the fanned beam away from the pier by activating a stepper motor which rotated the emitter mirror.

During the experiment, three types of images were collected: (1) a background image (the laser was switched off and each camera cap was off – accounting for N in Chapter 3), (2) a perpendicular image[21], and (3) a horizontal image (obtained by inserting a retarder plate of known transmittance – accounting for T_R in Chapter 3). Sequences of images at both perpendicular and parallel polarizations were collected over consecutive time slots until a satisfactory time frame was covered, as determined by the PSU/ARL team.

[21] Properly, it should read that the image was collected upon outgoing perpendicular polarization, but this terminological shortcut is often encountered in experimental documents and subsequent discussions.

Nine sets of images have been isolated for analyses. Their conditions are defined in Appendix H. Each set is referred to by its configuration filename in the plots of estimated concentrations. The last five sets are different from the previous ones in that the magnitude of their meteorological measurements varied over the collection period. The next subsection describes the estimation process applied to these image sets.

4.2.2 Estimation of concentrations from EOPACE images

This subsection summarizes the steps leading to the plots of the estimated concentrations from the collected EOPACE images.

As mentioned in Chapter 3, all images of the same polarization are averaged before being processed. The reasons for this action are twofold: (1) a desire to reduce noise (from both plume motion and CCD fluctuations) and (2) an attempt to approach the collection timeframe of the rotorod data. Despite having smeared the plume-like features both spatially and temporally, the resulting steady state is expected to preserve the mean spatial distribution in aerosol concentrations. Consequently, the current analysis focuses on average characteristics of the surf-zone aerosols where the notions of steady state and average remain relative both to the timeframe over which all images were collected and the projection onto the laser sheet of the dimension of the spatial filter (composed of a neighborhood of adjacent pixels) applied during the estimation process.

Images have, at times, captured more than scattering by the plumes. Spurious pixels contain airplane lights, moon lights, comet lights, star lights, building lights, coastal lights, cabin lights (at the end of the pier), transmissiometer lights, and reflection of lamppost lights off of breakers (which resulted in the elimination of an area of pixels contained in the plane of breakers). All of these are disregarded whenever they are amenable to being rejected.

A MATLAB computer program whose primary purpose is both to estimate and display the two-dimensional HCAM-concentrations from the EOPACE images has been written in an object oriented fashion. Its structure emphasizes a modular approach to programming in which modules were progressively replaced by ones of greater maturity. It includes both all the estimation equations contained in the present document and a Graphical User Interface to explore a variety of estimation directives. These directives consist of choices in: (1) the relative-humidity sensor (SIO, NRaD, or an arithmetic mean of the two); (2) cameras (A, B, or an association of the two); (3) the number of adjacent pixels associated into a neighborhood by each camera: 1, 3, or 5, and (4) the modes to estimate (from mode 0 to either mode 3 or mode 4). Once a estimation completed, the estimated concentrations n_j (in number per cm^3, $j \in [0,4]$) are displayed either on a linear scale or one logarithmic of base 10 ($log_{10}(n_j)$, n_j in cm^{-3}). Preliminary analyses

have shown that the latter scale reveals more information than the former. Plots of the estimated concentrations are displayed on the logarithmic scale.

4.3 Estimation of concentrations from EOPACE images: Reduction to one concentration per mode

The purpose of the present section is to assess the credibility of the instrument by comparing (cf. Fig. 4.1) the estimated concentrations (denoted $n_{B,0..4}$) from the sets of EOPACE images defined in Appendix H to those (denoted $n_{G,0..4}$) from fits onto the rotorod data (as described in Chapter 2) and to those (denoted $n_{D,0..3}$) from NOVAM (defined in Subsection 2.2.1). All three estimated concentrations use environmental parameters (NOVAM is completely defined by those parameters), but only the lidar estimated concentrations include optical information.

The procedure applied to estimate $n_{B,0..4}$ consists in (1) choosing a set of images, (2) selecting estimation directives (cf. Subsection 4.2.2), (3) conducting the estimation over a specified area, (4) displaying histograms of the estimated concentrations (one histogram per mode), and (5) reporting the concentration at the peak of the distribution[22].

Subsections 4.3.1 to 4.3.9 tabulate the estimated concentrations (from the procedure just described), one set of EOPACE images at a time. Subsections 4.3.1 to 3.4.4 also tabulate those from the rotorod data. Subsection 4.3.10 compares extinction coefficients from the estimated concentrations for modes 2 and 3 and the same sets of EOPACE images. Subsection 4.3.11 concludes the present section.

4.3.1 Image set referred to as configuration file Apr04F01 (cf. Appendix H)

The concentrations estimated from the rotorod data are tabulated in Table 4.2. Tables 4.3 and 4.4 display the maximum log-likelihood concentrations (cf. footnote #22) from a subset of EOPACE images upon completion of the estimations of modes 0 through 4 and modes 0 through 3, respectively. Table 4.2 confirms the proximity of each concentration despite differences in relative humidity (cf. Table 2.3).

---

[22] This procedure delivers the visually estimated (read off the histogram) maximum log-likelihood concentrations (at the peak of the histogram whose concentrations are logarithmically compressed). Subsequently, application of the **(visually estimated) maximum log-likelihood criterion** refers to the same procedure. In the absence of an actual parameterized probability density function to fit onto the estimated concentrations, the use of the expression **maximum log-likelihood** is unusual, although it captures the essence of the process carried out. A stricter terminology employed by Bevington and Robinson (1992, p. 9) refers to each concentration so estimated as either the mode value or the most probable value. The usual and formal definition of a maximum (log-)likelihood estimator can be found in Kay (1993, Chapter 7).

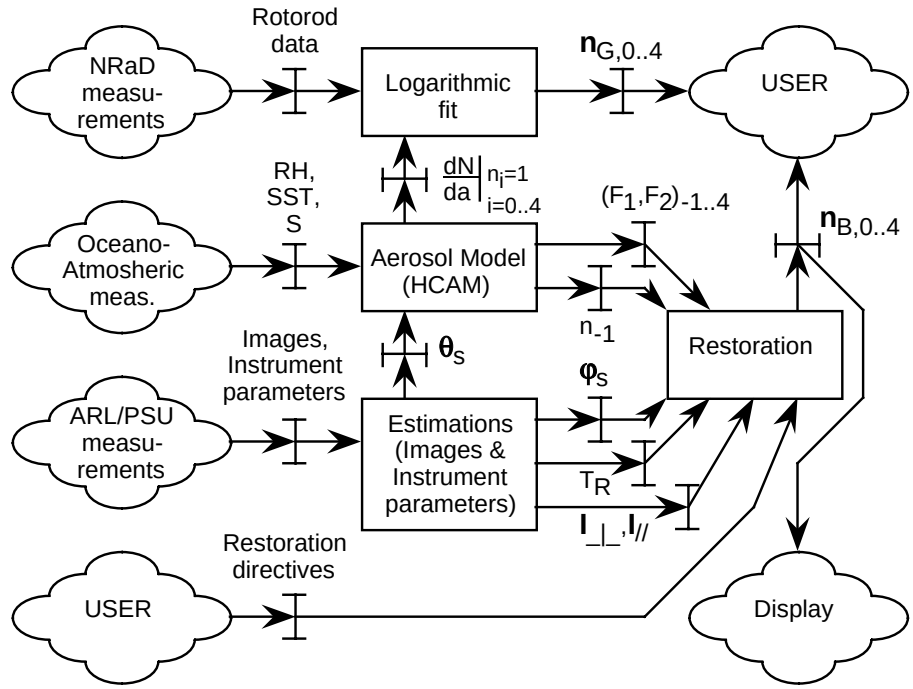

(a)

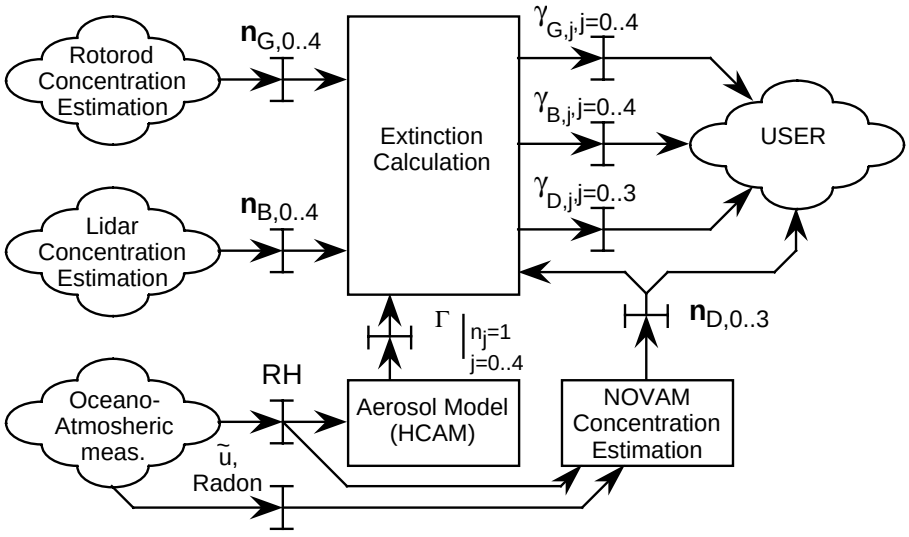

(b)

Figure 4.1. Diagrams (cf. Calvez, 1990, for meaning of symbols) showing the path followed by measurements to estimate both (a) concentrations and (b) extinctions from the rotorod data (NRaD measurements), from the lidar images (ARL/PSU measurements), and the NOVAM equations (NRaD and SIO measurements). Optical assumptions pertaining to HCAM are only taken into account in the estimation (by the block labeled "Restoration") of the HCAM concentrations. Relative humidity (RH), sea surface temperature (SST), and salinity (S) drive the aerosol radial distribution (dN/d*a*) of modes 0 though 4. The extinction coefficient for each modal distribution of particles of unit concentration (Γ) is the only optical information shared across all concentrations. Both diagrams describe the methodical road-map of comparisons whose results are presented in the present chapter.

Table 4.2. Estimated concentrations (n_j in cm^{-3}, j = 0…4) from rotorod data for an HCAM model assumed to include modes 0 to 4. An X denotes an irrelevant parameter. (Capture time PST: 21:02-21:03.)

Cameras	RH	Neighbors	$\log_{10}(n_0)$	$\log_{10}(n_1)$	$\log_{10}(n_2)$	$\log_{10}(n_3)$	$\log_{10}(n_4)$
X	Mean	X	-3.77	-3.87	+1.60	+0.59	-15.0
X	SIO	X	-3.88	-3.53	+1.60	+0.60	-15.0
X	NraD	X	-3.69	-3.59	+1.60	+0.59	-15.0

Table 4.3. Estimated concentrations (n_j in cm^{-3}, j = 0…4) when the HCAM model was assumed to include modes -1 to 4 (mode -1 is of fixed concentration). File Apr04F01 (cf. Appendix H).

Cameras	RH	Neighbors	$\log_{10}(n_0)$	$\log_{10}(n_1)$	$\log_{10}(n_2)$	$\log_{10}(n_3)$	$\log_{10}(n_4)$
(A,B)	Mean	3	+5.00	+5.80	+1.50	-0.90	-1.40
A	Mean	3	-2.00	-2.15	+1.70	-0.60	-0.50
B	Mean	3	-0.30	-0.60	+2.00	-0.10	-1.00
(A,B)	Mean	5	+5.00	+5.80	+1.40	-0.90	-1.40
A	Mean	5	+5.10	+5.80	+1.50	-1.00	-1.50
B	Mean	5	+5.10	+5.80	+1.50	-0.65	-1.50
(A,B)	SIO	3	+5.00	+5.80	+1.50	-0.90	-1.40
A	SIO	3	-2.00	-2.15	+1.70	-0.60	-0.50
B	SIO	3	-0.25	-0.60	+2.00	-0.05	-1.00
(A,B)	NRaD	3	+5.00	+5.75	+1.50	-0.95	-1.40
A	NRaD	3	-1.90	-2.20	+1.75	-0.60	-0.50
B	NRaD	3	-0.40	-0.75	+2.00	-0.10	-1.20

Table 4.4. Estimated concentrations (n_j in cm^{-3}, j = 0…3) when the HCAM model was assumed to include modes -1 to 3 (mode -1 is of fixed concentration). File Apr04F01 (cf. Appendix H).

Cameras	RH	Neighbors	$\log_{10}(n_0)$	$\log_{10}(n_1)$	$\log_{10}(n_2)$	$\log_{10}(n_3)$	$\log_{10}(n_4)$
(A,B)	Mean	3	+5.00	+5.80	+1.40	-1.25	X
A	Mean	3	+4.40	+4.15	+1.55	-1.55	X
B	Mean	3	+3.80	+3.50	+1.45	-0.15	X
(A,B)	Mean	5	+5.05	+6.30	+1.35	-1.65	X
A	Mean	5	+5.10	+5.80	+1.50	-1.00	X
B	Mean	5	+5.05	+6.00	+1.45	-0.65	X
(A,B)	SIO	3	+5.05	+6.10	+1.35	-1.20	X
A	SIO	3	+4.45	+4.05	+1.50	-1.50	X
B	SIO	3	+4.00	+3.70	+1.45	-0.05	X
(A,B)	NraD	3	+5.00	+5.65	+1.50	-1.20	X
A	NraD	3	+4.30	+4.10	+1.50	-2.15	X
B	NraD	3	+3.70	+3.45	+1.55	-0.20	X

To evaluate the reliability associated with each set of estimation directives, the following procedure is applied: (1) all estimated concentrations in Table 4.2 (from the rotorod data) are arithmetically averaged for each mode (in the logarithmic domain), defining a reference row vector of concentrations; (2) each row vector in either Table 4.3 or 4.4 is subtracted from the reference row vector (ignoring mode 4 in the latter case); (3) the absolute value of the difference from the previous step is summed; and (4) each set of estimation directives is ranked inversely proportionally to the outcome from the previous step.

In Table 4.3, estimations using camera A and 3 neighbors come first, followed by those using camera B and 3 neighbors, followed by those using both cameras and 3 neighbors, and followed by those using 5 neighbors. In Table 4.4, estimations using camera B and 3 neighbors come first, followed by those using camera A and 3 neighbors, followed by those using cameras A or B and 5 neighbors, followed by those using both cameras and 3 neighbors, and followed by those using both cameras and 3 neighbors. Simultaneous consideration of Tables 4.3 and 4.4 (while restricting the concentrations to modes 0 to 3 in the computation of difference) leads to the smallest difference (1) by estimated modes 0 to 4, camera A then camera B both with 3 neighbors, then (2) by estimated modes 0 to 3, camera B then camera A both with 3 neighbors, then (3) by estimated modes 0 to 4, cameras A and B together with 3 neighbors, and subsequent estimation directives fall relatively close.

Despite the influence of the estimation directives on the estimated concentrations, Tables 4.3 and 4.4 come close to each other on the concentrations for mode 2 followed by mode 3 which seems biased, whereas modes 0, 1, and 4 encounter the numerical limitations anticipated from analyses carried out in Chapter 3.

In contrast, logarithmically (base 10) compressed concentrations from NOVAM for modes 0, 1, 2 and 3 are 3.52, 3.89, 1.13, and -1.81. Concentrations for mode 2 of NOVAM are below those in Tables 4.2, 4.3, and 4.4. Concentrations for mode 3 of NOVAM are below those in Tables 4.2 and 4.3, but within the low-end of the range of values in Table 4.4.

4.3.2 Image set referred to as configuration file Apr04F02 (cf. Appendix H)

Preserving the organization from the previous subsection, Tables 4.5, 4.6, and 4.7 respectively tabulate the estimated concentrations from the rotorod data and from the visually-estimated maximum log-likelihood criterion (cf. footnote #22) from a subset of EOPACE images upon the completion of the estimations of modes 0 through 4 and modes 0 through 3.

In Table 4.6, camera B and 3 neighbors come first, followed by camera A and 3 neighbors, followed by camera B and 5 neighbors, followed by camera A and 5 neighbors, and followed by cameras A and B together with 3 then 5 neighbors. In Table 4.7 camera B and 3 neighbors come first, followed by camera A and 3 neighbors, followed by cameras B or A and 5 neighbors, followed by both cameras A and B together and 3 and 5 neighbors, and followed by camera A and 5 neighbors. All estimation directives considered (over estimated modes truncated at mode 3), camera B and 3 pixels come first, then camera A and 3 pixels, both for the estimation of modes 0 to 4.

Table 4.5. Estimated concentrations (n_j in cm^{-3}, j = 0…4) from rotorod data for an HCAM model assumed to include modes 0 to 4. An X denotes an irrelevant parameter. (Capture time PST: 21:21-21:27.)

Cameras	RH	Neighbors	$\log_{10}(n_0)$	$\log_{10}(n_1)$	$\log_{10}(n_2)$	$\log_{10}(n_3)$	$\log_{10}(n_4)$
X	Mean	X	-3.77	-3.87	+1.60	+0.59	-15.0
X	SIO	X	-3.88	-3.53	+1.60	+0.60	-15.0
X	NRaD	X	-3.69	-3.59	+1.60	+0.59	-15.0

Table 4.6. Estimated concentrations (n_j in cm^{-3}, j = 0…4) when the HCAM model was assumed to include modes -1 to 4 (mode -1 is of fixed concentration). File Apr04F02 (cf. Appendix H).

Cameras	RH	Neighbors	$\log_{10}(n_0)$	$\log_{10}(n_1)$	$\log_{10}(n_2)$	$\log_{10}(n_3)$	$\log_{10}(n_4)$
(A,B)	Mean	3	+5.00	+5.50	+1.10	-1.50	-1.65
A	Mean	3	-1.10	-1.50	+1.80	0.00	-0.40
B	Mean	3	-2.00	-2.25	+2.00	+0.25	-0.40
(A,B)	Mean	5	+4.95	+5.50	+1.10	-1.60	-1.60
A	Mean	5	+5.00	+5.50	+1.30	-1.40	-1.70
B	Mean	5	+5.00	+5.50	+1.30	-0.90	-1.30
(A,B)	SIO	3	+5.00	+5.45	+1.10	-1.50	-1.70
A	SIO	3	-1.15	-1.40	+1.80	-0.05	-0.35
B	SIO	3	-2.00	-2.20	+2.90	0.00	-0.40
(A,B)	NraD	3	+4.95	+5.60	+1.10	-1.40	-1.55
A	NraD	3	-1.10	-1.55	+2.00	0.00	-0.35
B	NraD	3	-1.90	-2.20	+2.00	+0.60	-0.35

Table 4.7. Estimated concentrations (n_j in cm^{-3}, j = 0…3) when the HCAM model was assumed to include modes -1 to 3 (mode -1 is of fixed concentration). File Apr04F02 (cf. Appendix H).

Cameras	RH	Neighbors	$\log_{10}(n_0)$	$\log_{10}(n_1)$	$\log_{10}(n_2)$	$\log_{10}(n_3)$	$\log_{10}(n_4)$
(A,B)	Mean	3	+5.05	+5.30	+1.40	-1.50	X
A	Mean	3	+5.20	+4.15	+1.45	-1.65	X
B	Mean	3	+4.20	+3.90	+1.50	-1.60	X
(A,B)	Mean	5	+5.00	+5.20	+1.35	-1.70	X
A	Mean	5	+5.05	+5.30	+1.35	-1.70	X
B	Mean	5	+5.05	+5.50	+1.35	-0.60	X
(A,B)	SIO	3	+5.00	+5.35	+1.40	-1.65	X
A	SIO	3	+5.10	+4.10	+1.45	-1.60	X
B	SIO	3	+4.75	+4.15	+1.50	-1.70	X
(A,B)	NRaD	3	+5.00	+5.30	+1.40	-1.50	X
A	NRaD	3	+5.15	+4.10	+1.55	-1.60	X
B	NRaD	3	+3.90	+3.65	+1.50	-1.70	X

Tables 4.6 and 4.7 share closeness for both modes 2 and 3. Logarithmic (base 10) compression of the concentrations from NOVAM modes 0, 1, 2 and 3 are 3.61, 3.98, 1.13, and -1.8, respectively. Concentrations for mode 2 of NOVAM are below those in Tables 4.5 and 4.7, but within the low-end of the range of values in Table 4.6. Concentrations for mode 3 of NOVAM are below those in Tables 4.5, 4.6, and 4.7.

Table 4.8. Estimated concentrations (n_j in cm^{-3}, j = 0…4) from rotorod data for an HCAM model assumed to include modes 0 to 4. An X denotes an irrelevant parameter. (Capture time PST: 21:51-22:16.)

Cameras	RH	Neighbors	$\log_{10}(n_0)$	$\log_{10}(n_1)$	$\log_{10}(n_2)$	$\log_{10}(n_3)$	$\log_{10}(n_4)$
X	Mean	X	-4.21	-5.71	1.57	-0.61	-15.0
X	SIO	X	-5.49	-3.49	1.57	-0.61	-15.0
X	NRaD	X	-4.69	-4.87	1.57	-0.61	-15.0

Table 4.9. Estimated concentrations (n_j in cm^{-3}, j = 0…4) when the HCAM model was assumed to include modes -1 to 4 (mode -1 is of fixed concentration). File Apr05F01 (cf. Appendix H).

Cameras	RH	Neighbors	$\log_{10}(n_0)$	$\log_{10}(n_1)$	$\log_{10}(n_2)$	$\log_{10}(n_3)$	$\log_{10}(n_4)$
(A,B)	Mean	3	+4.90	+5.35	+1.00	-1.95	-2.05
A	Mean	3	-0.80	-1.10	+2.25	-0.15	-0.40
B	Mean	3	-2.10	-2.35	+2.20	0.00	-0.10
(A,B)	Mean	5	+4.90	+4.80	+1.00	-1.90	-2.10
A	Mean	5	+4.90	+5.20	+1.00	-1.70	-1.95
B	Mean	5	+5.00	+5.30	+1.25	-1.25	-1.50
(A,B)	SIO	3	+4.85	+5.30	+0.95	-1.95	-2.00
A	SIO	3	-1.00	-1.10	+2.35	-0.15	-0.35
B	SIO	3	-2.10	-2.50	+2.20	0.00	-0.20
(A,B)	NRaD	3	+4.95	+5.30	+1.00	-1.95	-2.10
A	NRaD	3	-0.75	-1.15	+2.35	-0.20	-0.40
B	NRaD	3	-2.10	-2.40	+2.20	0.00	-0.20

Table 4.10. Estimated concentrations (n_j in cm^{-3}, j = 0…3) when the HCAM model was assumed to include modes -1 to 3 (mode -1 is of fixed concentration). File Apr05F01 (cf. Appendix H).

Cameras	RH	Neighbors	$\log_{10}(n_0)$	$\log_{10}(n_1)$	$\log_{10}(n_2)$	$\log_{10}(n_3)$	$\log_{10}(n_4)$
(A,B)	Mean	3	+4.95	+4.90	+1.24	-0.80	X
A	Mean	3	+4.10	+3.90	+1.75	-1.50	X
B	Mean	3	+3.75	+4.05	+2.10	-1.75	X
(A,B)	Mean	5	+4.95	+4.85	+1.20	-0.75	X
A	Mean	5	+4.95	+5.05	+1.20	-1.50	X
B	Mean	5	+4.90	+5.45	+1.20	-0.80	X
(A,B)	SIO	3	+4.95	+4.85	+1.20	-0.75	X
A	SIO	3	+4.05	+4.00	+1.65	-1.50	X
B	SIO	3	+3.70	+3.45	+2.00	-1.65	X
(A,B)	NRaD	3	+4.90	+4.85	+1.25	-0.75	X
A	NRaD	3	+5.05	+3.95	+1.60	-1.50	X
B	NRaD	3	+3.70	+4.10	+2.10	-1.75	X

4.3.3 Image set referred to as configuration file Apr05F01 (cf. Appendix H)

Following the format of Subsection 4.3.1, Tables 4.8, 4.9, and 4.10 respectively tabulate the estimated concentrations from the rotorod data and from the visually-estimated maximum log-likelihood criterion (cf. footnote #22) from a subset of EOPACE images upon the completion of the estimation of modes 0 through 4 and modes 0 through 3.

In Table 4.9, cameras B or A and 3 neighbors come first, followed by cameras A and B together and 5 neighbors, followed by camera B and 5 neighbors, followed by cameras A or B and 5 neighbors, followed by cameras A and B together and 3 neighbors. In Table 4.10, cameras A or B and 3 neighbors come first, followed by cameras A and B together and 3 then 5 neighbors, followed by cameras A and B with 5 neighbors. All estimation directives considered (over estimated modes truncated at mode 3), cameras A or B and 3 pixels for the estimation of modes 0 to 4 come first.

Logarithmic (base 10) compression of the concentrations from NOVAM modes 0, 1, 2 and 3 are -∞, 3.09, 0.68, and -2.02, respectively. Concentrations for modes 2 and 3 of NOVAM are below those in Tables 4.8, 4.9, and 4.10.

4.3.4 Image set referred to as configuration file Apr08F01 (cf. Appendix H)

Following the format of Subsection 4.3.1, Tables 4.11, 4.12, and 4.13 respectively tabulate the estimated concentrations from the rotorod data and from the visually-estimated maximum log-likelihood criterion (cf. footnote #22) from a subset of EOPACE images upon the completion of the estimations of modes 0 through 4 and modes 0 through 3.

In Table 4.12, cameras B or A and 3 neighbors come first, followed by cameras A and B together and 5 then 3 neighbors, followed by camera B or A and 5 neighbors. In Table 4.13, cameras A or B and 3 neighbors come first, followed by cameras A and B together and 5 then 3 neighbors, followed by cameras A or B and 5 neighbors. All estimation directives considered (over estimated modes truncated at mode 3), cameras A and B and 3 pixels for the estimation of modes 0 to 4 come first.

Logarithmic (base 10) compression of the concentrations from NOVAM modes 0, 1, 2 and 3 are -∞, 2.74, 0.73, and -2.03, respectively. Concentrations for modes 2 and 3 of NOVAM are below those in Tables 4.11, 4.12, and 4.13.

4.3.5 Image set referred to as configuration file Apr09F01 (cf. Appendix H)

The absence of rotorod data over this period of collection of EOPACE images leaves a void only filled by the experience of the previous subsections. Tables 4.14 and 4.15 respectively tabulate the estimated concentrations from the visually estimated maximum log-likelihood criterion (cf. footnote #22) from a subset of EOPACE images upon the completion of the estimations of modes 0 through 4 and modes 0 through 3.

Table 4.11. Estimated concentrations (n_j in cm^{-3}, j = 0…4) from rotorod data for an HCAM model assumed to include modes 0 to 4. An X denotes an irrelevant parameter. (Capture time PST: 20:51-21:31.)

Cameras	RH	Neighbors	$\log_{10}(n_0)$	$\log_{10}(n_1)$	$\log_{10}(n_2)$	$\log_{10}(n_3)$	$\log_{10}(n_4)$
X	Mean	X	-3.43	-3.32	1.31	0.06	-15.0
X	SIO	X	-3.39	-3.36	1.31	0.07	-15.0
X	NraD	X	-3.55	-3.54	1.31	0.06	-15.0

Table 4.12. Estimated concentrations (n_j in cm^{-3}, j = 0…4) when the HCAM model was assumed to include modes -1 to 4 (mode -1 is of fixed concentration). File Apr08F01 (cf. Appendix H).

Cameras	RH	Neighbors	$\log_{10}(n_0)$	$\log_{10}(n_1)$	$\log_{10}(n_2)$	$\log_{10}(n_3)$	$\log_{10}(n_4)$
(A,B)	Mean	3	+5.05	+5.00	+1.35	-0.95	-1.20
A	Mean	3	-1.80	-2.10	+2.00	+0.20	-0.35
B	Mean	3	-1.80	-2.00	+2.05	+0.40	-0.35
(A,B)	Mean	5	+5.10	+4.85	+1.35	-0.90	-1.30
A	Mean	5	+5.10	+5.50	+1.55	-0.70	-1.40
B	Mean	5	+5.10	+5.40	+1.55	-0.55	-1.10
(A,B)	SIO	3	+5.15	+4.90	+1.30	-0.90	-1.30
A	SIO	3	-1.70	-1.95	+2.00	+0.45	-0.45
B	SIO	3	-1.70	-2.15	+2.20	+0.45	-0.45
(A,B)	NRaD	3	+5.10	+5.00	+1.35	-0.90	-1.25
A	NRaD	3	-2.05	-1.90	+1.95	+0.35	-0.45
B	NRaD	3	-1.40	-1.75	+1.90	+0.50	-0.40

Table 4.13. Estimated concentrations (n_j in cm^{-3}, j = 0…3) when the HCAM model was assumed to include modes -1 to 3 (mode -1 is of fixed concentration). File Apr08F01 (cf. Appendix H).

Cameras	RH	Neighbors	$\log_{10}(n_0)$	$\log_{10}(n_1)$	$\log_{10}(n_2)$	$\log_{10}(n_3)$	$\log_{10}(n_4)$
(A,B)	Mean	3	+5.20	+4.85	+1.75	-1.50	X
A	Mean	3	+3.75	+3.50	+1.55	-1.45	X
B	Mean	3	+4.10	+4.30	+1.55	-0.05	X
(A,B)	Mean	5	+5.20	+4.60	+1.80	-1.50	X
A	Mean	5	+5.25	+5.20	+1.70	-1.40	X
B	Mean	5	+5.25	+5.25	+1.75	-1.40	X
(A,B)	SIO	3	+5.20	+4.90	+1.70	-1.50	X
A	SIO	3	+3.85	+3.60	+1.50	-1.40	X
B	SIO	3	+3.90	+4.25	+1.60	-1.40	X
(A,B)	NraD	3	+5.25	+4.80	+1.80	-1.40	X
A	NraD	3	+3.65	+4.30	+1.60	-1.30	X
B	NraD	3	+4.00	+4.30	+1.55	-1.30	X

Logarithmic (base 10) compression of the concentrations from NOVAM modes 0, 1, 2 and 3 are -∞, 3.09, 0.95, and -2.02, respectively. Concentrations for mode 2 of NOVAM are below those in Table 4.15, but within the low-end of the range of values in Table 4.14. Concentrations for mode 3 of NOVAM are below those in Table 4.14, but at the low-end of the range of the values in Table 4.15.

Table 4.14. Estimated concentrations (n_j in cm^{-3}, j = 0…4) when the HCAM model was assumed to include modes -1 to 4 (mode -1 is of fixed concentration). File Apr09F01 (cf. Appendix H).

Cameras	RH	Neighbors	$\log_{10}(n_0)$	$\log_{10}(n_1)$	$\log_{10}(n_2)$	$\log_{10}(n_3)$	$\log_{10}(n_4)$
(A,B)	Mean	3	+4.90	+5.50	+0.85	-1.60	-1.80
A	Mean	3	-2.10	-2.40	+2.10	-0.45	-0.25
B	Mean	3	-2.20	-2.45	+1.60	+0.30	-0.15
(A,B)	Mean	5	+4.90	+5.45	+0.90	-1.60	-1.70
A	Mean	5	+4.95	+5.35	+1.15	-1.30	-1.85
B	Mean	5	+4.85	+5.35	+1.20	-1.20	-1.55
(A,B)	SIO	3	+4.90	+5.40	+0.85	-1.60	-1.70
A	SIO	3	-2.15	-2.40	+2.00	-0.45	-0.25
B	SIO	3	-2.15	-2.35	+1.60	+0.25	-0.25
(A,B)	NRaD	3	+4.85	+5.50	+0.90	-1.60	-1.75
A	NRaD	3	-2.10	-2.35	+2.05	-0.45	-0.30
B	NRaD	3	-2.10	-2.35	+1.60	+0.20	-0.20

Table 4.15. Estimated concentrations (n_j in cm^{-3}, j = 0…3) when the HCAM model was assumed to include modes -1 to 3 (mode -1 is of fixed concentration). File Apr09F01 (cf. Appendix H).

Cameras	RH	Neighbors	$\log_{10}(n_0)$	$\log_{10}(n_1)$	$\log_{10}(n_2)$	$\log_{10}(n_3)$	$\log_{10}(n_4)$
(A,B)	Mean	3	+4.95	+5.35	+1.25	-2.00	X
A	Mean	3	+5.30	+4.30	+1.40	-2.00	X
B	Mean	3	+4.00	+4.05	+1.35	-1.80	X
(A,B)	Mean	5	+4.90	+5.30	+1.25	-1.75	X
A	Mean	5	+4.85	+5.90	+1.20	-2.00	X
B	Mean	5	+4.95	+5.45	+1.25	-1.70	X
(A,B)	SIO	3	+4.95	+5.30	+1.25	-2.00	X
A	SIO	3	+4.15	+4.30	+1.35	-1.70	X
B	SIO	3	+4.00	+4.05	+1.40	-1.85	X
(A,B)	NRaD	3	+4.95	+5.40	+1.20	-2.00	X
A	NRaD	3	+4.30	+4.25	+1.40	-1.60	X
B	NRaD	3	+3.95	+4.05	+1.40	-1.70	X

4.3.6 Image set referred to as configuration file Apr09F02 (cf. Appendix H)

The absence of rotorod data over this period of collection of EOPACE images leaves a void only filled by the experience of the previous subsections. Tables 4.16 and 4.17 respectively tabulate the estimated concentrations from the visually estimated maximum log-likelihood criterion (cf. footnote #22) from a sub-set of EOPACE images upon the completion of the estimations of modes 0 to 4 and those from 0 to 3.

Logarithmic (base 10) compression of the concentrations from NOVAM modes 0, 1, 2 and 3 are -∞, 3.09, 0.95, and -2.00, respectively. Concentrations for mode 2 of NOVAM are below those in Table 4.17, but within the low-end of the range of values in Table 4.16. Concentrations for mode 3 of NOVAM are below those in Table 4.16, but at the low-end of the range of values in Table 4.17.

Table 4.16. Estimated concentrations (n_j in cm^{-3}, j = 0…4) when the HCAM model was assumed to include modes -1 to 4 (mode -1 is of fixed concentration). File Apr09F02 (cf. Appendix H).

Cameras	RH	Neighbors	$\log_{10}(n_0)$	$\log_{10}(n_1)$	$\log_{10}(n_2)$	$\log_{10}(n_3)$	$\log_{10}(n_4)$
(A,B)	Mean	3	+4.90	+5.35	+0.90	-1.45	-1.80
A	Mean	3	-2.10	-2.35	+1.90	+0.05	-0.45
B	Mean	3	-2.10	-2.35	+1.85	+0.10	-0.20
(A,B)	Mean	5	+4.90	+5.40	+0.85	-1.45	-1.80
A	Mean	5	+4.90	+5.45	+1.15	-1.45	-2.10
B	Mean	5	+4.95	+5.35	+1.20	-1.20	-1.50
(A,B)	SIO	3	+4.95	+5.3	+0.90	-1.40	-1.70
A	SIO	3	-2.05	-2.25	+1.90	+0.05	-0.30
B	SIO	3	-2.00	-2.35	+1.90	+0.40	-0.25
(A,B)	NraD	3	+4.85	+5.30	+0.90	-1.55	-1.75
A	NraD	3	-2.15	-2.35	+1.85	+0.10	-0.40
B	NraD	3	-2.00	-2.40	+1.85	+0.15	-0.40

Table 4.17. Estimated concentrations (n_j in cm^{-3}, j = 0…3) when the HCAM model was assumed to include modes -1 to 3 (mode -1 is of fixed concentration). File Apr09F02 (cf. Appendix H).

Cameras	RH	Neighbors	$\log_{10}(n_0)$	$\log_{10}(n_1)$	$\log_{10}(n_2)$	$\log_{10}(n_3)$	$\log_{10}(n_4)$
(A,B)	Mean	3	+4.95	+5.10	+1.20	-1.95	X
A	Mean	3	+4.35	+4.30	+1.40	-1.70	X
B	Mean	3	+4.05	+3.70	+2.20	-1.75	X
(A,B)	Mean	5	+4.90	+4.70	+1.20	-2.00	X
A	Mean	5	+4.95	+5.15	+1.15	-1.90	X
B	Mean	5	+4.90	+5.30	+1.20	-0.75	X
(A,B)	SIO	3	+4.90	+5.00	+1.30	-1.90	X
A	SIO	3	+4.35	+4.25	+1.45	-1.65	X
B	SIO	3	+3.90	+4.05	+1.45	-1.75	X
(A,B)	NraD	3	+4.90	+5.10	+1.20	-2.00	X
A	NraD	3	+4.20	+4.00	+2.00	-1.75	X
B	NraD	3	+4.10	+3.80	+1.40	-1.80	X

4.3.7 Image set referred to as configuration file Apr09F03 (cf. Appendix H)

The absence of rotorod data over this period of collection of EOPACE images leaves a void only filled by the experience of the previous subsections. Tables 1.18 and 4.19 respectively tabulate the estimated concentrations from the visually estimated maximum log-likelihood criterion (cf. footnote #22) from a subset of EOPACE images upon the completion of the estimations of modes 0 through 4 and modes 0 through 3.

Logarithmic (base 10) compression of the concentrations from NOVAM modes 0, 1, 2 and 3 are -∞, 3.09, 0.96, and -1.92, respectively. Concentrations for mode 2 of NOVAM are below those in Table 4.19, but within the low-end of the range of values in Table 4.18. Concentrations for mode 3 of NOVAM are below those in Table 4.18, but within the middle of the range of values in Table 4.19.

Table 4.18. Estimated concentrations (n_j in cm^{-3}, j = 0…4) when the HCAM model was assumed to include modes -1 to 4 (mode -1 is of fixed concentration). File Apr09F03 (cf. Appendix H).

Cameras	RH	Neighbors	$\log_{10}(n_0)$	$\log_{10}(n_1)$	$\log_{10}(n_2)$	$\log_{10}(n_3)$	$\log_{10}(n_4)$
(A,B)	Mean	3	+4.95	+5.50	+0.90	-1.55	-1.80
A	Mean	3	-2.05	-2.35	+1.90	-0.45	-0.30
B	Mean	3	-2.05	-2.30	+1.95	-0.15	-0.40
(A,B)	Mean	5	+4.95	+5.40	+0.95	-1.55	-1.75
A	Mean	5	+4.90	+5.50	+1.25	-1.40	-2.00
B	Mean	5	+4.90	+5.45	+1.20	-1.35	-1.50
(A,B)	SIO	3	+4.95	+5.60	+1.00	-1.40	-1.75
A	SIO	3	-2.00	-2.30	+1.90	-0.50	-0.30
B	SIO	3	-2.05	-2.30	+1.95	+0.50	-0.30
(A,B)	NRaD	3	+4.90	+5.50	+0.90	-1.50	-1.75
A	NRaD	3	-2.10	-2.35	+2.00	-0.50	-0.35
B	NRaD	3	-2.15	-2.40	+2.05	+0.75	-0.40

Table 4.19. Estimated concentrations (n_j in cm^{-3}, j = 0…3) when the HCAM model was assumed to include modes -1 to 3 (mode -1 is of fixed concentration). File Apr09F03 (cf. Appendix H).

Cameras	RH	Neighbors	$\log_{10}(n_0)$	$\log_{10}(n_1)$	$\log_{10}(n_2)$	$\log_{10}(n_3)$	$\log_{10}(n_4)$
(A,B)	Mean	3	+4.95	+4.90	+1.20	-1.90	X
A	Mean	3	+4.25	-2.25	+2.10	-1.70	X
B	Mean	3	+3.95	+4.05	+1.40	-1.70	X
(A,B)	Mean	5	+4.95	+4.75	+1.25	-2.10	X
A	Mean	5	+4.90	+5.00	+1.25	-2.10	X
B	Mean	5	+4.95	+5.10	+1.25	-1.80	X
(A,B)	SIO	3	+4.95	+4.85	+1.25	-1.90	X
A	SIO	3	+4.50	+4.30	+1.45	-1.70	X
B	SIO	3	+3.80	+4.05	+1.45	-1.70	X
(A,B)	NRaD	3	+4.90	+5.00	+1.25	-2.00	X
A	NRaD	3	+4.25	+4.30	+2.00	-1.70	X
B	NRaD	3	+3.95	+4.05	+1.45	-1.80	X

4.3.8 Image set referred to as configuration file Apr09F04 (cf. Appendix H)

The absence of rotorod data over this period of collection of EOPACE images leaves a void only filled by the experience of the previous subsections. Tables 4.20 and 4.21 respectively tabulate the estimated concentrations from the visually estimated maximum log-likelihood criterion (cf. footnote #22) from a subset of EOPACE images upon the completion of the estimations of modes 0 through 4 and modes 0 through 3.

Logarithmic (base 10) compression of the concentrations from NOVAM modes 0, 1, 2 and 3 are -∞, 3.09, 0.96, and -1.84, respectively. Concentrations for mode 2 of NOVAM are below those in Table 4.21, but at the low-end of the range of values in Table 4.20. Concentrations for mode 3 of NOVAM are below those in Table 4.20, but within the middle of the range of values in Table 4.21.

Table 4.20. Estimated concentrations (n_j in cm^{-3}, j = 0…4) when the HCAM model was assumed to include modes -1 to 4 (mode -1 is of fixed concentration). File Apr09F04 (cf. Appendix H).

Cameras	RH	Neighbors	$\log_{10}(n_0)$	$\log_{10}(n_1)$	$\log_{10}(n_2)$	$\log_{10}(n_3)$	$\log_{10}(n_4)$
(A,B)	Mean	3	+4.90	+5.30	+0.95	-1.50	-1.80
A	Mean	3	-1.90	-2.25	+2.70	-0.55	-0.25
B	Mean	3	-1.95	-2.25	+2.80	+0.05	-0.35
(A,B)	Mean	5	+4.95	+5.15	+1.05	-1.55	-1.85
A	Mean	5	+5.00	+5.55	+1.25	-1.70	-1.90
B	Mean	5	+5.95	+5.55	+1.25	-1.15	-1.45
(A,B)	SIO	3	+4.95	+5.30	+1.05	-1.45	-1.75
A	SIO	3	-1.90	-2.20	+2.40	-0.65	-0.40
B	SIO	3	-1.90	-2.20	+2.70	+0.10	-0.30
(A,B)	NRaD	3	+4.95	+5.30	+0.95	-1.60	-1.80
A	NRaD	3	-2.00	-2.20	+2.60	-0.50	-0.40
B	NRaD	3	-1.90	-2.30	+2.70	0.00	-0.45

Table 4.21. Estimated concentrations (n_j in cm^{-3}, j = 0…3) when the HCAM model was assumed to include modes -1 to 3 (mode -1 is of fixed concentration). File Apr09F04 (cf. Appendix H).

Cameras	RH	Neighbors	$\log_{10}(n_0)$	$\log_{10}(n_1)$	$\log_{10}(n_2)$	$\log_{10}(n_3)$	$\log_{10}(n_4)$
(A,B)	Mean	3	+4.95	+4.75	+1.25	-2.00	X
A	Mean	3	+4.10	+4.30	+2.20	-1.70	X
B	Mean	3	+3.70	+3.50	+2.20	-1.65	X
(A,B)	Mean	5	+4.95	+4.60	+1.25	-1.95	X
A	Mean	5	+4.95	+5.05	+1.25	-2.10	X
B	Mean	5	+5.00	+5.15	+1.25	-2.00	X
(A,B)	SIO	3	+4.95	+4.90	+1.35	-1.90	X
A	SIO	3	+3.70	+3.40	+2.55	-1.65	X
B	SIO	3	+3.70	+3.50	+1.45	-1.60	X
(A,B)	NRaD	3	+4.95	+5.00	+1.25	-1.95	X
A	NRaD	3	+4.30	+4.35	+1.50	-1.70	X
B	NRaD	3	+3.90	+4.10	+1.40	-1.70	X

4.3.9 Image set referred to as configuration file Apr09F05 (cf. Appendix H)

The absence of rotorod data over this period of collection of EOPACE images leaves a void only filled by the experience of the previous subsections. Tables 4.22 and 4.23 respectively tabulate the estimated concentrations from the visually estimated maximum log-likelihood criterion (cf. footnote #22) from a subset of EOPACE images upon the completion of the estimations of modes 0 through 4 and modes 0 through 3.

Logarithmic (base 10) compression of the concentrations from NOVAM modes 0, 1, 2 and 3 are -∞, 3.09, 0.97, and -1.95, respectively. Concentrations for mode 2 of NOVAM are below those in Tables 4.22 and 4.23. Concentrations for mode 3 of NOVAM are below those in Table 4.22, but within the low-end of the range of values in Table 4.23.

Table 4.22. Estimated concentrations (n_j in cm^{-3}, j = 0…4) when the HCAM model was assumed to include modes -1 to 4 (mode -1 is of fixed concentration). File Apr09F05 (cf. Appendix H).

Cameras	RH	Neighbors	$\log_{10}(n_0)$	$\log_{10}(n_1)$	$\log_{10}(n_2)$	$\log_{10}(n_3)$	$\log_{10}(n_4)$
(A,B)	Mean	3	+4.95	+5.50	+1.00	-1.20	-1.65
A	Mean	3	-1.85	-2.15	+3.00	+0.55	-0.35
B	Mean	3	-1.90	-2.25	+2.05	+0.50	-0.30
(A,B)	Mean	5	+5.00	+5.45	+1.05	-1.20	-1.70
A	Mean	5	+4.95	+5.55	+1.20	-1.50	-1.85
B	Mean	5	+4.95	+5.40	+1.20	-1.00	-1.35
(A,B)	SIO	3	+4.95	+5.40	+1.05	-1.15	-1.60
A	SIO	3	-1.80	-2.15	+1.90	+0.50	-0.30
B	SIO	3	-1.90	-2.20	+2.00	+0.40	-0.35
(A,B)	NRaD	3	+4.90	+5.40	+1.05	-1.20	-1.75
A	NRaD	3	-1.85	-2.10	+2.90	+0.55	-0.35
B	NRaD	3	-2.00	-2.20	+2.00	+0.25	-0.35

Table 4.23. Estimated concentrations (n_j in cm^{-3}, j = 0…3) when the HCAM models was assumed to include modes -1 to 3 (mode -1 is of fixed concentration). File Apr09F05 (cf. Appendix H).

Cameras	RH	Neighbors	$\log_{10}(n_0)$	$\log_{10}(n_1)$	$\log_{10}(n_2)$	$\log_{10}(n_3)$	$\log_{10}(n_4)$
(A,B)	Mean	3	+4.95	+5.05	+1.30	-1.95	X
A	Mean	3	+3.75	+3.65	+1.60	-1.60	X
B	Mean	3	+3.65	+4.10	+1.50	-1.60	X
(A,B)	Mean	5	+5.00	+4.75	+1.30	-1.90	X
A	Mean	5	+5.05	+4.95	+1.35	-1.90	X
B	Mean	5	+4.95	+5.20	+1.35	-2.00	X
(A,B)	SIO	3	+5.00	+5.05	+1.40	-1.90	X
A	SIO	3	+5.15	+4.10	+1.60	-1.60	X
B	SIO	3	+3.60	+4.10	+1.45	-1.70	X
(A,B)	NRaD	3	+4.95	+5.00	+1.30	-1.95	X
A	NRaD	3	+4.25	+3.95	+1.50	-1.65	X
B	NRaD	3	+3.70	+3.40	+1.45	-1.60	X

4.3.10 Extinction over a homogeneous surf-zone

Subsection 2.3.4 defined extinction. The present section implicitly assumes a homogeneous spatial distribution of the concentrations over the surf zone (by simplifying each mode of estimated concentrations to its maximum log-likelihood value – cf. footnote #22).

Table 4.24 displays a subset of extinction coefficients above a homogeneous surf zone (cf. Appendix I for computation, generalization, and caution) for each configuration file (cf. Appendix H) computed from estimated concentrations *via* functional fits over rotorod data, polarization ratio onto EOPACE images, and NOVAM equations. These last equations estimate aerosol concentrations over the open ocean where coastal dynamics are neglected. The EOPACE images deliver higher concentrations than the NOVAM

Table 4.24. Extinction values for the most reliably estimated modes 2 (γ_2, in km^{-1}) and 3 (γ_3, in km^{-1}), and their combination ($\gamma_{-1,2,3}$, in km^{-1} where $\gamma_{-1} \approx 0.016$ km^{-1}). Comparison of extinction originating from the rotorod fits, the EOPACE images (Pol Rat.), and NOVAM show relatively close agreement among various sources. Rotorod data on April 9 (corresponding to the Apr09 prefix for the configuration filenames) were absent.

γ	Source	Configuration filename (cf. Appendix H)								
		Apr04		Apr05	Apr08	Apr09				
		F01	F02	F01	F01	F01	F02	F03	F04	F05
γ_2	Rotorod	0.0427	0.0427	0.0364	0.0255	-	-	-	-	-
	Pol. Rat.	0.0339	0.0135	0.0098	0.0280	0.0071	0.0079	0.0079	0.0090	0.0104
	NOVAM	0.0143	0.0143	0.0047	0.0068	0.0089	0.0089	0.0091	0.0093	0.0097
γ_3	Rotorod	0.2283	0.2283	0.0131	0.0791	-	-	-	-	-
	Pol. Rat.	0.0074	0.0019	0.0006	0.0077	0.0014	0.0019	0.0015	0.0017	0.0036
	NOVAM	0.0009	0.0009	0.0005	0.0006	0.0005	0.0005	0.0006	0.0008	0.0006
$\gamma_{-1,2,3}$	Rotorod	0.287	0.287	0.066	0.121	-	-	-	-	-
	Pol. Rat.	0.057	0.031	0.026	0.052	0.024	0.026	0.025	0.027	0.030
	NOVAM	0.031	0.031	0.021	0.023	0.025	0.026	0.026	0.026	0.026

equations, resulting in slightly larger (but consistent with each other) extinction coefficients, on average, as anticipated by the addition of surf-zone scatterers at modes 2 and 3.

4.3.11 Conclusion

Representative concentrations have been extracted from bi-dimensional spatial distributions of each estimated mode over a variety of estimation directives. Reviewing the tables of those representative concentrations whose rotorod counterparts exist (a total of 4 files) and focusing on estimations using 3 pixels, any camera association, and mean relative humidity lead to the following observations: (1) modes 0 and 1 are inconsistently estimated, (2) mode 2 is bound, in majority, by the directive using modes 0 to 4 (in 3 cases out of 4 vs. 1 out of 4 for the directive using modes 0 to 3), (3) mode 3 is exclusively bound (in 2 cases out of 4) by the directive using modes 0 to 4, and (4) mode 4 is consistently either overestimated when compared to the estimates from rotorod fits or underestimated when compared to measurements reported by de Leeuw (2000). Regularly, directives using modes 0 to 4, 3 pixels, and cameras A, B, or A and B together have outperformed other directives.

The confirmation that mode 2 is the most reliably estimated, followed by mode 3, associated with both the correlation of the concentrations from the rotorod data and the proximity of the NOVAM concentrations grant the instrument (including the polarization ratio method) the credibility which it needed to receive. This critical step has just been made for the very first time, successfully taking the instrument outside a completely controlled environment (i.e., a laboratory). Although those results are ultimately filtered through the eyes of the aerosol model (NOVAM – which was originally developed to operate over the open ocean) the consistency of their magnitudes confirms the meaningfulness estimation procedure

tested in Chapter 3 and refined in Chapter 4. The present analyses also confirm that the surf zone contributes additional scatterers at modes 2 and 3.

Modes 2 and 3 for the configuration files from Apr09F01 to Apr09F05 (cf. Appendix H) estimate the aerosol concentrations relatively consistently despite changes in both the exposure time and the difference in relative humidity measured by both the SIO and the NRaD sensors.

4.4 Estimation of concentrations from EOPACE images: Preservation of spatial distribution

The previous section has shown agreement in estimated average concentrations of the HCAM modes 2 and, at times, 3, from both the EOPACE data and those of the rotorod. The directives recommended at the end of Section 4.3 (mean relative humidity, cameras A and B together or independently, and a 1x3 neighborhood of pixels) are subsequently used in the spatial estimation of modes 0 to 4.

Subsections 4.4.1 to 4.4.9 both display and discuss the spatial distribution in concentrations of modes 2 and 3 for the selected sets of images and processing regions specified in Appendix H (for each case, Appendix J displays the averaged CCD images followed by the bi-dimensional estimated concentrations of modes 2 and 3 and Appendix K displays the bi-dimensional condition number and the bi-dimensional estimated concentrations of modes 0, 1, and 4). Subsection 4.4.10 comments on the presence of negative concentrations and Subsection 4.4.11 concludes.

4.4.1 Image set referred to as configuration file Apr04F01 (cf. Appendix H)

The image set was collected between 21:02 and 21:03 Pacific Standard Time (PST). Also measured were barometric pressure at 29.89 inHg (1012 mbars), wind direction[23] at 200°, wind speed at 5.5 m/s, and atmospheric temperature at 14.5 °C.

Figure 4.2(a) displays the spatial distribution of the estimated mode 2 with, as estimation directives, mean relative humidity, estimation of modes 0 to 4, and cameras A and B together, each of which contributing 3 pixels at a time. Two highest concentration areas dominate: one near 30 m along the pier and one between 200 and 250 m where concentrations reach 100 cm^{-3} and 60 cm^{-3} respectively. Those locations correspond to waves crashing onto the beach and those breaking for the first time. In the middle of the surf zone, concentrations reach about 5 cm^{-3}. Finally, near 400 m, concentrations of 3 cm^{-3} are indicative of the calmest region of all.

[23] Meteorological convention adopted for which the direction of the wind corresponds to the direction from which it reaches the experimental site.

Figure 4.2(b) displays the spatial distribution of the estimated mode 3 with, as estimation directives, mean relative humidity, estimation of modes 0 to 4, and cameras A and B together, each of which contributing 3 pixels. Again, two highest concentration areas dominate: one near 20 m along the pier and one between 180 and 350 m where concentrations reach 3 cm^{-3} and 1 cm^{-3} respectively. This mode is generated over a much larger distance than mode 2 where waves break for the first time. Data over the surf-zone result in negative concentrations. Near 400 m, concentrations reach 0.016 cm^{-3}, decrease to 0.003 cm^{-3} near 550 m, then 0.0003 cm^{-3} near 1000 m.

These two modes behave as expected in that they are stronger near the source and weaker near the sink, but mode 2 also shows that the middle of the surf zone does not produce as much as either end does. Concentrations away from the surf zone are much too low to be credible.

4.4.2 Image set referred to as configuration file Apr04F02 (cf. Appendix H)

The image set was collected between 21:21 and 21:27 Pacific Standard Time (PST). Also measured were barometric pressure at 29.89 inHg (1012 mbars), wind direction at 200°, wind speed at 5.7 m/s, and atmospheric temperature at 14.5 °C.

Figure 4.3(a) displays the spatial distribution of the estimated mode 2 with, as estimation directives, mean relative humidity, estimation of modes 0 to 4, and cameras A and B together, each of which contributing 3 pixels. Again, two highest concentration areas dominate: one near 40 m along the pier and one near 200 m where concentrations are observed to reach 60 cm^{-3} and 100 cm^{-3} respectively. Those locations correspond to waves crashing onto the beach and breaking for the first time. In the middle of the surf zone, concentrations reach about 10 cm^{-3}. Data beyond 210 m and in the vicinity of 30 m result in negative concentrations.

Figure 4.3(b) displays the spatial distribution of the estimated mode 3 with, as estimation directives, mean relative humidity, estimation of modes 0 to 4, and camera A contributing 3 pixels. Two highest concentration areas dominate (separated by an area of negative concentrations): one between 35 and 45 m along the pier and one near 125 m where concentrations are 30 cm^{-3} and 10 cm^{-3} respectively, although an 80 m area of negative concentrations separate them. The concentrations drop to 0.2 cm^{-3} near 200 m, then 0.1 cm^{-3} near 250 m, then 0.01 cm^{-3} near 400 m, and 0.003 cm^{-3} near 700 m. Estimated concentrations using camera B agree with those of camera A, but those from the simultaneous use of both cameras estimate concentrations near 0.0001 cm^{-3} at and beyond 700 m. The highest concentrations occur over the surf zone, progressively decreasing away from it.

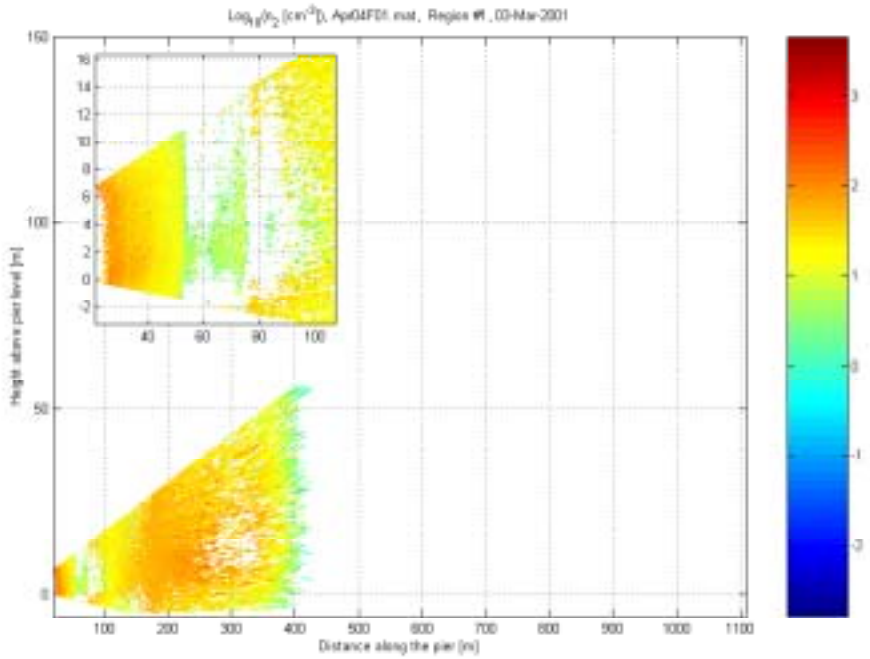

(a)

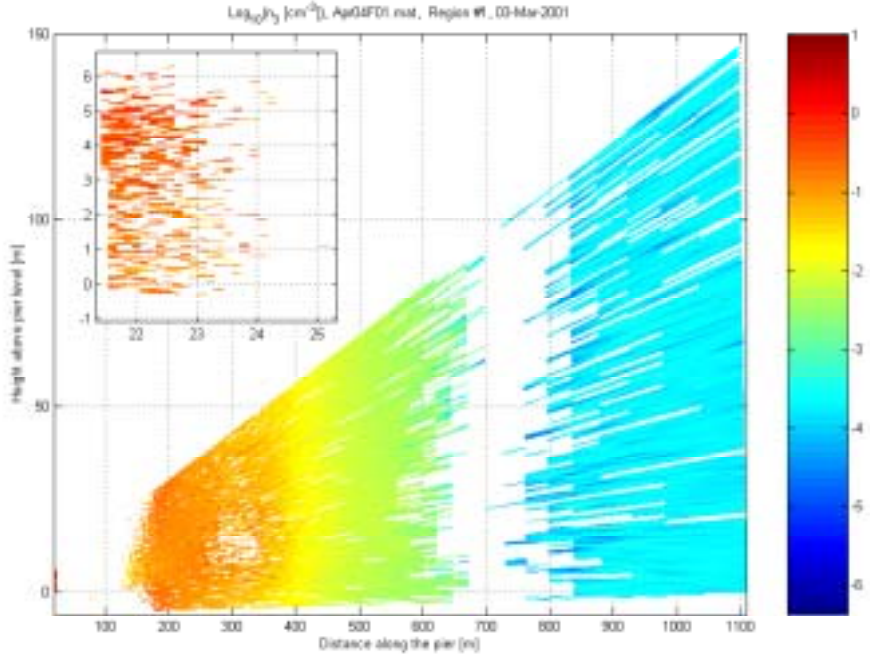

(b)

Figure 4.2. Estimated concentrations from file Apr04F01 for (a) mode 2 and (b) mode 3. Both estimations use both cameras (A and B), 3 pixels per camera, mean relative humidity and potential modes 0 to 4. Original images were taken with an exposure time of 5 seconds each.

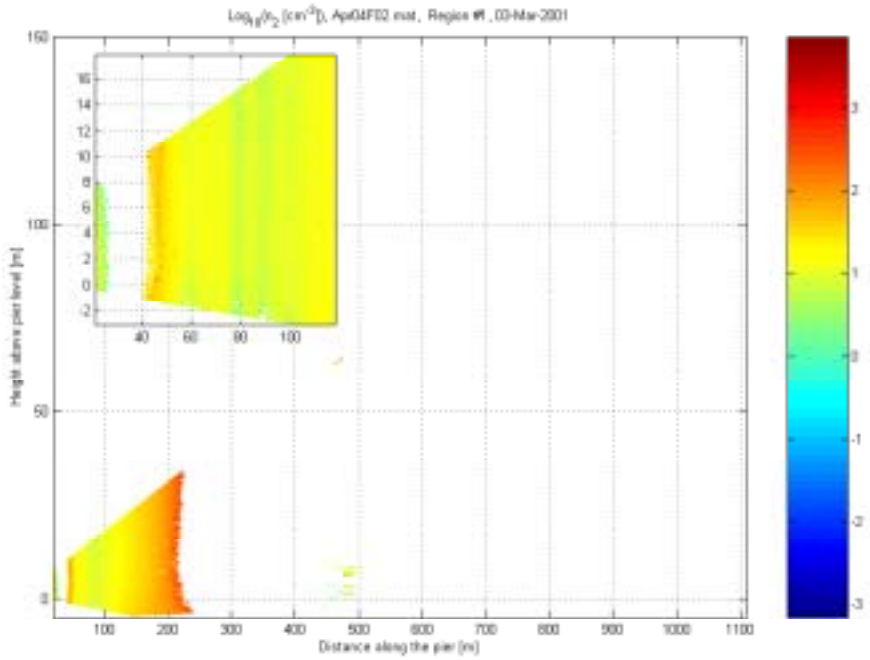

(a)

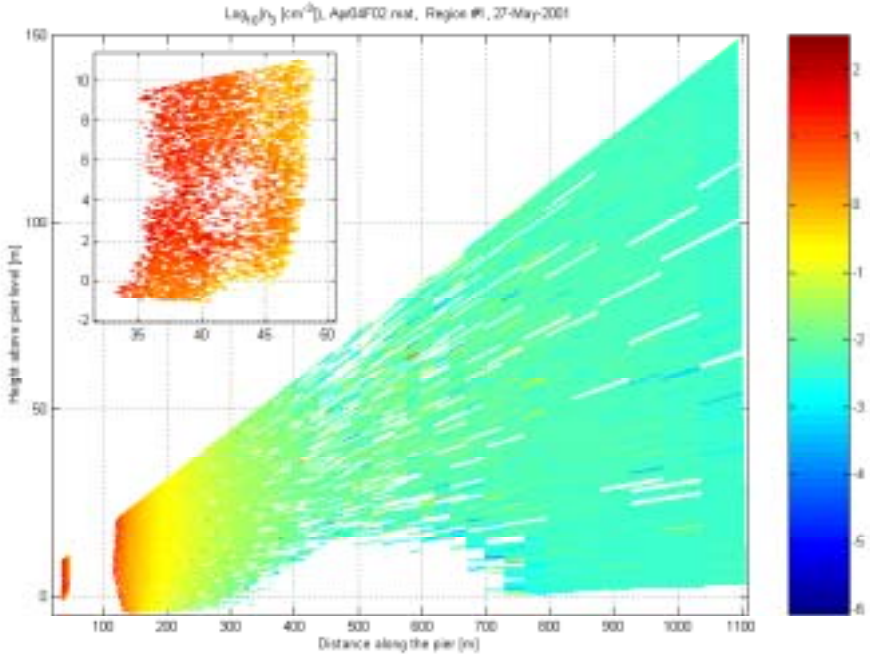

(b)

Figure 4.3. Estimated concentrations from file Apr04F02 for (a) mode 2 and (b) mode 3. Both cameras A and B were used for (a) but camera A only for (b). Other directives were 3 pixels per camera, mean relative humidity and potential modes 0 to 4. Original images were taken with an exposure time of 30 seconds each.

The apparent discrepancy in the location of the first breakers (200 vs. 125 m) is due to the precision with which the position of the laser sheet is estimated, as camera A gives 120 m, camera B reports 200 m, and cameras A and B together agree on 200 m. However, both modes are stronger over the source than over the sink. The middle of the surf zone does not produce as much as either end for mode 2, although mode 3 remains inconclusive in this area. Concentrations away from the surf zone are much too low to be credible.

4.4.3 Image set referred to as configuration file Apr05F01 (cf. Appendix H)

The image set was collected between 21:51 and 22:16 Pacific Standard Time (PST). Also measured were barometric pressure at 30 inHg (1016 mbars), wind direction at 180°, wind speed at 1.50 m/s, and atmospheric temperature at 14.6 °C.

Figure 4.4(a) displays the spatial distribution of the estimated mode 2 with, as estimation directives, mean relative humidity, estimation of modes 0 to 4, and cameras A and B together, each of which contributing 3 pixels. Again, two highest concentration areas dominate: one near 40 m along the pier and one near 200 m where concentrations are observed to reach 300 cm^{-3} and 30 cm^{-3} respectively. Those locations correspond to waves crashing onto the beach and breaking for the first time. In the middle of the surf zone, concentrations reach about 10 cm^{-3}. Data beyond 200 m and in the vicinity of 30 m result in negative concentrations.

Figure 4.4(b) displays the spatial distribution of the estimated mode 3 with, as estimation directives, mean relative humidity, estimation of modes 0 to 4, and camera B contributing 3 pixels. Two highest concentration areas dominate (separated by an area of negative concentrations): one between 35 and 55 m along the pier and one near 220 m where concentrations are 20 cm^{-3} and 10 cm^{-3} respectively, although an 170 m area of negative concentrations separate them. The concentrations decrease to 0.3 cm^{-3} near 300 m, 0.1 cm^{-3} near 400 m, 0.06 cm^{-3} near 600 m, 0.01 cm^{-3} near 900 m, and 0.001 cm^{-3} near 1400 m. As noted earlier, the highest concentrations occur over the surf zone, progressively decreasing away from it.

Both modes agree on the presence of higher concentrations over the source than over the sink. The middle of the surf zone does not produce as much as either end for mode 2, although mode 3 remains inconclusive on this area. Concentrations for mode 2 are inconclusive beyond 200 m. Concentrations away from the surf zone are much too low to be credible.

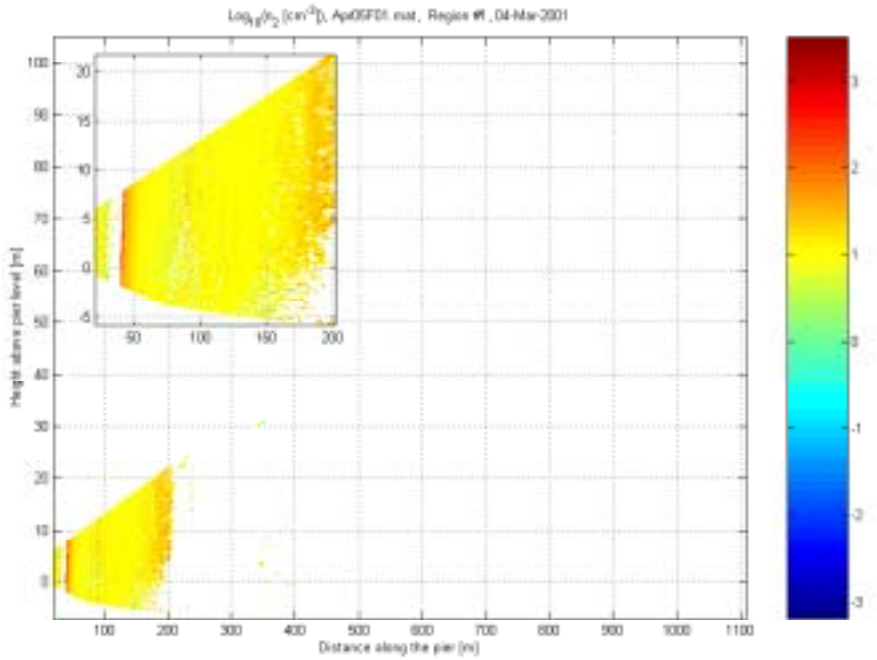

(a)

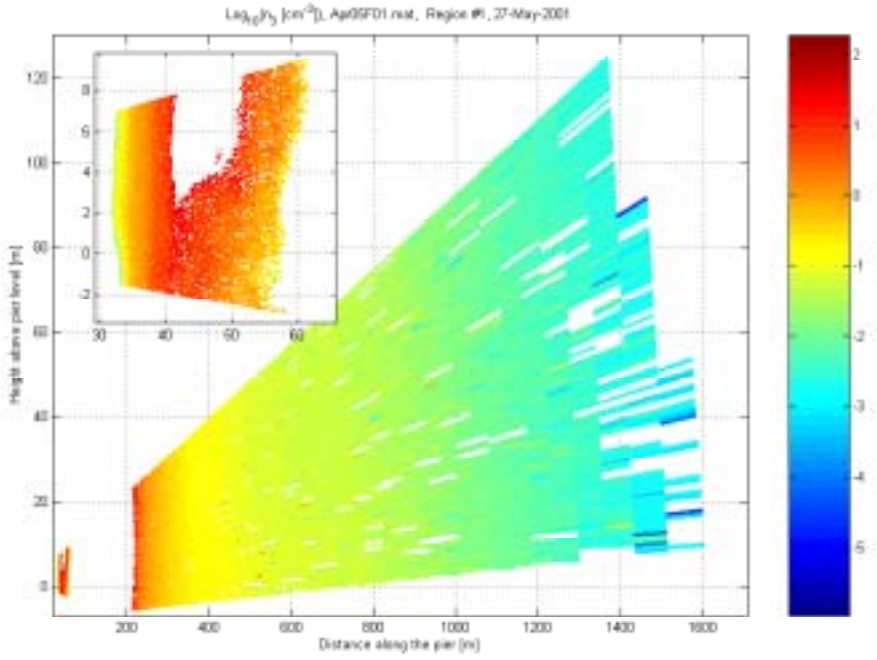

(b)

Figure 4.4. Estimated concentrations from file Apr05F01 for (a) mode 2 and (b) mode 3. Both cameras A and B were used for (a) but camera B only for (b). Other directives were 3 pixels per camera, mean relative humidity and potential modes 0 to 4. Original images were taken with an exposure time of 300 seconds each.

4.4.4 Image set referred to as configuration file Apr08F01 (cf. Appendix H)

The image set was gathered between 20:51 and 21:31 Pacific Standard Time (PST). Also measured were barometric pressure at 30.01 inHg (1017 mbars), wind direction at 256°, wind speed at 1.90 m/s, and atmospheric temperature at 15.6 °C.

Figure 4.5(a) displays the spatial distribution of the estimated mode 2 with, as estimation directives, mean relative humidity, estimation of modes 0 to 4, and cameras A and B together, each of which contributing 3 pixels. Almost uniform concentrations dominate the area with values reaching 25 cm^{-3} from 35 to 170 m along the pier. In the middle of the surf zone (between 60 and 100 m), about 4 vertical lines of 5 m each in width and 10 cm^{-3} in concentrations appear. Data beyond 180 m result in negative concentrations.

Figure 4.5(b) displays the spatial distribution of the estimated mode 3 with, as estimation directives, mean relative humidity, estimation of modes 0 to 4, and camera B contributing 3 pixels. Two distinctive highest concentration areas dominate (separated by areas of reduced and negative concentrations): one between 50 and 60 m along the pier and one near 150 m where concentrations reach 10 cm^{-3} and 30 cm^{-3} respectively, separated by a 30 m wide area of 1 cm^{-3} then by about 50 m of negative concentrations. Over the beach, concentrations decrease to 0.1 cm^{-3}. Beyond the source at 150 m, concentrations decrease to 0.5 cm^{-3} near 170 m, 0.1 cm^{-3} near 300 m, 0.025 cm^{-3} near 400 m, and 0.01 cm^{-3} near 500 m and beyond (despite a 200 m wide feature of negative concentrations near 700 m). This is the first case documenting the presence of reduced concentrations over the surf zone for mode 3.

Both modes agree on the presence of higher concentrations over the source than over the sink. The middle of the surf zone does not produce as much as either end for mode 2 and 3. The uniformity of the concentrations for mode 2 is unusual. Again, concentrations away from the surf zone are too low to be credible.

4.4.5 Image set referred to as configuration file Apr09F01 (cf. Appendix H)

The image set was gathered between 20:21 and 20:23 Pacific Standard Time (PST). Also measured were barometric pressure at 29.89 inHg (1012 mbars), wind direction at 36°, wind speed at 2.10 m/s, and atmospheric temperature at 15.0 °C.

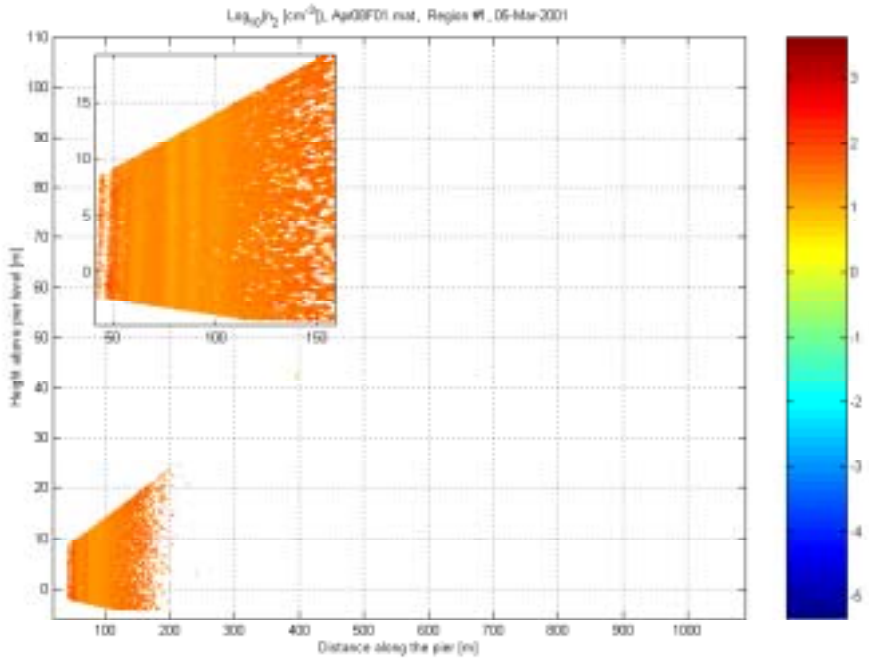

(a)

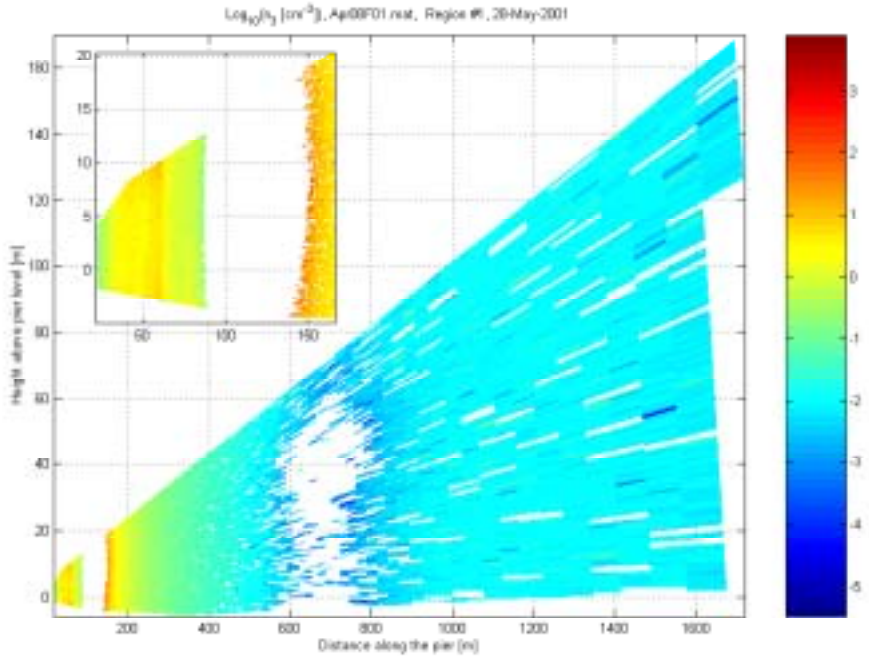

(b)

Figure 4.5. Estimated concentrations from file Apr08F01 for (a) mode 2 and (b) mode 3. Both cameras A and B were used for (a) but camera B only for (b). Other directives were 3 pixels per camera, mean relative humidity and potential modes 0 to 4. Original images were taken with an exposure time of 300 seconds each.

Figure 4.6(a) displays the spatial distribution of the estimated mode 2 with, as estimation directives, mean relative humidity, estimation of modes 0 to 4, and cameras A and B together, each of which contributing 3 pixels. Almost uniform concentrations dominate the area with values reaching 200 cm^{-3} from 25 to 230 m along the pier. In the middle of the surf zone (between 50 and 125 m), about 4 vertical lines of 7 m each in width and 4 cm^{-3} in concentrations appear. Data beyond 230 m result in negative concentrations.

Figure 4.6(b) displays the spatial distribution of the estimated mode 3 with, as estimation directives, mean relative humidity, estimation of modes 0 to 4, and camera B contributing 3 pixels. Two distinctive highest concentration areas dominate (separated by areas of reduced and negative concentrations): one between 30 and 55 m along the pier and one near 225 m where concentrations reach 2 cm^{-3} and 30 cm^{-3} respectively, separated by a 30 m area of 0.3 cm^{-3} then by about 170 m of negative concentrations. Over the beach, concentrations decrease to 0.01 cm^{-3}. Beyond the source at 225 m, concentrations decrease to 0.5 cm^{-3} near 275 m, 0.1 cm^{-3} near 350 m, 0.015 cm^{-3} near 500 m, and 0.008 cm^{-3} near 1000 m.

Both modes agree on the presence of higher concentrations over the source than over the sink. The middle of the surf zone does not produce as much as either end for mode 2 and 3. The uniformity of the concentrations for mode 2 is unusual. Again, concentrations away from the surf zone are much too low to be credible.

4.4.6 Image set referred to as configuration file Apr09F02 (cf. Appendix H)

The image set was gathered between 20:33 and 20:39 Pacific Standard Time (PST). Also measured were barometric pressure at 29.89 inHg (1012 mbars), wind direction at 356°, wind speed at 2.40 m/s, and atmospheric temperature at 15.0 °C.

Figure 4.7(a) displays the spatial distribution of the estimated mode 2 with, as estimation directives, mean relative humidity, estimation of modes 0 to 4, and cameras A and B together, each of which contributing 3 pixels. Two highest concentration areas dominate: one near 40 m along the pier and one near 220 m where concentrations are observed to reach 100 cm^{-3} and 300 cm^{-3} respectively. Those locations correspond to waves crashing onto the beach and breaking for the first time. In the middle of the surf zone, concentrations reach about 3 cm^{-3} through a monotonic decrease from either end. Between 70 and 100 m, 3 vertical structures of 8 m in width each are noticeable. Data beyond 220 m result in negative concentrations. The cut out region near the shore contained comet light.

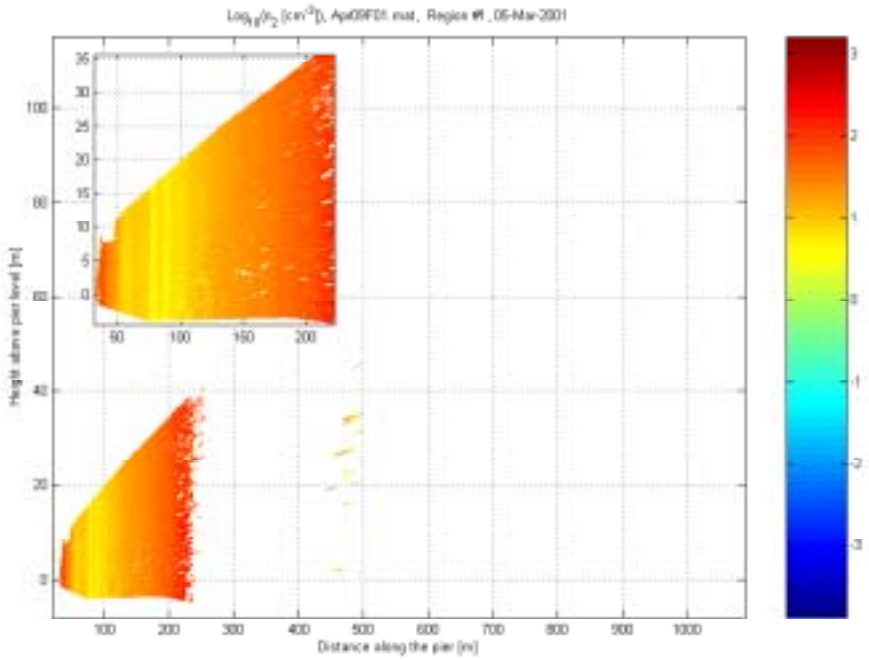

(a)

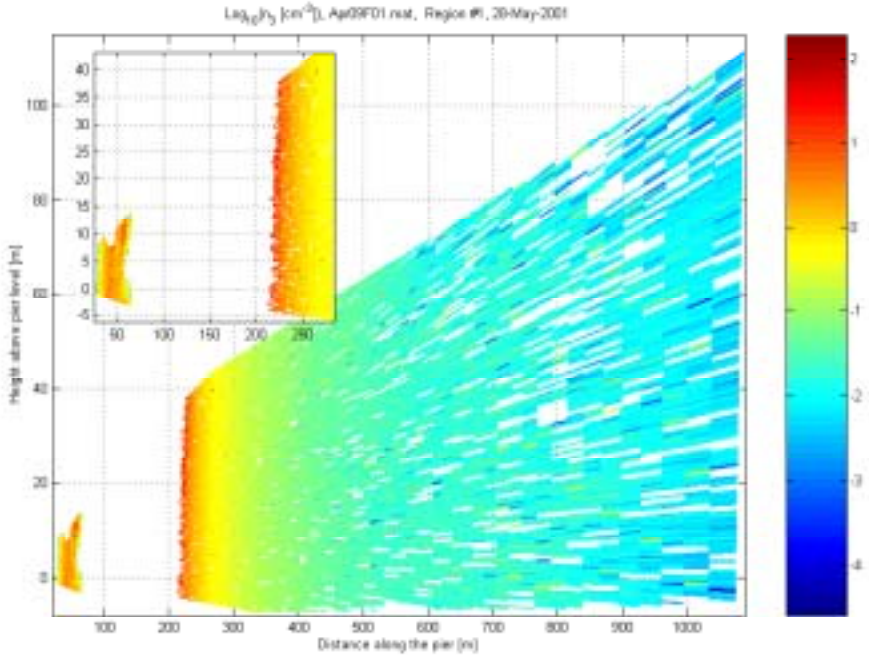

(b)

Figure 4.6. Estimated concentrations from file Apr09F01 for (a) mode 2 and (b) mode 3. Both cameras A and B were used for (a) but camera B only for (b). Other directives were 3 pixels per camera, mean relative humidity and potential modes 0 to 4. Original images were taken with an exposure time of 10 seconds each.

Figure 4.7(b) displays the spatial distribution of the estimated mode 3 with, as estimation directives, mean relative humidity, estimation of modes 0 to 4, and camera A contributing 3 pixels. Two distinctive highest concentration areas dominate (separated by areas of reduced and negative concentrations): one near 25 m along the pier and one near 130 m where concentrations reach 10 cm^{-3} and 30 cm^{-3} respectively, separated by a 10 m wide area of 1 cm^{-3} then by about 90 m of negative concentrations. Beyond the source at 130 m, concentrations decrease to 1 cm^{-3} near 160 m, 0.5 cm^{-3} near 180 m, 0.1 cm^{-3} near 250 m, and 0.01 cm^{-3} near 600 m and beyond.

Both modes agree on the presence of higher concentrations near the edges of the surf zone. The middle of the surf zone does not produce as much as its edges for mode 2 (mode 3 is inconclusive on this issue due to negative concentrations) and the concentrations of mode 3 decrease away from the surf zone (mode 2 is inconclusive on this issue due to negative concentrations). Again, concentrations away from the surf zone are too low to be credible.

4.4.7 Image set referred to as configuration file Apr09F03 (cf. Appendix H)

The image set was gathered between 20:46 and 20:58 Pacific Standard Time (PST). Also measured were barometric pressure at 29.89 inHg (1012 mbars), wind direction at 347°, wind speed at 3.63 m/s, and atmospheric temperature at 14.9 °C.

Figure 4.8(a) displays the spatial distribution of the estimated mode 2 with, as estimation directives, mean relative humidity, estimation of modes 0 to 4, and cameras A and B together, each of which contributing 3 pixels. Two highest concentration areas dominate: one near 40 m along the pier and one near 220 m where concentrations are observed to reach 100 cm^{-3} in both cases. Those locations correspond to waves crashing onto the beach and breaking for the first time. In the middle of the surf zone, concentrations reach about 10 cm^{-3} through a monotonous decrease from either end. Between 70 and 100 m, 3 vertical structures of 8 m in width and 2 cm^{-3} in concentrations each are noticeable. Data beyond 220 m result in negative concentrations.

Figure 4.8(b) displays the spatial distribution of the estimated mode 3 with, as estimation directives, mean relative humidity, estimation of modes 0 to 4, and camera A contributing 3 pixels. Two distinctive highest concentration areas dominate (separated by areas of reduced and negative concentrations): one near 30 m along the pier and one near 140 m where concentrations reach 20 cm^{-3} in both cases, separated by a 4 m wide area of 0.2 cm^{-3} then by about 100 m of negative concentrations. Beyond the source at 140 m, concentrations decrease to 0.3 cm^{-3} near 200 m, 0.05 cm^{-3} near 350 m, 0.005 cm^{-3} near 750 m, and 0.001 cm^{-3} near 1050 m and beyond.

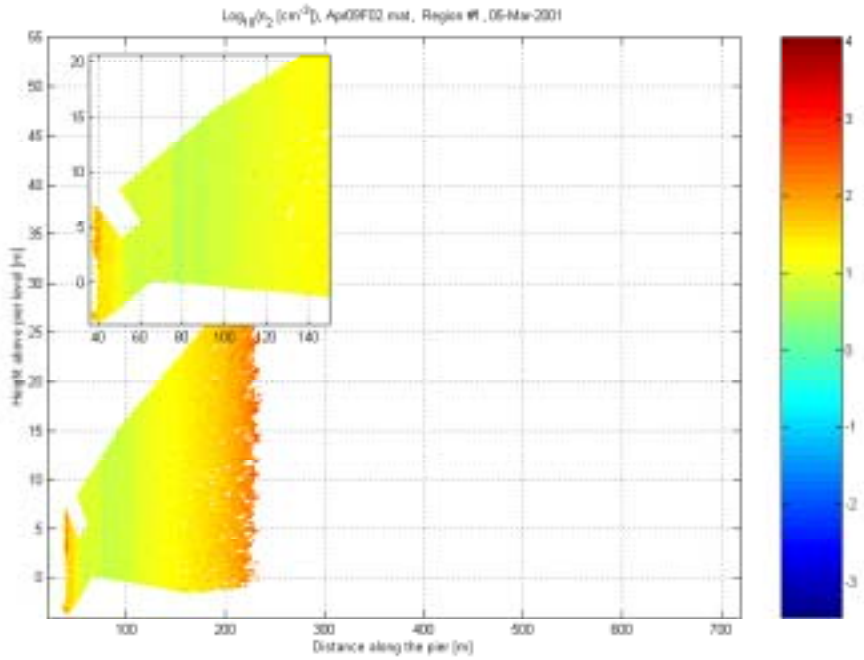

(a)

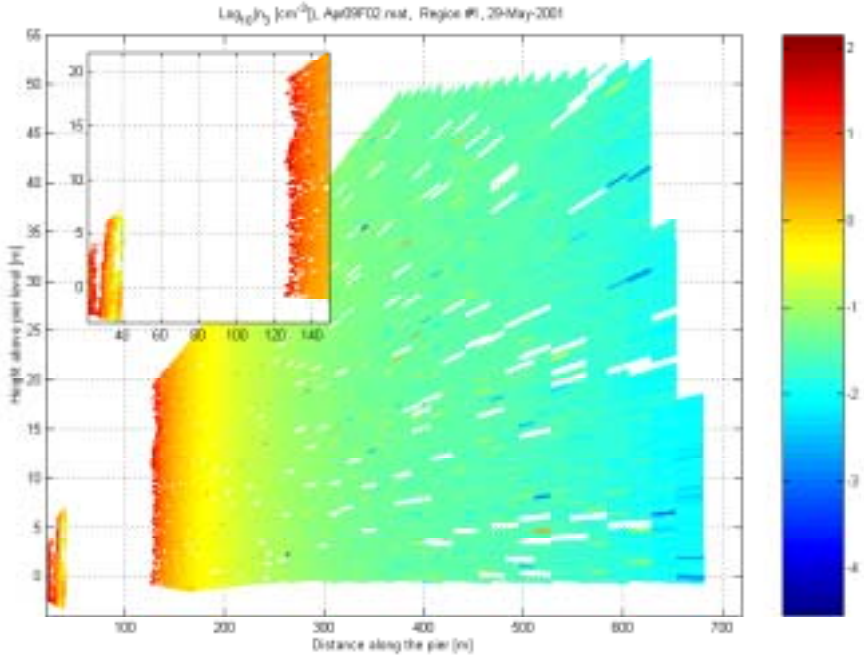

(b)

Figure 4.7. Estimated concentrations from file Apr09F02 for (a) mode 2 and (b) mode 3. Both cameras A and B were used for (a) but camera A only for (b). Other directives were 3 pixels per camera, mean relative humidity and potential modes 0 to 4. Original images were taken with an exposure time of 30 seconds each.

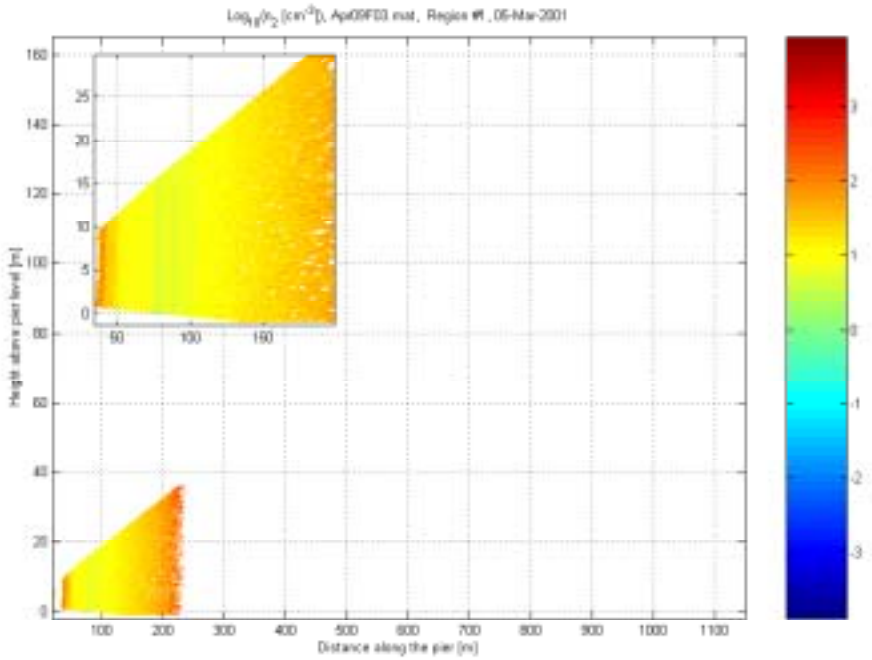

(a)

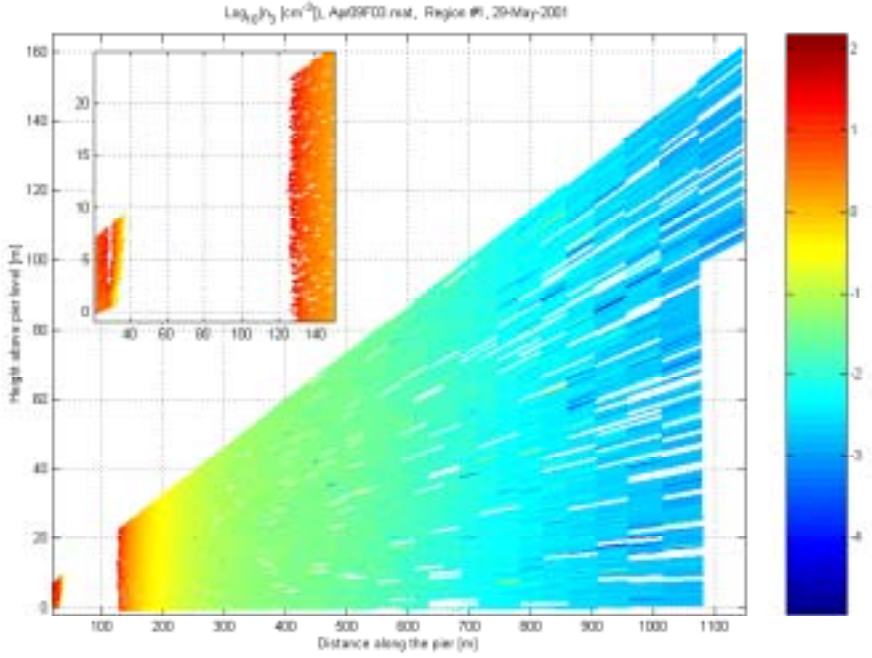

(b)

Figure 4.8. Estimated concentrations from file Apr09F03 for (a) mode 2 and (b) mode 3. Both cameras A and B were used for (a) but camera A only for (b). Other directives were 3 pixels per camera, mean relative humidity and potential modes 0 to 4. Original images were taken with an exposure time of 60 seconds each.

Again, both modes agree on the presence of higher concentrations near the edges of the surf zone. The middle of the surf zone does not produce as much as its edges for mode 2 (mode 3 is inconclusive on this issue due to negative concentrations) and the concentrations of mode 3 decrease away from the surf zone (mode 2 is inconclusive on this issue due to negative concentrations). Again, concentrations away from the surf zone are much too low to be credible.

4.4.8 Image set referred to as configuration file Apr09F04 (cf. Appendix H)

The image set was gathered between 21:04 and 21:20 Pacific Standard Time (PST). Also measured were barometric pressure at 29.89 inHg (1012 mbars), wind direction at 356°, wind speed at 5.00 m/s, and atmospheric temperature at 14.9 °C.

Figure 4.9(a) displays the spatial distribution of the estimated mode 2 with, as estimation directives, mean relative humidity, estimation of modes 0 to 4, and cameras A and B together, each of which contributing 3 pixels. Two highest concentration areas dominate: one near 40 m along the pier and one near 200 m where concentrations are observed to reach 60 cm^{-3} in both cases. Those locations correspond to waves crashing onto the beach and breaking for the first time. In the middle of the surf zone, concentrations reach about 10 cm^{-3} through a monotonous decrease from either end. Between 70 and 100 m, 3 vertical structures of 8 m in width and 3 cm^{-3} in concentrations each are noticeable. Data beyond 210 m result in negative concentrations.

Figure 4.9(b) displays the spatial distribution of the estimated mode 3 with, as estimation directives, mean relative humidity, estimation of modes 0 to 4, and camera A contributing 3 pixels. Two distinctive highest concentration areas dominate (separated by negative concentrations): one between 30 and 40 m along the pier and one near 120 m where concentrations reach 3 cm^{-3} and 30 cm^{-3} respectively, separated by about 80 m of negative concentrations. Beyond the source at 120 m, concentrations decrease to 0.5 cm^{-3} near 160 m, 0.1 cm^{-3} near 250 m, 0.015 cm^{-3} near 650 m, and 0.003 cm^{-3} near 1000 m and beyond.

Again, both modes agree on the presence of higher concentrations near the edges of the surf zone. The middle of the surf zone does not produce as much as its edges for mode 2 (mode 3 is inconclusive on this issue due to negative concentrations) and the concentrations of mode 3 decrease away from the surf zone (mode 2 is inconclusive on this issue due to negative concentrations). Again, concentrations away from the surf zone are much too low to be credible.

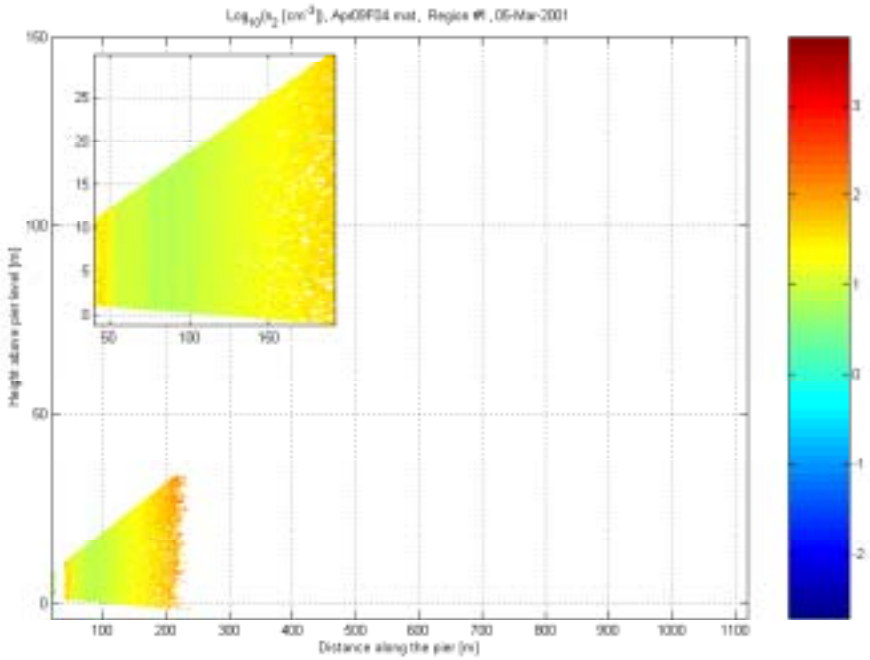

(a)

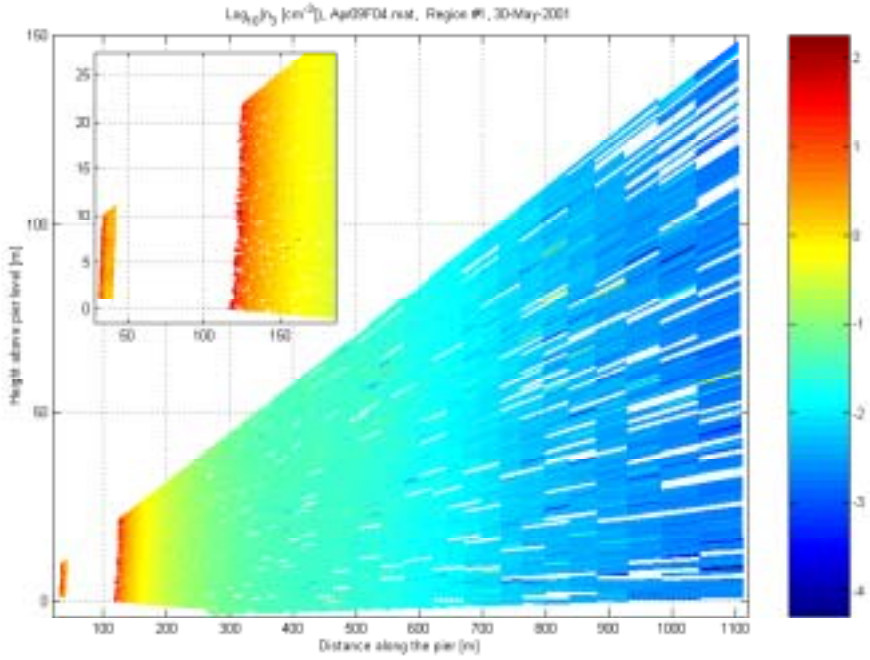

(b)

Figure 4.9. Estimated concentrations from file Apr09F04 for (a) mode 2 and (b) mode 3. Both cameras A and B were used for (a) but camera A only for (b). Other directives were 3 pixels per camera, mean relative humidity and potential modes 0 to 4. Original images were taken with an exposure time of 120 seconds each.

4.4.9 Image set referred to as configuration file Apr09F05 (cf. Appendix H)

The image set was gathered between 21:28 and 22:08 Pacific Standard Time (PST). Also measured were barometric pressure at 29.89 inHg (1012 mbars), wind direction at 54.7°, wind speed at 3.24 m/s, and atmospheric temperature at 14.6 °C.

Figure 4.10(a) displays the spatial distribution of the estimated mode 2 with, as estimation directives, mean relative humidity, estimation of modes 0 to 4, and cameras A and B together, each of which contributing 3 pixels. Two highest concentration areas dominate: one near 40 m along the pier and one near 200 m where concentrations are observed to reach approximately 100 cm^{-3} in both cases. Those locations correspond to waves crashing onto the beach and breaking for the first time. In the middle of the surf zone, concentrations reach about 10 cm^{-3} through a monotonous decrease from either end. Between 70 and 100 m, 3 vertical structures of 8 m in width and 3 cm^{-3} in concentrations each are noticeable. Data beyond 210 m result in negative concentrations.

Figure 4.10(b) displays the spatial distribution of the estimated mode 3 with, as estimation directives, mean relative humidity, estimation of modes 0 to 4, and camera A contributing 3 pixels. Two distinctive highest concentration areas dominate: one between 20 and 30 m along the pier and one near 120 m where concentrations reach 30 cm^{-3} and 60 cm^{-3} respectively, separated by a 20 m wide area of 0.2 cm^{-3} then by about 100 m of negative concentrations. Beyond the source at 120 m, concentrations decrease to 0.5 cm^{-3} near 160 m, 0.1 cm^{-3} near 250 m, 0.01 cm^{-3} near 650 m, and 0.003 cm^{-3} near 1050 m and beyond.

Again, both modes agree on the presence of higher concentrations near the edges of the surf zone. The middle of the surf zone does not produce as much as its edges for mode 2 (mode 3 is inconclusive on this issue due to negative concentrations) and the concentrations of mode 3 decrease away from the surf zone (mode 2 is inconclusive on this issue due to negative concentrations). Again, concentrations away from the surf zone are much too low to be credible.

4.4.10 See-through areas in images of estimated concentrations

The see-through areas in the spatial distribution of the estimated concentrations either were outside a selected processing region or contained either infinite polarization ratios (minority of cases in selected areas) or negative concentrations (majority of cases in selected areas).

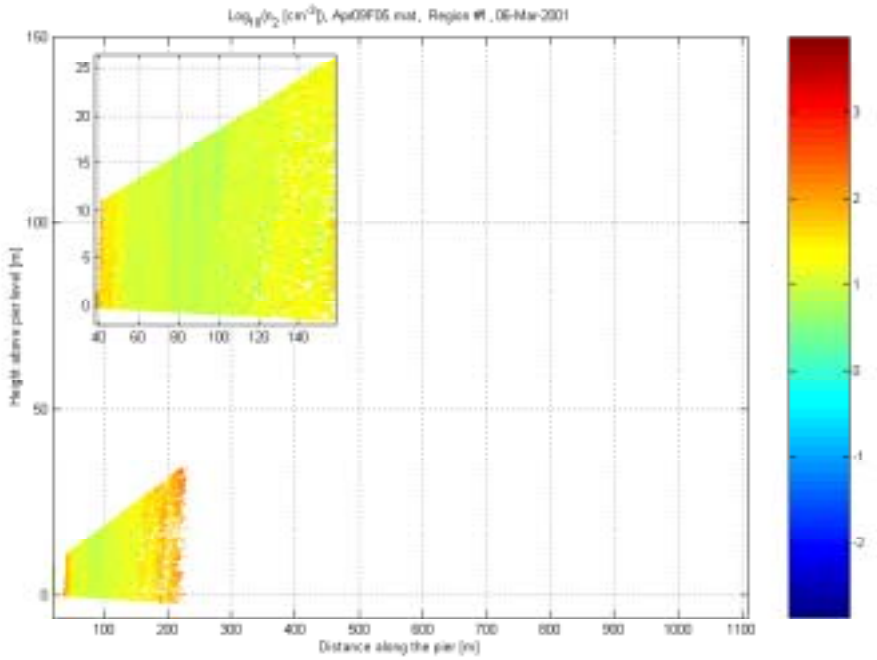

(a)

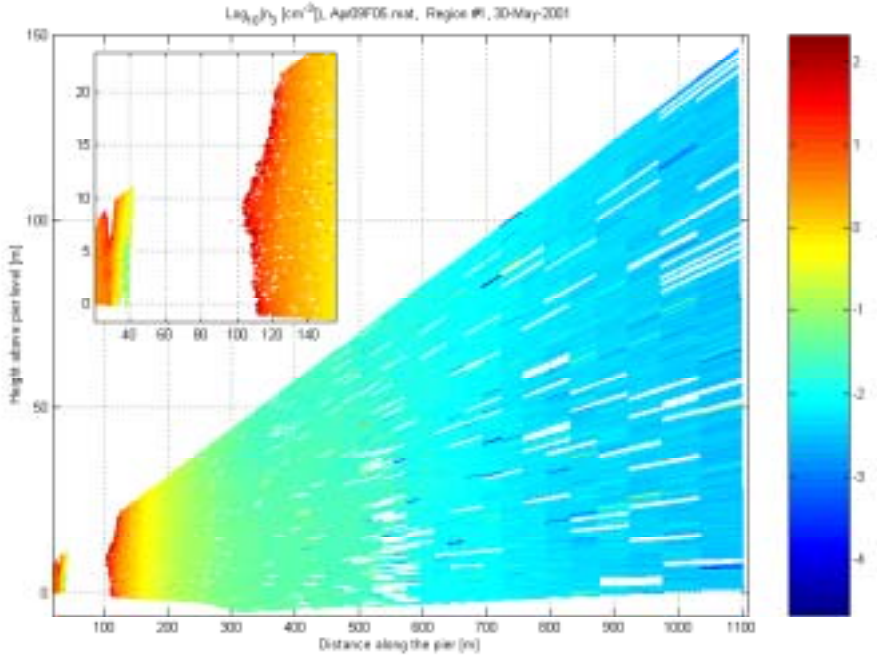

(b)

Figure 4.10. Estimated concentrations from file Apr09F05 for (a) mode 2 and (b) mode 3. Both cameras A and B were used for (a) but camera A only for (b). Other directives were 3 pixels per camera, mean relative humidity and potential modes 0 to 4. Original images were taken with an exposure time of 300 seconds each

Although increasing either the integration time of each image or the number of images to average reduces the number of pixels having an infinite polarization ratio, the number of negative concentrations involves the complete chain of theoretical assumptions and experimental estimations including correctness of the aerosol model, actual position of the laser sheet, actual transmittance through the retarder plate, and minimization of aerosol motion between images of complementary polarization.

Modes 2 and 3 regularly produce negative concentrations between segments whose locations along the pier approximately range from 30 m to 40 m and from 210 m to the end of the processing area for the former mode and from 50 m to 150 m for the latter mode. Observations from a partial investigation of this phenomenon consider individual contributions by the retarder plate, the Laser Sheet Angle, and time.

Both modes 2 and 3 see their number and location of negative pixels change, but not disappear. Modification of the transmittance of the retarder plate (T_R) from 0.92 to 0.9926 significantly reduces the total number of negative pixels. Manual adjustment of the Laser Sheet Angle results in both shifting and re-sizing the areas of negative pixels. Pairs of images indicate that the number of negative concentrations consistent in location decreases as time between images of complementary polarization increases. Atmospheric motion unlikely generates this structured noise (the shorter the time between two images the more alike the features). As the number of consecutive images of the same polarization are averaged prior to processing, the number of negative estimated concentrations consistent in location increases (a longer total observation time is obtained, although the exposure time for each image remains the same). As exposure time decreases, the above-identified regions of negative concentrations become blurred (i.e., 300 seconds vs. 5 seconds). An analysis in Appendix L concludes that concentrations estimated *via* the maximum log-likelihood criterion (cf. footnote #22) remain unaffected by timing issues (a parallel exists between atmospheric motion and incorrect values for T_R).

These observations suggest that atmospheric motion has limited responsibility for the presence of negative concentrations, but that the appropriateness of both the aerosol model and the estimation of the position of the parts of the instrument (the mirror at the emitter and the cameras) may be questioned.

4.4.11 Conclusion

Subsections 4.4.1 to 4.4.9 displayed the estimated concentrations of modes 2 and 3 over the surf zone as seen by the aerosol model of Chapter 2 combined with the estimation procedure detailed in Chapter 3. Appendix K displays similar figures for modes 0, 1, and 4 (because of the magnitude of the expected discrepancy in estimated concentrations from both the rotorod data and the EOPACE images, as predicted in Chapter 3) and Appendix J shows the original EOPACE images.

Those EOPACE images suggest that wind direction influences the width of the region displaying relatively large scattering signatures. On-shore winds rarely produce noticeable scattering regions, except for a few localized spots (cf. results from Apr04F02 and Apr08F01 in Appendix H). Off-shore winds produce the widest scattering regions (cf. results from Apr09F01 and Apr09F05 with respective widths of 100 m and 175 m for a 33% decrease in radiant energy from its maximum value, and 150 m and 230 m for a 50% criterion). Along-shore winds produce narrow scattering regions (cf. results from Apr05F01 and Apr09F02 whose widths respectively are 50 m and 80 m with a 33% criterion and 100 m and 130 m with a 50% criterion). The widths of those areas remain unnoticed by the estimated concentrations of modes 2 and 3 (changes in the magnitude of the signature may be attributed to various factors other than changes in concentrations such as the decrease in incident irradiance from within the fanned beam, the behavior of the F-functions, spatial changes in the model behavior over the surf zone, as stated in Chapter 2, or atmospheric stability). Appendix M shows that the features described by the estimated concentrations depend on the number of simultaneously processed pixels (those included in the processed neighborhood) confirming the inhomogeneous distribution of scatterers above the surf zone. Section 4.3 successfully estimated the concentrations of modes 2 and 3 by inverting small neighborhoods (comprised only of a few pixels) and by applying a most-likely criterion. The application of large neighborhood sizes results in less reliable estimated concentrations.

The images of estimated concentrations suggest that the regions of highest concentrations are at both ends of the surf zone (waves crashing onto the beach and waves breaking for the first time), followed by its middle. Concentrations decrease away from the surf zone, confirming the role of the surf zone as a source of aerosols. Uniform concentrations for mode 2 appear when the wind direction follows the coastline. The location of the first breaker depends on the camera chosen to estimate the concentrations, confirming that the location of each camera should be precisely measured. In many cases, concentrations for mode 3 beyond the surf zone drop off by a hundredfold over pier distances between 50 and 75 m. However, concentrations estimated by NOVAM are expected to define a lower bound, especially for concentrations reported toward the open ocean.

The vertical distributions of the concentrations for modes 2 and 3 neither match the anticipated behavior by Gathman (1989) nor that measured by de Leeuw et al. (2000). Indeed, the conditions of operation report the same magnitude in concentration independently of the height above the water surface, independently of the estimation directives. The absence of vertical features suggests (besides strong atmospheric convection) either a reduction of the influence of atmospheric motion onto the estimated concentrations or the need to improve the aerosol model (HCAM cannot accommodate for adjustable logarithmic widths without encountering computational limitations – cf. Chapter 2), perhaps by integrating

a simpler aerosol model such as the one by Zieliński et al. (1994). Furthermore, atmospheric motion between consecutive images of complementary polarization seems to have compromised the estimation of valid concentrations both in and within the vicinity of dynamic areas, including those containing the surf-zone plumes (especially for images of short exposure time). Even if such estimation were possible, it would not answer the means to characterize multi-modal plumes.

The spatial distributions of the concentrations of mode 2 and 3 suggest that most aerosol sources are the strongest at both ends of the surf zone, but do not support their vertical distributions previously measured in other experiments.

4.5 Conclusion

The present chapter has shown that modes 2 and 3 are the most reliably estimated, as anticipated from the simulations of Chapter 3, although concentrations are presented on a logarithmic scale which smooth out relatively small fluctuations.

The claim is made that the concentrations (of both modes 2 and 3, mainly) estimated from the polarization-ratio method are in agreement with those from the functional fits onto the rotorod data, those from NOVAM, and those from the simulations of Chapter 3. Agreement in extinction values add to the credibility of the instrument (although the lidar-estimated extinction shows slightly stronger values than those from NOVAM). However, the presence of negative concentrations for modes 2 and 3 prevents the computation of the spatial transmittance above the inhomogeneous surf zone.

To qualify the instrument as good necessitates that both the accuracy and precision of estimated values (i.e., concentration and extinction) comply with requirements designed around specific needs. Indeed, agreement among the estimates, the data, and NOVAM results suggest that improvements of the polarization ratio methods are needed to make it a better instrument (EOPACE addresses improvements in the Navy aerosol models).

The main points of the study carried herein consist in the first substantiation of the applicability of the polarization-ratio method to a bi-static lidar to estimate multiple concentrations in an experimental setting and the confirmation that the surf zone is a source of aerosol for modes 2 and 3 (particularly at both ends of the surf zone).

CHAPTER 5
CONCLUSION AND RECOMMENDATIONS

5.1 Introduction

Chapter 1 introduced the goal of the EOPACE experiment and the use of the collected data. Chapter 2 focused on building the necessary tools to reconstruct the EOPACE images. Chapter 3 derived an objective estimator of aerosol concentrations and predicted that only a few modes would be estimated reliably. Chapter 4 established the credibility of the polarization-ratio method through the correlation of estimated concentrations from various means and displayed the spatial distribution of the most reliable modes for several cases.

Section 5.2 discusses the research philosophy applied to the present analysis, Section 5.3 reviews accomplishments contained within the present document, Section 5.4 advises on the use of the present material, and Section 5.5 suggests future opportunities. Section 5.6 concludes.

5.2 Research perspective on the present work

Research in the context of EOPACE operated by defining objectives and by conducting a series of experiments in support of those objectives. If A denotes the starting point and B the accomplishment of those objectives, then the direction of investigation seems clearly defined. However, progress made during the journey from A toward B, whose exact location contained uncertainties, described a tortuous path of investigation (although not presented as such).

A point C was launched ahead of A (similarly to light sensing its own path one wavelength ahead) in the assumed direction of B. The role of C is to decompose the A-to-B segment into manageable subsegments. Research was conducted: (1) by both iteratively and recursively breaking the A-B segment into subsegments, (2) by evaluating the credibility of each subsegment (by contrasting methods, assumptions, and data quality), (3) by stopping the recursion whenever the best compromise (among methods, assumptions, and data quality) had been reached (potentially including unnecessary details), and moving C one step forward.

Hence, only a subset of the conducted investigation is contained in the present document, but the path so defined describes a solid baseline for future investigations wishing to use the polarization-ratio method.

5.3 Accomplishments

The present document advances the field of remote sensing within two major classes of accomplishments: (1) its final outcome and (2) all decisions made to support this final outcome. Sections 5.3.1 and 5.3.2 approach those accomplishments from the respective perspectives of result exploitation and both duplication and method improvement. Section 5.3.3 concludes.

5.3.1 Major accomplishments

The present document contains important accomplishments for estimating both aerosol concentrations and their extinction, remotely. Those accomplishments are:

The ratification of the polarization-ratio method from its first substantiation:

The consistency in both concentrations and extinction among several sources confirms the success of the polarization-ratio method as implemented herein. The agreement was correctly predicted to apply exclusively to modes 2 and 3 and was confirmed both by experimental data (i.e., fits onto rotorod data and publication – Zieliński, 1999) and by NOVAM, although those results were seen through the eyes of the aerosol model (originally designed to operate over the open-ocean).

The original derivation of a simple but powerful new estimator of aerosol concentrations:

The new estimator of concentrations is both simple and versatile. It delivers objective results, proceeds from a handful of pixels or more (supporting both local – i.e., inhomogeneous environments – and global – i.e., homogeneous environments – analyses), and is expansion-ready to the next-generation of bi-static lidars using the polarization-ratio method. Its structure accommodates any number of cameras simulta-neously used in the estimation process as well as any neighborhood size.

The elimination of two both lengthy and contentious analytical steps:

The combination of the polarization-ratio method with the new estimator results in the removal of two time-consuming and subjective steps: calibration and the need for the first good guess (Stevens, 1996). The integrity of the results is preserved by preventing injection of subjectivity in both the instrument characteristics and in the concentrations to estimate.

Those three major accomplishments are supported by detailed accomplishments (cf. Subsection 5.3.2). Section 5.5 lists opportunities for further breakthroughs.

5.3.2 Supportive accomplishments

The present subsection divides detailed accomplishments into three categories: correction, refinement, and original contribution. Items included in the first category result from correcting past omissions, those in the second category improve upon validated work, and those in the third category have been generated by the author. The categories of improvements and original contributions do overlap as refinements involve special needs. However, depth in refinement is interpreted as an original contribution.

Correction: accounting for the transmittance through the retarder plate

The computation of the polarization ratio by Stevens (1996) neglected the loss of energy through a retarder plate whose purpose was to rotate the outgoing polarization from perpendicular to parallel. The numerical outcome (obtained from the Newton-Raphson numerical driver attached to the aerosol model) was subsequently compared to a biased experimental polarization ratio. Their difference was fed back into the iterative estimator for further changes in the nine-parameter aerosol-model (3 per mode) until the difference was minimized. As the most accurate results are sought, inclusion of the transmittance through the retarder plate has become a necessity (consequences of its omission can be observed in Fig. 3.1(a)).

Refinement: the aerosol model

The aerosol models extensively tested by the US Navy were adapted for optical use. This adaptation was carried out in two dimensions: addition of the molecular background (mode -1) and confinement of the influence exerted by meteorological parameters. The endorsed aerosol models present advantages of maturity both in behavior (removing the desire to develop yet another model) and in publication (including the frequency-dependent values of the complex indices of refraction as functions).

Refinement: the number of parameters to estimate from the aerosol model

The aerosol model imposed fixed logarithmic widths and mode radii depending upon relative humidity only (excluding height dependency). These restrictions decreased from three to one the number of parameters to estimate per mode.

Refinement: the extent of the homogeneous physical area used for each estimate

Incidentally, the restriction in the number of parameters to estimate led to a reduction in the surveyed physical area per estimated set of modes. The use of two cameras improved the quality of the estimated concentrations over an expansion of a neighborhood size and one camera. An increased neighborhood size

translates into an increased area over which concentrations are assumed to be homogeneous. Thus, only a handful of pixels are now necessary. This improvement allows the study of inhomogeneous areas.

Refinement: the numerical means to estimate aerosol concentrations

The estimator of concentrations derived from the limited number of parameters to estimate over a narrowly defined area only require a small-matrix inversion (cf. Subsection 3.2.2) rather than the Newton-Raphson (iterative) numerical driver equipped with a good first guess (Stevens, 1996). The procedure has been made objective for which all results are reproducible.

Refinement: interface and optimization with the Mie program by Bohren and Huffman (1983)

The modifications brought to the original Mie program by Bohren and Huffman (1983) were designed both to integrate the program into MATLAB (to obtain a consistent central computational platform for the complete work) and to optimize both calculation speed and the size of returned results (the original program returned the complex functions S_1 and S_2 according to a specific angular scheme but $|S_1|^2$ and $|S_2|^2$ were needed at various angles).

Original contributions: computation of the F-functions

The procedure to compute the quadrature of the F-functions in Subsection 2.3.3 showed that a narrow step in radius (of 0.1 nm) increases both the accuracy of the F-functions and the convergence time of the calculations.

Original contributions: features selected for the aerosol model

The aerosol model has been confined to one unknown parameter per mode: its concentration. This restriction opened the cascade of simplifications. One of them is the definition of the F-functions (F_1 and F_2) and the extinction function (Γ) for each mode, which eased overall computational complexity once calculated for unit concentrations ($n_j = 1$). Several schemes to compute the quadrature of the F-functions revealed discrepancies among them (a linear step size of 0.1 nm was applied in an *ad-hoc* computational scheme). Those functions suggest that scattering by homogeneously distributed modes 2 and 3 produces plume-like features. Observed plumes result from the interaction among the aerosols above the surf zone (depending on both chemical composition and modal decomposition), the incident illumination (polarization, wavelength, and power), their angle of observation (scattering angle), and on the visual system of their observer. In a multimodal environment, an objective definition of the plumes has yet to be formulated.

Original contributions: derivation of an estimator of concentrations using the polarization ratio

Another simplification resulting from the constrained aerosol model is the derivation of an original estimator of concentrations specifically designed for the polarization-ratio method. The estimator is simple but powerful as its structure is preserved despite changes in the number of cameras, modes, or frequencies. Properties of the polarization ratio have been discussed for the first time (cf. Subsection 3.2.3), especially in cases yielding irrecoverable results. In other cases, a trivial inversion leads to estimated concentrations (cf. Subsection 3.2.2). A representative concentration for each mode from the estimated bi-dimensional spatial distribution of concentrations is successfully obtained when applying the maximum log-likelihood criterion (cf. footnote #22). Also suggested is the use of the condition number to assess the health of an experimental design in a simulated, noise-free, environment. Simulations have also quantified the sensitivity of the polarization-ratio method in four instrumental parameters (cf. Fig. 3.1). Unfortunately, systematic errors (such as those produced by those four parameters) do not consistently improve upon increasing the number of pixels simultaneously processed (although this usual approach is successful on stochastic errors). Increasing the number of cameras contributing the same number of pixels improves results in most cases.

Original contributions: EOPACE-related findings

The lore described in Chapters 2 and 3 was applied onto the EOPACE images (collected by two CCD cameras) to successfully correlate the estimated concentrations (and extinction values) with both those from fits onto rotorod data and those from NOVAM. However, the experimental context showed disagreement between the two cameras in the location of the intersection of the vertical laser sheet and the water surface which motivated the implementation of an original iterative procedure to refine the position of the Laser Sheet Angle (*LSA*), resulting in a better agreement in estimated concentrations. The bi-dimensional estimated concentrations for modes 2 and 3 suggest that the two major sources of aerosol are located at either end of the surf zone. However, doubt subsists on the validity of this observation, requiring further studies.

Original contributions: centralization of the material needed to replicate the results in one document

The present self-contained document is a repository of all the information needed (experimental conditions, mathematical expressions, and computer programs – in exclusion of the EOPACE images themselves) to confirm the major accomplishments. Mathematical expressions reconstruct the topology of the experimental set-up toward the determination of (1) the orientation of the cameras, (2) the position of the Laser Sheet Angle (*LSA*), and (3) the values of both the scattering and tilt angles for each pixel. Mathematical expressions also estimate the concentrations of each mode from images captured by multiple

cameras, using the polarization-ratio method. Computer programs deliver modal radii, logarithmic widths, and indices of refraction as functions of both relative humidity and optical wavelength, and the modified program by Bohren and Huffman (1983) returns values proper to the interaction of the aerosol model (one radius at a time) with light.

5.3.3 Conclusion

The success of the polarization-ratio method has been achieved by paying attention, throughout the entire estimation process, to factors which would have made it fail, followed by both tracking and constraining them. Some of them were fairly straightforward (such as keeping all units consistent). Others were less straightforward (such as computing the F-functions and selecting an appropriate aerosol model). A few of those factors have not been addressed (i.e., the laser beam divergence), but will need to be in the future (such as the aerosol model whose alteration is inevitable, as coastal pollution changes the chemical composition of each mode).

5.4 Potential use of the current material

The present section suggests two situations in which to use the present material while improving upon the quality of the estimates. The first one is concerned with subsequent experiments similar to EOPACE (Subsection 5.4.1) and the second one deals with the establishment of a baseline prior to furthering its improvement (Subsection 5.4.2)

5.4.1 Experiments similar to EOPACE

Experiments usually contain three identified stages: preparation, measurement, and processing.

Preparation encompasses designs of potential experimental stages, in particular, the determination of the sensitivity and location of each instrument to acquire data of appropriate quality (contingency plans included). Measurement encompasses verification of both all hypotheses to select the best processing algorithm possible and the quality of the data while considering activation of any contingency plan. Processing encompasses estimation of parameters from experimental data.

Experiments of the scale of EOPACE are expensive and their field conditions irreplaceable (although vehicle-generated plumes can be observed on rainy days on roads of moderate traffic). Simulations help both assess the extent to which instrumental parameters influence the accuracy of the results and define conditions under which the results meet expected quality bounds. Compromised quality in the collected data results in additional post-experimental signal-processing schemes to minimize the effect of noise

(uncertainty). Furthermore, the use of simulations to formulate proposals helps in assessing both strengths and weaknesses of existing instruments (including both devices and methods), to define a tangible direction of research, and to substantiate claims of expertise in the relevant field of research. Also, these factors contribute to the financial support requested.

5.4.2 Baseline establishment

Assumptions within the present document define both a baseline and its limits. The modification of an assumption implies the replacement of a baseline module by its modified version. As Section 5.5 suggests improvements to the current work, integration of all modules into a single computer program would solve three main challenges: (1) to allow simulator-training prior to collecting data (this is especially valuable when a technical crew is sent to an experimental site with limited scientific assistance), (2) to expedite trials of tentative algorithms (this is especially valuable in improving one specific module), and (3) to centralize knowledge integration to prevent its loss as projects terminate and people move on (a knowledge management issue).

5.5 Recommendations

Development opportunities have been confirmed within the present document. Three main factors for improvement have been isolated: computational (Subsection 5.5.1), experimental (Subsection 5.5.2), and instrumental (Subsection 5.5.3). Implementation of those improvements releases the next-generation of bi-static lidar using the polarization-ratio method.

5.5.1 The computational challenge

The computation of the F-Functions is time consuming. To lessen the total computational load, each calculation (one per mode and relative humidity[24] – except for both modes -1and 0) was assigned either to a Windows or a UNIX platform, simultaneously crunching numbers on approximately 5 processors (UNIX allows background processes). Computer programs should be written so as both to save intermediate results at regular time intervals and to resume calculations from the last intermediate results saved. Compu-

[24] The larger the differences in relative humidity (RH) measured by two distant sensors, the larger the differences between estimated concentrations in Section 4.3. For instance, a 4% RH dispersion (cf. Table 4.20) near a mean value of 65% resulted in differences in concentration by 10% at mode 2 and 40% at mode 3.

ted calculations converge in a matter of days whereas nature completes (optically) the same calculations almost instantaneously. Surely, further improvements should be possible.

5.5.2 The experimental challenge

The experimental site presents challenges. Improvements focus on both estimating the location of devices (or variables affected by the position of those devices, such as the Laser Sheet Angle – *LSA*) and capturing the experimental background scene.

Estimation of the Laser Sheet Angle

Currently, an automatic procedure adjusts the *LSA* so as to overlap two independently drawn lines (one per camera) corresponding to the intersection of the laser sheet and the water surface. A more advanced procedure would automatically refine the *LSA* by correlating spatial features of the estimated concentrations resolved by at least two cameras.

Experimental background scenes

Images of background scenes were captured with the laser switched off (one background image was captured before each series at parallel and perpendicular outgoing polarizations). During EOPACE, local background scenes evolved faster than the collection time of the images of the plumes (i.e., waves seen through the plumes) ultimately resulting in rejection of the affected areas. The sampling rate should be increased to capture a background scene between each pair of images (parallel and perpendicular). Along similar observations, additional opportunities exist in quantifying the scale of dynamics (in time) of the plumes above the surf zone (cf. Subsection 5.5.3).

5.5.3 The instrumental challenge

The ultimate goal of the instrument (defined by its set of devices and algorithms) is to outperform any other instrument at estimating instantaneously the spatial and temporal distributions of aerosols. To this aim, the present document has identified the following areas of improvement related to the instrument:

Adequate selection of aerosol models

The aerosol model needs careful consideration prior to its parameterization, as the analysis delivers incorrect answers from an incorrect model. The major difficulty in either selecting or refining an aerosol model is that it is an inverse problem in itself (modal and functional decompositions, chemical compositions, etc.). Once the representativeness of the model is confirmed for a specific environment, it

remains to be exploited. The main factor to take into account is the ease of access of the parameters to estimate via the polarization-ratio method (priority is to preserve an objective estimation process).

Augmentation in the visibility of modes of interest

Only a subset of modes may be visible at a given wavelength and camera position. The EOPACE experiment showed little visibility of modes 0, 1, and 4 at both the wavelength and cameras used from representative concentrations determined by curve fitting onto the rotorod data. A simulated experimental design might enhance buried modes by relocating cameras, increasing the number of cameras, or tuning the outgoing wavelength. To a certain extent, several wavelengths might be needed to improve the visibility of all modes of interest.

Reduction of sensitivity to atmospheric motion.

Reducing errors introduced by atmospheric motion is a priority to see within the plumes. Atmospheric motion influenced the collected data through both exposure time and disjointed timeframes (one timeframe for parallel polarization followed by another timeframe for perpendicular polarization, etc.). During EOPACE, exposure times of 300 seconds have smoothed out the plumes without reaching a complete stationary state over consecutive images of complementary polarization and exposure times of 5 seconds have sharpened the plumes without maintaining them over consecutive images of complementary polarization. This last issue can be solved either by increasing the pace at which images are captured or by implementing a dual-wavelength and dual-polarization instrument.

The first solution preserves the current collection sequence, but at a higher sampling rate. The success of this solution can be evaluated by determining an acceptable amount of atmospheric motion over the collection timeframe (which encompasses two consecutive images of complementary polarization) while maintaining a significant signal-to-noise ratio (which may motivate the integration of additional cameras) and by checking that the actual amount of motion is less than the one determined. A trade off exists between exposure-time and signal strength which may result in the use of a fast-scanning pencil laser-beam (Williams, 2000). Simulations can significantly help in assessing the functional relationship between atmospheric motion and errors in estimates.

The second solution consists in substantially redesigning both the transmitter and each receiver of the instrument. The transmitter allows two separate wavelengths to coexist in the same beam (one wavelength per linear polarization). Each receiver must contain two separate channels (one per transmitted wavelength), simultaneously capturing two images over the same exposure time (tricolor digital cameras are more common than bicolor ones – cf. model MS3100 by Duncan Technologies, Inc.). The estimator of Chapter 3 can be simply modified to accommodate for this new approach by expressing the bi-wavelength

polarization ratio. However, in-laboratory calibration is required which amalgamates all the cross-wavelength losses into one transmittance loss per camera and wavelength-pair (the two wavelengths likely differ in signal strengths, the retarder plate engenders losses, and the two CCD channels differ in losses).

To evaluate all these options, simulations should play a significant role in assessing their sensitivity as the estimation process is relatively non-trivial.

5.6 Conclusion

This document contains all the necessary tools (programs and equations) to establish an analytical baseline for further studies aimed at estimating aerosol characteristics via the polarization-ratio method. The method, supported by several originally derived equations, has proven to be successful for the first time through the consistency with which estimated concentrations agree with those estimated from alternative means.

However, further breakthrough opportunities do exist. Data analyses reveal that aerosol concentrations dominate above both ends of the surf zone, followed by its center, and decrease farther out toward the open ocean. The instrument needs to be modified to confirm the first location, in a subsequent experiment.

REFERENCES

Bard, Yonathan, 1974. *Nonlinear Parameter Estimation*, Academic Press, New York.

Bas, Christophe F., Kane, Timothy J., and Ruf, Christopher S., 1997. "Enhanced-Resolution Lidar," *Journal of the Optical Society of America A*, Vol. 14, No. 5, pp. 1044-1050.

Bevington, Philip R., and Robinson, D. Keith, 1992. *Data reduction and error analysis for the physical sciences*, Second Edition, McGraw-Hill, Inc., New York.

Bohren, Craig F., and Donald R. Huffman, 1983. *Absorption and Scattering of Light by Small Particles*, Wiley-Interscience Publication, John Wiley & Sons, New York, New York.

Bohren, Craig F., 1999. Personal communication.

Bohren, Craig F., 2002. Personal communication.

Calvez, Jean Pierre, 1990. *Spécification et Conception des Systèmes: Une Méthodologie*, Masson, Paris.

Chomka, Maria, and Patelski, Tomasz, 1997. "Sea Spray Emission Over the Coastal Zone," *Journal of Aerosol Science*, Vol. 28, Supplement 1, pp. S103-S104.

"Coastal cautions: Sea panel at work." *CNN Interactive*. 5 October 2001. Cable News Network. 5 October 2001 <http://www.cnn.com/2001/TECH/science/10/05/pew.oceans.commission.ap/index.html>.

Collis, R. T. H., and P. B. Russel, 1976. "Lidar Measurements of Particles and Gases by Elastic Backscattering and Differential Absorption," *Laser Monitoring of the Atmosphere*, Hinkley Editor, Springer-Verlag.

De leeuw, Gerritt, 1986. "Vertical Profiles of Giant Particles Close Above the Sea Surface," *Tellus, Ser. B*, Vol. 38, pp. 51-61.

De Leeuw, Gerrit, Neele, Filip P., Hill, Martin, Smith, Michael H., and Vignati, Elisabetta, 2000. "Production of sea spray aerosol in the surf zone," *Journal of Geophysical Research*, Vol. 105, No. D24, pp. 9,397-29,409.

Demmel, James W., 1988. "The probability That A Numerical Analysis Problem Is Difficult," *Mathematics of Computations*, Vol. 50, pp. 449-480.

Edelman, A., 1992. "On the distribution of a scaled condition number," *Math. Comp.*, vol. 58, pp. 185-190.

Fieller, E. C., 1932. "The Distribution of the Index in a Normal Bivariate Population," *Biometrika*, Vol. 24, pp. 428-440.

Gathman, Stuart G., 1983. "Optical Properties of the Marine Aerosol as Predicted by a BASIC Version of the NAVY Aerosol Model," *NRL Memorandum Report 5157*.

Gathman, Stuart G., 1989. "A Preliminary Description of NOVAM, the Navy Oceanic Vertical Aerosol Model," *NRL Memorandum Report 9200*.

Gathman, Stuart G., 1992. "Ocean Aerosol Measurements and Models in the Straits of Florida (The KEY-90 Experiment)", *SPIE Proceedings, Vol. 1688*, 21-23 April, pp. 2-13.

Gathman, Stuart G., and Kenneth L. Davidson, 1993. "The Navy Oceanic Vertical Aerosol Model," *NRaD Technical Report 1634*.

Gathman, Stuart G., and Smith, Michael H., 1997. "On the nature of surf generated aerosol and their effect on electro-optical systems," *Proceedings of SPIE*, Vol. 3125, pp. 2-13.

Gathman, Stuart G., and van Eijk, Alexander M. J., 1998. "Electro-optical propagation just above wave tops as predicted by ANAM, the Advanced Navy Aerosol Model", *RTA Conference*, Naples, Italy.

Goldberg, David E., 1989. *Genetic Algorithms in Search, Optimization, and Machine Learning*, Addison-Wesley Publishing Company, Inc., Reading, Massachusetts.

Grandqvist, C.G., and R.A. Buhrman, 1976. "Ultrafine metal particles," Journal of Applied Physics, Vol. 47, p. 2200.

Gustafsson, Mats E. R., and Franzén, Lars G., 1996. "Dry Deposition and Concentation of Marine Aerosols in a Coastal Area, SW Sweden," *Atmospheric Environment*, Vol. 30, No. 6, pp. 977-989.

Hooper, William P., and Martin, Lee U., 1999. "Scanning Lidar Measurements of Surf-Zone Aerosol Generation," *Optical Engineering*, Vol. 38, no. 2, pp. 250-255.

Huibers, Paul D. T., 1997. "Model for the wavelength dependence of the Index of refraction of water," *Applied Optics*, Vol. 36, No. 16, pp. 3785-3787.

Jacobson, Mark Z., 1999. *Fundamentals of atmospheric modeling*, Cambridge University press, Oxford.

Janesick, James R., Elliott, Tom, Collins, Stewart, Blouke, Morley M., and Freemand, Jack, 1987. "Scientific Charge Coupled Devices," *Optical Engineering*, Vol. 26, No. 8, pp. 692-714.

Kay, Steven M., 1993. *Fundamentals of Statistical Signal Processing: Estimation Theory*, Prentice Hall PTR, Upper Saddle River, New Jersey.

Kendall, Maurice G., and Stuart, Alan, 1967. *The Advanced Theory of Statistics*, Charles Griffin & Company Limited, London.

Kiser, Robert E., 1997. "The Generation and Characterization of Surf Zone Aerosols and Their Impact on Naval Electro-Optical Systems," M.S. Thesis, Naval Postgraduate School, Monterey, California.

Kraus, Eric B., and Businger, Joost A., 1994. *Atmosphere-ocean interaction*, 2nd ed., Oxford monographs on geology and geophysics, no. 27, Oxford University Press, New York.

Kunkel, K. E., Eloranta, E. W., and Shipley, S.T., 1977. "Lidar Observation of the Convective Boundary Layer," *Journal of Applied Meteorology*, Vol. 16, pp. 1306-1311.

Kumar, Susmit, Kurtz, Stewart K., and Cieplak, Marek, 1997. "Topological Disorder in Cellular Microstructures," *Phil. Mag.*, Vol. 75B, No.5, pp. 669-679.

Kurtz, Stewart K., Kumar, Susmit, Banavar, J. R., and Zhang, H., 1993. "Normal Grain Growth in Metals and Ceramics," *Modeling of Coarsening and Grain Growth*, C. S. Pande and S. P. Marsch Eds., pp. 165-182, Minerals, Metals and Materials Society, Warrendale, Pennsylvania.

Kurtz, Stewart K., and Carpey, F. M. A., 1980. "Microstructure and Normal Grain Growth in Metals and Ceramics, Parts I and II," *Journal of Applied Physics*, Vol. 51, pp. 5725-5754.

Kurtz, Stewart K., Philbrick, C. Russell, and Novitsky, Ed., 2002. Personal communication.

Marsaglia, George, 1965. "Ratios of Normal Variables and Ratios of Sum of Uniform Variables," *Journal of the American Statistical Association*, Vol. 60, March, pp. 193-204.

Mobley, Curtis D., 1994. *Light and Water: Radiative Transfer in Natural Waters,* Academic Press, Inc., Orlando, Florida.

Nahi, Nasser E., 1969. *Estimation Theory and Applications*, John Wiley and Sons, Inc., New York.

National Research Council (U.S.) Panel on Coastal Meteorology, *Coastal Meteorology: a review of the state of the science/ Panel on Coastal Meteorology, Committee on Meteorological Analysis, Prediction, and Research, Board on Atmospheric Sciences and Climate, Commission on Geosciences, Environment, and Resources, National Research Council*, Washington, D.C., National Academic Press, 1992.

Panin, G. N., Nasonov, A. E., Petelski, T., Raabe, A., and Schoenfeldt, H.-J., 1997. "Parameterization of the Surface Turbulent Fluxes in a Coastal Zone," *Journal of Aerosol Science*, Vol. 28, Supplement 1, pp. S39-S40.

Papoulis, Athanasios, 1991. *Probability, Random Variables, And Stochastic Processes*, 3rd ed., McGraw-Hill, Inc., New York.

Penndorf, Rudolf, 1957. "Tables of the Refractive Index for Standard Air and the Rayleigh Scattering Coefficient for the Spectral Region between 0.2 and 20.0 μ and Their Application to Atmospheric Optics," *Optical Society of America*, Vol. 47, No. 2, pp. 176-182.

Philbrick, C. Russell, 1997. Personal communication.

Philbrick, C. Russell, 2002. Personal communication.

Press, William H., Flannery, Brian P., Teukolsky, Saul A., and Vetterling, William T., 1992. *Numerical Recipies in C*, Cambridge University Press, Cambridge.

Prytherch, Huw, 1996. "Dark Signal Anomalies in the Kodak KAF 1300-L Charge Coupled Device," *Optical Engineering*, Vol. 35, No. 6, pp.1796-1798**.**

Quan, Xiaohong, and Fry, Edward S., 1995. "Empirical equation for the index of refraction of seawater," *Applied Optics*, Vol. 34, No. 18, pp. 3477-3480.

Roth, B., and Okada, K., 1997. "Study of the Modification of Sea-Salt Particles in the Coastal Atmosphere: Observation and Laboratory Experiments," *Journal of Aerosol Science*, Vol. 28, Supplement 1, pp. S9-S10.

Shettle, Eric P., and Fenn, Robert W., 1979. "Models for the Aerosols of the Lower Atmosphere and the Effects of Humidity Variations on Their Optical Properties," *AFGL-TR-79-0214, Environmental Research Paper No. 676, NTIS ADA 085951*.

Sinclair, David, and La Mer, Victor K., 1948. "Light Scattering As a Measure of Particle Size in Aerosols," *Symposium on Aerosols*, 113th National Meeting of the American Chemical Society, Chicago, IL, April 22nd.

Stevens, Timothy D., 1996. *"Bistatic Lidar Measurements of Lower Tropospheric Aerosols,"* Ph.D. Dissertation, The Pennsylvania State University.

Twomey, Sean, 1977. *Atmospheric Aerosols*, Elsevier Scientific Publishing Company.

van de Hulst, H. C., 1957. *Light Scattering by Small Particles*, Dover Publications, Inc., New York, New York.

Vignati, Elisabetta, de Leeuw, Gerrit, and Plate, Elke, 1997. "Coastal Aerosols,Air Mass History and Meteorological Conditiond," *Journal of Aerosol Science*, Vol. 28, Supplement 1, pp. S5-S6.

Williams, Earle R., 2000. Personal communication.

Zieliński , Andrzej, Piskozub, Jacek, and Zieliński, Tymon, 1994. "Lidar Method Investigations of Marine Aerosols," *Bulletin of the Polish Academy of Sciences, Earth Sciences*, Vol. 42, No. 1, pp. 77-88.

Zieliński, Andrzej, Zieliński, Tymon, and Piskozub, Jacek, 1997. "Aerosol Size Distribution Function in the Coastal Area," *Journal of Aerosol Science*, Vol. 28, Supplement 1, pp. S41-S42.

Zieliński, Tymon, Zieliński, Andrzej, Piskozub, Jacek, Drozdowska, Violetta, and Irczuk, Miroslaw, 1999. "Aerosol Optical Thickness Over the Coastal Area of the Southern Baltic Sea," *Optical Applicata,* Vol. 29, No. 4, pp. 439-447.

APPENDIX A

BEST FIT ON ROTOROD DATA

The present appendix contains computer programs and results to which they have contributed. The programs included below are key functions to complete the best-fits onto the rotorod data toward the estimation of the lognormal concentrations for modes 0 through 4 of HCAM. Results are displayed in Tables A.1, A.2, and A.3, each of which corresponds to different relative humidity conditions.

Computer programs

The function lognormal.m returns concentrations at each radius of interest from shape-parameters. The function RSmf.m translates NOVAM parameters into those of HCAM. The function Refraction-Growth.m centralizes the computation of the indices of refraction. The functions SeaRefractiveIndex.m and ErrorRealm.m estimate the complex index of refraction for mode 4.

```
function DNovDA=lognormal(N0,A0,S0,R)
% LOGNORMAL:                                              (Bas Oct. 1999)
%  Generation of the distribution of particles as a function of its
%  parameters: Number density per unit radius (N0 [(#/cm^3)/um]), the
%  mode radius (A0, [um]), and widths (S0). R is the vector at which
%  the function is evaluated.
% SYNTAX:
%  f=lognormal(N0,A0,S0,R)
DNovDA=N0*exp(-(log(R/A0)).^2/(2*S0^2))./(R*S0*sqrt(2*pi));


function [R,S,m,f]=RSmf(Mode,RH)
% RSMF:                                                   (Bas Oct. 1999)
%  This function generates the appropriate NOVAM parameters (R,C,m,f)
% translated into our lognormal parameters (R,S,m,f) except its magni-
% tude.  Inputs are the aerosol Mode (-1...3) and Relative Humidity
% (RH: %). (cf. Research Notebook IV p. 70 for details of conversion).
% m is the complex index of refraction and f is the growth factor.
% Molecular characteristics are added under mode -1.
%  Motivation for this function is the magnitude-independent lognormal
% curve to generate the accurate van de Hulst's F-functions at a given
% relative humidity, according to the aerosol model.
% SYNTAX:
%  [R,S,m,f]=RSmf(Mode,RH)

if Mode==-1
   %-----------------------------------------
   % Molecular Component:
   %-----------------------------------------
   R=0.2e-3;      % Median radius in um
   S=NaN;         % Distribution is Kronecker delta
```

```
   m=1.36;
   f=1;
elseif Mode==0
   %-----------------------------------------
   % Non-soluble dust.  Volz: mixture of different soil minerals
   % and fly ashes with traces of soot and carbon particles (p.74).
   %-----------------------------------------
   % In NOVAM's lognormal terms
   C0=1; R0=0.03; % radius in um
   % Influence of relative humidity on index of refraction and growth
   % and conversion from NOVAM to statistical log-normal:
   [m,f]=RefractionGrowth(0,RH);
   R=R0*f; C=C0;  S=1/sqrt(2*C);
elseif Mode==1
   %-----------------------------------------
   % Water-soluble. Volz: mixture of ammonium and calcium sulfate
   % and organic compounds (p. 755).
   %-----------------------------------------
   % In NOVAM's lognormal terms
   C1=1; R1=0.03; % radius in um at 80% RH
   % Influence of relative humidity on index of refraction and growth
   % and conversion from NOVAM to statistical log-normal:
   [m,f]=RefractionGrowth(1,RH);
   R=R1*f; C=C1;  S=1/sqrt(2*C);
elseif Mode==2
   %-----------------------------------------
   % Soluble: Sea-salt and water
   %-----------------------------------------
   % In NOVAM's lognormal terms
   C2=1; R2=0.24; % radius in um at 80% RH
   % Influence of relative humidity on index of refraction and growth
   % and conversion from NOVAM to statistical log-normal:
   [m,f]=RefractionGrowth(2,RH);
   R=R2*f; C=C2;  S=1/sqrt(2*C);
elseif Mode==3
   %-----------------------------------------
   % Soluble: Sea-salt and water
   %-----------------------------------------
   % In NOVAM's lognormal terms
   C3=1; R3=2;    % radius in um at 80% RH
   % Influence of relative humidity on index of refraction and growth
   % and conversion from NOVAM to statistical log-normal:
   [m,f]=RefractionGrowth(3,RH);
   R=R3*f; C=C3;  S=1/sqrt(2*C);
elseif Mode==4
   %-----------------------------------------
   % Soluble: Sea-salt and water ejected by surf!
   %-----------------------------------------
   % In NOVAM's lognormal terms
   C4=5; R4=15;   % radius in um at 80% RH
   % Influence of relative humidity on index of refraction and growth
   % and conversion from NOVAM to statistical log-normal:
   [m,f]=RefractionGrowth(4,RH);
   R=R4; C=C4;    S=1/sqrt(2*C);
end
```

```
function [m,f]=RefractionGrowth(Mode,RH)
% REFRACTIONGROWTH:                                    (Bas Oct. 1999)
%   This function returns the value of the index of refraction
%  and the growth factor both influenced by Relative Humidity
%  (in [%]) for requested Mode ({0,1,2,3}).
% SYNTAX:
%   [m,f]=RefractionGrowth(Mode,RH)

%-- Indices of refraction --
m_dust=1.53-i*8e-3;           % at 0.5145 um
m_soluble=1.53-i*5e-3;        % at 0.5145 um
m_salt=1.5-i*1e-8;            % at 0.5145 um
m_water=1.334-i*1.18e-9;      % at 0.5145 um

%-- Matching Mode at requested RH
if Mode==0
   % Mode # 0: Dust
   f=1; % i.e., no change for this non-hygroscopic aerosol
   m=m_dust;
elseif Mode==1
   % Mode # 1: Soluble Aerosols
   f=((1.17-RH/100)/(1.87*(1-RH/100)))^(1/3);
   f0=(1.17/1.87)^(1/3);
   % Index of refraction
   m=m_water+(m_soluble-m_water)*(f0/f)^3;
elseif Mode==2
   % Mode # 2: Salted-Water Aerosols
   f=((1.83-RH/100)/(5.13*(1-RH/100)))^(1/3);
   f0=(1.83/5.13)^(1/3);
   % Index of refraction
   m=m_water+(m_salt-m_water)*(f0/f)^3;
elseif Mode==3
   % Mode # 3: Salted-Water Aerosols
   f=((1.97-RH/100)/(5.83*(1-RH/100)))^(1/3);
   f0=(1.97/5.83)^(1/3);
   % Index of refraction
   m=m_water+(m_salt-m_water)*(f0/f)^3;
elseif Mode==4
   % Mode # 4: Freshly ejected Salted-Water Aerosols
   S=RH(1); % Salinity [o/oo]
   T=RH(2); % Temperature [C]
   Lambda=RH(3); % Wavelength [nm]
   % Real part of the index of refraction
   Rem=SeaRefractiveIndex(S,T,Lambda);
   % Calling the routine to explore the proportionality
   f=fmin('ErrorRealm',0,1,[],m_water,m_salt,Rem);
   % Final value of the index of refraction
   m=m_water+(m_salt-m_water)*f;
else
   error(['Mode ' num2str(Mode) ' not defined!']);
end
```

```
function z=SeaRefractiveIndex(S,T,lambda)
% SEAREFRACTIVEINDEX:                                    (Bas May 1998)
%  This function returns the value of the refractive index of seawater
% at a given temperature (0<T<30 degrees C), salinity (0<S<35 per
% thousand), and incident wavelength (200<lambda<1100 nm).  The size of
% the result is a matrix of dimension equal to length(S) x length(T) x
% length(lambda).  Input parameters can only be vectors.
% SYNTAX:
%   z=SeaRefractiveIndex(S,T,lambda)
% AUTHORS:
%   Equation: Quan and Fry, with additional check by Huibers.

[iS,jS]=size(S);[iT,jT]=size(T);[iL,jL]=size(lambda);
if ~(iS==1 | jS==1) | ~(iT==1 | jT==1) ~(iL==1 | jL==1)
   error('S, T, and lambda must be vectors!');
elseif min(S)<0 | max(S)>35
   error('S is out its valid domain.')
elseif min(T)<0 | max(T)>30
   error('T is out its valid domain.')
elseif min(lambda)<200 | max(lambda)>1100
   error('Lambda is out its valid domain.')
end
[S,T,lambda]=meshgrid(S,T,lambda);
%z=zeros(max(iS,jS),max(iT,jT),max(iL,jL));
z1=1.31405;
z2=(1.779e-4-1.05e-6*T+1.6e-8*T.^2).*S;
z3=-2.02e-6*T.^2;
z4=(15.868+0.01155*S-0.00423*T)./lambda;
z5=-4382*ones(size(lambda))./(lambda.^2);
z6=1.1455e6*ones(size(lambda))./(lambda.^3);
z=z1+z2+z3+z4+z5+z6;


function AbsError=ErrorRealm(f,m_water,m_salt,Rem);
% ERRORREALM:                                            (Bas Nov. 1999)
%  Recursively determines the proportionality factor which
%  minimizes the error between the (real) index of refraction
%  of Quan and Fry, and Huibers (see SeaRefractiveIndex.m)
%  and the real part of the index of refraction determined by
%  proportion of salt and water.
% SYNTAX:
%  AbsError=ErrorRealm(f,m_water,m_salt,RealmFromQuanFryHuibers);

% Index of refraction from proportion
m=m_water+(m_salt-m_water)*f;

% Error
AbsError=abs(Rem-real(m));
```

Best-fit results of the HCAM lognormal model (less mode -1) onto the rotorod data

Table A.1. Estimated concentrations from fitting the HCAM model (modes 0 through 4) onto the rotorod data when relative humidity is the arithmetic mean of those measured by both the NRaD and the SIO sensors. Calculated indices of refraction, *m*, via Eq. (2.3) are also tabulated (rounded for display purpose).

Filename (Error Fit)	**HCAM Parameters**	**Mode (*j*)**				
		***j*=0**	***j*=1**	***j*=2**	***j*=3**	***j*=4**
A04d21h30.txt (6.7196)	m	1.53 -i 0.008	1.4814 -i 0.0038	1.4158 -i 5.53×10^{-9}	1.4124 -i 5.35×10^{-9}	1.3424 -i 1.63×10^{-9}
	$a_{0,j}$ (μm)	0.03	0.0282143	0.215472	1.78862	15
	$\sigma_{0,j}$	0.70711	0.70711	0.70711	0.70711	0.31623
	$n_{0,j}$ (cm^{-3})	1.702×10^{-4}	1.354×10^{-4}	39.82	3.912	1.000×10^{-15}
A05d21h00.txt (3.8976)	m	1.53 -i 0.008	1.4917 -i 0.0040	1.4284 -i 6.20×10^{-9}	1.425 -i 6.02×10^{-9}	1.3424 -i 1.62×10^{-9}
	$a_{0,j}$ (μm)	0.03	0.0275899	0.205474	1.70209	15
	$\sigma_{0,j}$	0.70711	0.70711	0.70711	0.70711	0.31623
	$n_{0,j}$ (cm^{-3})	1.066×10^{-4}	0.902×10^{-4}	38.060	0.266	1.000×10^{-15}
A05d21h30.txt (4.1827)	m	1.53 -i 0.008	1.4917 -i 0.0040	1.4284 -i 6.20×10^{-9}	1.425 -i 6.02×10^{-9}	1.3424 -i 1.62×10^{-9}
	$a_{0,j}$ (μm)	0.03	0.0275899	0.205474	1.70209	15
	$\sigma_{0,j}$	0.70711	0.70711	0.70711	0.70711	0.31623
	$n_{0,j}$ (cm^{-3})	0.433×10^{-4}	0.299×10^{-4}	41.41	0.2221	1.000×10^{-15}
A05d22h00.txt (3.5328)	m	1.53 -i 0.008	1.4917 -i 0.0040	1.4284 -i 6.20×10^{-9}	1.425 -i 6.02×10^{-9}	1.3424 -i 1.62×10^{-9}
	$a_{0,j}$ (μm)	0.03	0.0275899	0.205474	1.70209	15
	$\sigma_{0,j}$	0.70711	0.70711	0.70711	0.70711	0.31623
	$n_{0,j}$ (cm^{-3})	0.621×10^{-4}	0.195×10^{-5}	37.38	0.2462	1.000×10^{-15}
A08d20h30.txt (2.9959)	m	1.53 -i 0.008	1.4644 -i 0.0033	1.3986 -i 4.61×10^{-9}	1.3953 -i 4.44×10^{-9}	1.3424 -i 1.62×10^{-9}
	$a_{0,j}$ (μm)	0.03	0.0293939	0.233186	1.94115	15
	$\sigma_{0,j}$	0.70711	0.70711	0.70711	0.70711	0.31623
	$n_{0,j}$ (cm^{-3})	0.440×10^{-4}	1.829×10^{-4}	20.24	1.2260	1.000×10^{-15}
A08d21h00.txt (2.7612)	m	1.53 -i 0.008	1.4644 -i 0.0033	1.3986 -i 4.61×10^{-9}	1.3953 -i 4.44×10^{-9}	1.3424 -i 1.62×10^{-9}
	$a_{0,j}$ (μm)	0.03	0.0293939	0.233186	1.94115	15
	$\sigma_{0,j}$	0.70711	0.70711	0.70711	0.70711	0.31623
	$n_{0,j}$ (cm^{-3})	3.730×10^{-4}	4.77×10^{-4}	20.34	1.1550	1.000×10^{-15}

Table A.2. Estimated concentrations from fitting the HCAM model (modes 0 through 4) onto the rotorod data when relative humidity is measured by the NRaD sensor. Calculated indices of refraction, *m*, via Eq. (2.3) are also tabulated (rounded for display purpose).

Filename (Error Fit)	**HCAM Parameters**	**Mode (*j*)**				
		***j*=0**	***j*=1**	***j*=2**	***j*=3**	***j*=4**
A04d21h30.txt (6.7838)	m	1.53 -i 0.008	1.4802 -i 0.0037	1.4145 -i 5.45×10^{-9}	1.4111 -i 5.27×10^{-9}	1.3424 -i 1.63×10^{-9}
	$a_{0,j}$ (μm)	0.03	0.0282927	0.216694	1.79916	15
	$\sigma_{0,j}$	0.70711	0.70711	0.70711	0.70711	0.31623
	$n_{0,j}$ (cm^{-3})	2.022×10^{-4}	2.584×10^{-4}	39.730	3.8640	1.000×10^{-15}
A05d21h00.txt (3.8996)	m	1.53 -i 0.008	1.4915 -i 0.0040	1.4282 -i 6.18×10^{-9}	1.4248 -i 6.01×10^{-9}	1.3424 -i 1.62×10^{-9}
	$a_{0,j}$ (μm)	0.03	0.0275976	0.205601	1.70319	15
	$\sigma_{0,j}$	0.70711	0.70711	0.70711	0.70711	0.31623
	$n_{0,j}$ (cm^{-3})	0.115×10^{-4}	0.747×10^{-5}	38.03	0.2652	1.000×10^{-15}
A05d21h30.txt (4.1845)	m	1.53 -i 0.008	1.4915 -i 0.0040	1.4282 -i 6.18×10^{-9}	1.4248 -i 6.01×10^{-9}	1.3424 -i 1.62×10^{-9}
	$a_{0,j}$ (μm)	0.03	0.0275976	0.205601	1.70319	15
	$\sigma_{0,j}$	0.70711	0.70711	0.70711	0.70711	0.31623
	$n_{0,j}$ (cm^{-3})	0.487×10^{-4}	0.725×10^{-5}	41.38	0.2217	1.000×10^{-15}
A05d22h00.txt (3.5342)	m	1.53 -i 0.008	1.4915 -i 0.0040	1.4282 -i 6.18×10^{-9}	1.4248 -i 6.01×10^{-9}	1.3424 -i 1.62×10^{-9}
	$a_{0,j}$ (μm)	0.03	0.0275976	0.205601	1.70319	15
	$\sigma_{0,j}$	0.70711	0.70711	0.70711	0.70711	0.31623
	$n_{0,j}$ (cm^{-3})	0.202×10^{-4}	0.136×10^{-5}	37.35	0.2458	1.000×10^{-15}
A08d20h30.txt (3.0505)	m	1.53 -i 0.008	1.4628 -i 0.0033	1.3972 -i 4.54×10^{-9}	1.3940 -i 4.37×10^{-9}	1.3424 -i 1.62×10^{-9}
	$a_{0,j}$ (μm)	0.03	0.0295098	0.234859	1.95551	15
	$\sigma_{0,j}$	0.70711	0.70711	0.70711	0.70711	0.31623
	$n_{0,j}$ (cm^{-3})	1.102×10^{-4}	5.344×10^{-4}	20.18	1.2070	1.000×10^{-15}
A08d21h00.txt (2.8011)	m	1.53 -i 0.008	1.4628 -i 0.0033	1.3972 -i 4.54×10^{-9}	1.3940 -i 4.37×10^{-9}	1.3424 -i 1.62×10^{-9}
	$a_{0,j}$ (μm)	0.03	0.0295098	0.234859	1.95551	15
	$\sigma_{0,j}$	0.70711	0.70711	0.70711	0.70711	0.31623
	$n_{0,j}$ (cm^{-3})	2.851×10^{-4}	2.879×10^{-4}	20.26	1.1390	1.000×10^{-15}

Table A.3. Estimated concentrations from fitting the HCAM model (modes 0 through 4) onto the rotorod data when relative humidity is measured by the SIO sensor. Calculated indices of refraction, *m*, via Eq. (2.3) are also tabulated (rounded for display purpose).

Filename (Error Fit)	**HCAM parameters**	**Mode (*j*)**				
		***j*=0**	***j*=1**	***j*=2**	***j*=3**	***j*=4**
A04d21h30.txt (6.6579)	m	1.53 -i 0.008	1.4826 -i 0.0038	1.4172 -i 5.6×10^{-9}	1.4138 -i 5.42×10^{-9}	1.3424 -i 1.63×10^{-9}
	$a_{0,j}$ (μm)	0.03	0.028139	0.214292	1.77842	15
	$\sigma_{0,j}$	0.70711	0.70711	0.70711	0.70711	0.31623
	$n_{0,j}$ (cm^{-3})	1.333×10^{-4}	2.935×10^{-4}	39.91	3.959	1.000×10^{-15}
A05d21h00.txt (3.8957)	m	1.53 -i 0.008	1.4918 -i 0.0040	1.4285 -i 6.20×10^{-9}	1.4252 -i 6.02×10^{-9}	1.3424 -i 1.62×10^{-9}
	$a_{0,j}$ (μm)	0.03	0.0275822	0.205348	1.701	15
	$\sigma_{0,j}$	0.70711	0.70711	0.70711	0.70711	0.31623
	$n_{0,j}$ (cm^{-3})	0.876×10^{-4}	0.335×10^{-4}	38.08	0.266	1.000×10^{-15}
A05d21h30.txt (4.1809)	m	1.53 -i 0.008	1.4918 -i 0.0040	1.4285 -i 6.20×10^{-9}	1.4252 -i 6.02×10^{-9}	1.3424 -i 1.62×10^{-9}
	$a_{0,j}$ (μm)	0.03	0.0275822	0.205348	1.701	15
	$\sigma_{0,j}$	0.70711	0.70711	0.70711	0.70711	0.31623
	$n_{0,j}$ (cm^{-3})	0.470×10^{-4}	0.333×10^{-4}	41.44	0.2225	1.000×10^{-15}
A05d22h00.txt (3.5314)	m	1.53 -i 0.008	1.4918 -i 0.0040	1.4285 -i 6.20×10^{-9}	1.4252 -i 6.02×10^{-9}	1.3424 -i 1.62×10^{-9}
	$a_{0,j}$ (μm)	0.03	0.0275822	0.205348	1.701	15
	$\sigma_{0,j}$	0.70711	0.70711	0.70711	0.70711	0.31623
	$n_{0,j}$ (cm^{-3})	3.235×10^{-6}	3.211×10^{-4}	37.41	0.2466	1.000×10^{-15}
A08d20h30.txt (2.9436)	m	1.53 -i 0.008	1.4659 -i 0.0034	1.4 -i 4.68×10^{-9}	1.3967 -i 4.51×10^{-9}	1.3424 -i 1.62×10^{-9}
	$a_{0,j}$ (μm)	0.03	0.0292832	0.231578	1.92734	15
	$\sigma_{0,j}$	0.70711	0.70711	0.70711	0.70711	0.31623
	$n_{0,j}$ (cm^{-3})	9.472×10^{-4}	0.183×10^{-4}	20.29	1.2450	1.000×10^{-15}
A08d21h00.txt (2.7229)	m	1.53 -i 0.008	1.4659 -i 0.0034	1.4 -i 4.68×10^{-9}	1.3967 -i 4.51×10^{-9}	1.3424 -i 1.62×10^{-9}
	$a_{0,j}$ (μm)	0.03	0.0292832	0.231578	1.92734	15
	$\sigma_{0,j}$	0.70711	0.70711	0.70711	0.70711	0.31623
	$n_{0,j}$ (cm^{-3})	4.031×10^{-4}	4.380×10^{-4}	20.42	1.1710	1.000×10^{-15}

APPENDIX B

MODIFIED VERSION OF THE CALLBH.F PROGRAM FROM BOHREN AND HUFFMAN (1983)

The original program has been adapted to be directly interfaced with MATLAB both by including and merging the gateway headers and footers unique to each platform (this results in two programs: one for compilation on the Windows platform and the other one on SUN Solaris workstation).

BMIE.F on Windows platform:

```
C  ------------------------------------------------------------
C  BMIE:
C     Gateway to a modified-version of the program in Bohren and Huf-
C    fman, Absorption and Scattering of Light by small particles,
C    John Wiley and Sons, Inc., 1983, for spherical scattering.
C    Modifications include: (1) interface for direct-access from
C    within MATLAB (via MEX-DLL calls), (2) removal of parameters
C    requiring recompilation of the program for each run, and (3)
C    removal of the features to use the symmetry in the scattering
C    angles.
C     Present version allows submission of: (1) the size-parameter
C    (X=2*pi*radius/Lambda), (2) the relative refractive index (m)
C    (whose values are the complex-conjugate of the one used in the
C    MieS1S2*.m programs), and (3) a row-vector of scattering-angles
C    in radians.
C     Generated by the program are: (1) I1=S1*conj(S1), (2) I2=S2*
C    conj(S2), (3) Qext(inction), and (4) Qsca(ttering).
C  SYNTAX:
C    [I1,I2,QEXT,QSCA]=BMIE(X,Re(m),Im(m),ThetaS);
C  F.Y.I.:
C    Bohren and Huffman for the original BHMIE subroutine:
C      - Scattering and Absorption of light by small particles
C      - John Wiley and Sons, Inc., 1983.
C    Christophe Bas for interface and modifications:
C      - Thesis, Nov. 1999.
C  ------------------------------------------------------------
C  This code includes the FORTRAN-interface for a .MEX file to
C  MATLAB.  This subroutine includes the main gateway to MATLAB
C  developed by The MathWorks, Inc., for $Revision: 1.5 $.
C  ------------------------------------------------------------
      SUBROUTINE MEXFUNCTION(NLHS, PLHS, NRHS, PRHS)

C  ------------------------------------------------------------
C  This is the point of entry into the Fortran code from MATLAB.
C  (integer) Replace integer by integer*8 on the DEC Alpha and the
C  SGI 64-bit platforms
C  ------------------------------------------------------------
      INTEGER PLHS(*), PRHS(*)
      INTEGER NLHS, NRHS
```

```
      INTEGER MXCREATEFULL, MXGETPR
      INTEGER MXGETM, MXGETN

C  -----------------------------------------------------------------
C  DECLARATION OF IN/OUT POINTERS AND LOCAL SIZE VARIABLES
C  -----------------------------------------------------------------
      INTEGER I1P, I2P, QEXTP, QSCAP, XP, RMP, IMP, THETAP
      INTEGER MX, NX, MRM, NRM, MIM, NIM, MT, NT, SIZE

C  -----------------------------------------------------------------
C  CHECK FOR PROPER NUMBER OF ARGUMENTS
C  -----------------------------------------------------------------
      IF (NRHS .NE. 4) THEN
        CALL MEXERRMSGTXT('BMIE inputs: X, Re(m), Im(m), and Theta.')
      ELSEIF (NLHS .NE. 4) THEN
        CALL MEXERRMSGTXT('BMIE outputs: I1, I2, Qext, and Qsca.')
      ENDIF

C  -----------------------------------------------------------------
C  CHECK THE DIMENSIONS OF INPUT PARAMETER X.
C  -----------------------------------------------------------------
      MX = MXGETM(PRHS(1))
      NX = MXGETN(PRHS(1))
      IF (MAX(MX,NX) .NE. 1) THEN
        CALL MEXERRMSGTXT('BMIE input X must be a real scalar.')
      ENDIF

C  -----------------------------------------------------------------
C  CHECK THE DIMENSIONS OF INPUT PARAMETER Re(m).
C  -----------------------------------------------------------------
      MRM = MXGETM(PRHS(2))
      NRM = MXGETN(PRHS(2))
      IF (MAX(MRM,NRM) .NE. 1) THEN
        CALL MEXERRMSGTXT('BMIE input Re(m) must be a real scalar.')
      ENDIF

C  -----------------------------------------------------------------
C  CHECK THE DIMENSIONS OF INPUT PARAMETER Im(m).
C  -----------------------------------------------------------------
      MIM = MXGETM(PRHS(3))
      NIM = MXGETN(PRHS(3))
      IF (MAX(MIM,NIM) .NE. 1) THEN
        CALL MEXERRMSGTXT('BMIE input Im(m) must be a real scalar.')
      ENDIF

C  -----------------------------------------------------------------
C  CHECK THE DIMENSIONS OF INPUT PARAMETER THETA.
C  -----------------------------------------------------------------
      MT = MXGETM(PRHS(4))
      NT = MXGETN(PRHS(4))
      IF ((MAX(MT,NT) .GT. 1000) .OR. (MIN(MT,NT) .GT. 1)) THEN
        CALL MEXERRMSGTXT('BMIE input ThetaS <1000 scalar points.')
      ENDIF
      SIZE = MT*NT

C  -----------------------------------------------------------------
```

```
C  CREATE A MATRIX FOR RETURN ARGUMENT
C  ----------------------------------------------------------------
      PLHS(1) = MXCREATEFULL(MT,NT,0)
      PLHS(2) = MXCREATEFULL(MT,NT,0)
      PLHS(3) = MXCREATEFULL(1,1,0)
      PLHS(4) = MXCREATEFULL(1,1,0)

C  ----------------------------------------------------------------
C  ASSIGN POINTERS TO THE VARIOUS PARAMETERS
C  ----------------------------------------------------------------
      I1P = MXGETPR(PLHS(1))
      I2P = MXGETPR(PLHS(2))
      QEXTP = MXGETPR(PLHS(3))
      QSCAP = MXGETPR(PLHS(4))
      XP = MXGETPR(PRHS(1))
      RMP = MXGETPR(PRHS(2))
      IMP = MXGETPR(PRHS(3))
      THETAP = MXGETPR(PRHS(4))

C  ----------------------------------------------------------------
C  DO THE ACTUAL COMPUTATIONS IN THE BHMIE SUBROUTINE.
C  ----------------------------------------------------------------
      CALL BHMIE(%VAL(XP),%VAL(RMP),%VAL(IMP),%VAL(THETAP),
     1%VAL(I1P),%VAL(I2P),%VAL(QEXTP),%VAL(QSCAP),SIZE)

C  ----------------------------------------------------------------
C  DONE.
C  ----------------------------------------------------------------
      RETURN
      END

C  ----------------------------------------------------------------
C  SUBROUTINE BHMIE CALCULATES AMPLITUDE SCATTERING MATRIX ELEMENTS
C  AND EFFICIENCIES FOR EXTINCTION, TOTAL SCATTERING AND BACKSCAT-
C  TERING FOR A GIVEN SIZE PARAMETER AND RELATIVE REFRACTIVE INDEX.
C  ----------------------------------------------------------------
      SUBROUTINE BHMIE(X,REFRE,REFIM,THETA,I1,I2,QEXT,QSCA,SIZE)

      REAL*8 X, REFRE, REFIM, THETA(1000), I1(1000), I2(1000)
      REAL*8 QEXT, QSCA
      DIMENSION AMU(1000), PI(1000), TAU(1000), PI0(1000), PI1(1000)
      COMPLEX D(5000), Y, REFREL, XI, XI0, XI1, AN, BN
      COMPLEX S1(2000), S2(2000)
      DOUBLE PRECISION PSI0, PSI1, PSI, DN, DX
      INTEGER SIZE

      REFREL=CMPLX(REFRE,REFIM)
      DX=X
      Y=X*REFREL
C  ----------------------------------------------------------------
C  SERIES TERMINATED AFTER NSTOP TERMS
C  ----------------------------------------------------------------
      XSTOP=X+4.05*X**.3333+2.0
      IF (X .GT. 5000.0) THEN
        CALL MEXERRMSGTXT('BHMIE is limited to 5000 terms for D().')
      END IF
```

```
      NSTOP=XSTOP
      YMOD=CABS(Y)
      NMX=AMAX1(XSTOP,YMOD)+15
C  ---------------------------------------------------------------------
C  LOGARITHMIC DERIVATIVE D(J) CALCULATED BY DOWNWARD RECURRENCE
C  BEGINNING WITH INITIAL VALUE 0.0 + i * 0.0 AT J=NMX
C  ---------------------------------------------------------------------
      D(NMX)=CMPLX(0.0,0.0)
      NN=NMX-1
      DO 120 N=1,NN
      RN=NMX-N+1
  120 D(NMX-N)=(RN/Y)-(1./(D(NMX-N+1)+RN/Y))
      DO 777 J=1,SIZE
      AMU(J)=COS(THETA(J))
      PI0(J)=0.0
      PI1(J)=1.0
      S1(J)=CMPLX(0.0,0.0)
  777 S2(J)=CMPLX(0.0,0.0)
C  ---------------------------------------------------------------------
C  RICATTI-BESSEL FUNCTIONS WITH REAL ARGUMENT X CALCULATED BY
C  UPWARD RECURRENCE
C  ---------------------------------------------------------------------
      PSI0=DCOS(DX)
      PSI1=DSIN(DX)
      CHI0=-SIN(X)
      CHI1=COS(X)
      APSI0=PSI0
      APSI1=PSI1
      XI0=CMPLX(APSI0,-CHI0)
      XI1=CMPLX(APSI1,-CHI1)
      QSCA=0.0
      N=1
  200 DN=N
      RN=N
      FN=(2*RN+1.)/(RN*(RN+1.))
      PSI=(2*DN-1.)*PSI1/DX-PSI0
      APSI=PSI
      CHI=(2.*RN-1.)*CHI1/X-CHI0
      XI=CMPLX(APSI,-CHI)
      AN=(D(N)/REFREL+RN/X)*APSI-APSI1
      AN=AN/((D(N)/REFREL+RN/X)*XI-XI1)
      BN=(REFREL*D(N)+RN/X)*APSI-APSI1
      BN=BN/((REFREL*D(N)+RN/X)*XI-XI1)
      QSCA=QSCA+(2.*RN+1.)*(CABS(AN)*CABS(AN)+CABS(BN)*CABS(BN))
      DO 789 J=1,SIZE
      PI(J)=PI1(J)
      TAU(J)=RN*AMU(J)*PI(J)-(RN+1.)*PI0(J)
      S1(J)=S1(J)+FN*(AN*PI(J)+BN*TAU(J))
      S2(J)=S2(J)+FN*(AN*TAU(J)+BN*PI(J))
  789 CONTINUE
      PSI0=PSI1
      PSI1=PSI
      APSI1=PSI1
      CHI0=CHI1
      CHI1=CHI
      XI1=CMPLX(APSI1,-CHI1)
```

```
      N=N+1
      RN=N
      DO 999 J=1,SIZE
      PI1(J)=((2.*RN-1.)/(RN-1.))*AMU(J)*PI(J)
      PI1(J)=PI1(J)-RN*PI0(J)/(RN-1.)
  999 PI0(J)=PI(J)
      IF(N-1-NSTOP) 200,300,300
  300 QSCA=(2./(X*X))*QSCA
      QEXT=(4./(X*X))*REAL(S1(1))
C  -------------------------------------------------------------------
C  NEITHER S1 NOR S2 ARE NEEDED, BUT THEIR MAGNITUDES ARE.  THIS
C  REDUCES THE SIZE OF THE ARGUMENTS TO PASS AND SAVE.
C  -------------------------------------------------------------------
      DO 400 J=1,SIZE
      I1(J)=(CABS(S1(J))*CABS(S1(J)))
      I2(J)=(CABS(S2(J))*CABS(S2(J)))
  400 CONTINUE
      RETURN
      END
```

BMIE.F on SUN-Solaris Platform:

```
#include <fintrf.h>
C  -------------------------------------------------------------------
C       MIE scattering program ready to be mex-compiled within MATLAB
C        5.3.X on a SUN Sparc Solaris 2.6 platform.  This file shall
C        be compiled as follows if one has the GNU f77 (i.e., g77)
C        Fortran compiler which is NOT supported by MATLAB:
C        >> mex Bmie.F -f g77opts.sh
C        where g77opts.sh is a mex-option file provided in the current
C        directory.
C  -------------------------------------------------------------------
C  BMIE:
C     Gateway to a modified-version of the program in Bohren and Huf-
C    fman, Absorption and Scattering of Light by small particles,
C    John Wiley and Sons, Inc., 1983, for spherical scattering.
C    Modifications include: (1) interface for direct-access from
C    within MATLAB (via MEX-SH calls), (2) removal of parameters
C    requiring recompilation of the program for each run, and (3)
C    removal of the features to use the symmetry in the scattering
C    angles.
C     Present version allows submission of: (1) the size-parameter
C    (X=2*pi*radius/Lambda), (2) the relative refractive index (m)
C    (whose values are the complex-conjugate of the one used in the
C    MieS1S2*.m programs), and (3) a row-vector of scattering-angles
C    in radians.
C     Generated by the program are: (1) I1=S1*conj(S1), (2) I2=S2*
C    conj(S2), (3) Qext(inction), and (4) Qsca(ttering).
C  SYNTAX:
C    [I1,I2,QEXT,QSCA]=BMIE(X,Re(m),Im(m),ThetaS);
C  F.Y.I.:
C    Bohren and Huffman for the original BHMIE subroutine:
C      - Scattering and Absorption of light by small particles
C      - John Wiley and Sons, Inc., 1983.
C    Christophe Bas for interface and modifications:
C      - Thesis, Dec. 1999.
```

```
C  ------------------------------------------------------------------
C  This code includes the FORTRAN-interface for a .MEX file to
C  MATLAB.  This subroutine includes the main gateway to MATLAB
C  developed by The MathWorks, Inc., for $Revision: 1.5 $.
C  ------------------------------------------------------------------
      SUBROUTINE MEXFUNCTION(NLHS, PLHS, NRHS, PRHS)

C  ------------------------------------------------------------------
C  This is the point of entry into the Fortran code from MATLAB.
C  (integer) Replace integer by integer*8 on the DEC Alpha and the
C  SGI 64-bit platforms
C  ------------------------------------------------------------------
      MWPOINTER PLHS(*), PRHS(*)
      INTEGER NLHS, NRHS
      MWPOINTER MXCREATEFULL, MXGETPR
      INTEGER MXGETM, MXGETN

C  ------------------------------------------------------------------
C  DECLARATION OF IN/OUT POINTERS AND LOCAL SIZE VARIABLES
C  ------------------------------------------------------------------
      MWPOINTER I1P, I2P, QEXTP, QSCAP, XP, RMP, IMP, THETAP
      INTEGER MX, NX, MRM, NRM, MIM, NIM, MT, NT, SIZE

C  ------------------------------------------------------------------
C  CHECK FOR PROPER NUMBER OF ARGUMENTS
C  ------------------------------------------------------------------
      IF (NRHS .NE. 4) THEN
        CALL MEXERRMSGTXT('BMIE inputs: X, Re(m), Im(m), and Theta.')
      ELSEIF (NLHS .NE. 4) THEN
        CALL MEXERRMSGTXT('BMIE outputs: I1, I2, Qext, and Qsca.')
      ENDIF

C  ------------------------------------------------------------------
C  CHECK THE DIMENSIONS OF INPUT PARAMETER X.
C  ------------------------------------------------------------------
      MX = MXGETM(PRHS(1))
      NX = MXGETN(PRHS(1))
      IF (MAX(MX,NX) .NE. 1) THEN
        CALL MEXERRMSGTXT('BMIE input X must be a real scalar.')
      ENDIF

C  ------------------------------------------------------------------
C  CHECK THE DIMENSIONS OF INPUT PARAMETER Re(m).
C  ------------------------------------------------------------------
      MRM = MXGETM(PRHS(2))
      NRM = MXGETN(PRHS(2))
      IF (MAX(MRM,NRM) .NE. 1) THEN
        CALL MEXERRMSGTXT('BMIE input Re(m) must be a real scalar.')
      ENDIF

C  ------------------------------------------------------------------
C  CHECK THE DIMENSIONS OF INPUT PARAMETER Im(m).
C  ------------------------------------------------------------------
      MIM = MXGETM(PRHS(3))
      NIM = MXGETN(PRHS(3))
      IF (MAX(MIM,NIM) .NE. 1) THEN
```

```
        CALL MEXERRMSGTXT('BMIE input Im(m) must be a real scalar.')
      ENDIF

C  -----------------------------------------------------------------
C  CHECK THE DIMENSIONS OF INPUT PARAMETER THETA.
C  -----------------------------------------------------------------
      MT = MXGETM(PRHS(4))
      NT = MXGETN(PRHS(4))
      IF ((MAX(MT,NT) .GT. 1000) .OR. (MIN(MT,NT) .GT. 1)) THEN
        CALL MEXERRMSGTXT('BMIE input ThetaS <1000 scalar points.')
      ENDIF
      SIZE = MT*NT

C  -----------------------------------------------------------------
C  CREATE A MATRIX FOR RETURN ARGUMENT
C  -----------------------------------------------------------------
      PLHS(1) = MXCREATEFULL(MT,NT,0)
      PLHS(2) = MXCREATEFULL(MT,NT,0)
      PLHS(3) = MXCREATEFULL(1,1,0)
      PLHS(4) = MXCREATEFULL(1,1,0)

C  -----------------------------------------------------------------
C  ASSIGN POINTERS TO THE VARIOUS PARAMETERS
C  -----------------------------------------------------------------
      I1P = MXGETPR(PLHS(1))
      I2P = MXGETPR(PLHS(2))
      QEXTP = MXGETPR(PLHS(3))
      QSCAP = MXGETPR(PLHS(4))
      XP = MXGETPR(PRHS(1))
      RMP = MXGETPR(PRHS(2))
      IMP = MXGETPR(PRHS(3))
      THETAP = MXGETPR(PRHS(4))

C  -----------------------------------------------------------------
C  DO THE ACTUAL COMPUTATIONS IN THE BHMIE SUBROUTINE.
C  -----------------------------------------------------------------
      CALL BHMIE(%VAL(XP),%VAL(RMP),%VAL(IMP),%VAL(THETAP),
     1%VAL(I1P),%VAL(I2P),%VAL(QEXTP),%VAL(QSCAP),SIZE)

C  -----------------------------------------------------------------
C  DONE.
C  -----------------------------------------------------------------
      RETURN
      END

C  -----------------------------------------------------------------
C  SUBROUTINE BHMIE CALCULATES AMPLITUDE SCATTERING MATRIX ELEMENTS
C  AND EFFICIENCIES FOR EXTINCTION, TOTAL SCATTERING AND BACKSCAT-
C  TERING FOR A GIVEN SIZE PARAMETER AND RELATIVE REFRACTIVE INDEX.
C  -----------------------------------------------------------------
      SUBROUTINE BHMIE(X,REFRE,REFIM,THETA,I1,I2,QEXT,QSCA,SIZE)

      REAL*8 X, REFRE, REFIM, THETA(1000), I1(1000), I2(1000)
      REAL*8 QEXT, QSCA
      DIMENSION AMU(1000), PI(1000), TAU(1000), PI0(1000), PI1(1000)
      COMPLEX D(5000), Y, REFREL, XI, XI0, XI1, AN, BN
```

```
      COMPLEX S1(2000), S2(2000)
      DOUBLE PRECISION PSI0, PSI1, PSI, DN, DX
      INTEGER SIZE

      REFREL=CMPLX(REFRE,REFIM)
      DX=X
      Y=X*REFREL
C  ---------------------------------------------------------------------
C  SERIES TERMINATED AFTER NSTOP TERMS
C  ---------------------------------------------------------------------
      XSTOP=X+4.05*X**.3333+2.0
      IF (X .GT. 5000.0) THEN
        CALL MEXERRMSGTXT('BHMIE is limited to 5000 terms for D().')
      END IF
      NSTOP=XSTOP
      YMOD=CABS(Y)
      NMX=AMAX1(XSTOP,YMOD)+15
C  ---------------------------------------------------------------------
C  LOGARITHMIC DERIVATIVE D(J) CALCULATED BY DOWNWARD RECURRENCE
C  BEGINNING WITH INITIAL VALUE 0.0 + i * 0.0 AT J=NMX
C  ---------------------------------------------------------------------
      D(NMX)=CMPLX(0.0,0.0)
      NN=NMX-1
      DO 120 N=1,NN
      RN=NMX-N+1
  120 D(NMX-N)=(RN/Y)-(1./(D(NMX-N+1)+RN/Y))
      DO 777 J=1,SIZE
      AMU(J)=COS(THETA(J))
      PI0(J)=0.0
      PI1(J)=1.0
      S1(J)=CMPLX(0.0,0.0)
  777 S2(J)=CMPLX(0.0,0.0)
C  ---------------------------------------------------------------------
C  RICATTI-BESSEL FUNCTIONS WITH REAL ARGUMENT X CALCULATED BY
C  UPWARD RECURRENCE
C  ---------------------------------------------------------------------
      PSI0=DCOS(DX)
      PSI1=DSIN(DX)
      CHI0=-SIN(X)
      CHI1=COS(X)
      APSI0=PSI0
      APSI1=PSI1
      XI0=CMPLX(APSI0,-CHI0)
      XI1=CMPLX(APSI1,-CHI1)
      QSCA=0.0
      N=1
  200 DN=N
      RN=N
      FN=(2*RN+1.)/(RN*(RN+1.))
      PSI=(2*DN-1.)*PSI1/DX-PSI0
      APSI=PSI
      CHI=(2.*RN-1.)*CHI1/X-CHI0
      XI=CMPLX(APSI,-CHI)
      AN=(D(N)/REFREL+RN/X)*APSI-APSI1
      AN=AN/((D(N)/REFREL+RN/X)*XI-XI1)
      BN=(REFREL*D(N)+RN/X)*APSI-APSI1
```

```
      BN=BN/((REFREL*D(N)+RN/X)*XI-XI1)
      QSCA=QSCA+(2.*RN+1.)*(CABS(AN)*CABS(AN)+CABS(BN)*CABS(BN))
      DO 789 J=1,SIZE
      PI(J)=PI1(J)
      TAU(J)=RN*AMU(J)*PI(J)-(RN+1.)*PI0(J)
      S1(J)=S1(J)+FN*(AN*PI(J)+BN*TAU(J))
      S2(J)=S2(J)+FN*(AN*TAU(J)+BN*PI(J))
  789 CONTINUE
      PSI0=PSI1
      PSI1=PSI
      APSI1=PSI1
      CHI0=CHI1
      CHI1=CHI
      XI1=CMPLX(APSI1,-CHI1)
      N=N+1
      RN=N
      DO 999 J=1,SIZE
      PI1(J)=((2.*RN-1.)/(RN-1.))*AMU(J)*PI(J)
      PI1(J)=PI1(J)-RN*PI0(J)/(RN-1.)
  999 PI0(J)=PI(J)
      IF(N-1-NSTOP) 200,300,300
  300 QSCA=(2./(X*X))*QSCA
      QEXT=(4./(X*X))*REAL(S1(1))
C  -------------------------------------------------------------------
C  NEITHER S1 NOR S2 ARE NEEDED, BUT THEIR MAGNITUDES ARE.  THIS
C  REDUCES THE SIZE OF THE ARGUMENTS TO PASS AND SAVE.
C  -------------------------------------------------------------------
      DO 400 J=1,SIZE
      I1(J)=(CABS(S1(J))*CABS(S1(J)))
      I2(J)=(CABS(S2(J))*CABS(S2(J)))
  400 CONTINUE
      RETURN
      END
```

Directives for mex-compilation on SUN-Solaris are contained in the g77opts.sh file below:

```
#-------------------------------------------------------------------------
#- This file is the mex-option file to guide the compilation and
#- linkage of BMie.F within MATLAB 5.3.X on any SUN Sparc Solaris
#- 2.6 of EEWEST at PSU (i.e., Nyquist, Edison, etc.).
#-------------------------------------------------------------------------
            CC='cc'
            CFLAGS='-dalign -KPIC'
            CLIBS=''
            COPTIMFLAGS='-O -DNDEBUG'
            CDEBUGFLAGS='-g'
#
            FC='g77'
            FFLAGS=''
            FLIBS='-lg2c'
            FOPTIMFLAGS='-O'
            FDEBUGFLAGS='-g'
#
            LD='/usr/ccs/bin/ld'
            LDFLAGS="-G -M $MATLAB/extern/lib/sol2/$MAPFILE -
L/usr/local/lib/gcc-lib/sparc-sun-solaris2.6/2.95.1"
```

```
            LDOPTIMFLAGS=''
            LDDEBUGFLAGS=''
#-----------------------------------------------------------------------
```

APPENDIX C
QUADRATURE LIMITATIONS IN THE CALCULATIONS OF F_1 AND F_2

This Appendix presents the MATLAB quadrature methods and resulting errors.

The 8 prepackaged quadrature techniques in MATLAB are called (descriptions originate from Using MATLAB: Version 5, 1996): ode45 (Runge-Kutta (4,5)), ode23 (Runge-Kutta (2,3)), ode113 (variable-order Adams-Bashforth-Moulton PECE), ode15s (variable-order based on numerical differentiation formulas, optionally uses Gear's method), ode23s (modified Rosenbrock formula of order 2), quad (adaptive Simpson's rule), quad8 (adaptive Newton-Cotes 8 panel rule), and gaussq (1st option: Gauss-Legendre). Most results from the above methods improved when increasing the number of recursive calls, but also met "Resource Limitations" on a desktop equipped with Windows NT 4.0, 450 MHz, 256 MB RAM, and 6 GB of hard-drive which, when pushed, ultimately resulted either in a frozen system or the Blue Screen Of Death (a.k.a. BSOD).). Table C.1 lists the resulting errors with respect to the method which uses a linear step-size of 0.1 nm.

Stevens (1996) described an alternative approach consisting in sampling the integrand in logarithmic step-sizes. The author has been unable to confirm the claim that the calculation of the F-functions is highly accurate using this approach (Kurtz et. al, 2002) from the implementation of the quadrature in Stevens' (1996) Appendix C.

The accuracy with which the F-functions are computed is relevant for the estimation process of the parameters of any aerosol model. To illustrate this assertion, the following simplest expression for the polarization ratio is considered:

Table C.1 Mean fractional error (over all scattering angles and relative humidity values) between pre-packaged MATLAB methods and a summation scheme using a linear step of 0.1 nm.

	Error [%] at ⊥-polarization			Error [%] at //-polarization		
Method-name	Mode 1	Mode 2	Mode 3	Mode 1	Mode 2	Mode 3
ode 45	0.28	2.66	3.95	0.86	2.53	3.52
ode 23	0.23	1.42	4.09	0.31	1.46	3.68
ode 113	0.18	1.36	3.38	0.21	1.58	3.51
ode 15s	0.51	2.17	6.55	0.59	2.66	6.09
ode 23s	0.18	2.27	6.71	0.22	2.40	6.06
Quad	0.07	0.10	1.40	0.04	0.11	1.72
Quad8	0.06	0.04	0.38	0.02	0.06	0.42
Gaussq (Gauss-Legendre)	0.06	0.30	1.21	0.03	0.32	1.27

Table C.2. This table contains the F-functions computed with a linear step-size which we have shown generates the most accurate values of the polarization ratio. The table also lists values (provided by C. R. Philbrick) of the same F-functions made using an equal logarithmic step-size interval. These two sets of F values were then used in the estimation of the Fractional error function FE_j (see Eq. C.3) for the resultant mode number densities $n_{0,j}$ from original values arbitrarily set to 10,000 for mode 1, 35 for mode 2, and 4 for mode 3 when the wavelength is 514.5 nm, the relative humidity is 67.1%, and the scattering angle is 170°. The range of integration was from 0.001 μm to 250 μm, for consistency with Stevens (1996, p. 62).

	Linear step-size of 0.1 nm		Logarithmic step-size of 0.01		FE_j [%]
	F_1	F_2	$\hat{F}_1$	$\hat{F}_2$	
Mode 1	0.011087	0.012581	0.011106	0.012605	0.5
Mode 2	3.6415	4.644	3.7137	4.6072	17.4
Mode 3	244.7732	305.866	269.0	282.93	143.0

$$PR \triangleq \frac{n_{0,-1}F_{2,-1} + n_{0,j}F_{2,j}}{n_{0,-1}F_{1,-1} + n_{0,j}F_{1,j}} \tag{C.1}$$

where Eq. (C.1) describes an aerosol model which includes atmospheric molecules (cf. Section 2.4) and one mode j which is chosen among 1, 2, and 3 (cf. Subsection 2.2.2). Equation (C.1) can be simply inverted to estimate the value of the concentration $n_{0,j}$ assuming accurately calculated functions $\hat{F}_1$ and $\hat{F}_2$:

$$\hat{n}_{0,j} = \frac{n_{0,-1}\left[F_{2,-1} - F_{1,-1}PR\right]}{\hat{F}_{1,j}PR - \hat{F}_{2,j}} \tag{C.2}$$

The Fractional Error for mode j (denoted FE_j) was computed as follows:

$$FE_j \triangleq 100 \times \frac{\left|\hat{n}_{0,j} - n_{0,j}\right|}{n_{0,j}} \tag{C.3}$$

The results from Eq. (C.2) (see Table C.2) demonstrate that relatively small errors in the computation of the F-functions have a significant impact on the estimation of the concentrations. Implicitly or explicitly any estimator using the polarization-ratio method has to negotiate the F-function discrepancies.

APPENDIX D

χ^2 TESTS FOR GAUSSIAN, POISSON, AND MODIFIED-POISSON PROBABILITY DENSITY FUNCTIONS

In the quest for high-performance estimators, proper modeling the observed data is a necessary step. Three potentially viable models were selected, all of which were subsequently included in a χ^2 test, to observe their appropriateness to model images captured by the CCD cameras: (1) a Gaussian distribution, (2) a Poisson distribution, and (3) a Poisson distribution to which a constant (unique for each pixel - to be estimated) was added.

Post-experimental images of uniform intensity fields at exposure times of 10, 30, 120, and 300 seconds were recorded by both CCD cameras. A computer program loaded in all the 56 images acquired in the same conditions, extracted a vector of recorded intensities at each pixel, estimated the parameters of each model assuming its validity, applied the test for each one of the three models, and continued with subsequent pixels until a total of 227.5 thousand pixels were so assessed.

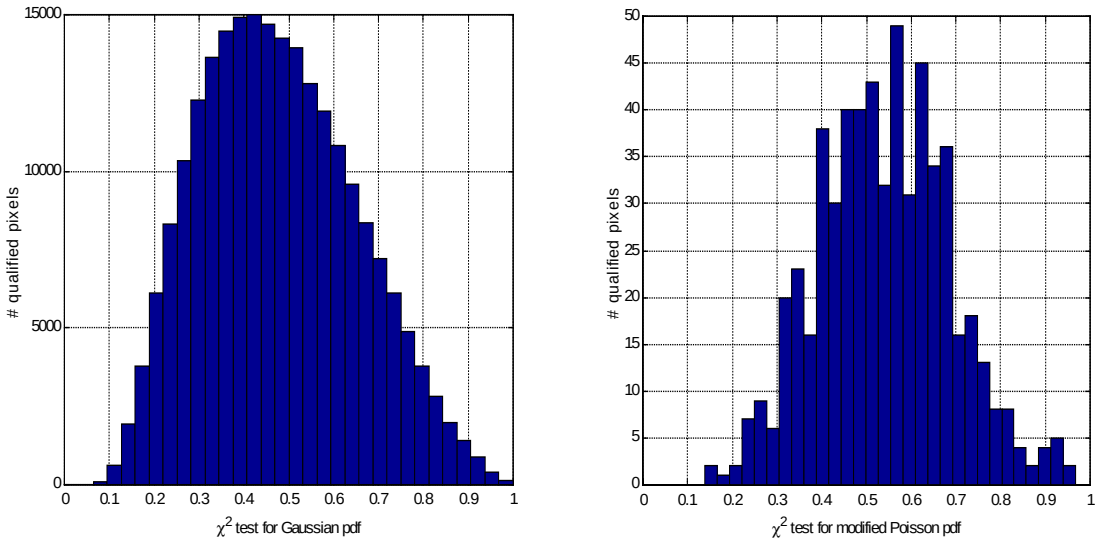

(a) (b)

Figure D. Sample distributions of the χ^2 test for (a) the Gaussian and (b) the modified-Poisson distributions with a 10 second exposure time from 56 images from the CCD of camera A. The means are 0.48 and 0.54 for (a) and (b), respectively. Slightly larger means were obtained with a closed shutter over the same exposure time.

The Gaussian test was the most successfully applied, followed by the modified Poisson. No pixel passed the true Poisson test. Figure D displays sample distributions of the χ^2 test itself. In designing the χ^2 test, a required minimum of 5 degrees of freedom led a substantial number of pixels to fail the modified Poisson distribution. In this sense, the Gaussian distribution revealed its robustness.

APPENDIX E
ON THE PROBABILITY DENSITY FUNCTION OF THE RATIO OF TWO GAUSSIAN RANDOM VARIABLES

This appendix details the derivation of Eq. (3.11). Variables are defined then the derivation is undertaken.

Definitions:

Let X be a Gaussian random variable of mean m_x and standard deviation σ_x. Let Y be a Gaussian random variable of mean m_y and standard deviation σ_y. Both X and Y are related to each other *via* the correlation coefficient r. Let Z denote the ratio of the two Gaussian random variables X and Y whose probability density function (pdf) $f_Z(z)$ is derived subsequently.

Derivation:

The original direction of the derivation is given by Papoulis (1991), p. 138, in Eq. (6-43):

$$f_Z(z) = \int_{-\infty}^{+\infty} |y|\, f(zy, y)\, dy = -\int_{-\infty}^{0} y\, f(zy, y)\, dy + \int_{0}^{+\infty} y\, f(zy, y)\, dy \tag{E.1}$$

The joint normal probability density function for both X and Y is expressed on p. 127 (Papoulis, 1991) by combining Eqs. (6-15) and (6-16):

$$f(x, y) = \frac{1}{2\pi\sigma_x\sigma_y\sqrt{1-r^2}} \exp\left\{-\frac{1}{2(1-r^2)}\left[\frac{(x-m_x)^2}{\sigma_x^2} - 2r\frac{(x-m_x)}{\sigma_x}\frac{(y-m_y)}{\sigma_y} + \frac{(y-m_y)^2}{\sigma_y^2}\right]\right\}$$

which, once substituting $x = z\,y$, can be rewritten as follows:

$$f(zy, y) = \frac{1}{2\pi\sigma_x\sigma_y\sqrt{1-r^2}} \exp\left\{-a\,y^2 + b\,y - c\right\} \tag{E.2}$$

where

$$a \triangleq \frac{1}{2\left(1-r^2\right)}\left(\frac{z^2}{\sigma_x^2}+\frac{1}{\sigma_y^2}-\frac{2zr}{\sigma_x\sigma_y}\right)$$

$$b \triangleq \frac{1}{\left(1-r^2\right)}\left(\frac{m_x}{\sigma_x^2}z+\frac{m_y}{\sigma_y^2}-\frac{r}{\sigma_x\sigma_y}\left(z\,m_y+m_x\right)\right)$$

$$c \triangleq \frac{1}{2\left(1-r^2\right)}\left(\frac{m_x^2}{\sigma_x^2}+\frac{m_y^2}{\sigma_y^2}-\frac{2r}{\sigma_x\sigma_y}m_x m_y\right)$$

The determinant of the expression within the exponential function of Eq. (E.2) remains positive (strictly, as long as r is not unity). Placing (E.2) into (E.1) yields:

$$f_Z(z) = -\int_{-\infty}^{0}\frac{y}{2\pi\sigma_x\sigma_y\sqrt{1-r^2}}\exp\left(-a\,y^2+b\,y-c\right)dy+\int_{0}^{+\infty}\frac{y}{2\pi\sigma_x\sigma_y\sqrt{1-r^2}}\exp\left(-a\,y^2+b\,y-c\right)dy$$

$$= \frac{\exp(-c)}{2\pi\sigma_x\sigma_y\sqrt{1-r^2}}\left[-\int_{-\infty}^{0} y\exp\left(-a\,y^2+b\,y\right)dy+\int_{0}^{+\infty} y\exp\left(-a\,y^2+b\,y\right)dy\right]$$

$$\Leftrightarrow \qquad f_Z(z) = \frac{\exp(-c)}{2\pi\sigma_x\sigma_y\sqrt{1-r^2}}\left(I_1+I_2\right)$$

where

$$I_1 \triangleq \int_{-\infty}^{0} y\exp\left(-a\,y^2+b\,y\right)dy = \frac{1}{2a}\left\{\sqrt{\pi}\,\frac{b}{2\sqrt{a}}\exp\left(\frac{b^2}{4a}\right)\left[1-erf\left(\frac{b}{2\sqrt{a}}\right)\right]-1\right\}$$

$$I_2 \triangleq \int_{0}^{+\infty} y\exp\left(-a\,y^2+b\,y\right)dy = \frac{1}{2a}\left\{\sqrt{\pi}\,\frac{b}{2\sqrt{a}}\exp\left(\frac{b^2}{4a}\right)\left[1+erf\left(\frac{b}{2\sqrt{a}}\right)\right]+1\right\}$$

whose details include the following template:

$$\int(-2\,a\,y+b)\exp\left(-a\,y^2+b\,y\right)dy = \exp\left(-a\,y^2+b\,y\right)$$

$$\Leftrightarrow \qquad -2\,a\int y\exp\left(-a\,y^2+b\,y\right)dy+b\int\exp\left(-a\,y^2+b\,y\right)dy = \exp\left(-a\,y^2+b\,y\right)$$

$$\Leftrightarrow \qquad \int y\exp\left(-a\,y^2+b\,y\right)dy = \frac{b}{2\,a}\int\exp\left(-a\,y^2+b\,y\right)dy-\frac{1}{2\,a}\exp\left(-a\,y^2+b\,y\right)$$

which is individually applied onto I_1 then I_2:

$$
\begin{aligned}
I_1 &\triangleq \int_{-\infty}^{0} y \exp\left(-a\,y^2 + b\,y\right) dy \\
&= \frac{b}{2a} \int_{-\infty}^{0} \exp\left(-a\,y^2 + b\,y\right) dy - \frac{1}{2a} \left[\exp\left(-a\,y^2 + b\,y\right)\right]_{-\infty}^{0} \\
&= \frac{b}{2a} \int_{-\infty}^{0} \exp\left(-a\,y^2 + b\,y\right) dy - \frac{1}{2a} \\
&= \frac{b}{2a} \left\{ \frac{\sqrt{\pi}}{2\sqrt{a}} \exp\left(\frac{b^2}{4a}\right) \left[1 - erf\left(\frac{b}{2\sqrt{a}}\right)\right] \right\} - \frac{1}{2a}
\end{aligned}
$$

$$
\Leftrightarrow \qquad I_1 = \frac{1}{2a} \left\{ \sqrt{\pi}\, \frac{b}{2\sqrt{a}} \exp\left(\frac{b^2}{4a}\right) \left[1 - erf\left(\frac{b}{2\sqrt{a}}\right)\right] - 1 \right\}
$$

$$
\begin{aligned}
I_2 &\triangleq \int_{0}^{+\infty} y \exp\left(-a\,y^2 + b\,y\right) dy \\
&= \frac{b}{2a} \int_{0}^{+\infty} \exp\left(-a\,y^2 + b\,y\right) dy - \frac{1}{2a} \left[\exp\left(-a\,y^2 + b\,y\right)\right]_{0}^{+\infty} \\
&= \frac{b}{2a} \int_{0}^{+\infty} \exp\left(-a\,y^2 + b\,y\right) dy + \frac{1}{2a} \\
&= \frac{b}{2a} \left\{ \frac{\sqrt{\pi}}{2\sqrt{a}} \exp\left(\frac{b^2}{4a}\right) \left[1 + erf\left(\frac{b}{2\sqrt{a}}\right)\right] \right\} + \frac{1}{2a}
\end{aligned}
$$

$$
\Leftrightarrow \qquad I_2 = \frac{1}{2a} \left\{ \sqrt{\pi}\, \frac{b}{2\sqrt{a}} \exp\left(\frac{b^2}{4a}\right) \left[1 + erf\left(\frac{b}{2\sqrt{a}}\right)\right] + 1 \right\}
$$

Consequently,

$$
f_Z(z) = \frac{\exp(-c)}{2\pi\sigma_x\sigma_y\sqrt{1-r^2}} \left(I_1 + I_2\right) = \frac{\exp(-c)}{2\pi a\sigma_x\sigma_y\sqrt{1-r^2}} \left\{ \sqrt{\pi}\, \frac{b}{2\sqrt{a}} \exp\left(\frac{b^2}{4a}\right) erf\left(\frac{b}{2\sqrt{a}}\right) + 1 \right\}
$$

which is the same expression as Eq. (3.11).

The derivation is checked by setting the means of both X and Y to zero and by simplifying Eq. (3.11) to the same Cauchy expression as the one on p. 138 of Papoulis (1991).

APPENDIX F
DECOMPOSITION AND BIAS STUDY OF THE $\hat{PR}$ AND $\check{PR}$ ESTIMATORS

The present appendix both details the decomposition of the Equation set (3.14) and proves that neither $\hat{PR}$ nor $\check{PR}$ is biased. While completing the former goal, expressions for both noise components $w_{\wedge}$ and $w_{\vee}$ are derived.

Definitions:

Let X be a Gaussian random variable of mean m_x and standard deviation σ_x. Let Y be a Gaussian random variable of mean m_y and standard deviation σ_y. The correlation coefficient between X and Y is assumed to be zero and *M* denotes the number of collected samples available at each polarization.

Decomposition: $\hat{PR}$

The first expression in the Eq. set (3.14) intends to estimate the numerical value of the polarization ratio by averaging the *M* pixel-values collected upon the same outgoing polarization. In mathematical terms, this first estimator uses the sample-mean operator at both the numerator and the denominator, as follows:

$$\hat{PR} = \frac{\frac{1}{M}\sum_{i=1}^{M} X_i}{\frac{1}{M}\sum_{i=1}^{M} Y_i} = \frac{\frac{1}{M}\sum_{i=1}^{M}\left(m_x + w_{x,i}\right)}{\frac{1}{M}\sum_{i=1}^{M}\left(m_y + w_{y,i}\right)} \tag{F.1}$$

where $w_{x,i} \sim N(0,\sigma_x)$ and $w_{y,i} \sim N(0,\sigma_y)$ as each random variable is decomposed into a mean component and a fluctuating part. Samples are assumed to be stationary. Equation (F.1) may be simplified as follows:

$$\hat{PR} = \frac{m_x + \frac{1}{M}\sum_{i=1}^{M}\left(w_{x,i}\right)}{m_y + \frac{1}{M}\sum_{i=1}^{M}\left(w_{y,i}\right)} = \frac{m_x + \overline{w_x}}{m_y + \overline{w_y}} \tag{F.2}$$

where $\overline{w_x} \sim N\left(0, \sigma_x / \sqrt{M}\right)$, $\overline{w_y} \sim N\left(0, \sigma_y / \sqrt{M}\right)$, and the overhead bar denotes the sample-mean operator. To study potential bias in the estimator, the following form of Eq. (F.2) is preferred:

$$\hat{PR} = \frac{m_x}{m_y} + w_{\wedge} \tag{F.3}$$

where the expression for $w_{\wedge}$ needs to be determined. To this aim, Eqs. (F.2) and (F.3)are equated:

$$\frac{m_x + \overline{w_x}}{m_y + \overline{w_y}} = \frac{m_x}{m_y} + w_{\wedge}$$

$$\Leftrightarrow \quad w_{\wedge} = \frac{m_x + \overline{w_x}}{m_y + \overline{w_y}} - \frac{m_x}{m_y}$$

$$= \frac{m_y\left(m_x + \overline{w_x}\right) - m_x\left(m_y + \overline{w_y}\right)}{m_y\left(m_y + \overline{w_y}\right)}$$

$$\Leftrightarrow \quad w_{\wedge} = \frac{m_y\,\overline{w_x} - m_x\,\overline{w_y}}{m_y\left(m_y + \overline{w_y}\right)}$$

The numerator consists of the difference between two random variables $N\left(0, m_y\sigma_x / \sqrt{M}\right)$ and $N\left(0, m_x\sigma_y / \sqrt{M}\right)$ and the denominator is $N\left(m_y^2, m_y\sigma_y / \sqrt{M}\right)$. Hence, the expression for $w_{\wedge}$ is:

$$w_{\wedge} \sim \frac{N\left(0, \sqrt{m_y^2\sigma_x^2 + m_x^2\sigma_y^2} / \sqrt{M}\right)}{N\left(m_y^2, m_y\sigma_y / \sqrt{M}\right)} \tag{F.4}$$

Decomposition: $\check{PR}$

This second expression in the Eq. set (3.14) intends to estimate the numerical value of the polarization ratio by averaging the *M* ratios of the pixel-values collected upon complementary outgoing polarization. In mathematical terms:

$$\check{PR} = \frac{1}{M}\sum_{i=1}^{M}\frac{X_i}{Y_i} = \frac{1}{M}\sum_{i=1}^{M}\frac{\left(m_x + w_{x,i}\right)}{\left(m_y + w_{y,i}\right)} \tag{F.5}$$

where both $w_{x,i}$ and $w_{y,i}$ have the same expression as in the decomposition of $\hat{PR}$. To study potential bias in the estimator, the following form of Eq. (F.5) is preferred:

$$\check{PR} = \frac{m_x}{m_y} + w_{\vee} \tag{F.6}$$

where the expression for $w_{\vee}$ needs to be determined. To this aim, Eq. (F.6) is re-written as follows:

$$\frac{m_x}{m_y} + w_{\vee} = \frac{m_x}{m_y} + \frac{1}{M}\sum_{i=1}^{M} w_{\vee,i} = \frac{1}{M}\sum_{i=1}^{M}\left(\frac{m_x}{m_y} + w_{\vee,i}\right) \tag{F.7}$$

Hence, $w_{\vee}$ consists of the sample-mean average of $w_{\vee,i}$ whose expression is sought. Equations. (F.5) and (F.7) provide this key:

$$\frac{m_x + w_{x,i}}{m_y + w_{y,i}} = \frac{m_x}{m_y} + w_{\vee,i}$$

$$\Leftrightarrow \qquad w_{\vee,i} = \frac{m_x + w_{x,i}}{m_y + w_{y,i}} - \frac{m_x}{m_y}$$

$$= \frac{m_y\left(m_x + w_{x,i}\right) - m_x\left(m_y + w_{y,i}\right)}{m_y\left(m_y + w_{y,i}\right)}$$

$$\Leftrightarrow \qquad w_{\vee,i} = \frac{m_y w_{x,i} - m_x w_{y,i}}{m_y\left(m_y + w_{y,i}\right)} \tag{F.8}$$

The numerator consists of the difference between two random variables $N\left(0, m_y\sigma_x/M\right)$ and $N\left(0, m_x\sigma_y/M\right)$ and the denominator is $N\left(m_y^2, m_y\sigma_y/M\right)$. Hence, the expression for $w_{\wedge,i}$ is:

$$w_{\vee,i} \sim \frac{N\left(0, \sqrt{m_y^2\sigma_x^2 + m_x^2\sigma_y^2}\right)}{N\left(m_y^2, m_y\sigma_y\right)} \tag{F.9}$$

and the one for $w_{\vee}$ is the sample-mean of $w_{\wedge,i}$.

Bias study: $\hat{PR}$

The above decomposition of $\hat{PR}$ significantly helps in assessing the bias of this estimator:

$$E\left\{\hat{PR}\right\} = E\left\{\frac{m_x}{m_y} + w_\wedge\right\} = \frac{m_x}{m_y} + E\{w_\wedge\} \tag{F.10}$$

The $\hat{PR}$ estimator is unbiased if $E\{w_\wedge\}$ reduces to zero in Eq. (F.10). Equation (F.4) shows that the probability density function of $w_\wedge$ is that of the ratio of two Gaussian random variables (cf. Appendix E). As both X and Y have already been used, $U \sim N(0, \sigma_u)$ shall denote the random variable at the numerator and $V \sim N(m_v, \sigma_v)$ the random variable at the denominator. Noticing that $m_v = 0$, the terms in Eq. (E.2) become:

$$a = \frac{1}{2}\left(\frac{w^2}{\sigma_u^2} + \frac{1}{\sigma_v^2}\right);\ b = \frac{m_v}{\sigma_v^2};\ c \hat{=} \frac{1}{2}\frac{m_v^2}{\sigma_v^2}$$

and

$$f_W(w) = \frac{\exp(-c)}{2\pi a \sigma_u \sigma_v}\left\{\sqrt{\pi}\,\frac{b}{2\sqrt{a}}\exp\left(\frac{b^2}{4a}\right) erf\left(\frac{b}{2\sqrt{a}}\right) + 1\right\} \tag{F.11}$$

This detour was necessary to continue the analysis of the bias of $\hat{PR}$:

$$\begin{aligned}
E\{w_\wedge\} &= \int_{-\infty}^{+\infty} w_\wedge \cdot f_{W_\wedge}(w_\wedge)\, dw_\wedge \\
&= \int_{-\infty}^{0} w_\wedge \cdot f_{W_\wedge}(w_\wedge)\, dw_\wedge + \int_{0}^{+\infty} w_\wedge \cdot f_{W_\wedge}(w_\wedge)\, dw_\wedge \\
&= \int_{\infty}^{0} -w_\wedge \cdot f_{W_\wedge}(-w_\wedge)\, d(-w_\wedge) + \int_{0}^{+\infty} w_\wedge \cdot f_{W_\wedge}(w_\wedge)\, dw_\wedge \\
&= -\int_{0}^{\infty} w_\wedge \cdot f_{W_\wedge}(-w_\wedge)\, d(w_\wedge) + \int_{0}^{+\infty} w_\wedge \cdot f_{W_\wedge}(w_\wedge)\, dw_\wedge \\
E\{w_\wedge\} &= 0
\end{aligned}$$

because $f_W(-w) = f_W(w)$. Hence, $\hat{PR}$ is an unbiased estimator.

Bias study: $\check{PR}$

The above decomposition of $\check{PR}$ significantly helps in assessing the bias of this estimator:

$$E\left\{\check{PR}\right\} = E\left\{\frac{m_x}{m_y} + w_\vee\right\} = \frac{m_x}{m_y} + E\{w_\vee\} = \frac{m_x}{m_y} + \frac{1}{N}\sum_{i=1}^{N} E\{w_{\vee,i}\} \tag{F.12}$$

The $\overset{\vee}{PR}$ estimator is unbiased if $E\{w_{\vee,i}\}$ reduces to zero in Eq. (F.12). The mean of the numerator of Eq. (F.9) is also zero which, by similarity with the previous case, testifies that $\overset{\vee}{PR}$ is an unbiased estimator.

APPENDIX G

IS $\hat{PR}$ OR $\check{PR}$ A BETTER ESTIMATOR?

The variance of both unbiased estimators distinguishes the one of better performance. Appendix G details the content of Fig. 3.2(a). Analytically, from Subsection 3.4.3, the variance of each estimator is (with notational shortcuts):

$$\mathrm{var}\left(\hat{PR}\right) = E\left\{w_{\wedge}^2\right\} = \mathrm{var}\left(w_{\wedge}\right) \text{ where } w_{\wedge} \sim \frac{N\left(0, \sqrt{m_y^2\sigma_x^2 + m_x^2\sigma_y^2}\,/\sqrt{M}\right)}{N\left(m_y^2, m_y\sigma_y/\sqrt{M}\right)} \text{ and}$$

$$\mathrm{var}\left(\check{PR}\right) = E\left\{w_{\vee}^2\right\} = \mathrm{var}\left(w_{\vee}\right) = \frac{\mathrm{var}\left(w_{\vee,i}\right)}{M} \text{ where } w_{\vee,i} = \frac{N\left(0, \sqrt{m_y^2\sigma_x^2 + m_x^2\sigma_y^2}\right)}{N\left(m_y^2, m_y\sigma_y\right)} \text{ and } w_{\vee} = \frac{1}{M}\sum_{i=1}^{M} w_{\vee,i}\,.$$

If only one image is collected at each incident polarization, then the performance of both estimators is the same (*M=1*). Another similarity between these two estimators is their infinite variance due to their Cauchy terms, as shown below using the generalized notations $Z = X/Y$ where $X \sim N\left(0, \sigma_x\right)$, $Y \sim N\left(m_y, \sigma_y\right)$, and $r = 0$:

$$\begin{aligned}
\mathrm{var}(Z) &\hat{=} \int_{-\infty}^{+\infty} z^2 f_Z(z)dz = \int_{-\infty}^{+\infty} z^2 \frac{\exp(-c)}{2\pi\sigma_x\sigma_y a}\left[\sqrt{\pi}\frac{b}{2\sqrt{a}}\exp\left(\frac{b^2}{4a}\right)\mathrm{erf}\left(\frac{b}{2\sqrt{a}}\right)+1\right]dz \\
&= \underbrace{\int_{-\infty}^{+\infty} z^2 \frac{\exp(-c)}{2\pi\sigma_x\sigma_y a}\sqrt{\pi}\frac{b}{2\sqrt{a}}\exp\left(\frac{b^2}{4a}\right)\mathrm{erf}\left(\frac{b}{2\sqrt{a}}\right)dz}_{I_{Non-Cauchy}} + \underbrace{\int_{-\infty}^{+\infty} z^2 \frac{\exp(-c)}{2\pi\sigma_x\sigma_y a}dz}_{I_{Cauchy}} \\
&= I_{Non-Cauchy} + \frac{\sigma_x}{\sigma_y}\frac{\exp(-c)}{\pi}\left[z - \arctan\left(z\frac{\sigma_y^2}{\sigma_x^2}\right)\right]_{-\infty}^{+\infty} \to +\infty
\end{aligned}$$

The responsibility of the Cauchy term for the divergence of the variance suggests dividing the probability density function $f_Z(z)$ into two approximations emphasizing either the Cauchy or non-Cauchy term, as described in Subsection 3.4.3, resulting in a total of 4 quadrants (two per estimator) which is reduced to 3 due to the impossibility of occurrence of one of them: (1) both estimators in non-Cauchy regions, (2) both estimators in Cauchy regions, and (3) $\hat{PR}$ in non-Cauchy region and $\check{PR}$ in Cauchy

region. In each case, the sign of the difference between the variances of $\hat{PR}$ and $\check{PR}$ awards the better estimator.

To focus on dissimilarities between estimators, generalized notations for $Z = X/Y$ are adopted in which *a*, *b*, and *c* follow Equ. (3.12) where $m_x = 0$ and $r = 0$:

$$\text{var}\left(\hat{PR}\right) \hat{=} \int_{-\infty}^{+\infty} z^2 \hat{f}_Z(z)dz = \int_{-\infty}^{+\infty} z^2 \frac{\exp(-\hat{c})}{2\pi \frac{\sigma_x}{\sqrt{M}} \frac{\sigma_y}{\sqrt{M}} \hat{a}} \left[\sqrt{\pi} \frac{\hat{b}}{2\sqrt{\hat{a}}} \exp\left(\frac{\hat{b}^2}{4\hat{a}}\right) \text{erf}\left(\frac{\hat{b}}{2\sqrt{\hat{a}}}\right) + 1 \right] dz$$

$$\text{var}\left(\check{PR}\right) = \frac{1}{M} \int_{-\infty}^{+\infty} z^2 \ \check{f}_Z(z)\, dz = \frac{1}{M} \int_{-\infty}^{+\infty} z^2 \frac{\exp(-c)}{2\pi\sigma_x\sigma_y a} \left[\sqrt{\pi} \frac{b}{2\sqrt{a}} \exp\left(\frac{b^2}{4a}\right) \text{erf}\left(\frac{b}{2\sqrt{a}}\right) + 1 \right] dz$$

where $\hat{a} = M\,a$, $\hat{b} = M\,b$, and $\hat{c} = M\,c$. Hence, the general but explicit difference thereafter approximated in each case is:

$$\begin{aligned} \Delta \text{ var} &\hat{=} \text{var}\left(\hat{PR}\right) - \text{var}\left(\check{PR}\right) \\ &= \frac{1}{2\pi\sigma_x\sigma_y} \int_{-\infty}^{+\infty} \frac{z^2}{a} \left\{ \begin{array}{l} \exp(-Mc)\left[\sqrt{\pi} \frac{b\sqrt{M}}{2\sqrt{a}} \exp\left(\frac{b^2 M}{4a}\right) \text{erf}\left(\frac{b\sqrt{M}}{2\sqrt{a}}\right) + 1 \right] \\ -\frac{\exp(-c)}{M}\left[\sqrt{\pi} \frac{b}{2\sqrt{a}} \exp\left(\frac{b^2}{4a}\right) \text{erf}\left(\frac{b}{2\sqrt{a}}\right) + 1 \right] \end{array} \right\} dz \end{aligned} \qquad \text{(G.1)}$$

Case 1: $\hat{PR}$ and $\check{PR}$ non-Cauchy terms dominate

Equation (G.1) becomes:

$$\Delta \text{ var} \approx \frac{\sqrt{\pi} b}{4\pi\sigma_x\sigma_y} \int_{-\infty}^{+\infty} \frac{z^2}{aM\sqrt{a}} \exp\left(\frac{b^2}{4a} - c\right) \text{erf}\left(\frac{b}{2\sqrt{a}}\right) g(z)dz \qquad \text{(G.2)}$$

where

$$g(z) = M\sqrt{M} \exp\left[\left(\frac{b^2 M}{4a} - c \right)(M-1) \right] \frac{\text{erf}\left(b\sqrt{M}/2\sqrt{a}\right)}{\text{erf}\left(b/2\sqrt{a}\right)} - 1 \approx M^2 \exp\left[\left(\frac{b^2 M}{4a} - c \right)(M-1) \right] - 1$$

where *erf(x) ~ sqrt(1-exp(-4x²/π))* at "small" *x*, in agreement with the current case. The sign of the integrand in Equ. (G.2) is determined by the sign of *g(z)* which, in turn, determines the better estimator. The function *g(z)* is positive (or null) at the origin, then decreases with increasing z. Should *g(z)* remain positive as z becomes infinite, Equ. (G.2) keeps its positive sign, granting $\check{PR}$ a preferred estimator status. But should g(z) change sign, so would the selection in better estimator. The toggle point (at infinity) between these two situations is located at (notations translated back into the original ones):

$$SNR_y = \frac{m_y^2}{\sigma_y^2} = \frac{4}{M-1}\ln(M) \qquad \text{(G.3)}$$

Hence, conditionally to being in the quadrant where both estimators are dominated by their non-Cauchy terms, an SNR_y above Equ. (G.3) results in $\hat{PR}$ as the better estimator, as supported by Fig. 3.2(b). The situation below Equ. (G.3) is more confused due to the arbitrary choice of the threshold value (*T*) above which the Cauchy terms dominate.

Case 2 : $\hat{PR}$ and $\check{PR}$ Cauchy terms dominate

This case is concerned with two estimators of infinite variances, but for which one is hoped to be less bad than the other. The derivation proceeds in a similar fashion as in Case 1 where the new approximated expression of Equ. (G.1) is:

$$\Delta \text{var} \approx \frac{1}{2\pi\sigma_x\sigma_y M}\int_{-\infty}^{+\infty}\frac{z^2}{a}\exp(-c)g(z)dz$$

where

$$g(z) = M\exp\left[-c(M-1)\right]-1$$

which leads to a toggle point (independent of z) located at:

$$SNR_y = \frac{m_y^2}{\sigma_y^2} = \frac{2}{M-1}\ln(M) \qquad \text{(G.4)}$$

Equations (G.3) and (G.4) only differ by 3 dB. Due to the arbitrary threshold (*T*) set to 0.5, $\check{PR}$ is the better estimator over the complete region. A lower value to the threshold is suggested by Fig. 3.2(b).

Case 3 : $\check{P}R$ Cauchy term and $\hat{P}R$ non-Cauchy term dominate

A comparison involving a Cauchy term with a non-Cauchy term is a loosing battle for the former estimator. Proceeding as objectively as before, Equ. (G.1) becomes:

$$\Delta \text{var} \approx \frac{1}{2\pi\sigma_x\sigma_y M}\int_{-\infty}^{+\infty}\frac{z^2}{a}\exp(-c)g(z)dz$$

where

$$g(z) = M\sqrt{\pi}\,\frac{b\sqrt{M}}{2\sqrt{a}}\exp\left(\frac{Mb^2}{4a} - c(M-1)\right)\text{erf}\left(\frac{b\sqrt{M}}{2\sqrt{a}}\right) - 1$$

which becomes negative at "large" values of z, making $\hat{P}R$ the better estimator.

In conclusion, the above calculations were based on sharply drawn boundaries to study well-defined cases, boundaries which have been blurred by approximations in the above expressions, the choice of threshold (T) for each estimator, and the closeness of the numbers in the simulations to result in the observed differences between Fig. 3.4(a) and 3.4(b). The most important outcome from the study is the agreement in $\hat{P}R$ as the better estimator at an SNR_y greater than (about) 0 dB.

APPENDIX H
TABULATED EOPACE PROCESSING-CONTEXT

Each table below associates a reference name to both a time-segment and the corresponding EOPACE-images. These images were stored on a CDROM which was mounted on the D:\ drive for processing. The processing region seen by each camera is delimited by the position of consecutive vertices in the Image Space.

Table H.1. Case Number 1 (PolRat configuration-filename Apr04F01).

Device/Variable	Value [Units]
Exposure time	5 [s]
Mean Relative Humidity (RH)	69.4 [%]
Sea Surface Temperature (SST)	15.9 [C]
Camera A: Path to images	D:\Cam_a\970404
Camera A: Parallel images	BSAPI001,BSAPI002,BSAPI003,BSAPI004,BSAPI005
Camera A: Perpendicular images	BSAPO001,BSAPO002,BSAPO003,BSAPO004,BSAPO005
Camera A: Background image	BKA01
Camera A: Processing region	{(587,247), (495,319),(228,324),(226,66),(587,14)}
Camera B: Path to image	D:\Cam_b\970404
Camera B: Parallel images	BSBPI001,BSBPI002,BSBPI003,BSBPI004,BSBPI005
Camera B: Perpendicular images	BSBPO001,BSBPO002,BSBPO003,BSBPO004,BSBPO005
Camera B: Background image	BKB01
Camera B: Processing region	{(593,255),(447,328),(9,335),(7,66),(592,22)}

Table H.2. Case Number 2 (PolRat configuration-filename Apr04F02).

Device/Variable	Value [Units]
Exposure time	30 [s]
Mean Relative Humidity (RH)	69.4 [%]
Sea Surface Temperature (SST)	15.9 [C]
Camera A: Path to images	D:\Cam_a\970404
Camera A: Parallel images	BSAPI006,BSAPI007,BSAPI008,BSAPI009,BSAPI010
Camera A: Perpendicular images	BSAPO006,BSAPO007,BSAPO008,BSAPO009,BSAPO010
Camera A: Background image	BKA02
Camera A: Processing region	{(587,240),(495,312),(229,334),(227,37),(587,10)}
Camera B: Path to image	D:\Cam_b\970404
Camera B: Parallel images	BSBPI006,BSBPI007,BSBPI008,BSBPI009,BSBPI010
Camera B: Perpendicular images	BSBPO006,BSBPO007,BSBPO008,BSBPO009,BSBPO010
Camera B: Background image	BKB02
Camera B: Processing region	{(593,248),(447,321),(12,345),(9,37),(592,18)}

Table H.3. Case Number 3 (PolRat configuration-filename Apr05F01).

Device/Variable	Value [Units]
Exposure time	300 [s]
Mean Relative Humidity (RH)	62.6 [%]
Sea Surface Temperature (SST)	15.9 [C]
Camera A: Path to images	D:\Cam_a\970405
Camera A: Parallel images	BSAPI003,BSAPI004
Camera A: Perpendicular images	BSAPO003,BSAPO004
Camera A: Background image	BKA02
Camera A: Processing region	{(587,240),(495,312),(229,334),(227,37),(587,10)}
Camera B: Path to image	D:\Cam_b\970405
Camera B: Parallel images	BSBPI003,BSBPI004
Camera B: Perpendicular images	BSBPO003,BSBPO004
Camera B: Background image	BKB02
Camera B: Processing region	{{(593,248),(447,321),(12,345),(9,37),(592,18)}

Table H.4. Case Number 4 (PolRat configuration-filename Apr08F01).

Device/Variable	Value [Units]
Exposure time	300 [s]
Mean Relative Humidity (RH)	77.6 [%]
Sea Surface Temperature (SST)	16.4 [C]
Camera A: Path to images	D:\Cam_a\970408
Camera A: Parallel images	BSAPI001,BSAPI002,BSAPI003
Camera A: Perpendicular images	BSAPO001,BSAPO002,BSAPO003
Camera A: Background images	BKA001,BKA002
Camera A: Processing region	{(579,249),(532,294),(529,291),(460,330),(223,385),(224,171), (321,87), (580,79)}
Camera B: Path to image	D:\Cam_b\970408
Camera B: Parallel images	BSBPI001,BSBPI002,BSBPI003
Camera B: Perpendicular images	BSBPO001,BSBPO002,BSBPO003
Camera B: Background images	BKB01,BKB02
Camera B: Processing region	{(596,181),(521,227),(517,224),(407,263),(18,322),(18,99),(180,14), (598,10)}

Table H.5. Case Number 5 (PolRat configuration-filename Apr09F01).

Device/Variable	Value [Units]
Exposure time	10 [s]
Mean Relative Humidity (RH)	64.0 [%]
Sea Surface Temperature (SST)	16.4 [C]
Camera A: Path to images	D:\Cam_a\970409
Camera A: Parallel images	BSAPI001,BSAPI002,BSAPI003,BSAPI004,BSAPI005
Camera A: Perpendicular images	BSAPO001,BSAPO002,BSAPO003,BSAPO004,BSAPO005
Camera A: Background images	BKA01,BKA02
Camera A: Processing region	{(548,279),(516,312),(483,312),(387,373),(201,371),(201,96), (279,50),(291,117),(321,123),(325,62),(345,42),(450,10),(505,15), (549,90)}
Camera B: Path to image	D:\Cam_b\970409
Camera B: Parallel images	BSBPI001,BSBPI002,BSBPI003,BSBPI004,BSBPI005
Camera B: Perpendicular images	BSBPO001,BSBPO002,BSBPO003,BSBPO004,BSBPO005
Camera B: Background images	BKB01,BKB02
Camera B: Processing region	{(571,296),(519,329),(468,329),(313,391),(3,391),(5,106),(135,60), (155,129),(205,135),(212,73),(243,53),(414,23),(501,30),(571,106)}

Table H.6. Case Number 6 (PolRat configuration-filename Apr09F02).

Device/Variable	Value [Units]
Exposure time	30 [s]
Mean Relative Humidity (RH)	64.1 [%]
Sea Surface Temperature (SST)	16.4 [C]
Camera A: Path to images	D:\Cam_a\970409
Camera A: Parallel images	BSAPI006,BSAPI007,BSAPI008,BSAPI009,BSAPI010
Camera A: Perpendicular images	BSAPO006,BSAPO007,BSAPO008,BSAPO009,BSAPO010
Camera A: Background images	BKA03,BKA04
Camera A: Processing region	{(533,252),(493,262),(464,278),(362,281),(329,339),(292,392), (186,410),(185,173),(193,205),(201,202),(203,151),(280,105), (325,198),(350,178),(321,98),(406,48),(513,37),(530,108)}
Camera B: Path to image	D:\Cam_b\970409
Camera B: Parallel images	BSBPI006,BSBPI007,BSBPI008,BSBPI009,BSBPI010
Camera B: Perpendicular images	BSBPO006,BSBPO007,BSBPO008,BSBPO009,BSBPO010
Camera B: Background images	BKB03,BKB04
Camera B: Processing region	{(578,289),(515,299),(468,316),(304,319),(250,378),(189,434), (12,453),(12,207),(25,240),(39,237),(41,184),(169,138),(243,234), (283,214),(236,132),(376,83),(545,73),(573,145)}

Table H.7. Case Number 7 (PolRat configuration-filename Apr09F03).

Device/Variable	Value [Units]
Exposure time	60 [s]
Mean Relative Humidity (RH)	64.1 [%]
Sea Surface Temperature (SST)	16.4 [C]
Camera A: Path to images	D:\Cam_a\970409
Camera A: Parallel images	BSAPI011,BSAPI012,BSAPI013,BSAPI014,BSAPI015
Camera A: Perpendicular images	BSAPO011,BSAPO012,BSAPO013,BSAPO014,BSAPO015
Camera A: Background images	BKA05,BKA06
Camera A: Processing region	{(542,249),(448,278),(269,281),(186,325),(185,59),(377,13),(543,3),(550,131)}
Camera B: Path to image	D:\Cam_b\970409
Camera B: Parallel images	BSBPI011,BSBPI012,BSBPI013,BSBPI014,BSBPI015
Camera B: Perpendicular images	BSBPO011,BSBPO012,BSBPO013,BSBPO014,BSBPO015
Camera B: Background images	BKB05,BKB06
Camera B: Processing region	{(591,286),(443,316),(151,319),(12,365),(12,89),(328,46),(593,40),(605,168)}

Table H.8. Case Number 8 (PolRat configuration-filename Apr09F04).

Device/Variable	Value [Units]
Exposure time	120 [s]
Mean Relative Humidity (RH)	65.25 [%]
Sea Surface Temperature (SST)	16.4 [C]
Camera A: Path to images	D:\Cam_a\970409
Camera A: Parallel images	BSAPI016,BSAPI017,BSAPI018
Camera A: Perpendicular images	BSAPO016,BSAPO017,BSAPO018
Camera A: Background images	BKA07,BKA08
Camera A: Processing region	{(551,239),(492,281),(490,271),(183,274),(181,33),(221,9),(546,14)}
Camera B: Path to image	D:\Cam_b\970409
Camera B: Parallel images	BSBPI016,BSBPI017,BSBPI018
Camera B: Perpendicular images	BSBPO016,BSBPO017,BSBPO018
Camera B: Background images	BKB07,BKB08
Camera B: Processing region	{(607,276),(515,319),(510,309),(9,312),(7,63),(73,40),(599,51)}

Table H.9. Case Number 9 (PolRat configuration-filename Apr09F05).

Device/Variable	Value [Units]
Exposure time	300 [s]
Mean Relative Humidity (RH)	67.5 [%]
Sea Surface Temperature (SST)	16.4 [C]
Camera A: Path to images	D:\Cam_a\970409
Camera A: Parallel images	BSAPI019,BSAPI020,BSAPI021
Camera A: Perpendicular images	BSAPO019,BSAPO020,BSAPO021
Camera A: Background images	BKA09,BKA10
Camera A: Processing region	{(547,242),(503,284),(492,275),(476,278),(181,325),(181,62),(196,30),(234,10),(546,17)}
Camera B: Path to image	D:\Cam_b\970409
Camera B: Parallel images	BSBPI019,BSBPI020,BSBPI021
Camera B: Perpendicular images	BSBPO019,BSBPO020,BSBPO021
Camera B: Background images	BKB09,BKB10
Camera B: Processing region	{(600,279),(530,322),(513,312),(488,316),(5,365),(5,92),(31,60),(94,40),(598,54)}

APPENDIX I
EXTINCTION ESTIMATION
FROM EOPACE DATA

Subsection 2.3.4 defines the concept of extinction and Subsection 4.3.10 presents extinction values. The present appendix addresses the issues of computation and substantiation of the claim that extinction values derived from the EOPACE data should be used with care.

Computational complexity:

Equation (2.13) encounters the same computational complexity as the F-functions (cf. Subsection 2.3.3) whose similarity inspires a redefinition of the extinction function to support multiple modal concentrations. The new function, for each mode *j* of the aerosol model is:

$$\Gamma_j \triangleq \frac{\gamma_j}{n_{0,j}} = \frac{1}{n_{0,j}} \int_0^{+\infty} Q_{ext} \left. \frac{dN}{da} \right|_j a^2 \pi \, da \qquad \text{(I.1)}$$

where the integration scheme is the same as the one discussed for the F-functions and the Q_{ext} value (a function of the incident wavelength) is returned for each numerical radius (denoted *a*) by the modified computer program of Bohren and Huffman (cf. Appendix B). Results from Equ. (I.1) are in units of μm^2, as the radius *a* is in μm (this unit scheme was driven by constraints over the integration of the F-functions). Finally, extinction for mode *j* is obtained as follows (in km^{-1}):

$$\gamma_j = n_{0,j} \, \Gamma_j \, 10^{-3} \qquad \text{(I.2)}$$

where $n_{0,j}$ is in cm^{-3}. The Γ_j values were computed once at all relative humidity values and all modes at the same time as the F-functions.

Tables of extinction derived from EOPACE data:

Concentrations available from the EOPACE data follow three different paths: (1) functional fits onto the rotorod data (cf. Subsection 2.2.3), (2) restoration from the polarization-ratio applied onto images captured by the bi-static lidar set-up, and (3) the NOVAM model (cf. Subsection 2.2.1). Table I.1 lists extinction by individual mode for those three paths and for each configuration file found in Appendix H.

Table I.1. Extinction (in km^{-1}) for each individual mode, configuration filename (cf. Appendix H), and methods of estimation of the concentrations. The estimation methods for the concentrations rely on the NRaD rotorod data through functional fits (described in Appendix A), restorations through the polarization ratio technique on collected images (described in Chapter 3), and application of the NOVAM model (described in Subsection 2.2.1). Concentrations considered are those estimated at mean relative humidity for the functional rotorod fits and, in addition, 3 neighbors, and both cameras for the polarization ratio (through the visually observed maximum log-likelihood criterion).

Config. File	Estimation	γ(Mode 0)	γ (Mode 1)	γ (Mode 2)	γ (Mode 3)	γ (Mode 4)
Apr04F01	Rotorod Fit	0.0000	0.0000	0.0427	0.2283	0.0000
	Polar. Ratio	0.6225	2.7098	0.0339	0.0074	0.0706
	NOVAM	0.0207	0.0033	0.0143	0.0009	0.0000
Apr04F02	Rotorod Fit	0.0000	0.0000	0.0427	0.2283	0.0000
	Polar. Ratio	0.6225	1.3581	0.0135	0.0019	0.0397
	NOVAM	0.0255	0.0411	0.0143	0.0009	0.0000
Apr05F01	Rotorod Fit	0.0000	0.0000	0.0364	0.0131	0.0000
	Polar. Ratio	0.4945	0.9117	0.0098	0.0006	0.0158
	NOVAM	0.0000	0.0050	0.0047	0.0005	0.0000
Apr08F01	Rotorod Fit	0.0000	0.0000	0.0255	0.0791	0.0000
	Polar. Ratio	0.6985	0.4748	0.0280	0.0077	0.1120
	NOVAM	0.0000	0.0026	0.0068	0.0006	0.0000
Apr09F01	Polar. Ratio	0.4945	1.3000	0.0071	0.0014	0.0281
	NOVAM	0.0000	0.0049	0.0076	0.0010	0.0000
Apr09F02	Polar. Ratio	0.4945	0.9210	0.0079	0.0019	0.0281
	NOVAM	0.0000	0.0051	0.0089	0.0005	0.0000
Apr09F03	Polar. Ratio	0.5548	1.3010	0.0079	0.0015	0.0281
	NOVAM	0.0000	0.0051	0.0091	0.0006	0.0000
Apr09F04	Polar. Ratio	0.4945	0.8277	0.0090	0.0017	0.0281
	NOVAM	0.0000	0.0051	0.0093	0.0008	0.0000
Apr09F05	Polar. Ratio	0.5548	1.3354	0.0104	0.0036	0.0397
	NOVAM	0.0000	0.0052	0.0097	0.0006	0.0000

In many cases, fair agreement exists on extinction values of mode 2 for all three paths and mode 3 for the last two paths. Extinction values from the polarization-ratio data at modes 0, 1, and 4 largely disagree with those obtained via other paths. This observation motivates the presentation of extinction from the association of subsets of modes, as displayed in Table I.2. However, every extinction in Table I.2 includes the contribution from the atmospheric molecules.

The most reliable extinction values for the polarization-ratio are limited to modes -1, 2, and 3, in Table I.2. From the contribution of mode 3, the rotorod fits define an upper bound. In the NOVAM model, all modes contribute to the final value of extinction (in the present cases, only modes -1, 1, 2, and 3 are necessary). On average, the most trusted values of extinction from the polarization-ratio and NOVAM differ by 30%, approximately. This number is both small and large. It is relatively small because Eq. (I.2) includes linear concentrations (not logarithmic ones). It is relatively large because errors in transmittance over long distances become large (a mean fractional error of the transmittance at 100 km reaches about 100%, based on the above numbers).

Table I.2. Total extinction (in km^{-1}) for combined modes whose numbers appear within parentheses (after γ) and whose individual extinction values are specified in Table I.1. When interpreted carefully, the numbers below add to the credibility of the instrument.

Config. File	Estimation	γ(-1, 2, and 3)	γ (-1, 1, 2, 3)	γ (-1, 0, 1, 2, 3, 4)
Apr04F01	Rotorod Fit	0.287	0.287	0.287
	Polar. Ratio	0.057	2.767	3.460
	NOVAM	0.031	0.065	0.085
Apr04F02	Rotorod Fit	0.287	0.287	0.287
	Polar. Ratio	0.031	1.390	2.052
	NOVAM	0.031	0.072	0.098
Apr05F01	Rotorod Fit	0.066	0.066	0.066
	Polar. Ratio	0.026	0.938	1.448
	NOVAM	0.021	0.026	0.026
Apr08F01	Rotorod Fit	0.121	0.121	0.121
	Polar. Ratio	0.052	0.527	1.337
	NOVAM	0.023	0.026	0.026
Apr09F01	Polar. Ratio	0.024	1.325	1.847
	NOVAM	0.025	0.030	0.030
Apr09F02	Polar. Ratio	0.026	0.947	1.470
	NOVAM	0.026	0.031	0.031
Apr09F03	Polar. Ratio	0.025	1.326	1.909
	NOVAM	0.026	0.031	0.031
Apr09F04	Polar. Ratio	0.027	0.855	1.377
	NOVAM	0.026	0.031	0.031
Apr09F05	Polar. Ratio	0.030	1.365	1.960
	NOVAM	0.026	0.032	0.032

In essence, a guided reading of the values of extinction listed in Table I.2 adds to the argument of credibility of the instrument (cf. Zieliński at al., 1999, for consistency with experimental values over the southern coastal Baltic sea), but it also warns that their relative closeness might not be good enough for all applications.

APPENDIX J
AVERAGED ORIGINAL EOPACE IMAGES AND BI-DIMENSIONAL ESTIMATED CONCENTRATIONS OF MODES 2 AND 3

Each configurations file of Appendix H lists files of EOPACE images. After arithmetically averaging all images of the same configuration (i.e., camera A, parallel polarization), corrections were applied to compensate for both the mean background noise ($\overline{N}$) and transmittance through the retarder plate (T_R). After selecting a region of interest in those adjusted images, restoration proceeded at estimating concentrations for the modes dictated by the selected restoration directives.

Each subsequent page of the appendix (one per configurations file of Appendix H) displays 6 figures. The first 4 images project against the pier the adjusted image intensity (in counts) seen by each camera at each polarization for the dual purpose of comparison and interpretation within a common geometrical frame of reference (they are **not** to be interpreted as scattered intensity observed from the corresponding location along pier). The last 2 images display the spatial distribution of the estimated concentrations of modes 2 and 3 (on a logarithmic scale – of base 10) within the same geometrical frame as the previous images.

A scale of artificial colors displayed by the side of each figure measures the range of values encountered. All else being equal, the longer the integration time, the larger the range of captured intensities.

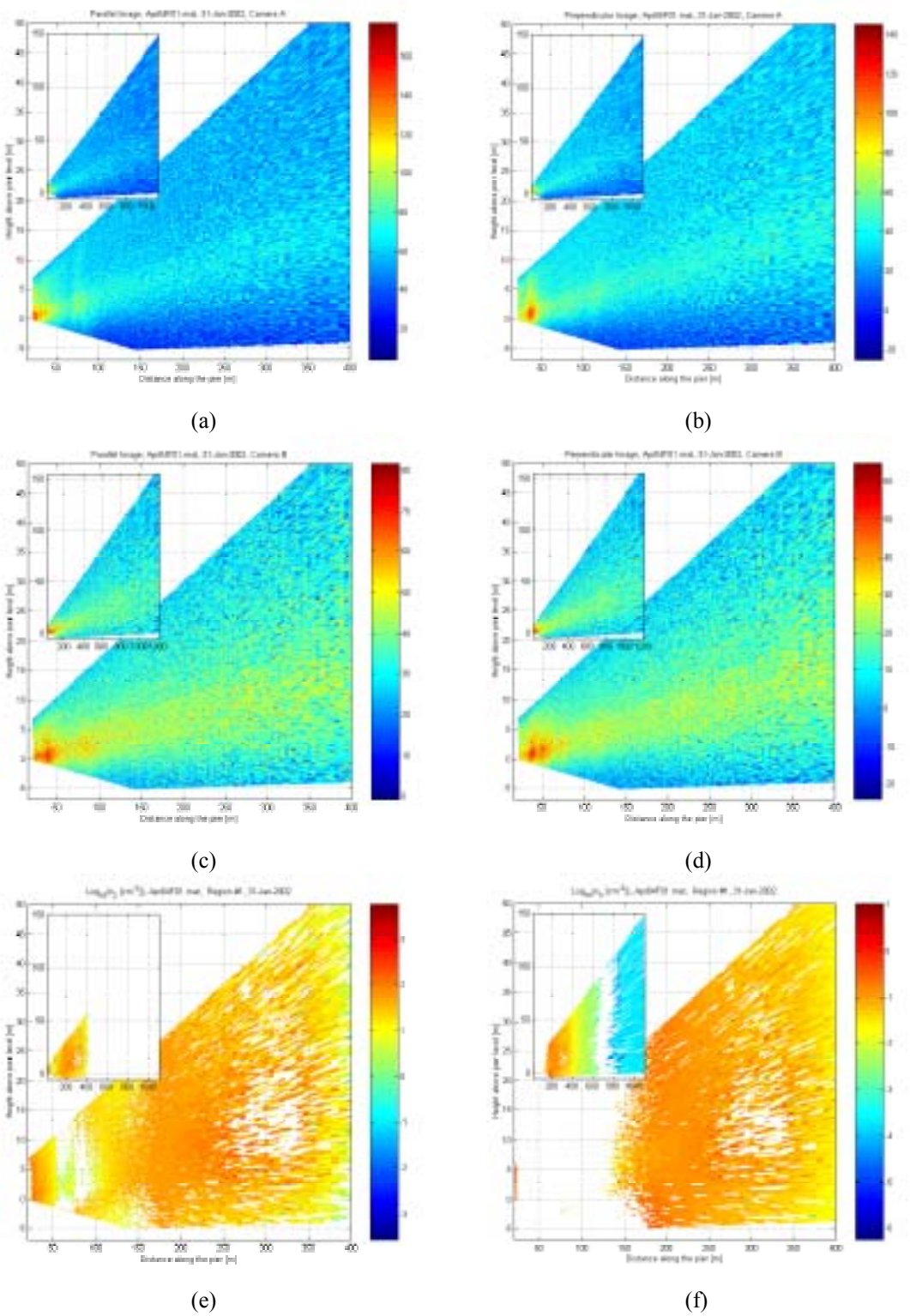

(a) (b)

(c) (d)

(e) (f)

Figure J.1. Projection along the pier of the intensity of the mean EOPACE images captured over a 5 second exposure time by (a) camera A at parallel outgoing polarization, (b) camera A at perpendicular outgoing polarization, (c) camera B at parallel outgoing polarization, and (d) camera B at perpendicular outgoing polarization. Estimated concentrations from from image set Apr04F01 using both cameras (A and B) for (e) mode 2 and (f) mode 3.

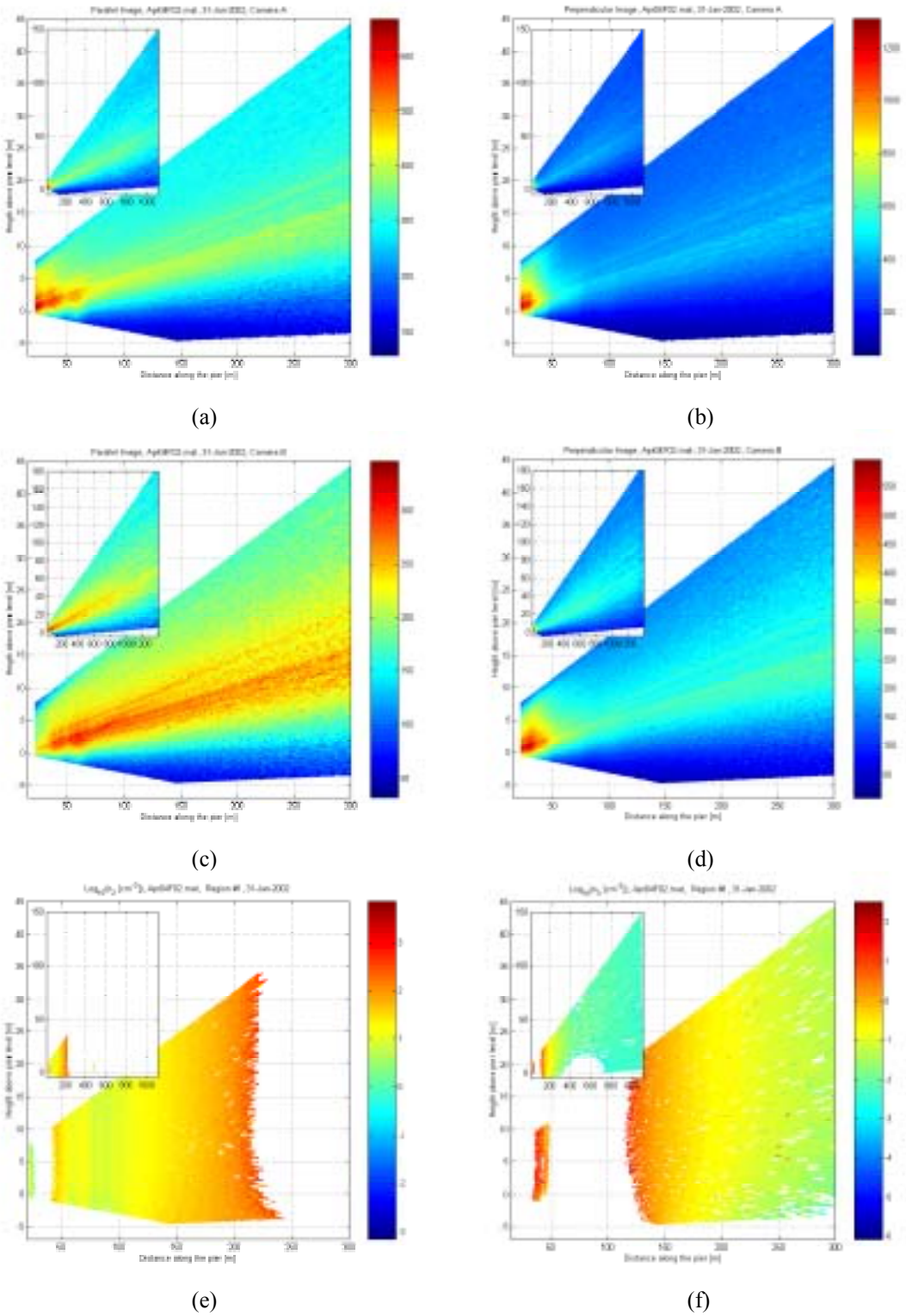

(a) (b)

(c) (d)

(e) (f)

Figure J.2. Projection along the pier of the intensity of the mean EOPACE images captured over a 30 second exposure time by (a) camera A at parallel outgoing polarization, (b) camera A at perpendicular outgoing polarization, (c) camera B at parallel outgoing polarization, and (d) camera B at perpendicular outgoing polarization. Estimated concentrations from image set Apr04F02 using (e) both cameras A and B for mode 2 and (f) camera A for mode 3.

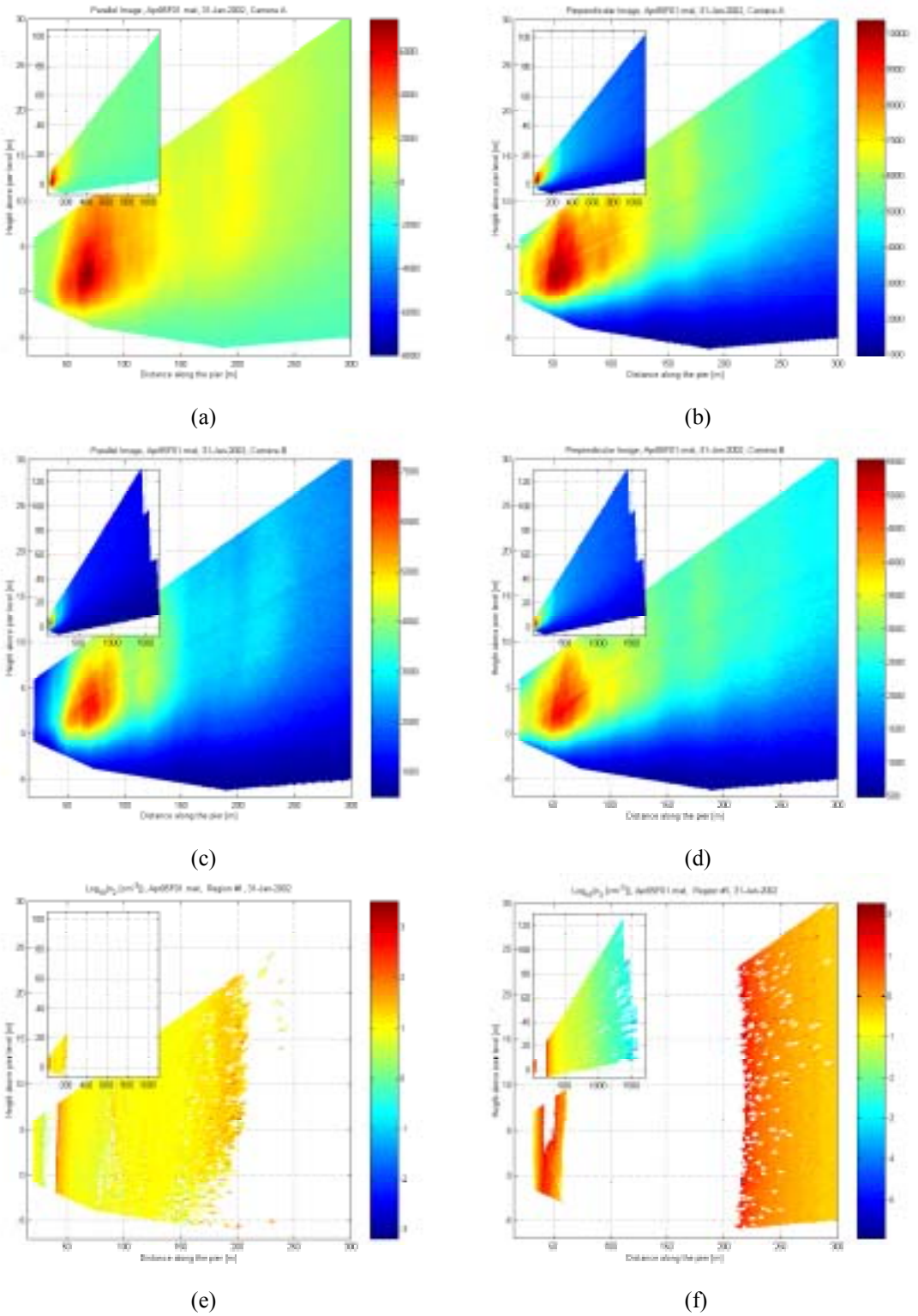

(a) (b)

(c) (d)

(e) (f)

Figure J.3. Projection along the pier of the intensity of the mean EOPACE images captured over a 300 second exposure time by (a) camera A at parallel outgoing polarization, (b) camera A at perpendicular outgoing polarization, (c) camera B at parallel outgoing polarization, and (d) camera B at perpendicular outgoing polarization. Estimated concentrations from image set Apr05F01 using (e) both cameras A and B for mode 2 and (f) camera B for mode 3.

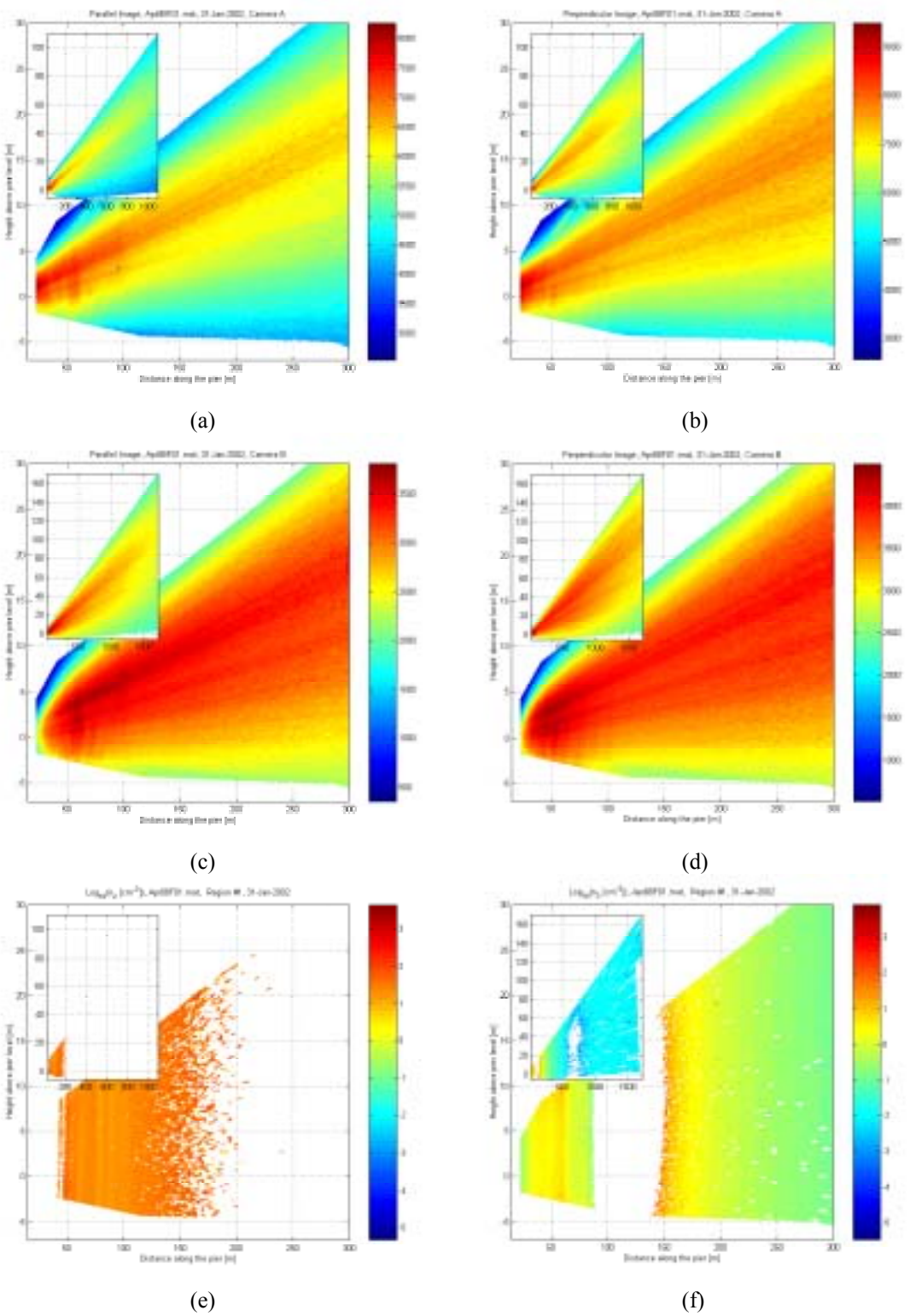

(a) (b)

(c) (d)

(e) (f)

Figure J.4. Projection along the pier of the intensity of the mean EOPACE images captured over a 300 second exposure time by (a) camera A at parallel outgoing polarization, (b) camera A at perpendicular outgoing polarization, (c) camera B at parallel outgoing polarization, and (d) camera B at perpendicular outgoing polarization. Estimated concentrations from image set Apr08F01 using (e) both cameras A and B for mode 2 and (f) camera B for mode 3.

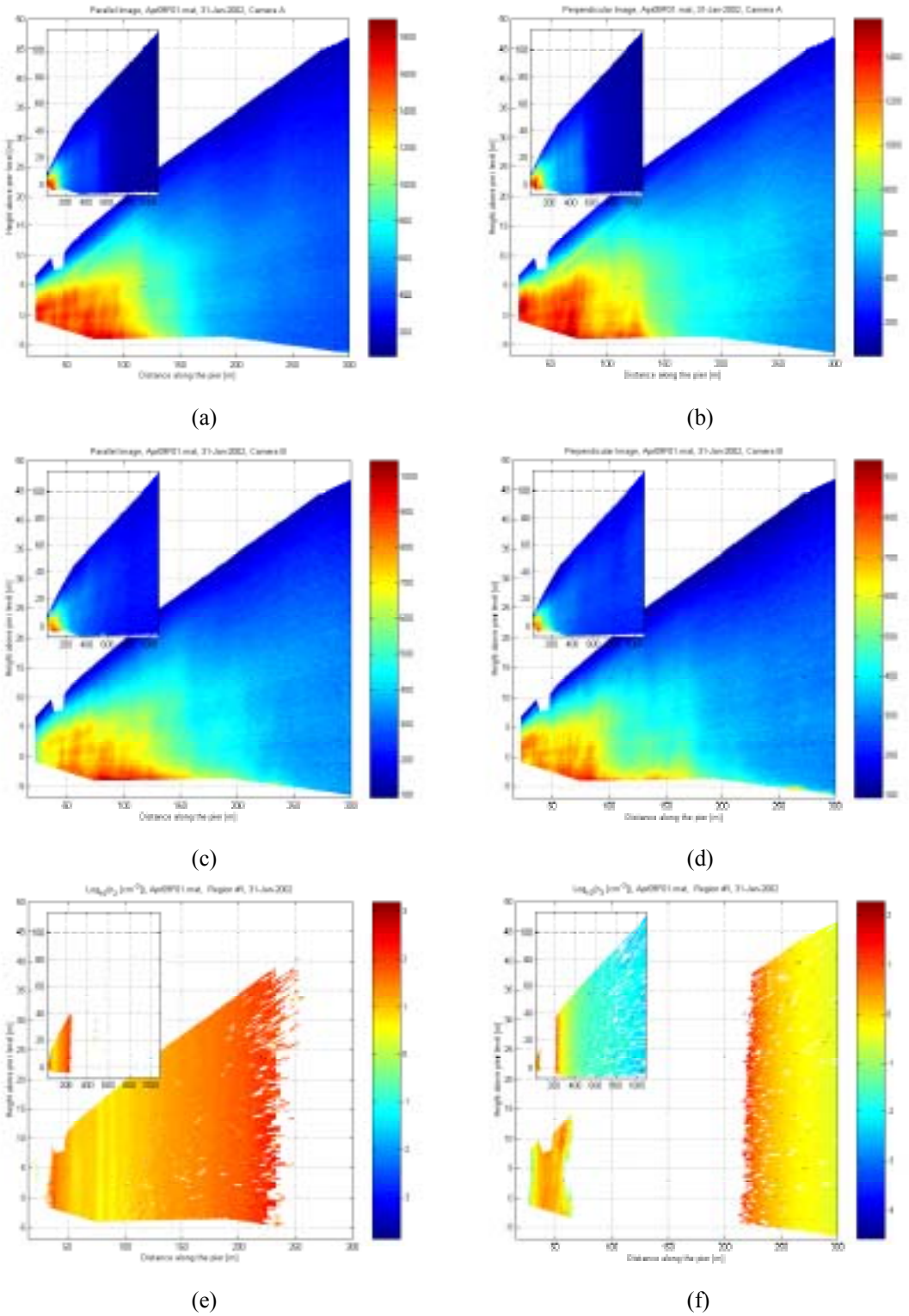

(a) (b)

(c) (d)

(e) (f)

Figure J.5. Projection along the pier of the intensity of the mean EOPACE images captured over a 10 second exposure time by (a) camera A at parallel outgoing polarization, (b) camera A at perpendicular outgoing polarization, (c) camera B at parallel outgoing polarization, and (d) camera B at perpendicular outgoing polarization. Estimated concentrations from image set Apr09F01 using (a) both cameras A and B for mode 2 and (b) camera B for mode 3.

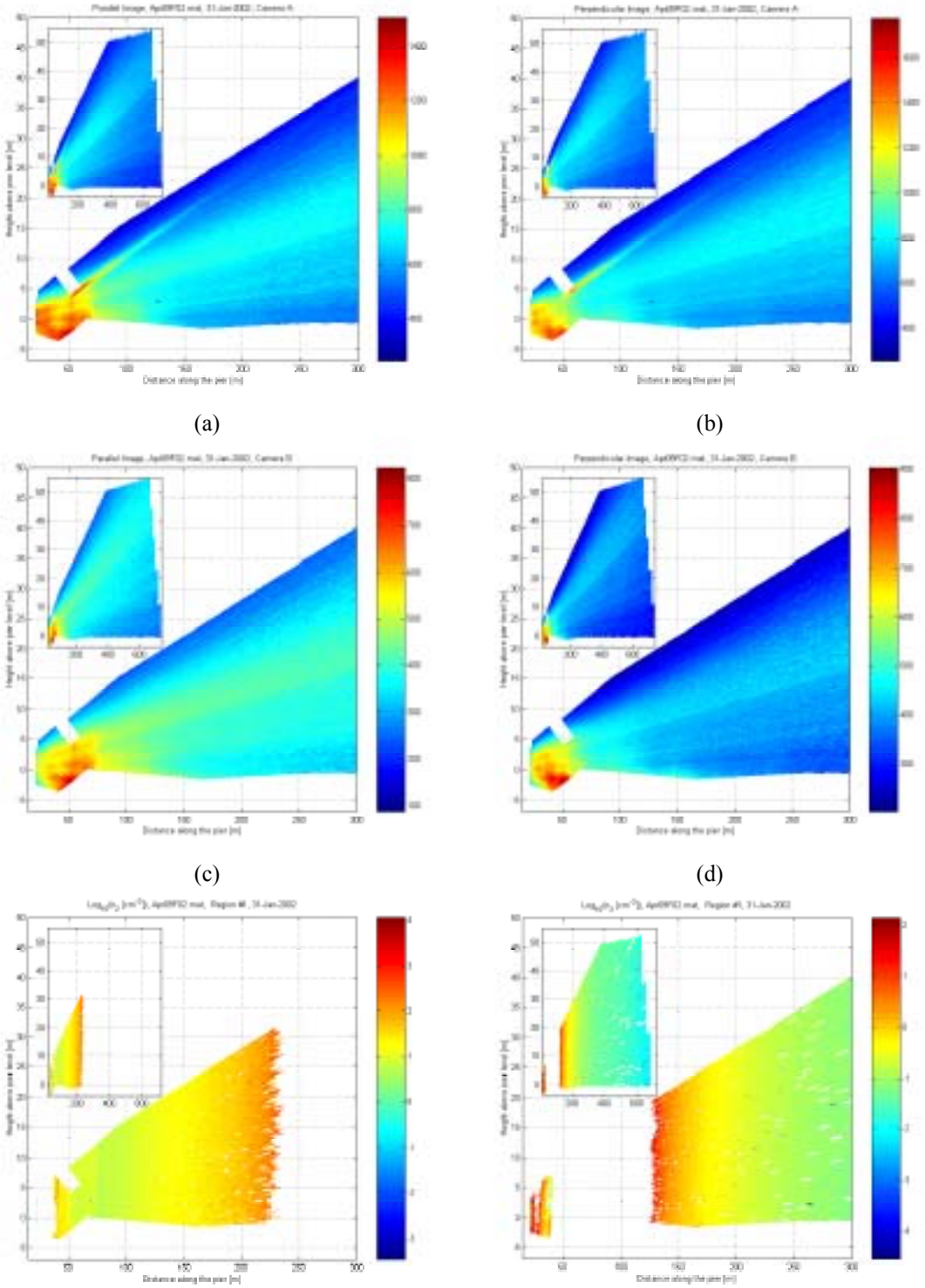

(a) (b)

(c) (d)

(e) (f)

Figure J.6. Projection along the pier of the intensity of the mean EOPACE images captured over a 30 second exposure time by (a) camera A at parallel outgoing polarization, (b) camera A at perpendicular outgoing polarization, (c) camera B at parallel outgoing polarization, and (d) camera B at perpendicular outgoing polarization. Estimated concentrations from image set Apr09F02 using (a) both cameras A and B for mode 2 and (b) camera A for mode 3.

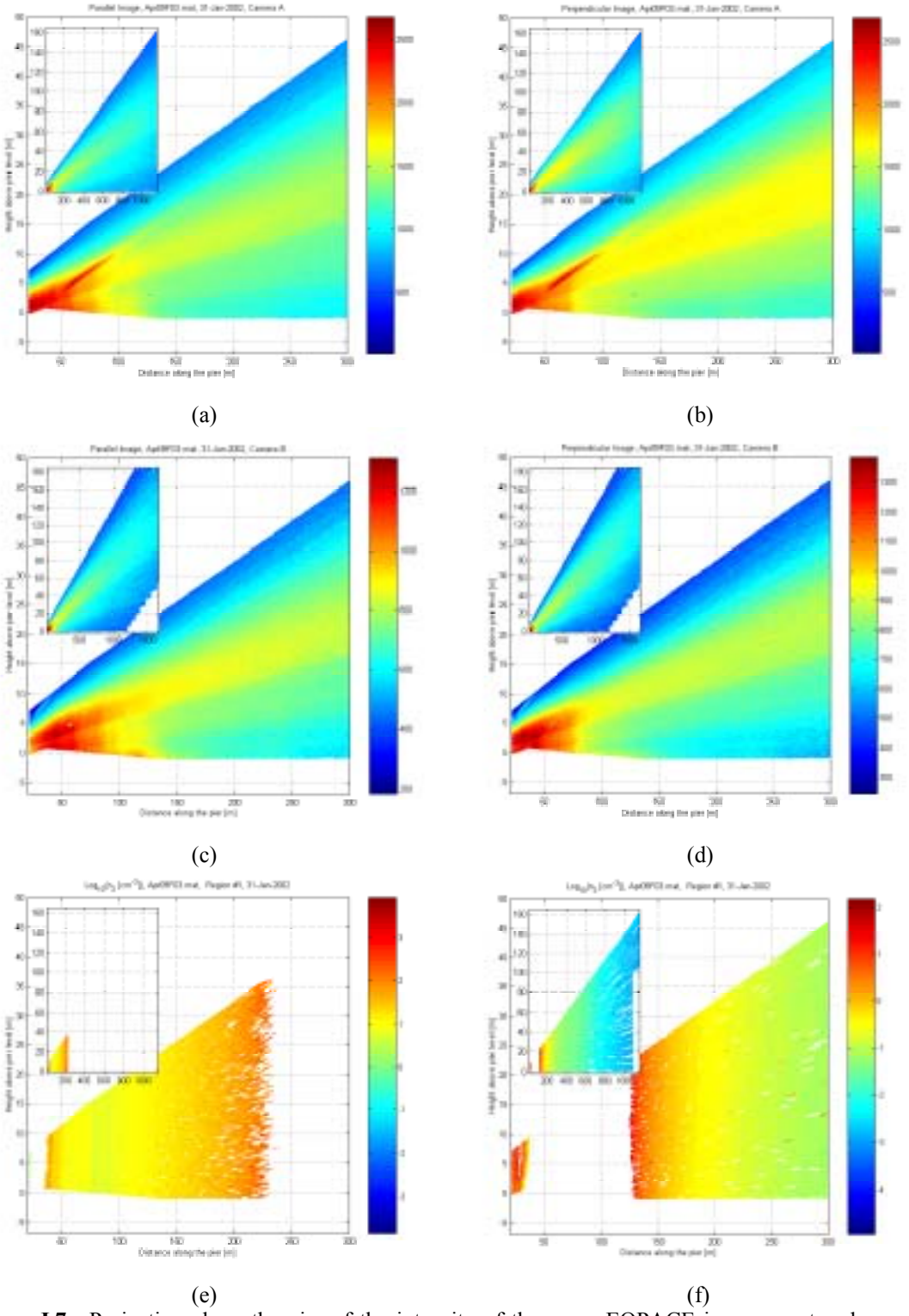

(a) (b)

(c) (d)

(e) (f)

Figure J.7. Projection along the pier of the intensity of the mean EOPACE images captured over a 60 second exposure time by (a) camera A at parallel outgoing polarization, (b) camera A at perpendicular outgoing polarization, (c) camera B at parallel outgoing polarization, and (d) camera B at perpendicular outgoing polarization. Estimated concentrations from image set Apr09F03 using (a) both cameras A and B for mode 2 and (b) camera A for mode 3.

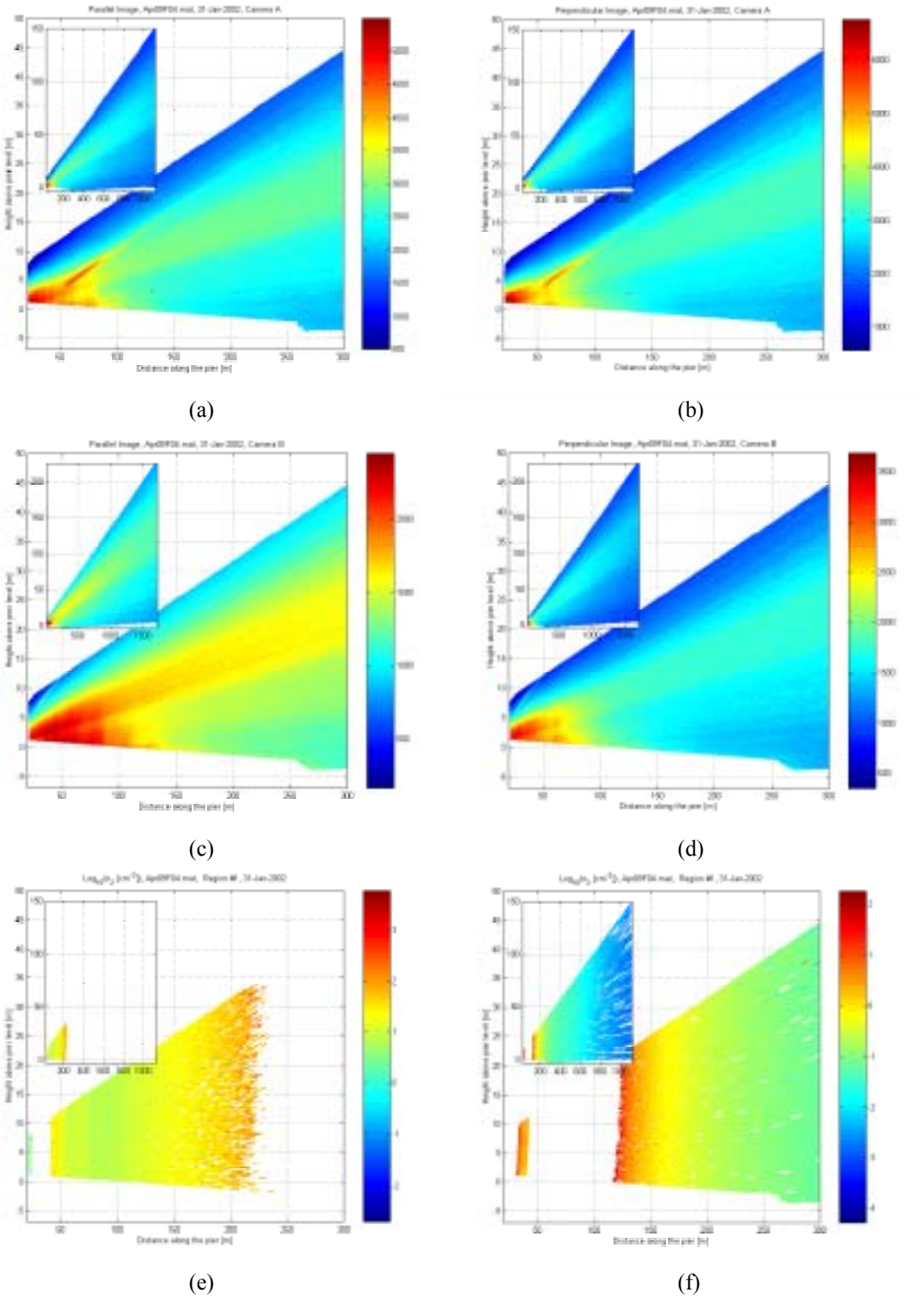

(a) (b)

(c) (d)

(e) (f)

Figure J.8. Projection along the pier of the intensity of the mean EOPACE images captured over a 120 second exposure time by (a) camera A at parallel outgoing polarization, (b) camera A at perpendicular outgoing polarization, (c) camera B at parallel outgoing polarization, and (d) camera B at perpendicular outgoing polarization. Estimated concentrations from image set Apr09F04 using (a) both cameras A and B for mode 2 and (b) camera A for mode 3.

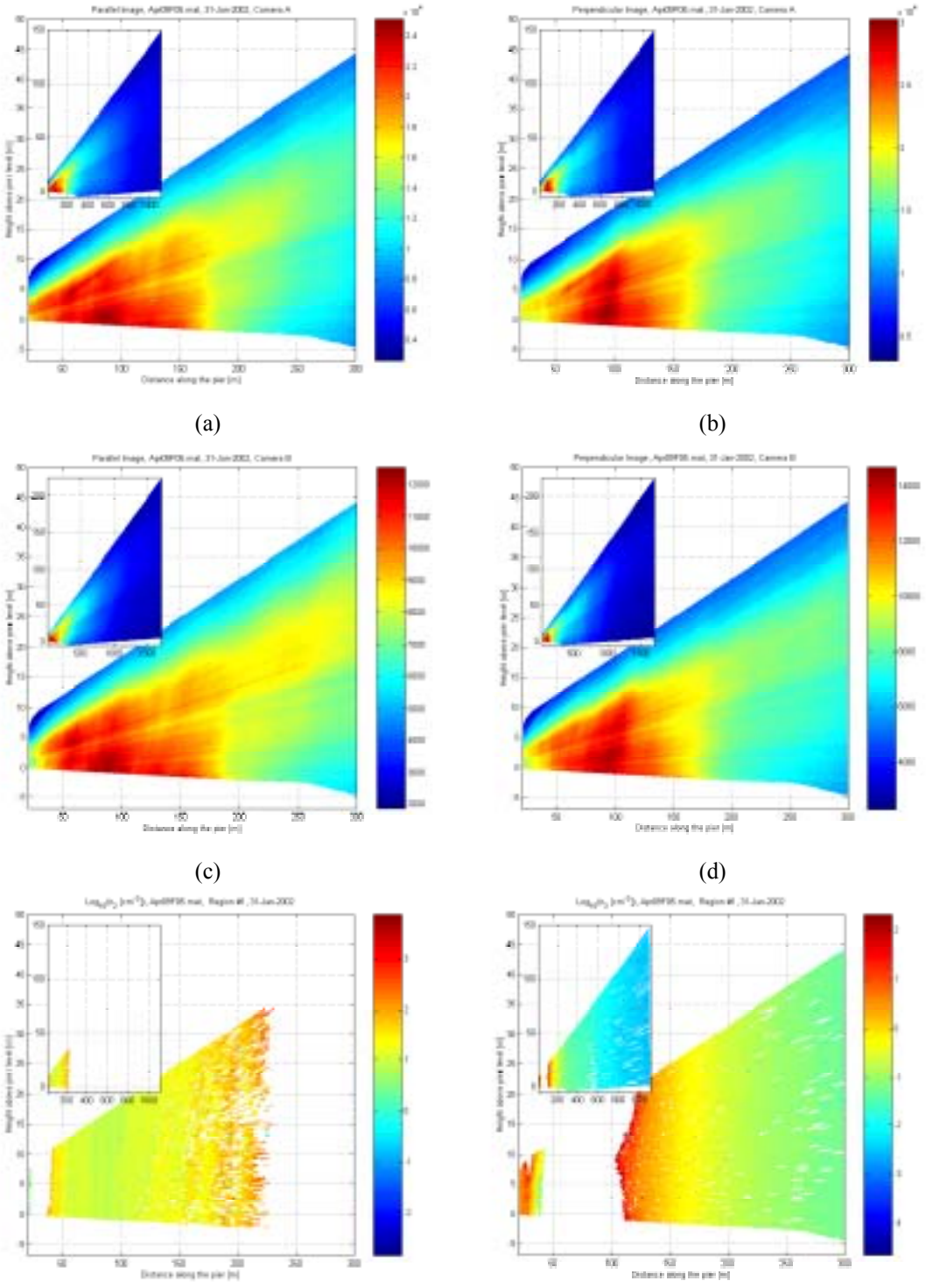

(a) (b)

(c) (d)

(e) (f)

Figure J.9. Projection along the pier of the intensity of the mean EOPACE images captured over a 300 second exposure time by (a) camera A at parallel outgoing polarization, (b) camera A at perpendicular outgoing polarization, (c) camera B at parallel outgoing polarization, and (d) camera B at perpendicular outgoing polarization. Estimated concentrations from image set Apr09F05 using (a) both cameras A and B for mode 2 and (b) camera A for mode 3.

APPENDIX K
BI-DIMENSIONAL CONDITION NUMBERS AND ESTIMATED CONCENTRATIONS OF MODES 0, 1, AND 4

Common approaches consisted in restricting the analysis to positive concentrations (in cm^{-3}) compressed by a logarithmic (base 10) scale from which a histogram was plotted and a visual maximum-likelihood criterion was applied. Typical values estimated in Chapter 2 are $\log_{10}(n_0) \approx -3.3$, $\log_{10}(n_1) \approx -3.3$, $\log_{10}(n_2) \approx 1.48$, $\log_{10}(n_3) \approx -0.125$, $\log_{10}(n_4) \approx -15$. All the following images were restored under the following directives: mean relative humidity, cameras A and B together, 3 pixels per camera, and expect modes 0 to 4 (mode -1 is implicitly present).

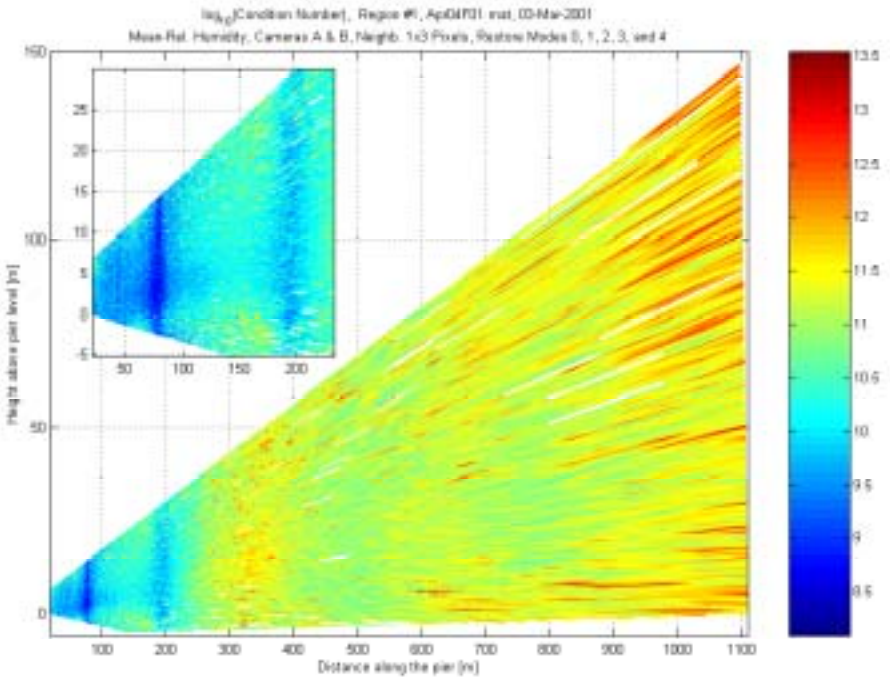

(a)

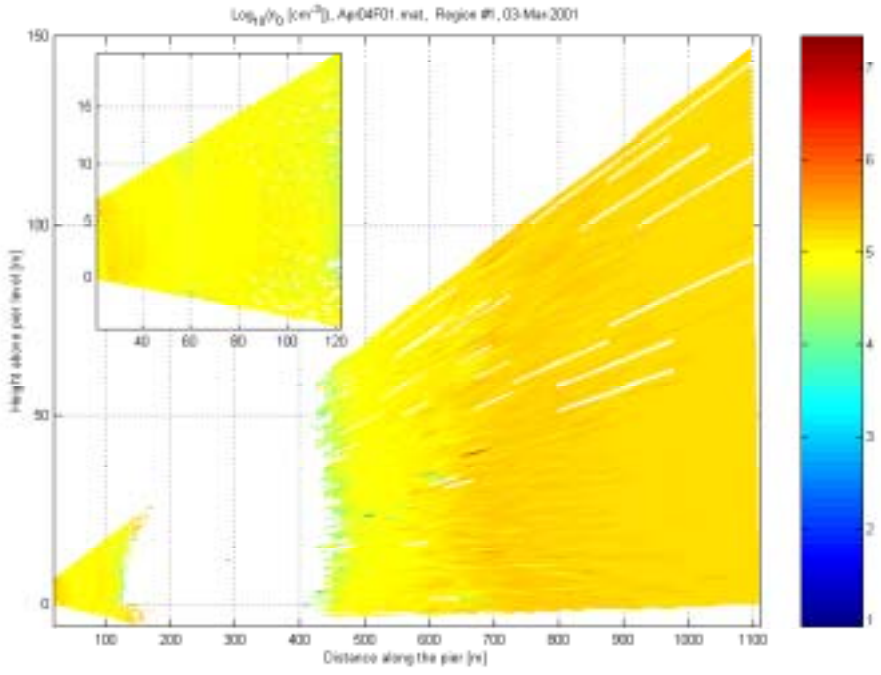

(b)

Figure K.1. (a) Condition number and (b) estimated concentrations for mode 0 from file Apr04F01.

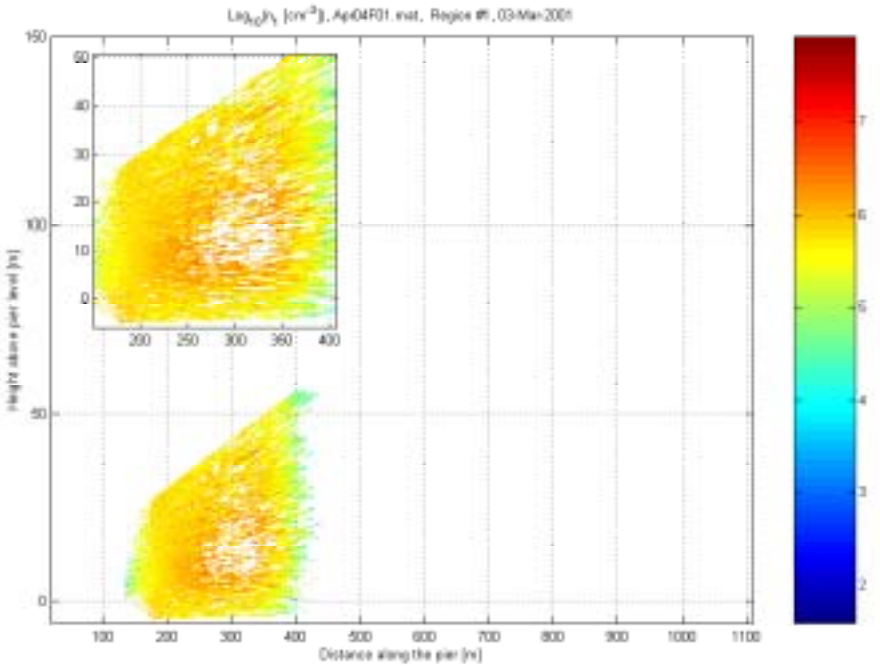

(a)

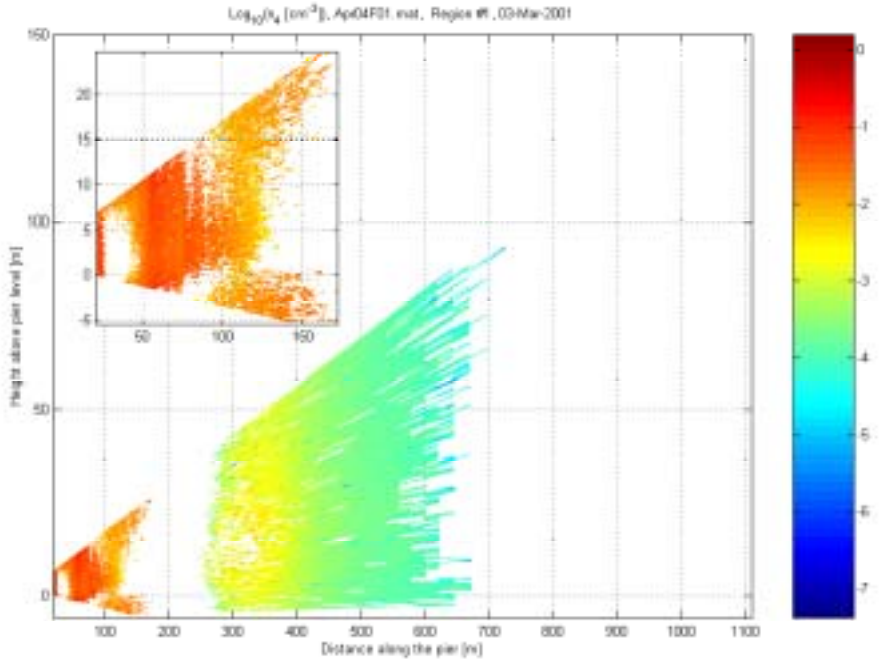

(b)

Figure K.2. Estimated concentrations from file Apr04F01 for (a) mode 1 and (b) mode 4.

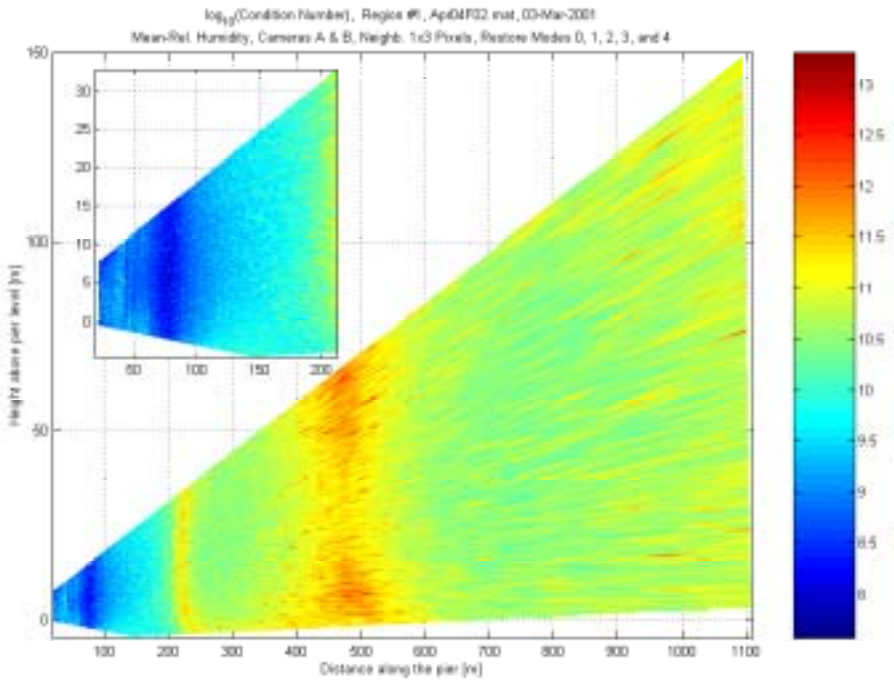

(a)

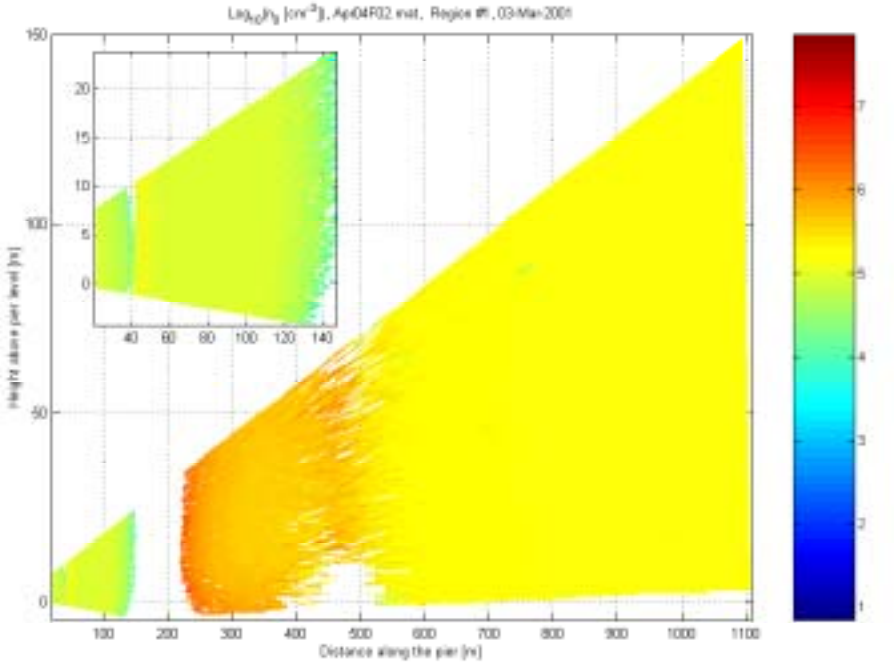

(b)

Figure K.3. (a) Condition number and (b) estimated concentrations for mode 0 from file Apr04F02.

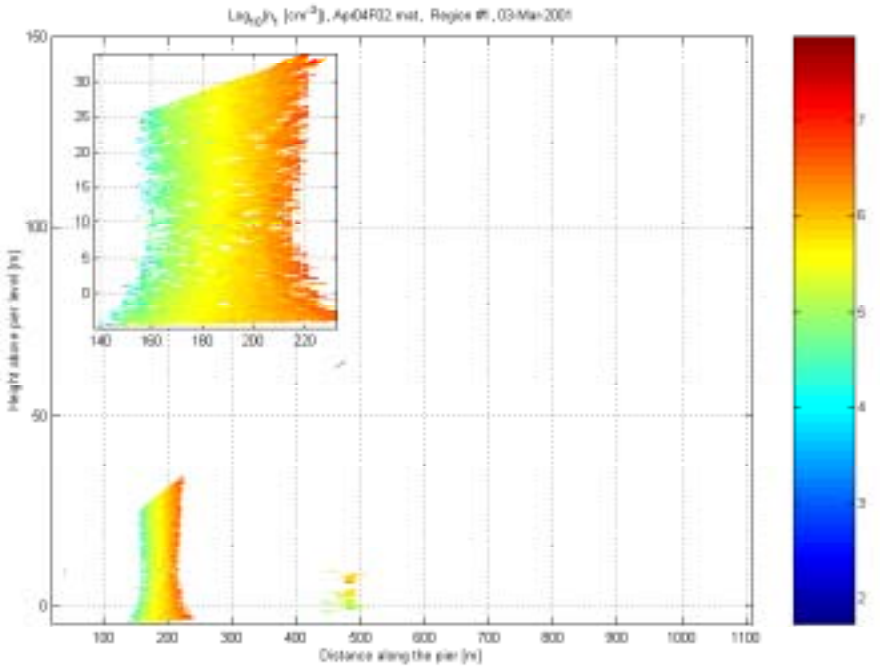

(a)

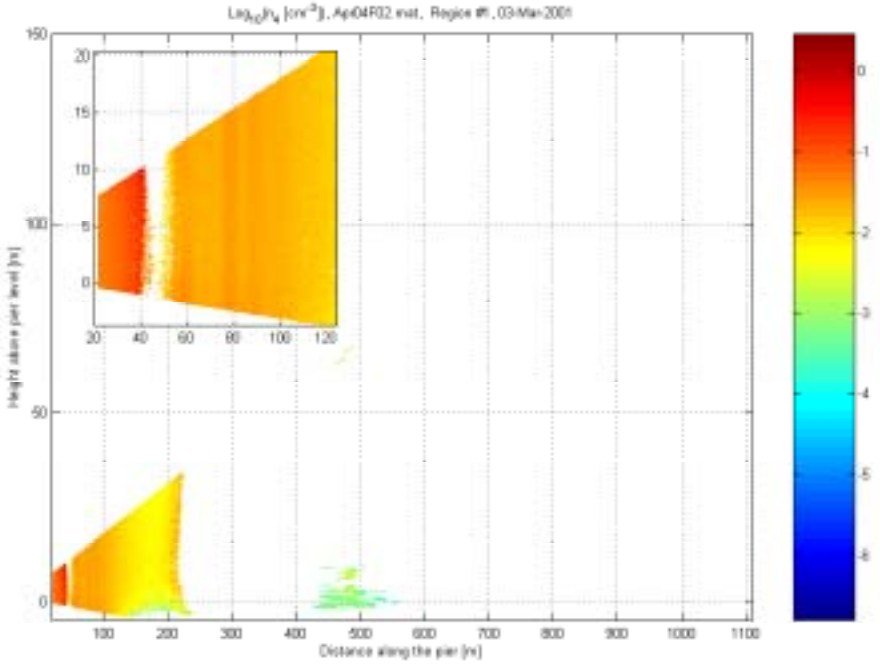

(b)

Figure K.4. Estimated concentrations from file Apr04F02 for (a) mode 1 and (b) mode 4.

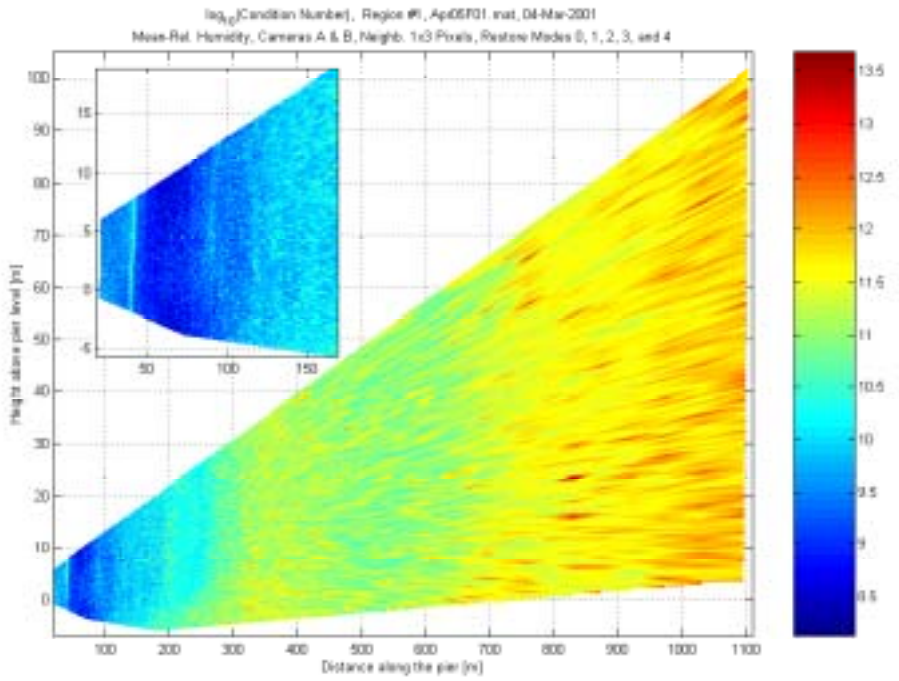

(a)

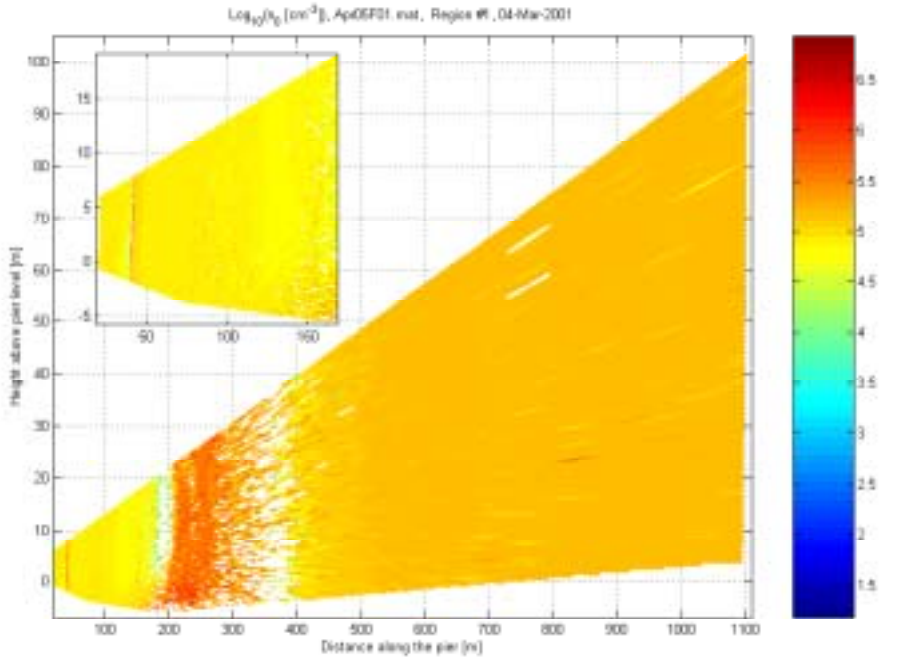

(b)

Figure K.5. (a) Condition number and (b) estimated concentrations for mode 0 from file Apr05F01.

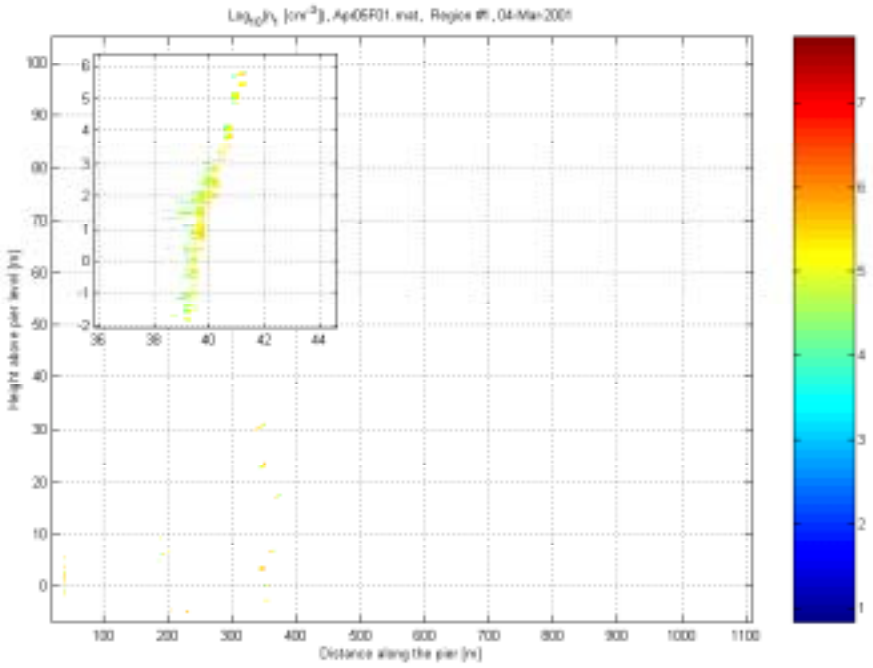

(a)

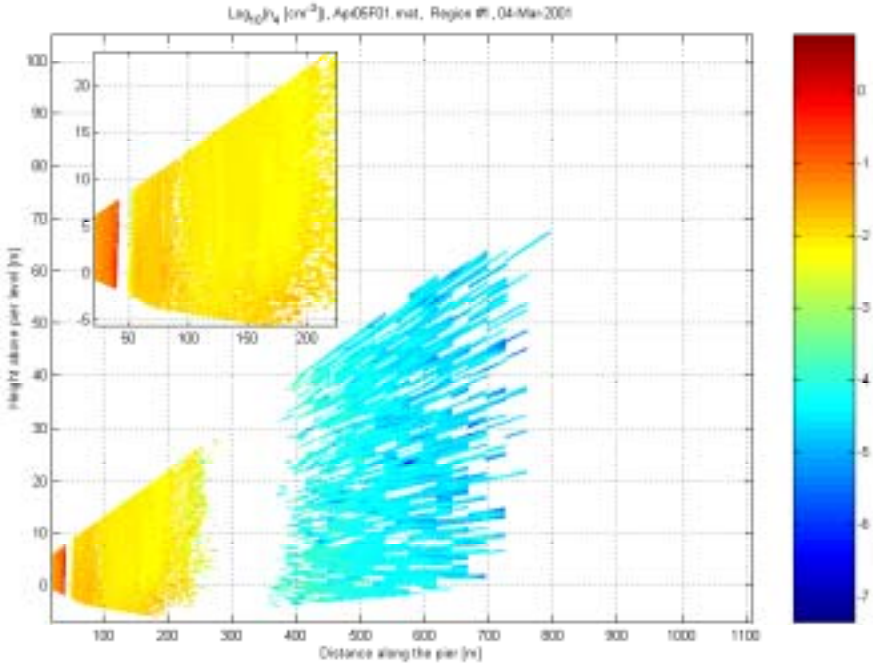

(b)

Figure K.6. Estimated concentrations from file Apr05F01 for (a) mode 1 and (b) mode 4.

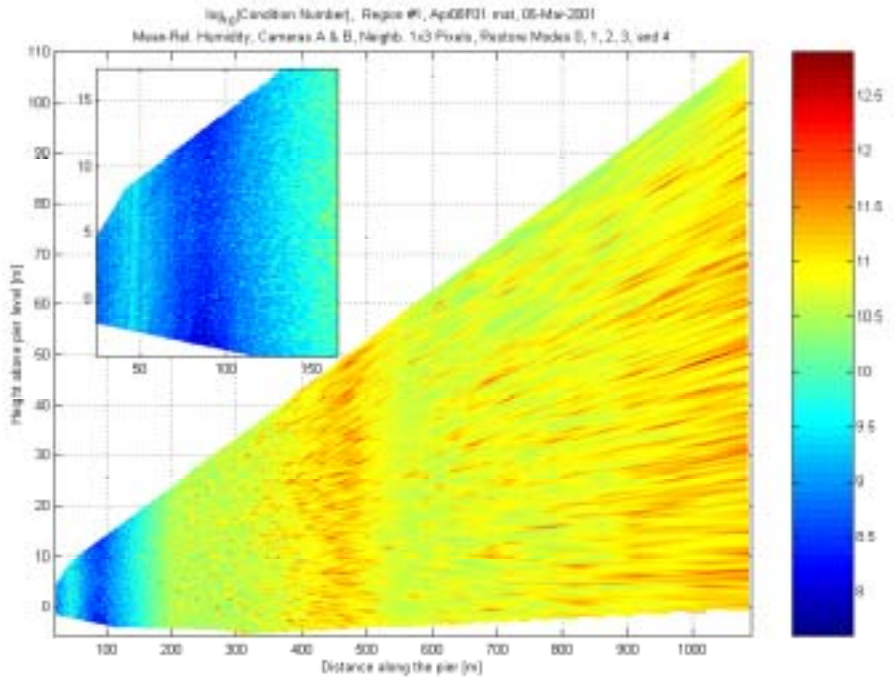

(a)

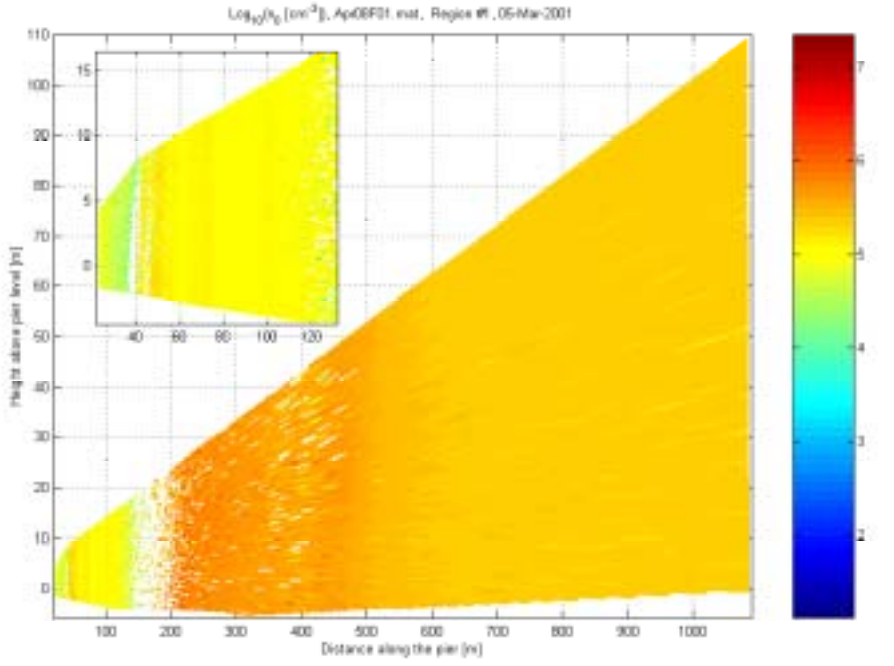

(b)

Figure K.7. (a) Condition number and (b) estimated concentrations for mode 0 from file Apr08F01.

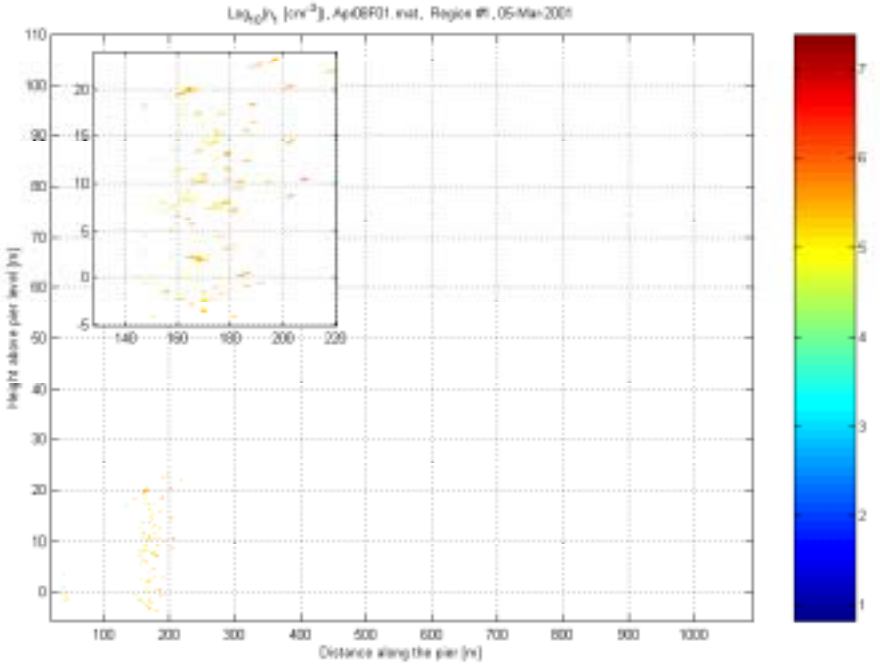

(a)

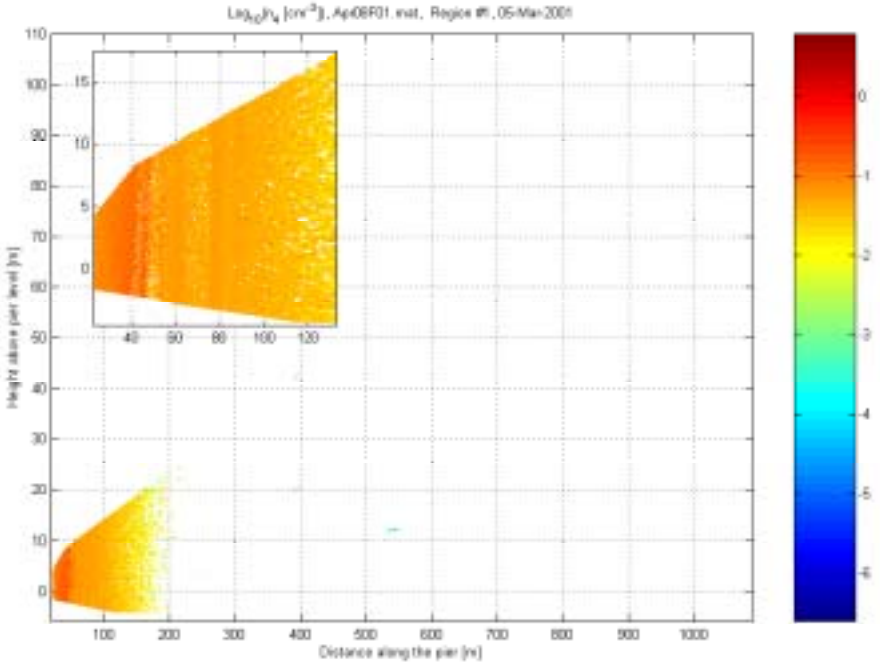

(b)

Figure K.8. Estimated concentrations from file Apr08F01 for (a) mode 1 and (b) mode 4.

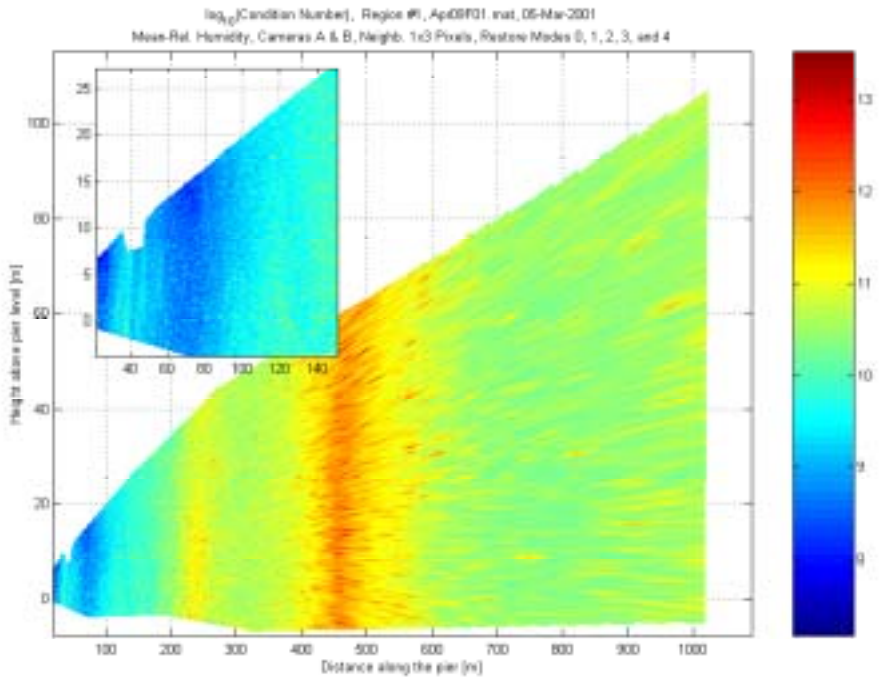

(a)

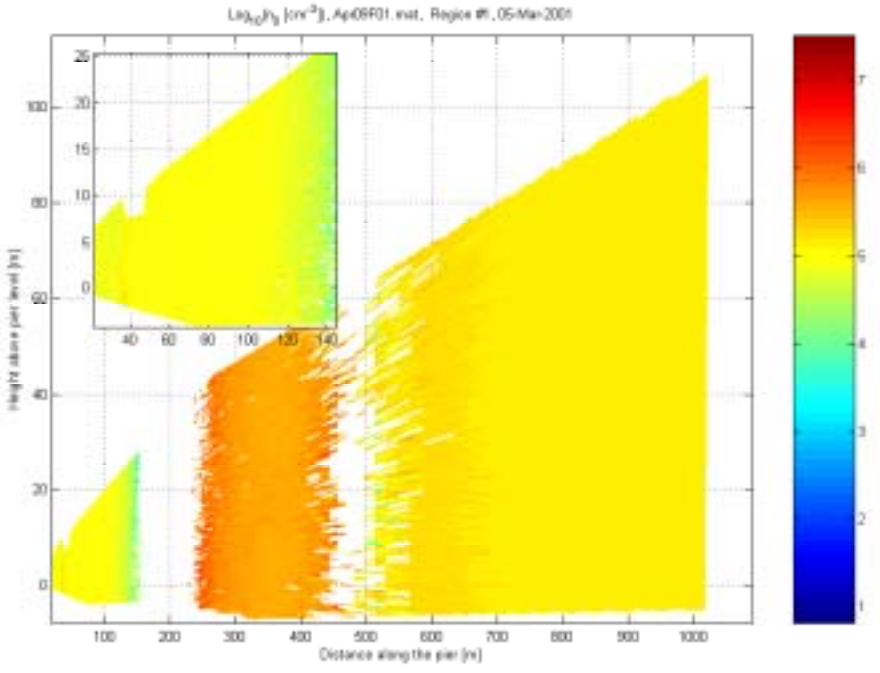

(b)

Figure K.9. (a) Condition number and (b) estimated concentrations for mode 0 from file Apr09F01.

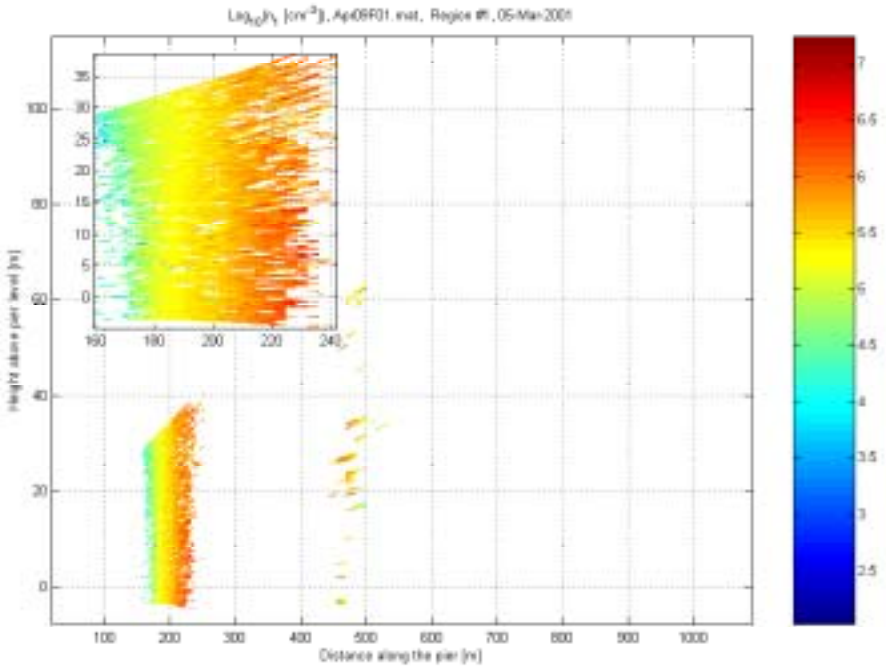

(a)

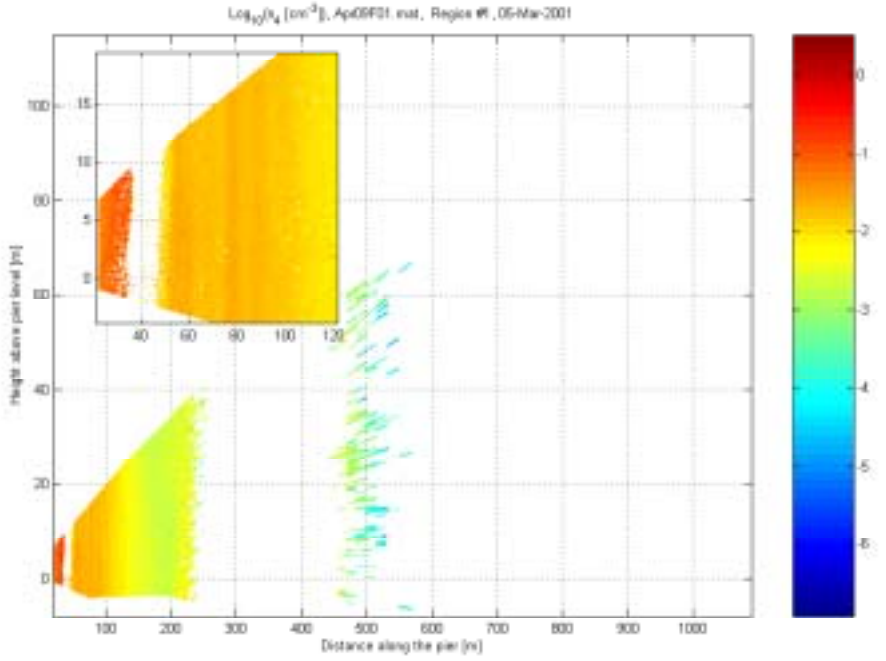

(b)

Figure K.10. Estimated concentrations from file Apr09F01 for (a) mode 1 and (b) mode 4.

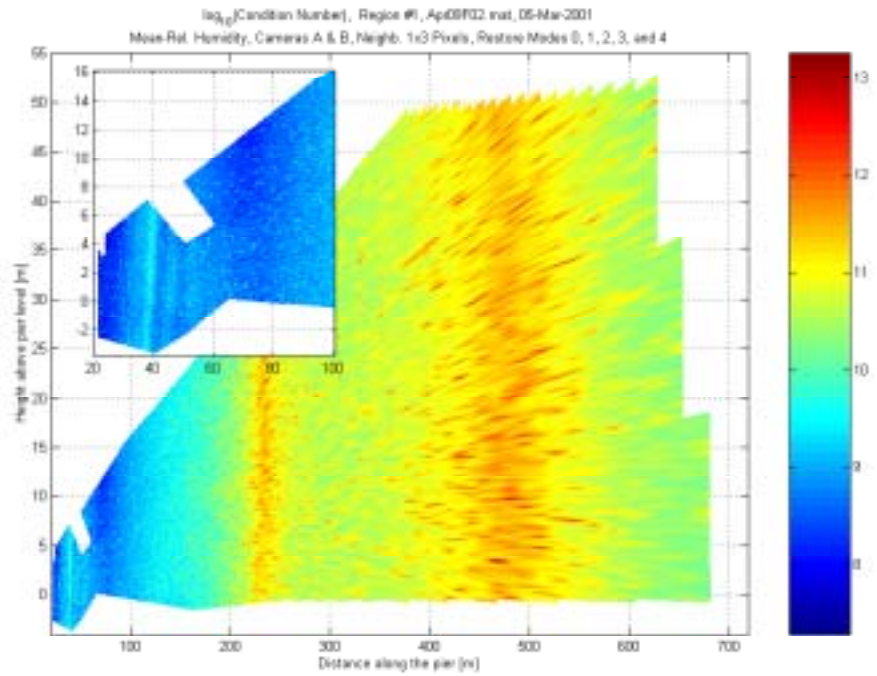

(a)

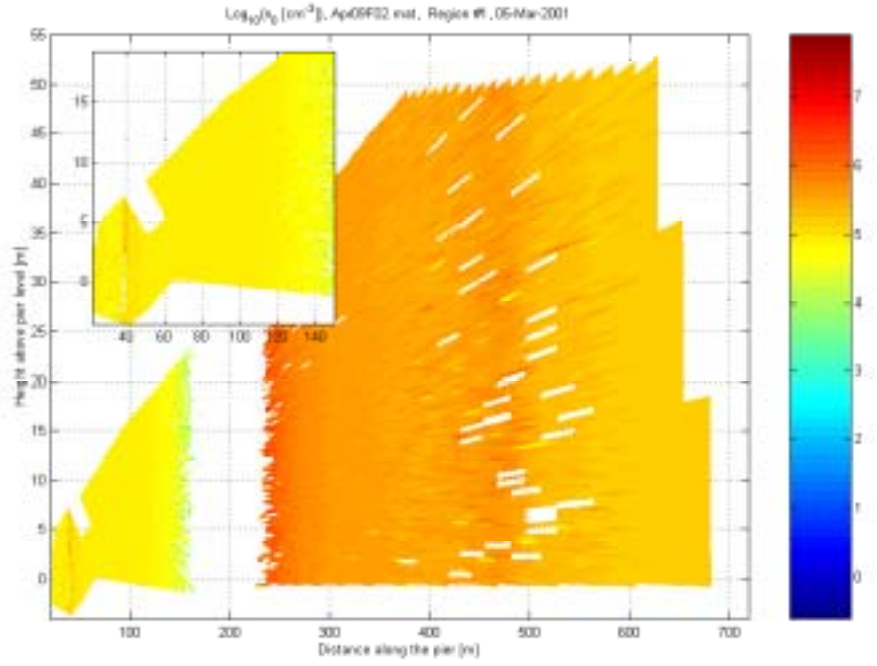

(b)

Figure K.11. (a) Condition number and (b) estimated concentrations for mode 0 from file Apr09F02.

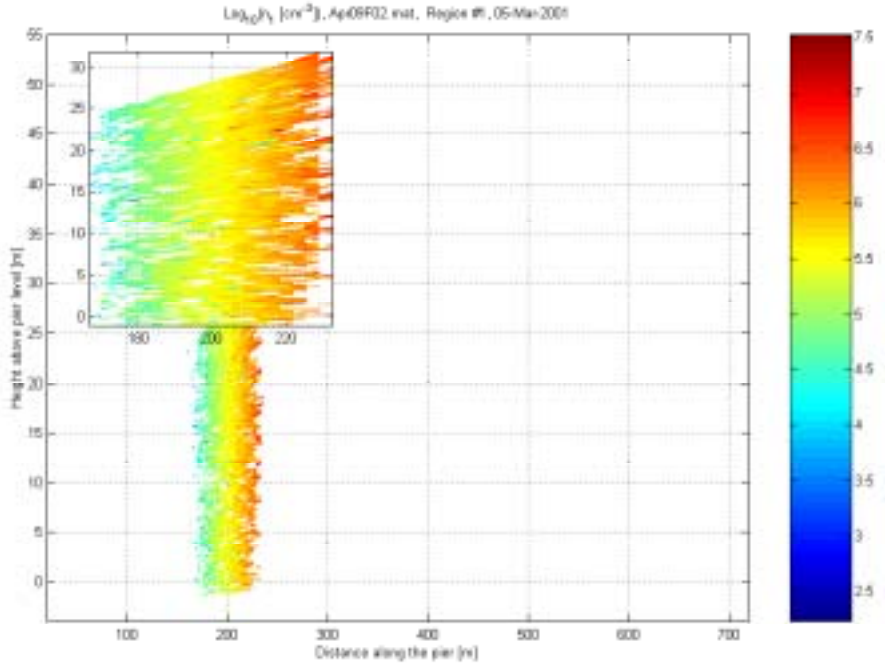

(a)

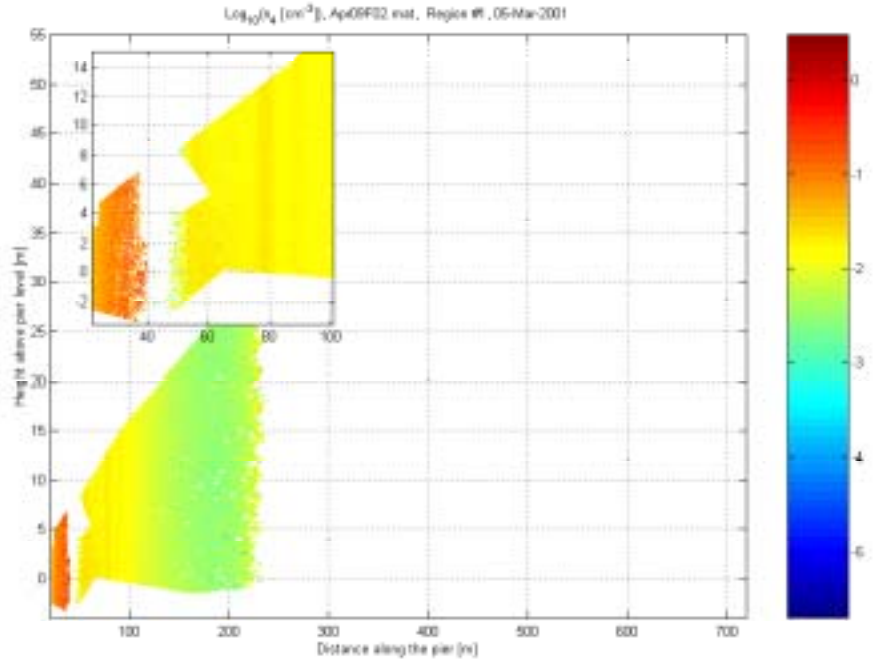

(b)

Figure K.12. Estimated concentrations from file Apr09F02 for (a) mode 1 and (b) mode 4.

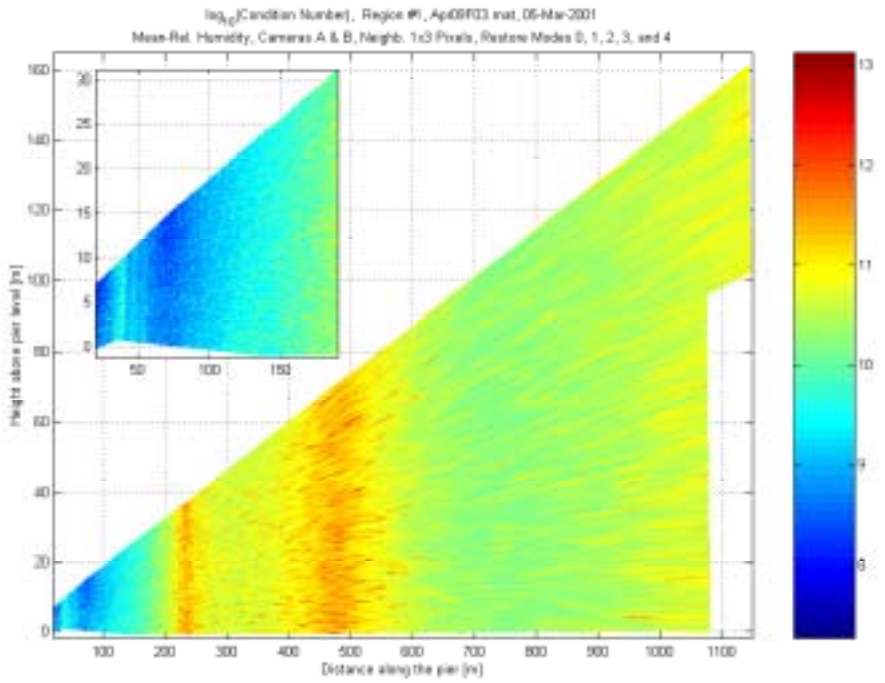

(a)

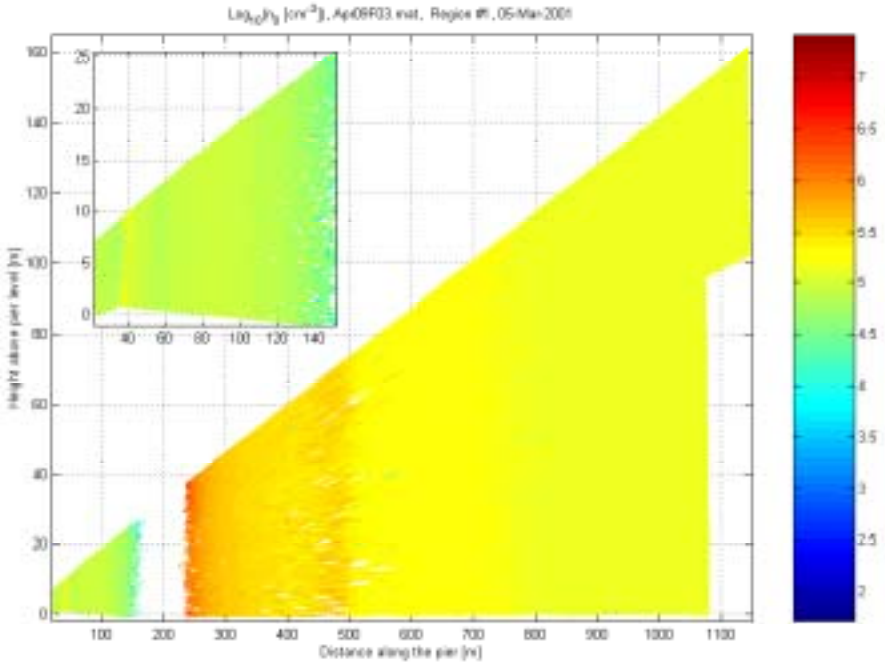

(b)

Figure K.13. (a) Condition number and (b) estimated concentrations for mode 0 from file Apr09F03.

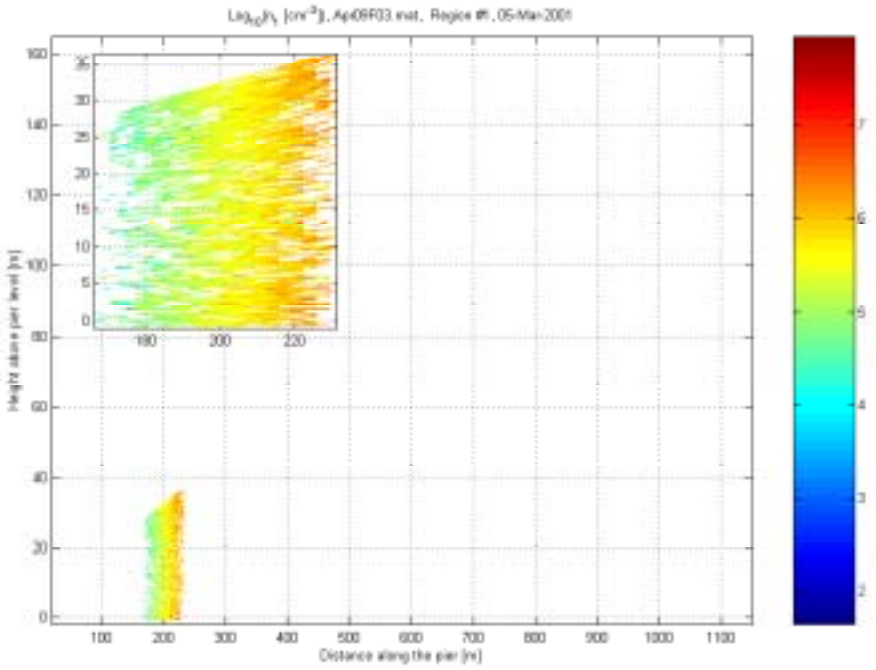

(a)

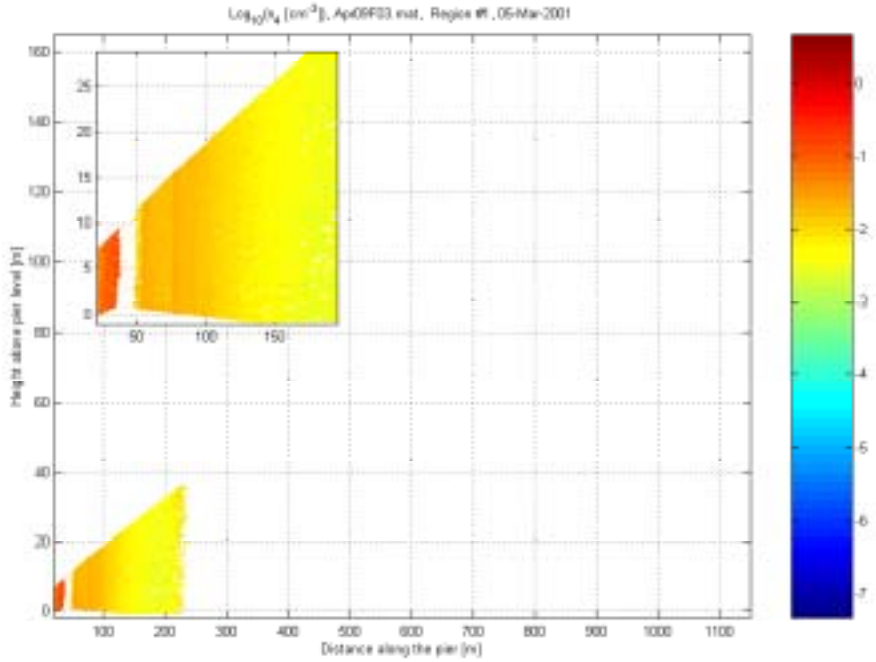

(b)

Figure K.14. Estimated concentrations from file Apr09F03 for (a) mode 1 and (b) mode 4.

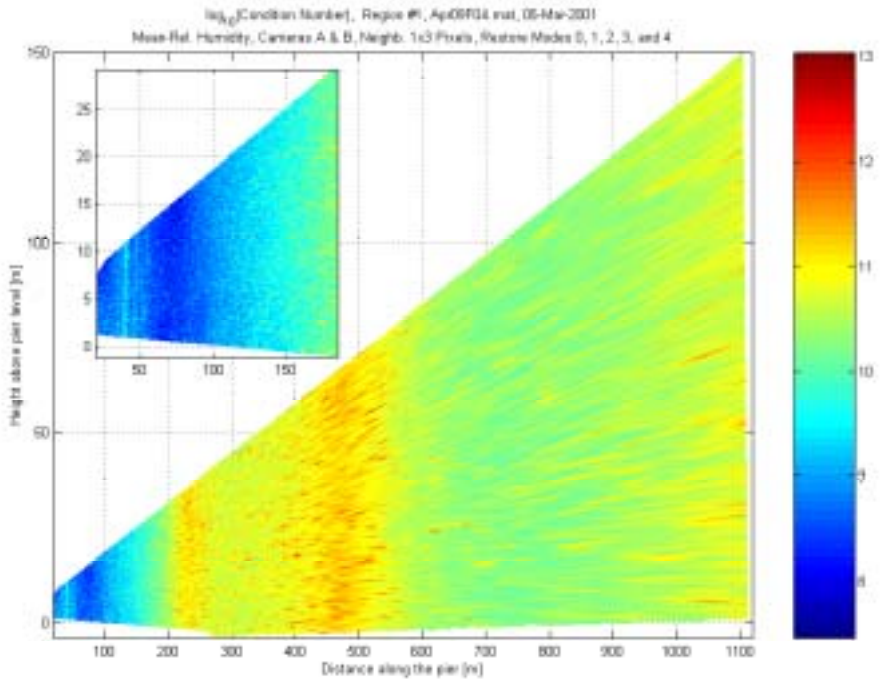

(a)

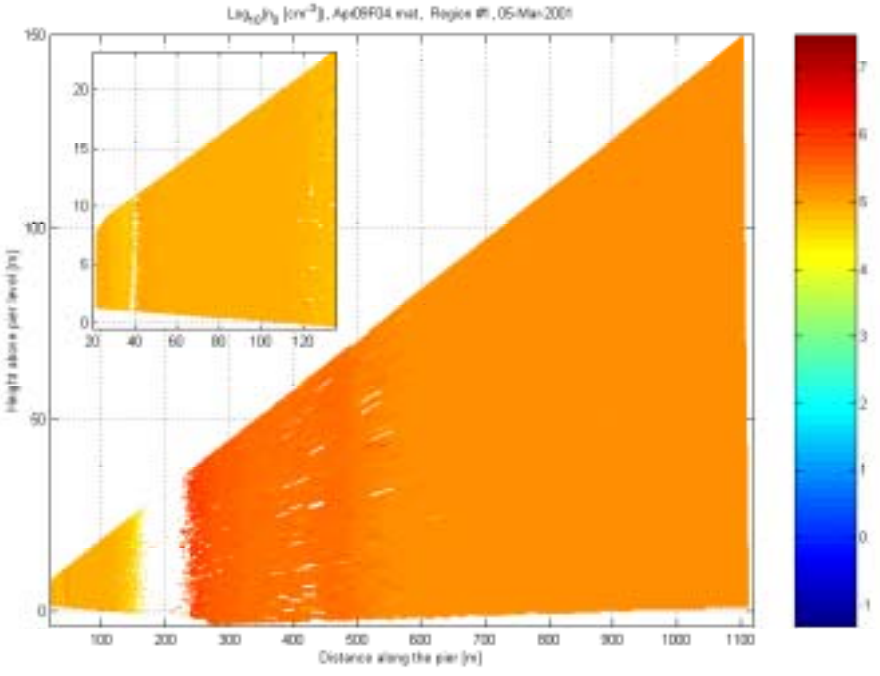

(b)

Figure K.15. (a) Condition number and (b) estimated concentrations for mode 0 from file Apr09F04.

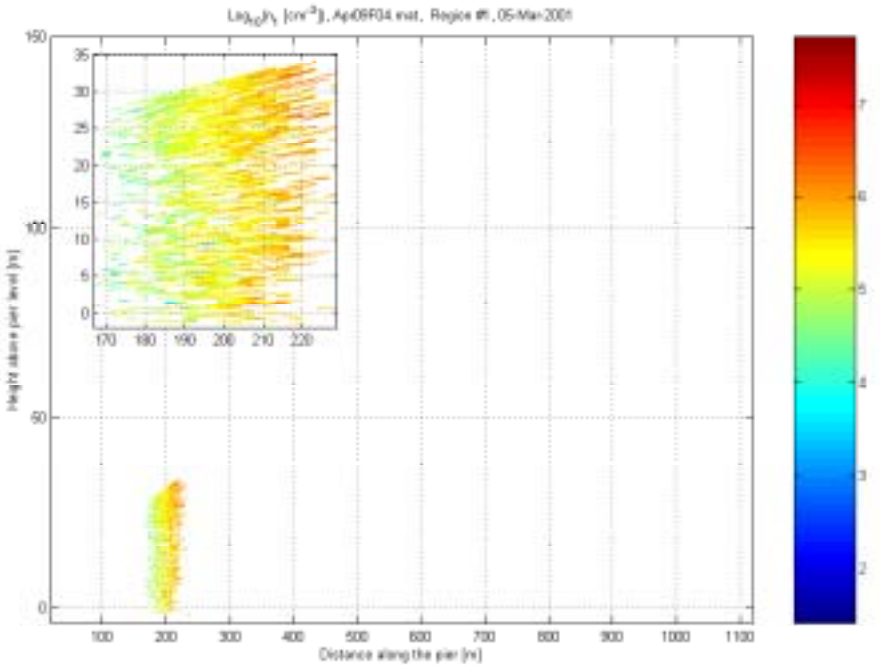

(a)

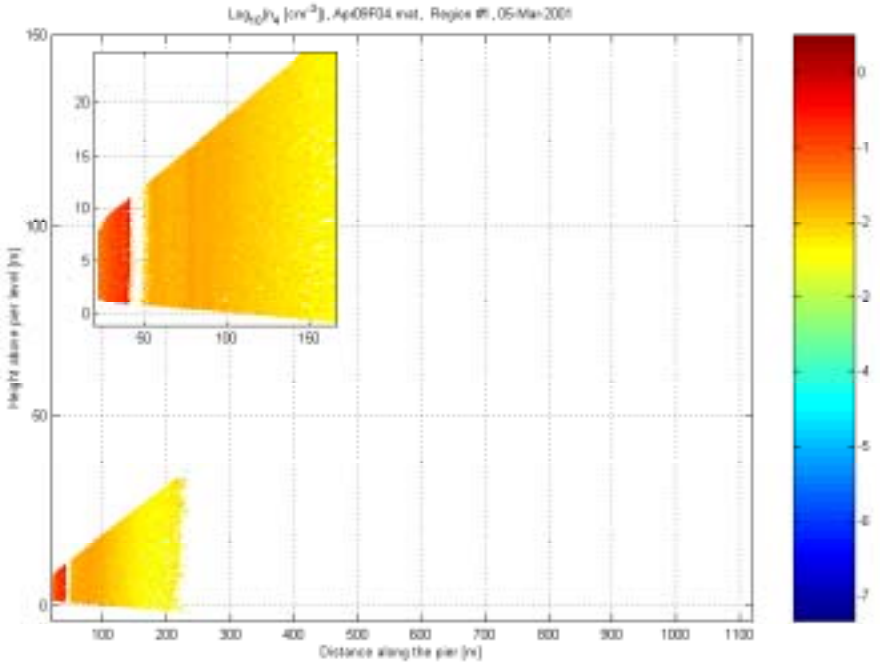

(b)

Figure K.16. Estimated concentrations from file Apr09F04 for (a) mode 1 and (b) mode 4.

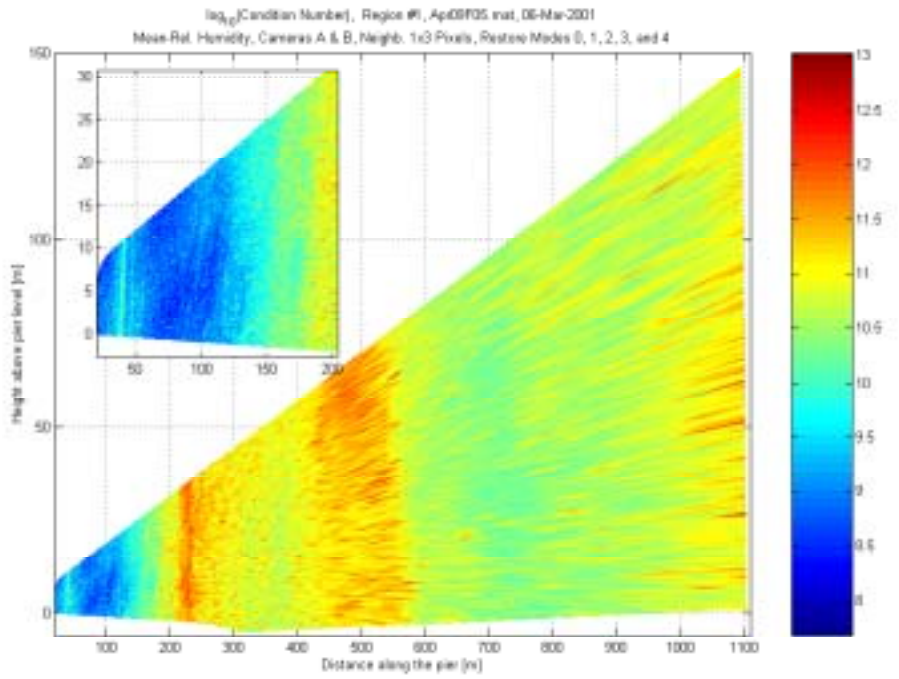

(a)

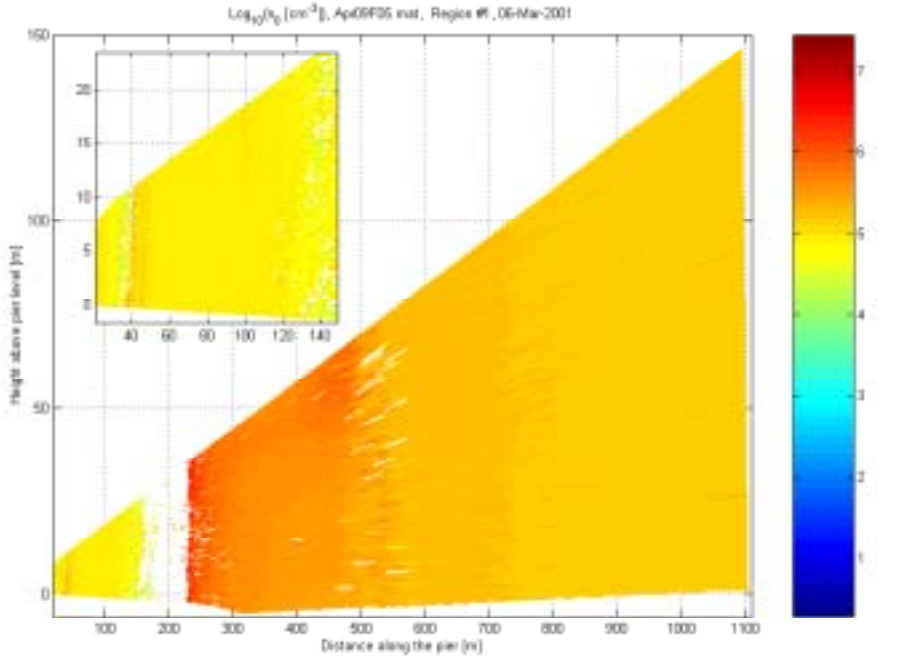

(b)

Figure K.17. (a) Condition number and (b) estimated concentrations for mode 0 from file Apr09F05.

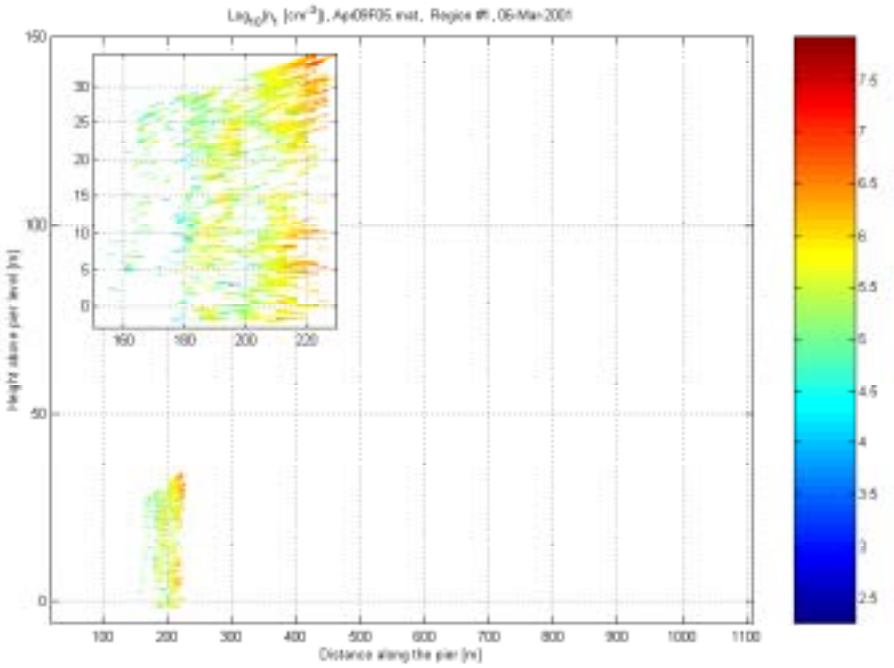

(a)

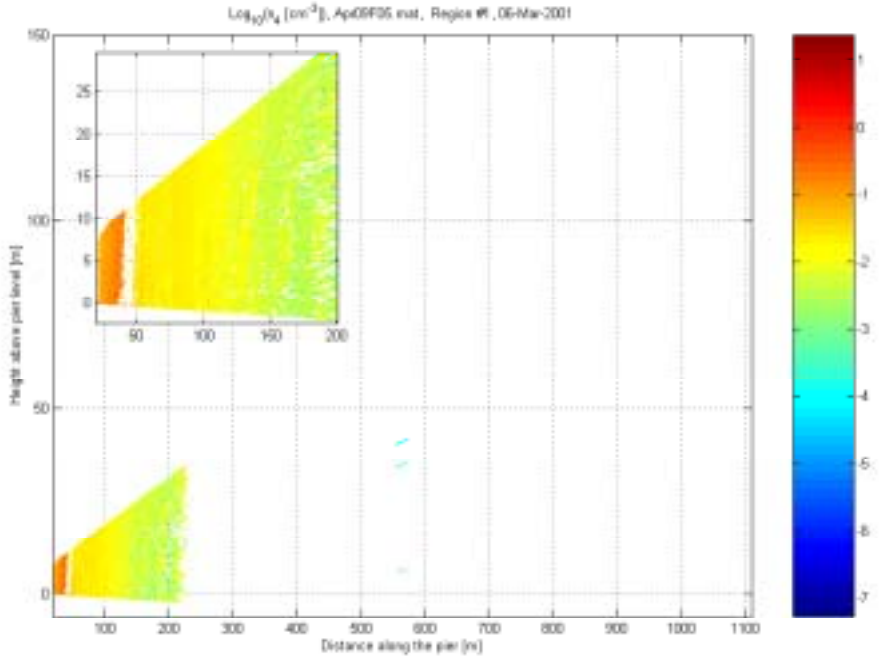

(b)

Figure K.18. Estimated concentrations from file Apr09F05 for (a) mode 1 and (b) mode 4.

APPENDIX L
INFLUENCE OF TIME ON EOPACE ESTIMATED CONCENTRATIONS

The present appendix aims at assessing the stability of the restored concentrations upon decreasing to a single pair the number of images of complementary polarization being processed. Any noticeable change would suggest a refinement in the estimation of the concentrations from a distribution of averaged aerosols above the surf-zone to those of the plumes themselves.

As described in Chapter 3, images within the same set have the same exposure time, but all of them have been captured over consecutive time frames (as opposed to overlapping ones). Chapter 4 combined all images of the same polarization prior to restoration to approach the conditions under which the rotorod measurements took place. The analytical procedure consists of four consecutive steps: (1) the composition of image sets of complementary outgoing polarization, (2) the bi-dimensional restoration of concentrations of modes 2 and 3 from the image sets, (3) their reduction to a single concentration per mode based on the visual maximum log-likelihood criterion (cf. footnote #22), (4) an arithmetic average (in the logarithmic domain) of the reduced concentrations obtained from the image sets composed of the same number of images, and (5) plot the resulting concentrations. Images from 4 configuration-files (cf. Appendix H for their definitions) have been analyzed: Apr04F01, Apr04F02, Apr05F01, and Apr08F01. The respective exposure time of each image within each set was 5, 30, 300, and 300 seconds.

Figure L testifies that all modes are appreciably stable, independently of the number of images included in the restoration. Hence, information about the plumes themselves is not accessible via the polarization ratio method. This observation should come as no surprise as Chapter 3 has already shown that an erroneously estimated transmittance through the retarder plate results in significant errors in the estimated concentrations (equivalently, the motion of the surf-zone plumes between images of complementary polarization can be seen as an error in transmittance). Interestingly enough, those areas have in many occasions resulted in local negative concentrations, ignored during analyses in the logarithmic domain.

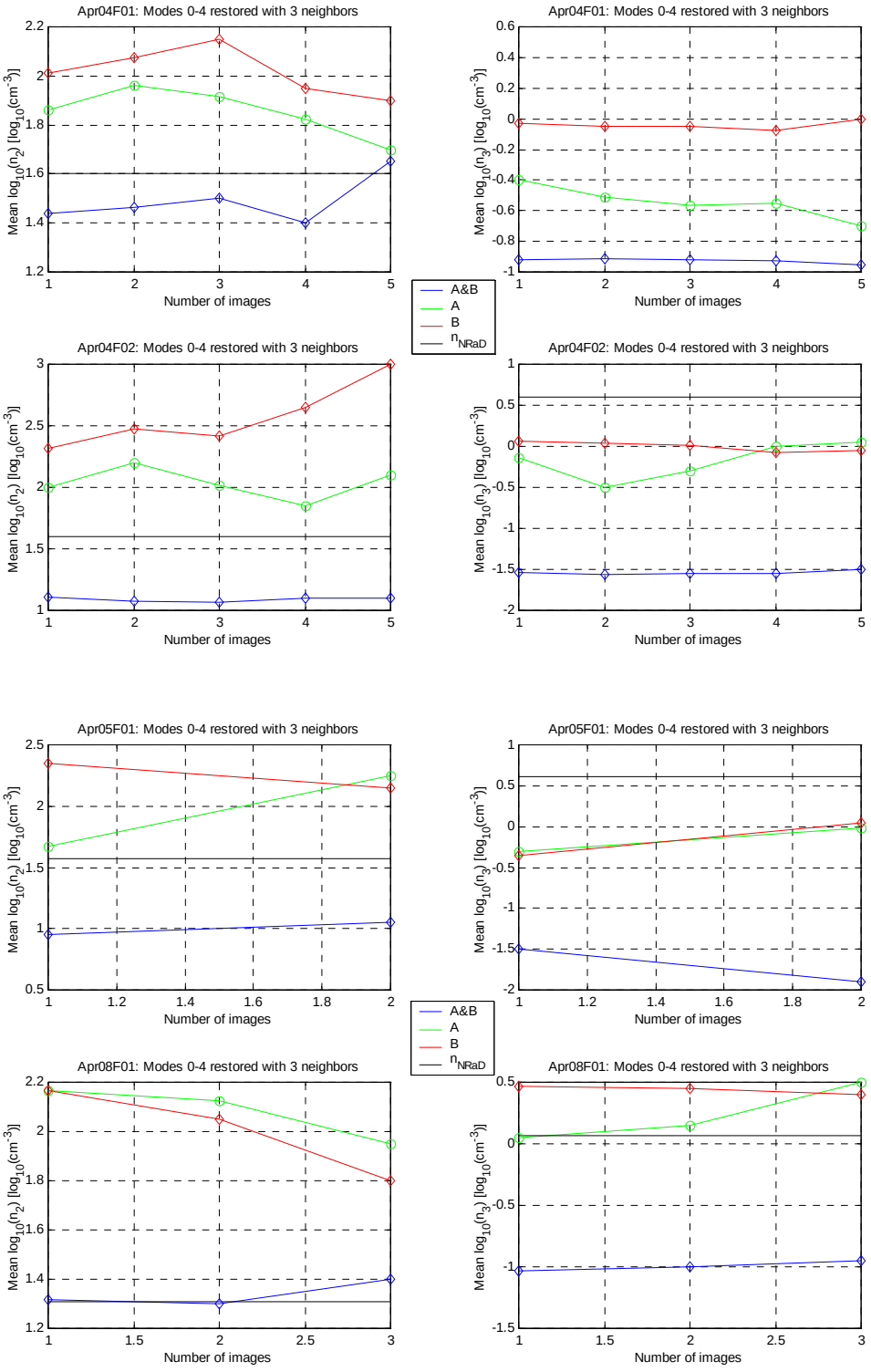

Figure L. Maximum log-likelihood estimated concentrations (cf. footnote #22) as the number of averaged images before applying the restoration procedure is reduced. The left (right) column displays mode 2 (3). The configuration filenames are specified in the title of the each figure. The plots show relatively stable modes, independently of the number of images used in the restoration.

APPENDIX M
INFLUENCE OF THE SIZE OF A NEIGHBORHOOD ON EOPACE ESTIMATED CONCENTRATIONS

One of the estimation directives is concerned with the choice in the number of neighboring pixels associated with a central pixel to estimate the concentrations of that central pixel (cf. Subsection 3.2.2). Chapter 3 has shown that increasing the number of neighbors improves the quality of the estimated concentrations, provided that systematic errors be corrected (otherwise, the redundancy in systematic errors in each pixel drives the estimated concentrations further away from the actual concentrations).

Figure M.1(a,b) shows the polarization ratios calculated from the images captured by cameras A and B, separately, as processed by Eq. (3.3). Figures M.1(c-f) and M.2(a-f) display the estimated bi-dimensional concentrations of modes 2 and 3 obtained from associating various numbers of pixels into neighborhoods (from 25 to 165 pixels). The neighborhoods form horizontal lines of pixels approximately covering 0.8° to 5.6° simultaneously (calculated by multiplying the number of pixels minus one by 0.034° between adjacent pixels).

The features described by modes 2 and 3 vary significantly as the size of a neighborhood is changed, confirming that the heterogeneity of the length-scales produces inhomogeneous distributions of scatterers above the surf-zone. This observation upholds the choice of a minimum neighborhood-size in Chapter 4, followed by a statistical rule to estimate the most likely concentration of each mode.

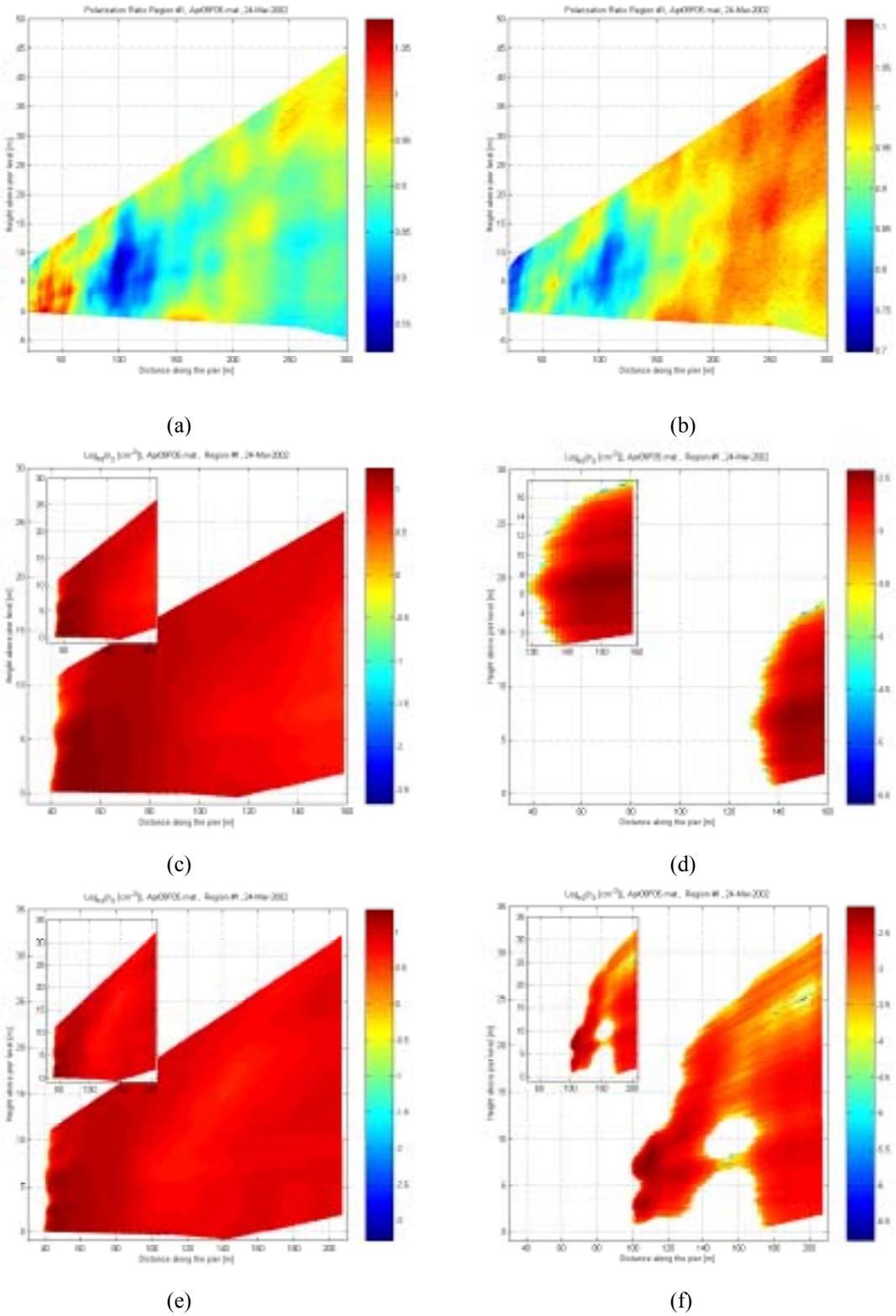

Figure M.1. Bi-dimensional polarization-ratios calculated from the mean EOPACE images of (a) camera A and (b) camera B. The spatial distribution of the concentrations of mode 2 estimated by simultaneously combining (c) 165 and (e) 125 neighborhood pixels. The spatial distribution of the concentrations of mode 3 estimated by simultaneously combining (d) 165 and (f) 125 neighborhood pixels.

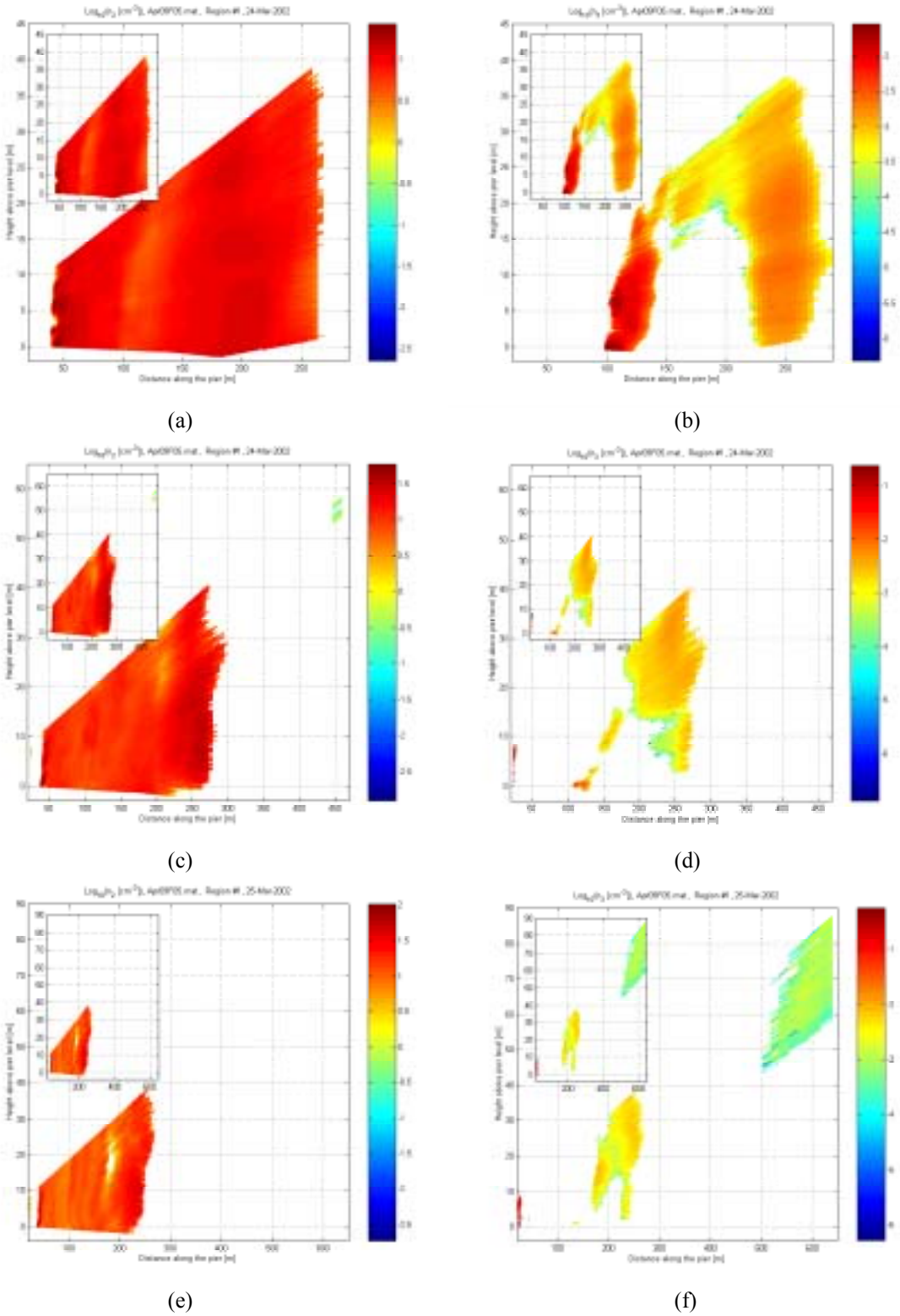

(a) (b)

(c) (d)

(e) (f)

Figure M.2. The spatial distribution of the concentrations of mode 2 estimated by simultaneously combining (a) 85, (c) 45, and (e) 25 neighborhood pixels. The spatial distribution of the concentrations of mode 3 estimated by simultaneously combining (b) 85, (d) 45, and (f) 25 neighborhood pixels.